

An Analysis of the Hotforming Process for High Strength Aluminium Sheet Metal Alloys

by

Julian Marc Schlosser, M.Sc.



PhD Thesis

A thesis submitted in partial fulfilment of Glasgow Caledonian University requirements
for the degree of Doctor of Philosophy

This research programme was carried out in collaboration with
Aalen University

July 2020

Abstract

Forming complex parts out of high and ultra-high strength aluminium alloys has proved to be more challenging in comparison to the currently used deep drawing steels. Nevertheless, aluminium alloys show a limited formability in contrast with, for example, deep drawing steels. Novel processes like Warm-forming, W-Temper or Hotforming, offer the potential to produce light and highly integrated one-piece components from such aluminium alloys at elevated temperatures. When considering aluminium alloys of the 7000 group, which can reach strength values (UTS) of about 600 MPa, crash components such as side impact bars would offer a suitable field of application.

Forming at elevated temperatures, in particular with the Hotforming process, offers high potential in the production of complex structural components on the one hand and in the use of existing press hardening equipment on the other. To date, the material behaviour of aluminium alloys in the 7000 group, applied in such processes and in the later final state after forming, is not sufficiently known.

Therefore, in this study, systematic investigations on the formability and the final strength during and after forming at elevated temperature of the EN AW-7075 aluminium wrought alloy from different suppliers are conducted. In general, material- and damage/failure models were created and implemented into simulation in order to make predictions. Characterisation of the plastic material properties on the basis of various tensile specimens as shear-, notched-, tensile- and Erichsen tests are carried out to adapt the complex material- and failure models such as Barlat YLD2000 and GISSMO to the experimental values using a parameter optimisation. These were made for the material conditions during forming, i.e. after solution heat treatment, the final condition after artificial ageing at 180°C for 20 minutes, which corresponds to the cathodic dip coating, and the T6 condition, which is the highest strength condition.

To evaluate a suitable friction coefficient for high temperature forming processes, anti-friction agents are screened, and the potential applicability evaluated by strip-drawing tests. Thereby, using an analytical relationship, friction coefficients are determined at room temperature and 180°C, which are used as corresponding friction model for the finite element forming simulation.

Crash simulations using the nonlinear finite element method (FEM) of side impact protection beams are used to demonstrate the weight saving potential of high and ultra-high strength aluminium alloys compared to a beam made of press hardened steel. A weight saving of about 20 % could be achieved with the same crash performance. This can be significantly increased to around 30 % - 40 % by using local reinforcements such as CFRP or GFRP (carbon/ glass fibre reinforced plastic) patch. For this reason, a novel process was developed which is based on the conventional Hotforming process with an integrated thermal direct joining step called "Extended Hotforming".

Subsequently, a heatable forming tool for the production of a serial like sheet metal side impact beam was developed to validate the finite element simulation and to demonstrate the potential of the forming processes at elevated temperatures for aluminium sheet metal components.

Acknowledgements

This thesis was done in collaboration with Aalen University and Glasgow Caledonian University between October 2016 and May 2020.

First and foremost, I would like to thank my supervisors, Professor Dr. David Harrison, Professor Dr. Martin Macdonald and Dr. Muditha Kulatunga, from the School of Engineering and Built Environment at Glasgow Caledonian University, for their helpful comments and unlimited support they have given to me throughout this work.

Furthermore, I would like to give special thanks to my supervisor and mentor from Aalen University, Dr. Wolfgang Rimkus, for his advice, all the helpful thoughts and inspiring discussions as well as for his overall and ongoing support and encouragement. Dr. Wolfgang Rimkus gave me the opportunity to start with the research project at Aalen University. During the project, he guided me through rough times and gave me the freedom I needed.

I am also very grateful to my local adviser and friend Prof. Dr. Robert Schneider from Ulm University of Applied Sciences (THU), for his scientific advice in materials sciences, forming technology and suggestions in general. He actively supports me in every situation. I am proud to have such a friend.

A further special thank you goes to my colleagues Serkan Mouchtar M.Sc., Michael Schmiedt M.Sc. and Tuncay Al M.Sc. for all the inspiring talks and their helpful assistance during the course of this work. I would also like to give sincere thanks to Prof. Dr. Lothar Kallien, Prof. Dr. rer. nat. Burkhard Heine and their laboratory directors Dipl.-Ing. Thomas Wolfgang Weidler and Mr. Wilfried Salzwedel for their helpful assistance.

Thank you.

Dedication

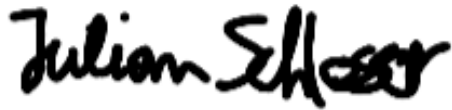
This thesis is dedicated to my family, without whom none of this would have been even possible. A special thank you goes to Jasmin, my caring and understanding wife, who has been supporting my work with energy and faith. Last, but not least, I would like to thank all my friends for their encouragement and support during the creation of this work.

“Making the best out of every day, that is the highest art.”

Henry David Thoreau

Author's Declaration

I declare that this thesis is original and my own work and that all material not my own has been identified and referenced.

A handwritten signature in black ink, reading "Julian Schlosser". The script is cursive and fluid, with the first name "Julian" and last name "Schlosser" clearly distinguishable.

Signed

21.07.2020

Date

Published Work

1. Schneider R., Grant R. J., Schlosser J. M., Rimkus W., Radlmayr K., Grabner F., Maier C. (2020): “An Investigation of the Deep Drawing Behavior of Automotive Aluminum Alloys at Very Low Temperatures”, Metall and Mat Trans A, May 2020, pp. 1123-1133, DOI 10.1007/s11661-019-05584-4
2. Schlosser J. M., Mouchtar S., Rimkus W., Schneider R. (2019): “Design optimisation of a side impact beam made out of high strength aluminium alloys using Barlat YLD2000 and GISSMO failure model for the Extended Hotforming Process”, 12. European LS-DYNA Conference, 14.-16. May 2019, Koblenz
3. Schlosser J. M., Rimkus W., Mouchtar S., Schneider R., Harrison D. K., Macdonald M. (2018): “Ermittlung und Optimierung von temperaturabhängigen Versagenskurven für hochfeste Aluminiumlegierungen im Hotforming-Prozess“ (engl. “Determination and optimization of temperature-dependent failure curves for high strength aluminum alloys in the Hotforming process”), Technologietag Leichtbau, October 2018, Schwäbisch Gmünd
4. Schlosser J. M., Rimkus W., Mouchtar S., Schneider R., Harrison D. K., Macdonald M. (2018): “Determination and Optimisation of a Temperature-Dependent-Failure curve for High Strength Aluminium Alloys applicable for Hotforming”, 15. LS-DYNA Forum, 15.-17. October 2018, Bamberg
5. Schlosser J. M., Mouchtar S., Schneider R., Schanz J., Rimkus W., Harrison D. K., Macdonald M. (2018): “Characterisation and optimisation of a failure-model for high strength aluminium alloy”, Advances in Manufacturing Technology XXXII, 11.-13. September 2018, Skövde Schweden, pp. 399-404, DOI 10.3233/978-1-61499-902-7-399

6. Schlosser J. M., Schneider R., Rimkus W., Kelsch R., Gerstner F., Harrison D. K., Grant R. J. (2017): “Material and simulation modelling of a crash-beam performance – a comparison study showing the potential for weight saving using warm-formed ultra-high strength aluminium alloys”, *Journal of Physics: Conference Series*, September 2017, Vol. 896, pp. 12091, DOI 10.1088/1742-6596/896/1/012091
7. Schlosser J. M., Schneider R. (2017): “Material and simulation modelling of a crash-beam – potential for weight saving using warm-formed ultra-high strength aluminium alloys”, 36th IDDRG Conference material modelling and testing for sheet metal forming, 2.-6. July 2017, München
8. Wacker A., Schlosser J. M., Rimkus W. (2017): “Comparison of FEM software for topology optimization”, Best Poster Award 2017 1st Place 4th European Altair Technology Conference, 26.-28. June 2017, Frankenthal
9. Schlosser J. M., Rimkus W. (2017): “Low Cost Materials Processing Technologies for Mass Production of Lightweight Vehicles”, *Technologietag Leichtbau*, April 2017, Schwäbisch Gmünd
10. Rimkus W., Schlosser J. M. (2016): „Topologieoptimierung im Leichtbau“, (eng. “Topology optimisation lightweight construction”), *Technologietag Leichtbau*, April 2017, Schwäbisch Gmünd
11. Schlosser J. M., Bernd K. (2016): “Stolpersteine vermeiden auf dem Weg vom 3D-Datensatz zum perfekten Objekt“, *International Trade Fair for Materials, Components and Systems Engineering Swisstech/ Prodex*, November 2016, Basel

Nomenclature

A_{50}	Section of measurement	[mm]
A_0	Initial section area	[mm ²]
A_{eff}	Effective section area	[mm ²]
b_0	Initial width	[mm]
b_1	Effective width	[mm]
C_0	Material dependant constant	[–]
c	Specific heat capacity	[J/kgK]
D_i	Johnson Cook parameter; i=1,2,3,4,5	[–]
D	Damage Parameter (GISSMO)	[–]
D_{crit}	Parameter (GISSMO)	[–]
D_e	Outside diameter	[mm]
D_h	Dome height	[mm]
D_i	Inside diameter	[mm]
d_p	Punch diameter	[mm]
E	Young's modulus	[MPa]
E_d	Damage modulus	[MPa]
e_s	Engineering strain	[%]
e_u	Uniform elongation	[%]
e_f	Fracture elongation	[%]
$FADEEXP$	GISSMO parameter	[–]
F_{BH}	Blank holder force	[N]
F_F	Friction force	[N]
F_N	Normal force	[N]
F_P	Punch force	[N]
F_Z	Drawing force	[N]
G	Shear modulus	[MPa]
g	Gravity	[m/s ²]
I_1	First stress invariant	[MPa]
l	Length	[mm]
m	Barlat parameter for fcc or bcc material	[–]
n	Strain hardening coefficient	[–]
P	Power	[Watt]
P_N	Surface pressure	[MPa]
r	Lankford parameter (0°, 45°, 90° & biaxial)	[–]
r_d	Die radius	[mm]
s_0	Initial thickness	[mm]
s_1	Effective thickness	[mm]

T	Temperature	[K]
T_{SHT}	Solution annealing temperature	[K]
t_0	Sheet thickness	[mm]
U_i	Displacement degree of freedom; i=1, 2, 3	[–]
UR_i	Rotation degree of freedom; i=1, 2, 3	[–]
UTS	Ultimate tensile strength	[MPa]
v_0	Initial velocity	[m/s]
v	Velocity	[m/s]
w	Width	[mm]
α	Barlat YLD2000 parameters	[–]
ε	True strain	[–]
$\dot{\varepsilon}$	Strain rate	[1/s]
ε_{eq}	Equivalent plastic strain	[–]
ε_f	True fracture elongation	[–]
ε_i	Principal strains; i=1,2,3	[–]
ε_{pl}	Plastic strains; i=1,2,3	[–]
η	Triaxiality	[–]
λ	Thermal conductivity	[W/mK]
μ	Friction coefficient	[–]
ξ	Lode angle	[–]
ρ	Density	[kg/m ³]
σ_0	Engineering stress	[MPa]
σ_i	Principal stresses; i=1,2,3	[MPa]
σ_{eff}	Effective stress	[MPa]
σ_f	Flow stress	[MPa]
σ_t	True stress	[MPa]
σ_{vm}	Von Mises stress	[MPa]
σ_y	Yield strength	[MPa]
σ^*	Reduced stress	[MPa]
τ	Shear stress	[MPa]

Abbreviations

AA	Aluminium Alloy
AHSS	Advanced and ultrahigh strength steels
Al	Aluminium
bcc	Body centred cubic
CAD	Computer-aided design
CAE	Computer-aided engineering
CAM	Computer-aided manufacturing
CFRP	Carbon fibre reinforced plastic
CVD	Chemical vapour deposition
DLC	Diamond-Like-Carbon
dof	Degree of freedom
EDT	Electro-discharge texturing
fcc	Face-centred cubic
FEM	Finite element method
FLC	Forming limit curve
FLD	Forming limit diagram
GFRP	Glass fibre reinforced plastic
GISSMO	Generalised incremental stress state dependent damage model
GOM	Gesellschaft für optische Messtechnik (organisation for optical measurement solutions)
GP	Guinier-Preston
HFQ	Solution Heat treatment, cold die Forming and Quenching
KTL	Cathaphoertic dip painting
LDR	Limiting drawing ratio
OEM	Original Equipment Manufacturer
PB	Paint bake cycle
PVD	Physical vapour deposition
ph	Precipitation hardenable
PHS	Press hardened steel
Q & T	Quenched and Tempered steel
SHT	Solution Heat Treatment
SIB	Side impact beam
TFC	Triaxial failure curve
TiN	Titanium nitride
UHSS	Ultrahigh strength steels
VDI	Verein Deutscher Ingenieure
VN	Vanadium nitride
wh	Work hardenable

Table of Contents

Abstract.....	I
Acknowledgements	II
Dedication	III
Author's Declaration	IV
Published Work.....	V
Nomenclature	VII
Abbreviations	IX
Table of Contents	X
List of Figures.....	XIV
List of Tables	XVIII
Chapter 1 Introduction.....	1
1.1 Introduction	2
1.2 Scope and Objectives.....	4
1.3 Patents	6
1.4 Organisation of the thesis	7
Chapter 2 Literature Review	9
2.1 Properties and classification of aluminium.....	10
2.2 Aluminium sheet metal forming	12
2.2.1 Forming behaviour of aluminium alloys at elevated temperatures	13
2.2.2 Conventional forming.....	14
2.2.3 Warm-forming	16
2.2.4 W-Temper	19
2.2.5 Hotforming (HFQ®)	22
2.2.6 Concluding remarks	25
2.3 Hardening mechanisms.....	26

2.3.1	Work hardening (Strain hardening)	27
2.3.2	Solid solution hardening	28
2.3.3	Precipitation hardening	31
2.4	Tribology in sheet metal forming.....	34
2.4.1	Friction mechanism	34
2.4.2	Tribological system of sheet metal, tool die and lubricant	37
2.4.3	Concluding remarks	39
2.5	Fundamentals of simulation techniques for the forming process	40
2.5.1	Material testing	41
2.5.2	Stress measures	46
2.5.3	Constitutive models for forming simulation	47
2.5.4	Material failure	50
2.5.5	Damage mechanics	53
2.5.6	Generalised Incremental Stress-State dependent Damage Model (a.k.a. GISSMO)	54

Chapter 3 Experimental techniques and applied

	methods	58
3.1	Material investigations of the delivery condition	59
3.1.1	Material and mechanical behaviour of AA7075 T6	59
3.1.2	Numerical calibration of a triaxial failure curve using parameter optimisation	62
3.1.3	Concluding remarks	64
3.2	Analysis of the strength behaviour at various quenching rates	65
3.2.1	Concluding remarks	67
3.3	Extended Hotforming process	68
3.3.1	Layout of the test bench	70
3.3.2	Mechanical behaviour at elevated temperatures	73
3.3.3	Concluding remarks	83
3.4	Final state of the material after one paint bake	84
3.4.1	Material model of the final state	85
3.4.2	Damage and failure model of the final state (GISSMO)	87
3.4.3	Concluding remarks	89
3.5	Friction analysis	90
3.5.1	Tribometry in sheet metal forming	90
3.5.2	Development of a flat strip drawing tool for the tensile testing machine	93
3.5.3	Pre-tests and measurements	108

3.5.4	Investigation of the friction properties of various lubricants and temperatures.....	112
3.5.5	Concluding remarks	116
Chapter 4 Production of a car body part.....		117
4.1	Selection of a car body part and industrial requirements	118
4.2	Pre-investigation of a crash-beam – a comparison study showing the potential for weight saving using warm-formed ultra-high strength aluminium alloys	119
4.2.1	Experimental	119
4.2.2	Simulation and optimisation of a crash-beam	122
4.2.3	Concluding remarks	126
4.3	Conception of a demonstration part.....	127
4.3.1	Determination of loads and boundary condition	127
4.3.2	Topology optimisation	130
4.3.3	Design of the demonstrator (functional model) and the tooling	132
4.4	Optimisation of a carbon fibre reinforcement patch	136
4.4.1	The challenge of optimisation	136
4.4.2	Setup of the simulation model	137
4.4.3	Free-Size optimisation.....	139
4.5	Design layout of the forming tool.....	141
4.5.1	Heating layout of the forming tool - Temperature field simulation.....	143
4.5.2	Quality inspection of the tool	146
4.6	Summary	149
Chapter 5 Manufacturing and investigations of the demonstrator with each forming process at elevated temperatures.....		150
5.1	Experimental forming set-up	151
5.2	Production of the demonstrator	153
5.3	Investigations of the material suppliers.....	158
5.3.1	Results of supplier comparison	159
5.4	Investigations of forming processes at elevated temperatures	162
5.4.1	Mechanical behaviour under different heat treatment conditions.....	162
5.4.2	Analysis of the springback of various forming processes	169

5.4.3	Analysis of the thickness of various forming processes	171
5.5	Drop-Tower test – dynamic three-point bending test	173
5.5.1	Test setup Drop-Tower test	173
5.5.2	Test execution and comparison with the simulation results	174
5.6	Development of an industrial scaled layout for each forming process ...	176
5.7	Summary	179
Chapter 6 Discussion, Conclusions and Further Work.....		181
6.1	Discussion.....	182
6.2	Conclusions	185
6.3	Further Work	186
References.....		188
Appendices		197
Appendix A		198
Appendix B		200
Appendix C		204
Appendix D		206
Appendix E		211
Appendix F		213
Appendix G		223
Appendix H		236
Appendix I		238

List of Figures

Figure 1-1: Lightweight design potential of metallic materials (Schneider 2015a).....	2
Figure 2-1: Designation and main elements of wrought alloys (after DIN EN 573).....	11
Figure 2-2: Recovery and recrystallisation mechanism of a deformed metallic structure (Ilschner & Singer 2016).....	13
Figure 2-3: Conventional forming process.....	14
Figure 2-4: Warm-forming process route.....	17
Figure 2-5: Temperature time diagram of rolling mill, press- and paint shop (Oberhauser et al. 2013)	18
Figure 2-6: Warm-forming example: side impact beam.....	18
Figure 2-7: W-Temper process route.....	20
Figure 2-8: Temperature time diagram of press and paint shop (Grohmann 2016)	21
Figure 2-9: W-Temper forming example: B-pillar component	21
Figure 2-10: HFQ® process route	22
Figure 2-11: Temperature time diagram of press and paint shop (Grohmann 2016)	23
Figure 2-12: Example of the Hotforming process (HFQ®) with a B-pillar component and its problems with adhesion and grooves	24
Figure 2-13: Movement of dislocation (Kammer 2012)	27
Figure 2-14: Solid solution with alloying element as substitutional (red) or interstitial (yellow) (Kammer 2012)	28
Figure 2-15: Distortion of the crystal lattice by a substitution atom (left) and an interstitial atom (right) (Schneider 2015a).....	29
Figure 2-16: Changing of microstructure after precipitation hardening (Totten 2016)	31
Figure 2-17: Mechanism of friction in a deep drawing process (Ostermann 2014).....	35
Figure 2-18: Friction behaviour and adhesion tendency of aluminium alloys in the strip drawing test (Mössle 1983).....	37
Figure 2-19: Influence of the surface structure on the friction behaviour (Ostermann 2014)	37
Figure 2-20: REM-recordings of surface structure of the aluminium alloy A) mill-finish; B) electrical discharge texturing (EDT) (source: (Zhou et al. 2011))	38
Figure 2-21: Crash simulation under consideration of the manufacturing process.....	40
Figure 2-22: Determination of the Lankford-Parameter ($0^\circ/45^\circ/90^\circ$ rolling direction) after (DIN EN ISO 10113).....	41
Figure 2-23: Illustration of the cross-section changes for different r-values (DIN EN ISO 10113)	42
Figure 2-24: Tensile test on flat tensile specimen for flow curve recording according to DIN 6892-1.....	43

Figure 2-25: Schematic illustration of a stress-strain diagram.....	44
Figure 2-26: Schematic of an Erichsen testing set-up (Ostermann 2014).....	45
Figure 2-27: Influence of load state, pre-damage and load path (Feucht et al. 2017).....	51
Figure 2-28: The current section area and the effective section area (Haufe et al. 2011).....	53
Figure 2-29: Ductile damage – illustration of damaging.....	54
Figure 2-30: Damage accumulation (Feucht et al. 2017)	55
Figure 2-31: Influence of FADEEXP (Feucht et al. 2017)	56
Figure 3-1: AA7075 T6 - Extrapolated flow curve after Hockett & Sherby	60
Figure 3-2: Tensile testing machine including GOM Aramis system to measure local strains	62
Figure 3-3: Triaxial-Failure Curve AA7075 T6.....	63
Figure 3-4: Procedure for the creation of test specimens (test setup see Chapter 3.3 Figure 3-8).....	65
Figure 3-5: Dependence of the yield strength on the quenching rate.....	66
Figure 3-6: Dependence of the ultimate tensile strength on the quenching rate	67
Figure 3-7: Novel Hotforming Process with integrated thermal direct joining	69
Figure 3-8: Test bench set-up for forming process at elevated temperature	70
Figure 3-9: Temperature profile during Extended Hotforming process.....	73
Figure 3-10: Extrapolated flow-curves after Hockett-Sherby in different rolling directions of the Extended Hotforming process	75
Figure 3-11: LS-OPT structure of the material and damage/ failure calibration	78
Figure 3-12: Triaxial failure curve and instability curve of the Extended Hotforming process AA7075.....	82
Figure 3-13: LS-OPT Overview (von Mises) calibration	85
Figure 3-14: Stress-strain diagram, tensile test experimental curve and simulation curve	86
Figure 3-15: Triaxial failure curve and instability curve of the final state of AA7075	88
Figure 3-16: Categories of tribological testing technology (Staeves 1998)	91
Figure 3-17: The test variants of the strip drawing test (Hoffmann, Spur & Neugebauer 2012).....	91
Figure 3-18: Possible force-displacement curves for strip drawing (Lange 1990).....	92
Figure 3-19: Tensile testing machine with climate chamber.....	95
Figure 3-20: Functional principle of the strip drawing tool	98
Figure 3-21: Strip drawing tool in $\frac{3}{4}$ sectional view	100
Figure 3-22: Friction jawplates geometry with different test surface sizes.....	102
Figure 3-23: External dimensions of the strip drawing tool.....	102
Figure 3-24: Dimensions of the friction jaw holder, positioning of the strain gauge rosette, deformation of the friction jaw holder and image from FEM simulation	103
Figure 3-25: Friction jaw plates geometries	105
Figure 3-26: Setup for strain gauge calibration.....	106
Figure 3-27: Calibration force-strain curve and mathematical function	107
Figure 3-28: Hardness measurement of pull-out strips and friction jaws in different conditions	108
Figure 3-29: Dry lubrication strip.....	110

Figure 3-30: Test set-up for the evaluation of the friction coefficient	112
Figure 3-31: Exemplary representation of a friction coefficient-displacement curve	113
Figure 3-32: Comparative study of different lubricants at room temperature	114
Figure 3-33: Friction as a function of temperature and pressure for the Omega 35 lubricant.....	115
Figure 4-1: Potential structural component for forming at elevated temperatures (Schneider 2015a)	118
Figure 4-2: Test setup drop tower test (front view)	121
Figure 4-3: Simulation model of a drop tower test.....	122
Figure 4-4: Validation of the simulation model compared to the experiment (reference crash- beam).....	122
Figure 4-5: Predicted and real deflection of the side impact protection beam during deformation.	123
Figure 4-6: Predicted and real velocity of the side impact protection beam during deformation.....	123
Figure 4-7: Deflection curves of side impact protection beams using different materials in the 3- point bending simulation.	124
Figure 4-8: Velocity curves of side impact protection beams using different materials in the simulation.....	124
Figure 4-9: Lightweight design potential of crash beams using different materials	125
Figure 4-10: Side impact of a car against a pole with a speed of 32 km/h - NCAP test (Euro NCAP 2015)	127
Figure 4-11: Side impact beam of a Toyota Yaris (U.S. Department of Transportation 2018).....	128
Figure 4-12: Full Toyota Yaris FE-model - NCAP pole test and simplify FE-Model	128
Figure 4-13: Design space for topology optimisation (a) and forming guidelines (b)	129
Figure 4-14: Simulation model for topology optimisation.....	130
Figure 4-15: Schematic procedure to find a suitable design that is manufacturable and has a good crash performance	132
Figure 4-16: Comparison of crash performance of various versions of the side impact beam - dynamic three-point bending test	135
Figure 4-17: Simulation model hybrid side impact beam and layer layout (A).....	137
Figure 4-18: Result of the Free-Size optimisation of the hybrid side impact beam.....	139
Figure 4-19: CFRP Patch cut of the hybrid side impact beam.....	139
Figure 4-20: Comparison of crash performance of various versions of the side impact beam - dynamic three-point bending test	140
Figure 4-21: Lightweight construction potential of the hybrid side impact beam.....	140
Figure 4-22: Tool surfaces	141
Figure 4-23: Side impact forming tool	142
Figure 4-24: Schematic representation of the sheet metal unfolding	142
Figure 4-25: Die and heating stage - heating channel (blue arrows)	144
Figure 4-26: Heating time of forming and heating stage of the tooling	144
Figure 4-27: Temperature - path curve for forming and heating station	145

Figure 4-28: Zeiss-DuraMax RT coordinate measuring machine with forming stage	146
Figure 4-29: Illustration of the programmed inspection lines.....	147
Figure 5-1: Experimental forming set-up	151
Figure 5-2: Temperature curve of the (Extended) Hotforming, Warm-forming and W-Temper process	153
Figure 5-3: Blank with two thermocouples.....	155
Figure 5-4: Measured temperature curve of each process at elevated temperature using thermocouple SI.....	155
Figure 5-5: Forming of the side impact beam and position of the specimens for the tensile tests	156
Figure 5-6: True von Mises strain of the elements after forming	156
Figure 5-7: Manufactured demonstrators with Warm-forming, W-Temper, Hotforming and Extended Hotforming processes.....	157
Figure 5-8: Test results of the supplier influence in the Hotforming process.....	159
Figure 5-9: Test results of the supplier influence in the W-Temper process	160
Figure 5-10: Strength comparison of forming processes and heat treatment.....	165
Figure 5-11: fracture elongation comparison of forming processes and heat treatment	167
Figure 5-12: Drop-Tower test bench at Aalen university – overview and detail.....	174
Figure 5-13: Acceleration-time curve, Force-time curve and optical comparison of the simulation with experimental component test	175
Figure 5-14: Schematic industrial layout of Warm-forming process	176
Figure 5-15: Schematic industrial layout of W-Temper process	177
Figure 5-16: Schematic industrial layout of (Extended) Hotforming	178
Appendix A: Overview about designation system of aluminium alloys based on DIN EN 573-3/4	199
Appendix B: Matlab script for calculation of the α -values for Barlat YLD2000 material model	201
Appendix C: GISSMO specimen for damage and failure curve.....	205
Appendix D: Overview of the equipment used and detailed specifications.....	207
Appendix E: Matlab script for calculation of von Mises flow curve in tabular form.....	212
Appendix F: Overview of the individual assembly steps of the strip drawing tool	214
Appendix G: Technical drawing of the side impact beam	224
Appendix H: Progress images of the production of the forming stage	237
Appendix I: Detailed overview of the comparison of the different heat treatments and forming processes et elevated temperatures. Hotforming (HT) – grey, W-Temper (WT) – blue, Warm- forming (HW)- brown and the heat treatments without (W) treatment, 1-5 paint bake (1-5PB) cycle.....	239

List of Tables

<i>Table 1-1: The patents owned by LoCoMaTech partners related to the HFQ® technology.....</i>	<i>6</i>
<i>Table 2-1: Major properties of aluminium (Ostermann 2014).....</i>	<i>10</i>
<i>Table 2-2: Aluminium forming process comparison.....</i>	<i>25</i>
<i>Table 2-3: Schematic representation of the specimens (Feucht et al. 2017).....</i>	<i>50</i>
<i>Table 2-4: Failure Models (Feucht et al. 2017).....</i>	<i>52</i>
<i>Table 2-5: Ductile damage (Feucht et al. 2017).....</i>	<i>53</i>
<i>Table 3-1: Chemical composition (wt.-%) and mechanical properties of AA 7075 T6 (Grohmann 2016).....</i>	<i>59</i>
<i>Table 3-2: Forming limit diagram AA 7075 T6 (Grohmann 2016).....</i>	<i>61</i>
<i>Table 3-3: Test results of various specimens for TFC.....</i>	<i>63</i>
<i>Table 3-4: Force-displacement diagram; experiment-blue, average measurement values-green, optimised-purple.....</i>	<i>64</i>
<i>Table 3-5: Detailed overview of used testing equipment (for further detail see Appendix D).....</i>	<i>71</i>
<i>Table 3-6: Anisotropic parameters.....</i>	<i>74</i>
<i>Table 3-7: Overview of the simulation models for material and damage/ failure model calibration.....</i>	<i>76</i>
<i>Table 3-8: Parameters for the calibrated Barlat YLD2000 material model of AA7075 Hotforming material.....</i>	<i>77</i>
<i>Table 3-9: Comparison of experimentally and numerically determined stress-strain curves and force-displacement diagrams using Barlat YLD2000 model.....</i>	<i>79</i>
<i>Table 3-10: Parameterisation and results of the failure and instability curve of the Extended Hotforming process.....</i>	<i>80</i>
<i>Table 3-11: Optimisation results for damage/ failure model stress-strain and force-displacement diagrams.....</i>	<i>81</i>
<i>Table 3-12: Parameterisation and results of the failure and instability curve of the finale state AA7075.....</i>	<i>87</i>
<i>Table 3-13: Optimisation results for damage/ failure model at finale state - stress-strain and force-displacement diagrams.....</i>	<i>89</i>
<i>Table 3-14: Requirements of the flat strip drawing tool.....</i>	<i>94</i>
<i>Table 3-15: Morphological box.....</i>	<i>96</i>
<i>Table 3-16: Technical data of disc springs.....</i>	<i>99</i>
<i>Table 3-17: Specimen thickness with the respective distance washer.....</i>	<i>101</i>
<i>Table 3-18: Mechanical properties of 42CrMo4 in tempered condition (Saarstahl AG 2017).....</i>	<i>103</i>
<i>Table 3-19: Boundary conditions for the numerical simulation.....</i>	<i>104</i>
<i>Table 3-20: Overview of tested anti-friction agents.....</i>	<i>109</i>

<i>Table 3-21: Microscopic examination of lubricants</i>	<i>111</i>
<i>Table 4-1: Chemical composition of used material</i>	<i>119</i>
<i>Table 4-2: Mechanical behaviour of various materials.....</i>	<i>120</i>
<i>Table 4-3: Input parameter and results of the topology optimisation</i>	<i>131</i>
<i>Table 4-4: Comparison of different developmental stages of the side impact beam.....</i>	<i>134</i>
<i>Table 4-5: Material data for CFRP and glue (Cherniaev, Montesano & Butcher 2018).....</i>	<i>138</i>
<i>Table 4-6: Thermal properties of the material</i>	<i>143</i>
<i>Table 4-7: Oversize measurement of the forming stage.....</i>	<i>148</i>
<i>Table 5-1: Detail overview of the set-up.....</i>	<i>152</i>
<i>Table 5-2: Procedure of the test series</i>	<i>154</i>
<i>Table 5-3: Comparison of the chemical and mechanical properties of the aluminium alloys from different suppliers.....</i>	<i>158</i>
<i>Table 5-4: Trial plan for mechanical properties investigations of different forming processes and paint bakes</i>	<i>162</i>
<i>Table 5-5: Heat treatments - schematic representation of the temperature profile</i>	<i>163</i>
<i>Table 5-6: Measured temperature profiles of each paint bake cycle.....</i>	<i>164</i>
<i>Table 5-7: Potential of different forming processes at elevated temperatures using artificial ageing (5 PB)</i>	<i>168</i>
<i>Table 5-8: Target-actual-comparison of Warm-forming, W-Temper & Hotforming processes with CAD geometry.....</i>	<i>170</i>
<i>Table 5-9: Comparison of Warm-forming, W-Temper and Hotforming processes with forming simulation.....</i>	<i>172</i>

Chapter 1 Introduction

This chapter gives an overview of metallic materials that are currently used in the automotive industry, including an illustration of their specific strength versus elongation. It shows the high lightweight construction potential of high strength aluminium alloys, in particular the 7000 series. Finally, the scope and objectives are revealed, patents and key aspects of this research are listed.

1.1 Introduction

Current forecasts indicate that in the next 50 years the conventional resources of fossil fuel will be considered to be depleted and this will be set against an increased demand for energy as the global population and affluence rise (Ostermann 2014; Nilmani 1997; Schneider et al. 2015b). Thus, the development of innovative and economical solutions to this demand, such as using lightweight aluminium alloy structures, is essential to curb this trend (Vogt 2009).

In its “National Industrial Strategy by the year 2030”, Germany's government declared lightweight design as a game changer technology, since economic strength depends on the availability of numerous and often critical raw materials. Relatively cheap aluminium alloys, such as from the 5xxx and 6xxx series, are produced in large quantities and are used for automotive body panels. With regard to crash-relevant car body components (inter alia B-pillars, bumpers, side impact bars, etc.), ultra-high strength aluminium alloys from the 7xxx group are currently used (Grohmann 2016).

However, steel materials dominate the market within the automotive sector due to their reasonable cost-performance ratio. Nevertheless, aluminium and its alloys play a major role for lightweight applications. In particular aluminium alloys of the 7000 series offer big advantages compared to press hardened steels if the specific strengths of corresponding materials are compared to each other (cf. Figure 1-1).

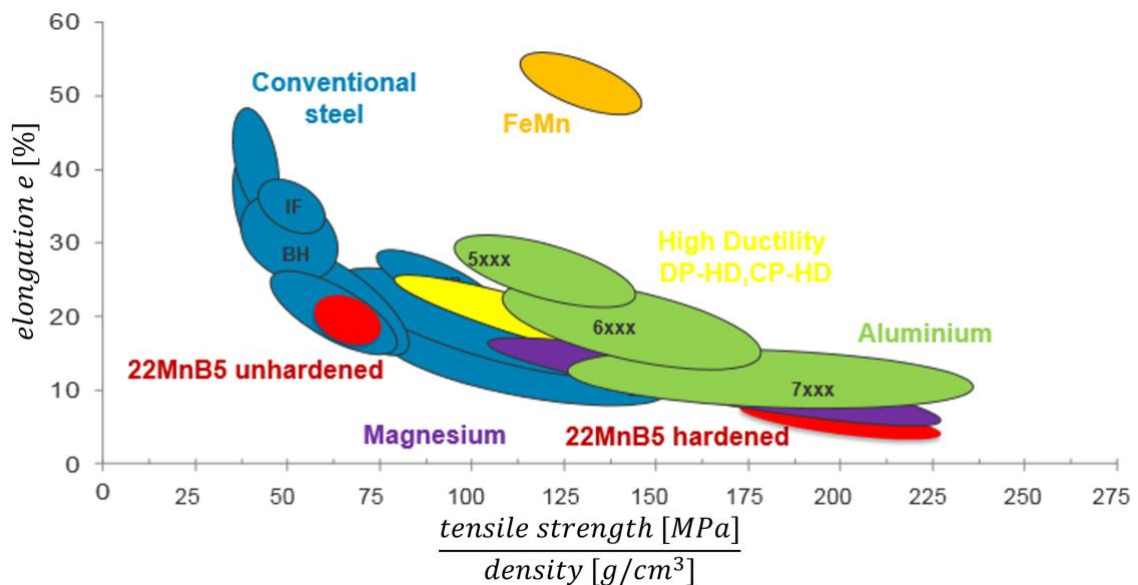


Figure 1-1: Lightweight design potential of metallic materials (Schneider 2015a)

This positive property can be used to reduce energy consumption during the life of a vehicle (Ostermann 2014). An example of such a development is the car body of the Ford F150, where steel has been replaced by aluminium alloy to reduce weight, which results in decreased fuel consumption and increased performance. The global car manufacturers need to reduce the weight of vehicles due to exhaust emissions and their economic objectives. Therefore, carmakers use lightweight materials, in particular aluminium alloys, while other lightweight materials such as composites and magnesium alloys are mainly used for racing cars, sport cars and luxury super-cars due to their cost. In terms of the forming behaviour of high and ultra-high strength aluminium alloys the production process is still restricted.

Without the invention of new production technologies, it is a challenge to meet the requirements of design trends (increasing complexity of the geometries of sheet metal components). With the aim of improving their formability, several forming methods have been studied in order to substitute the conventional cold forming process.

The range of aluminium applications can be expanded through adapted thermal forming processes. Currently, complex-shaped components made out of high and ultra-high strength aluminium alloys, such as from the 7000 group, can be produced economically using the Hotforming, the Warm-forming or the W-Temper process.

1.2 Scope and Objectives

Due to economic objectives and continuously decreasing fossil-resources, the automotive industry is forced to minimise the nominal weight of a car body (McKinsey & Company 2017). A weight reduction can be achieved if the car structure is made out of lightweight materials, such as aluminium alloys, instead of steel. Aluminium alloys not only show a high affinity for passivation, which results in corrosion resistance in many environments, but also provides high specific strengths (strength versus density see Figure 1-1) and rigidity (Young's modulus versus density). For this reason, ultra-high strength aluminium alloys from the 7xxx group are increasingly being used for structural components in car body constructions. Currently, ultra-high strength aluminium alloys from the 7xxx group are used for B-pillars, bumpers or side impact beams (Grohmann 2016).

The disadvantages of high strength aluminium alloys are the low formability at room temperature, tribology problems (inter alia grooves effects and adhesions), long ageing time needed to increase the strength and cost-effective stamping technologies compared with conventional forming techniques. Therefore, the forming behaviour of aluminium alloys needs to be improved, which can either be done by changing the alloying elements, applying heat treatment steps or rising the forming temperature to higher values.

The aim of this research project is the investigation and implementation of novel forming processes at elevated temperatures under series production conditions in order to manufacture more complex structural lightweight components from 7xxx aluminium sheets for automobiles, based on the principle of press hardening of steel in an efficient and material-compatible manner. For this purpose, forming parameters of the process in the process chain are investigated, such as the heating of the blank, the hot forming/cooling of the component, and the influence of subsequent heat treatment (e.g. paint baking) on the mechanical properties of the component. Furthermore, there are first approaches for the production of hybrid components made of high strength aluminium and local reinforcements CFRP or GFRP (carbon/ glass fibre reinforced plastic) patches through a combination of Hotforming process and thermal direct joining. For process layouts of temperature assisted forming technologies and for forming/ crash simulations, FEM simulation models need to be developed. To accomplish this aim it is important to create realistic material and damage/ failure models as input data for such FEM-calculations.

In this thesis a major contribution is made to the Hotforming process for high strength aluminium alloys in order to replace structural components made of steel by high strength aluminium alloys. Thus, the lightweight potential for car body parts can be significantly enhanced.

The overall aims of the research project are:

- increasing the formability of high strength aluminium sheet metal alloys by forming at elevated temperatures,
- implementing material and damage/ failure models for FE-Analysis,
- reducing the tribology effects (adhesion of aluminium onto the forming tool),
- cutting down process cost by using existing press hardened steel plants,
- improving the ageing time of high strength aluminium alloys for better post-forming strength values, and
- decreasing the weight of the vehicle components/ structures,

by applying a novel manufacturing technology, so called “Hotforming followed by cold die quenching” or “Extended Hotforming using a thermal direct joining step”. Those technologies should make it possible to manufacture high strength lightweight complex-shaped aluminium parts for mass production.

Key aspects of the thesis are:

- Characterisation of the material behaviour of the aluminium alloys during Hotforming followed by cold die quenching (investigation of lubricants, tribology behaviour, evaluation of friction values, analyses of strength values of high strength aluminium alloys and implementation of material cards for forming/ crash simulation),
- Creation of a demonstration model using simulation software,
- Generation of a FEM-model applicable for the “Extended” Hotforming process and experimental tests (thermally and mechanically) using the gained knowledge as input data for the simulation model,
- Optimisation of the simulation model and validation with real experiments, and demonstrating the applicability of forming at elevated temperatures in the industry by creating an ideal layout of a production line and by producing a demonstration part (representatively shaped car body component).

1.3 Patents

“A worldwide patent search confirmed that the technologies and prototype equipment to be developed which are focused on the mass production of aluminium lightweight components are unique developments and no similar ones have been reported - the whole LoCoMaTech¹ concept and individual technologies are novel and provide a breakthrough enabling widespread use of aluminium in low-cost cars and vehicles in general” (Lin 2016).

Table 1-1: The patents owned by LoCoMaTech partners related to the HFQ® technology

Patent No.	Awarding agency	Owner & Authors	Title of the Patent
W02010/032002A1	International Publication (2010) Europe. Also filed in Japan, Brazil, USA, Russia, China, Canada, India, etc.	A.D. Foster, T.A. Dean and J. Lin	Process for forming aluminium alloy sheet component (Original HFQ® for special alloys)
W02011/058332A1	Int. Publication (2010); Europe. Also filed in Japan, Brazil, USA, Russia, China, Canada, India, Australia, Mexico, South Korea	J Lin, T.A. Dean, A.D. Foster, L. Wang and D. Balint	A method of forming a component of complex shape from aluminium alloy sheet (two step HFQ® for special alloys)
WO 2015/136299	International publication (2015)	O. El-Fakir, J. Lin, L. Wang, T.A. Dean, J. Dear, D. Balint, etc.	A method of forming complex parts from sheet metal alloy (Low temperature HFQ®)
W 0 2013/045933A1	International publication (2013)	D. Balint, T.A. Dean and J. Lin	A method of forming parts from sheet steel (Low temperature Boron Steel)
Patent Application No: 1419460.9 (P60186GB)	UK patent filed on 31 Oct. 2014 PCT filed in 2015	K. Zheng, J. Lin, L. Wang, N. Li, O. El-Fakir, T.A. Dean, A. Foster, G. Adam	Material and Process for preparing and forming materials (T0 material blanks for HFQ®)
Patent Application No: 1513832.4 (P100255GB/PT)	UK patent filed on 5 Aug. 2015	N. Li, J. Zheng, K. Zheng, J. Lin and C. M. Davies	A fast ageing method for heat treatable alloys (Fast ageing)
Patent application No: 1514084.1 (P63473GB/PT)	UK patent filed on 10 Aug. 2015	Z. Shao, N. Li, J. Lin, Q. Bai	Planar test system (Obtaining FLD data at)
Patent in filing process	UK patent	L. Wang, K. Ji, O. Elfakir, J. Lin, T.A. Dean	Cost effective process for forming high strength aluminium panel components (Fast warm HFQ®)
Patent application No: GB1502734.5	UK Patent filed on 18 Feb. 2015	A.C.L. Lam, Z. Shi, X. Huang, Y. Zeng, Z. Li & J. Lin	A Die Mechanism, an Apparatus, and a Method for shaping a component for Creep-age Forming (Flexible tooling concept could be used for HFQ®)
UK application: GB1412486.1; PCT application: PCT/GB2015/052018	UK patent filed on 14 July 2014	G.J.S. Adam, M.W. Brazier, A.D. Foster	Method to Operate a Hydraulic Press for Metal Sheet Forming

¹ EU Project “Low Cost Materials Processing Technologies for Mass Production of Lightweight Vehicles”

1.4 *Organisation of the thesis*

Chapter 1 gives an overview of metallic materials that are currently used in the automotive industry, including an illustration of their specific strength versus elongation. It shows the high lightweight construction potential of high strength aluminium alloys, in particular the 7000 series. Finally, the scope and objectives are revealed, patents and key aspects of this research are listed.

Chapter 2 presents fundamental knowledge regarding aluminium and its aluminium alloys including relevant hardening mechanism. Moreover, currently applied sheet metal forming processes using aluminium wrought alloys are discussed and tribology conditions in sheet metal forming are shown. Various material testing procedures and constitutive models for forming simulation are demonstrated, which play an essential role for material characterisation and for subsequent feasibility studies by using finite element simulation techniques.

Chapter 3 shows a material investigation of the delivery conditions of AA7075 T6 and the influence of the quenching rate on the strength during forming. Furthermore, a novel process called “Extended Hotforming” to produce hybrid material composites of high strength aluminium alloys and CFRP patches is presented. Detailed material models and failure models have been designed for an exact simulation of the forming process and for the subsequent component simulation. Moreover, a friction test bench was constructed and built for the selection of a suitable lubricant for forming at higher temperatures and the creation of a friction model for the forming simulation.

In **Chapter 4** a car body part is selected, and a comparison study is presented, which shows the lightweight construction potential of high strength aluminium alloys using a side impact beam as an example. A dedicated side impact beam is then developed using the Toyota Yaris press hardening steel tube as industrial design guidelines and the EURO NCAP pole impact test as a crash standard for the boundary conditions. Based on topology optimisation result, a functional side impact beam model is designed in CAD. Some optimisation loops are carried out, which include a simulation of the producibility and the evaluation of the crash performance to obtain an optimal design of a lightweight side impact beam made of AA7075. In order to increase the lightweight potential, a local CFRP patch was developed using fibre optimisation.

Subsequently a forming tool was developed and designed to produce the side impact beam with the various forming processes at elevated temperatures, such as Warm-forming, W-Temper and Hotforming/ Extended Hotforming.

Chapter 5 illustrates the application of the previously evaluated tool design on a sheet metal forming tool. Demonstration parts are also produced using different forming processes and evaluated in terms of mechanical behaviour and springback. The influence of the supplier on the mechanical properties were also illustrated. For the validation of the FE-simulation a drop tower test (dynamic three-point bending test) was carried out and compared to the simulation results. Finally, industrial layouts were developed for each forming process at elevated temperature.

Chapter 6 provides a discussion and conclusion of this research. It is shown how the aims and objectives have been achieved, and the final results are listed. At the end of this chapter an outlook and suggestions for further work are given.

Chapter 2 Literature Review

This chapter presents fundamental knowledge regarding aluminium and its aluminium alloys including relevant hardening mechanism. Moreover, currently applied sheet metal forming processes using aluminium wrought alloys are discussed and tribology conditions in sheet metal forming are shown. Various material testing procedures and constitutive models for forming simulation are demonstrated, which play an essential role for material characterisation and for subsequent feasibility studies by using finite element simulation techniques.

2.1 Properties and classification of aluminium

Aluminium and its alloys, especially the 6xxx and 7xxx series, exhibit a high specific strength compared to advanced and ultra-high strength steels (AHSS and UHSS) (cf. Figure 1-1). Using 7xxx alloys instead of press hardened steels allows considerable weight saving potentials. In the table below (cf. Table 2-1) the major properties of aluminium are shown.

Table 2-1: Major properties of aluminium (Ostermann 2014)

Crystal structure	Face-centred cubic (fcc)	
Atomic radius	$[10^{-12}m]$	143.2
Density at room temperature	$[g/cm^3]$	2.7
Melting temperature	$[^{\circ}C]$	660
Boiling temperature	$[^{\circ}C]$	2500
Young's modulus	$[N/mm^2]$	70000
Poisson's ratio	-	0.32 to 0.40
Thermal expansion coefficient	$\left[\frac{\mu m}{m * K}\right]$	23.5
Thermal conductivity	$\left[\frac{W}{m * K}\right]$	209.4
Electrical conductivity	$\left[\frac{m}{\Omega * mm^2}\right]$	34 to 38
Electrochemical potential	$[V]$	-1.66

Aluminium is mostly used with alloying elements, which cause a change of its properties. After adding those elements in its metallic structure, aluminium becomes a valuable construction material (Kammer 2012). Aluminium materials can be subdivided into wrought alloys and cast alloys. For the deep drawing processes only, the wrought alloys are mainly used. Furthermore, aluminium alloys are divided into work hardenable (wh) and precipitation hardenable (ph).

Figure 2-1 shows a rough classification of the aluminium wrought alloys with the main alloying elements and the condition after DIN EN 573.

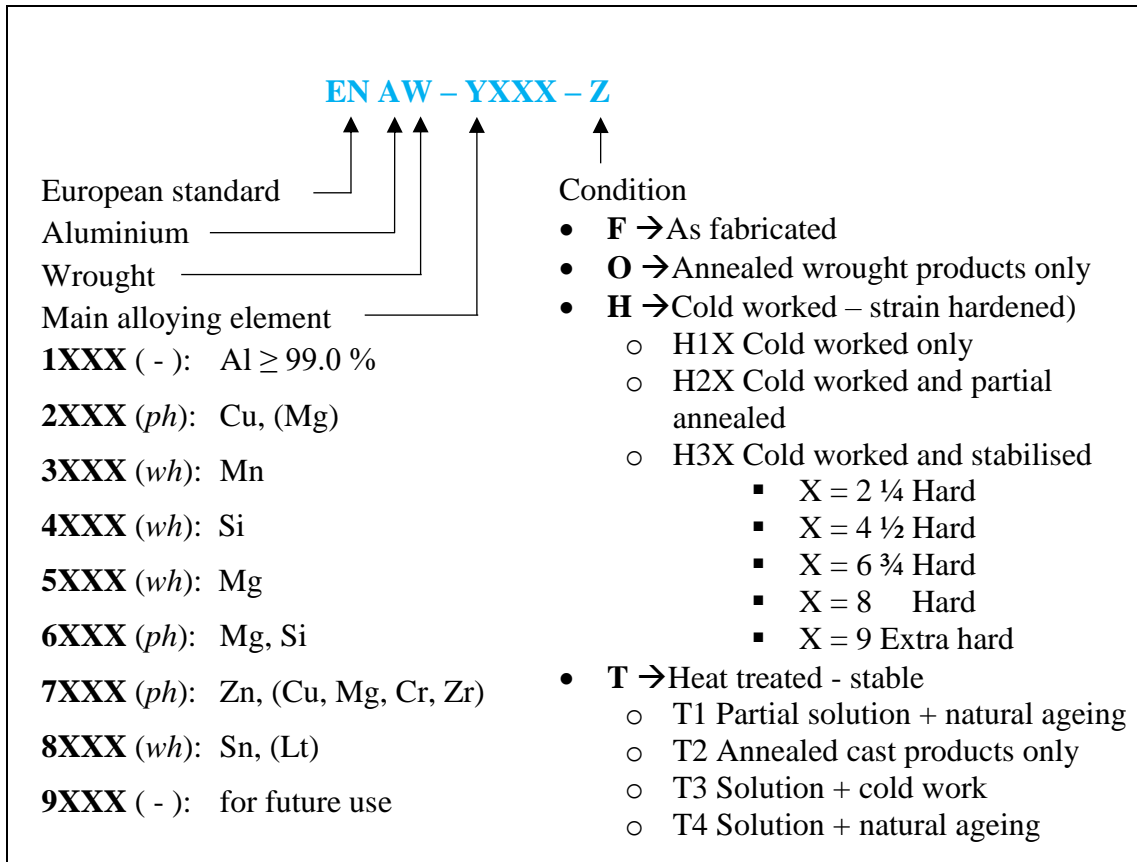


Figure 2-1: Designation and main elements of wrought alloys (after DIN EN 573)

An overview about aluminium wrought alloys is given in Appendix A, which includes the main alloying elements, range of strength, condition of aluminium alloys for the 1xxx to 8xxx series (heat treatment/ processing method) and comments on common usage, weldability and corrosion.

2.2 *Aluminium sheet metal forming*

Aluminium is an exceptionally well-known metal, it is widely used because it is abundant, malleable, light, strong, naturally resistant to corrosion and highly flexible in terms of the many methods by which it can be processed. The formability of the sheet metal materials is based on the movement of lattice defects and on the crystalline structure. Aluminium has four slip planes in face centred cubic (fcc) lattice, whereby for energetic reasons dislocation slips predominantly take place on closely packed planes in crystal lattice. By obstructing dislocations on slip planes due to lattice defects such as vacancy defects, interstitial defects, substitutional atom, etc. the formability is commonly reduced. The fracture of the material occurs if a further movement of dislocation is not possible anymore. In general, uniaxial up to biaxial tensile stresses occur in sheet metal forming. As a result of excessive plasticisation and imperfections, which are always present in real materials, the material begins to localise and the instabilities weaken the material. Nevertheless, the formability of aluminium alloys, which in particular high strength alloys generally have bad forming behaviour (due to bad anisotropy values and relatively large grain sizes), can be improved by hardening mechanisms (Heine 2017; Ilchner & Singer 2016; Domke 1994; Schneider 2015a).

For the formability and strength of the finished components, the process plays a significant role, in particular the temperature management in sheet metal. For this reason, different forming processes at elevated temperatures are investigated and, if necessary, further developed to apply local reinforcements patches made of CFRP or GFRP in a thermal direct joining step during forming.

2.2.1 Forming behaviour of aluminium alloys at elevated temperatures

The temperature is an essential factor in the forming of aluminium sheet metal alloys. The mechanical properties depend on temperature, in particular yield strength, ultimate tensile strength and fracture elongation. At elevated temperature the formability increases for most of the materials. This phenomenon of metallic materials can be tracked back to recovery and recrystallisation mechanism, which is illustrated in Figure 2-2. Through input of energy such as heat the mechanism of diffusion improves, which allows dislocations to cross slip onto other gliding planes and allows the movement of dislocations to be continued and in the further course either get impeded again or get annihilated.

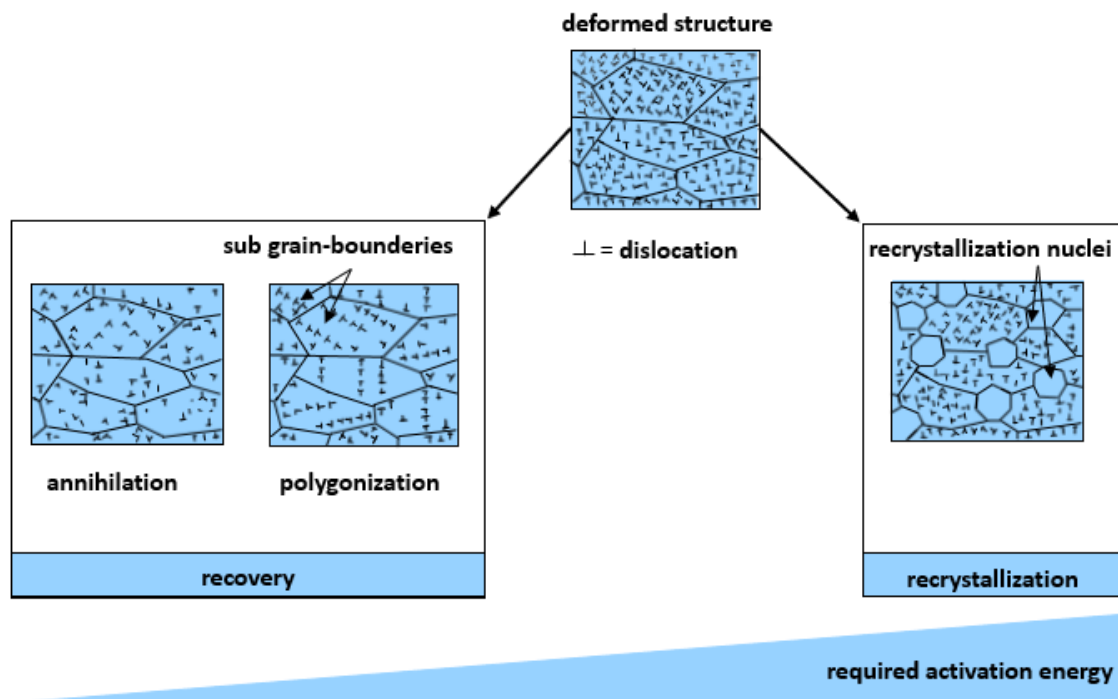


Figure 2-2: Recovery and recrystallisation mechanism of a deformed metallic structure

(Ilchner & Singer 2016)

In the polygonisation process, which is an energetically favourable state, the piled-up dislocations are re-arranged to sub-grain boundaries. Both processes annihilation and polygonisation are referred to as crystal recovery and take place at elevated temperatures. If a sufficiently high energy level is present or reached in the material, recrystallisation takes place parallel to the recovery process. This leads to a reduction of the strain hardening due to new and unstrained grains. Those softening effects lead to an enhanced formability of common aluminium alloys (Ilchner & Singer 2016; Schneider 2015a).

2.2.2 Conventional forming

The 5xxx and 6xxx aluminium alloys are most commonly used for automotive applications. The alloy used depends on its field of application.

For example, 5xxx alloys have an ultimate tensile strength from 125 to 350 MPa and cannot be heat-treated. They have relatively good formability and are highly resistant to corrosion. However, 5xxx alloys are prone to the formation of Lüders bands during forming (Lüders bands are negative for the surface quality in terms of visual perception), so they are mainly used for inner-panel applications. The 6xxx series alloys are heat treatable to reach ultimate tensile strength from 125 to 400 MPa. These alloys, especially AA6022 and AA6111, are often used for outer panels since they are precipitation hardenable and free of Lüders bands (Tingting & Taylan 2013). Figure 2-3 shows the cold forming process for mass production. Firstly, the blank or the coil is allocated at the press line. After allocation at the press line, the blank is formed and cut in the forming unit and sometimes laser cutting is needed afterwards. When the alloy is heat treatable, a paint bake cycle will be applied to enhance the strength. The temperature and ageing time depend on the E-coating condition and the customers' requirements.



Figure 2-3: Conventional forming process

Conventional aluminium forming aspects:

1. **Initial sheet temper:** T4 temper / O condition
2. **Quench:** at rolling mill
3. **Forming temperature:** room temperature
4. **Time-critical steps:** no
5. **Post-form ageing:** needed to enhance strength
6. **Suitable alloys:** 5xxx, 6xxx
7. **Formability:** adequate, but not suitable for complex shapes and high strength aluminium alloys
8. **Final mechanical properties:** up to 400 MPa depending on the alloy
9. **Economics:** suitable for mass production and cost-effective production processes, because no heating equipment is needed

For the stamping of car body parts, the reduced formability of aluminium compared to steel can be increased to some extent by using technologies such as advanced addendum design, local blank holding force control with multiple-point hydraulic cushions, or warm-forming. Warm-forming, using heated dies and heated blanks, has been investigated extensively and recent studies have shown that the use of heated dies complicates the process and increases the die costs. Present R&D efforts are focused on heating the sheet to warm-forming temperature while keeping the dies at room temperature (Fan et al. 2015). Researchers hope to establish a practical and robust process that increases the formability of aluminium sheet for forming more complex parts with difficult geometries.

2.2.3 Warm-forming

With the aim of improving the formability of aluminium alloys to expand the scope of their application, several new forming methods that may be used instead of the conventional cold forming process have been studied. One of them is hot blow forming, which was developed to achieve higher ductility in aluminium alloys than that attained in conventional cold forming. For the Warm-forming process a previously heated tool is used to deep-draw the material. For AA6xxx or AA7xxx materials, warm-forming offers better deep-drawability than cold forming, and there is no obvious decrease in strength up to a forming temperature of 250°C (Fan et al. 2013). Since the Warm-forming process can be carried out using a standard cold forming press equipment, the additional investment required is negligible.

Figure 2-4 and Figure 2-5 demonstrate a typical Warm-forming process route and its temperature regime applicable for high strength aluminium alloys.

Before the actual forming process, the material is solution annealed and immediately quenched in a water bath at the rolling mill. This is followed by artificial ageing in order to reach T6 condition, which is the highest strength condition of this material treatment and the initial state for the forming process (see Figure 2-5).

In the press shop the blank is heated up over 180°C within a couple of seconds via contact heating through e.g. the die to achieve a better formability of the aluminium alloys. The blank is then formed and cut in the forming unit, which is also heated above 180°C. Due to the high strength after ageing of approximately 600 MPa and a residual elongation of around 12%, the 7000 aluminium alloy is applicable for crash components such as side impact bars (cf. Figure 2-6). Due to the wide range of applications for 7000 alloys and the Warm-forming process described for cost-effective mass production, it might be possible to replace steel crash components by high strength aluminium alloys in order to use the lightweight design potential and thus to reduce weight (Oberhauser et al. 2013)

The advantages of this process are:

- short cycle times,
- low capital expenditure,
- no need for further heat treatment after forming because of low strength losses during Warm-forming in comparison to the initial state T6 → slight over-ageing of the material (after paint bake processes) ensures good corrosion behaviour,
- low forming temperature allows environment friendly lubricants,
- forming process can be laid out by isothermal FEM-simulation.

The disadvantages of this process are the low formability, slightly higher die costs and the high springback of the material. Therefore, it is only suitable for simple shaped components like side impact production beams, sills and bumpers.

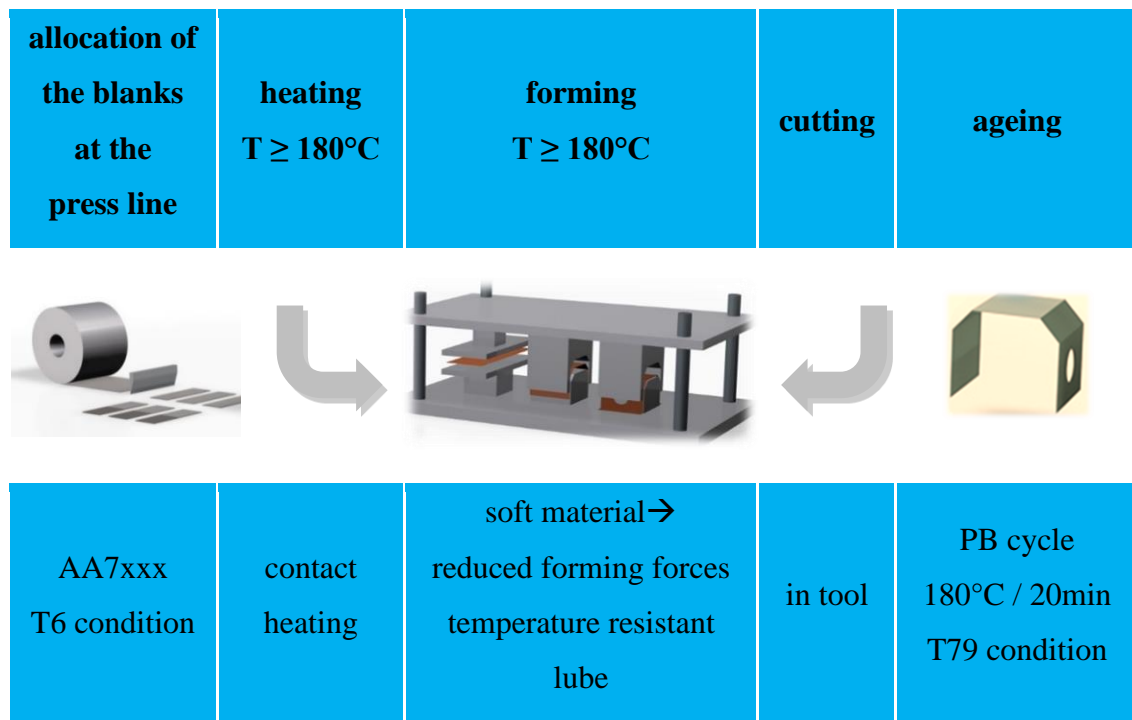


Figure 2-4: Warm-forming process route

Warm-forming of aluminium alloys is conducted using heated, matched die sets at 180 ~ 250°C, which is shown in Figure 2-4. In some publications (Fan et al. 2015; Fan et al. 2013) and the author's own research, results show that the blank and die temperature should not be higher than 250°C for the forming process to reach enough post-forming strength values of the material. Forming temperatures above this temperature result in a decrease of strength and an increase of adhesion effects between the aluminium and the die surface (galling).

Warm-forming of aluminium aspects:

1. **Initial sheet temper:** T6 temper
2. **Quench:** at rolling mill
3. **Forming temperature:** warm (180-250°C)
4. **Time critical steps:** heating, forming and cooling
5. **Post-form ageing:** not needed
6. **Suitable alloys:** 5xxx, 6xxx and 7xxx alloys
7. **Formability:** adequate, but not suitable for complex shapes
8. **Final mechanical properties:** up to 600 MPa (UTS), almost no loss of strength during forming
9. **Economics:** suitable for mass production and cost-effective production processes, because no artificial ageing needed but higher costs of heated dies

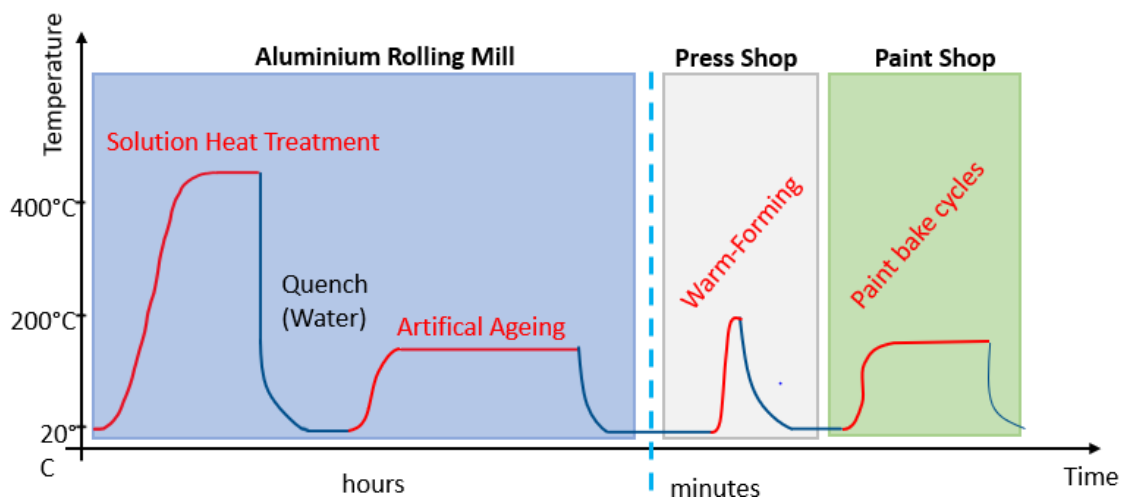


Figure 2-5: Temperature time diagram of rolling mill, press- and paint shop (Oberhauser et al. 2013)

Example: Side impact beam formed in the Warm-forming process



Figure 2-6: Warm-forming example: side impact beam

2.2.4 W-Temper

The W-Temper state of a heat treatable aluminium alloy (Figure 2-7) characterises a supersaturated metastable state after the solution annealing and quenching. This results in good forming properties. In the press shop the blank is firstly heated up to solution annealing temperature by a furnace or a contact heating unit, which is much faster. The temperature of solution annealing depends on the specific aluminium alloy. For the 7xxx series the solution annealing is usually carried out at a temperature range of $465^{\circ}\text{C} < T < 490^{\circ}\text{C}$. During the solution heat treatment (SHT) the metallic structure becomes a homogeneous solid solution with high ductility and hence good formability. After about 2-3 min at this solution annealing temperature the blank will be quenched in a water bath, flat plates, and spray cooling or high-pressure air. It depends on the material and the quenching rate to be achieved. The temperature curves of a common W-Temper process are schematically presented in Figure 2-8. Before conducting the forming, the blank will be coated with a dry lube inter alia mineral oil based lubrication, due to the high adhesion tendency of the aluminium material at this soft state. Subsequently, the cold blank is formed at ambient temperature and cut by laser or directly in die. For the final use, the strength and the corrosion resistance need to be enhanced by artificial ageing. This is carried out by specific paint bake cycles to generate a slightly over-aged material (T7x temper) (Oberhauser et al. 2013).

The advantages of this process are:

- forming of complex shaped components possible,
- forming at ambient temperature allows environment friendly lubricants, and
- process can be laid out by isothermal FEM-simulation.

The disadvantages of this process are higher investment costs and longer cycle times because of several individual process steps and the artificial ageing at the end. Therefore, this process is suitable for complex shaped components like B-pillars, door inner, etc.

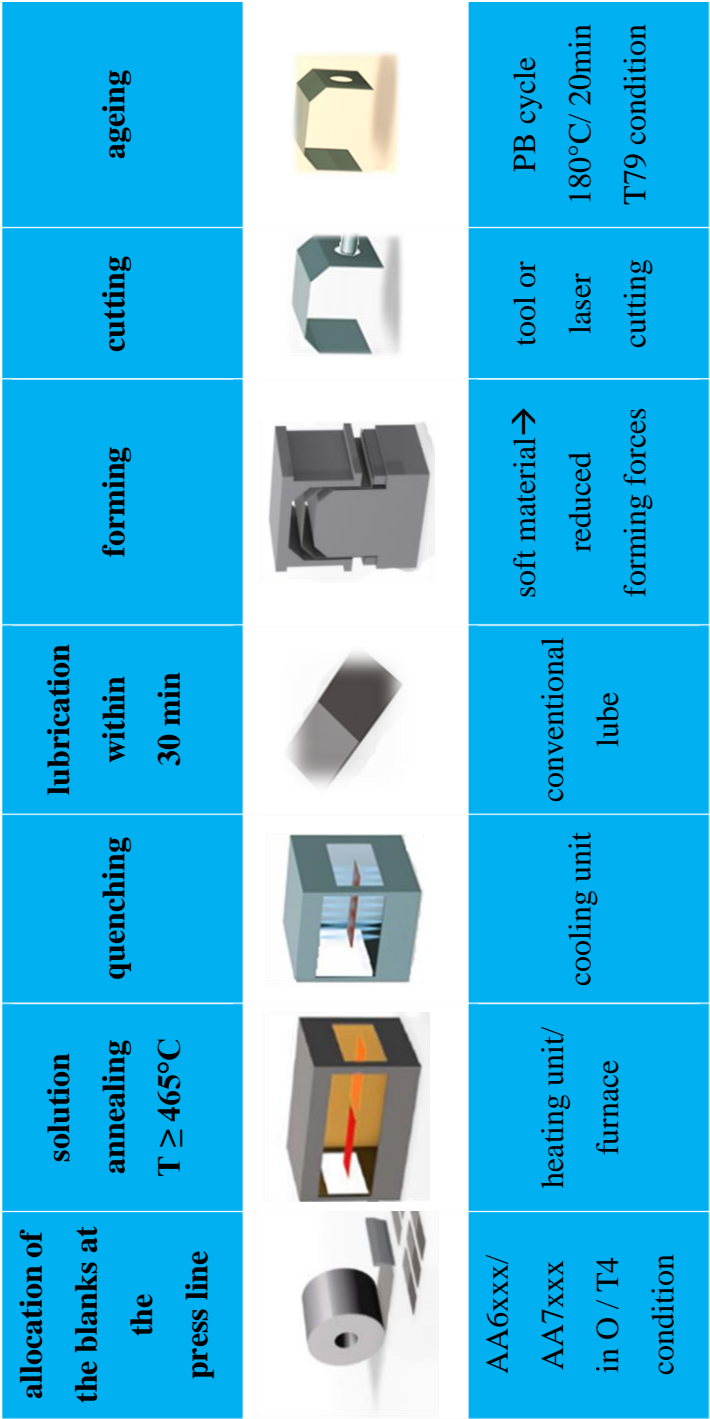


Figure 2-7: W-Temper process route

W-Temper aluminium forming aspects:

1. **Initial sheet temper:** as rolled (no temper)/ O/ T4
2. **Quench:** at press shop by water, forced air or flat plates
3. **Forming temperature:** cold
4. **Time critical steps:** quench to form, less than 10 min for optimum results
5. **Post-form ageing:** yes
6. **Suitable alloys:** 6xxx and 7xxx alloys
7. **Formability:** very good
8. **Final mechanical properties:** very good after paint baking
9. **Economics:** a separate cooling unit and ageing steps are required to recover the strength. But the process is also suitable for mass production

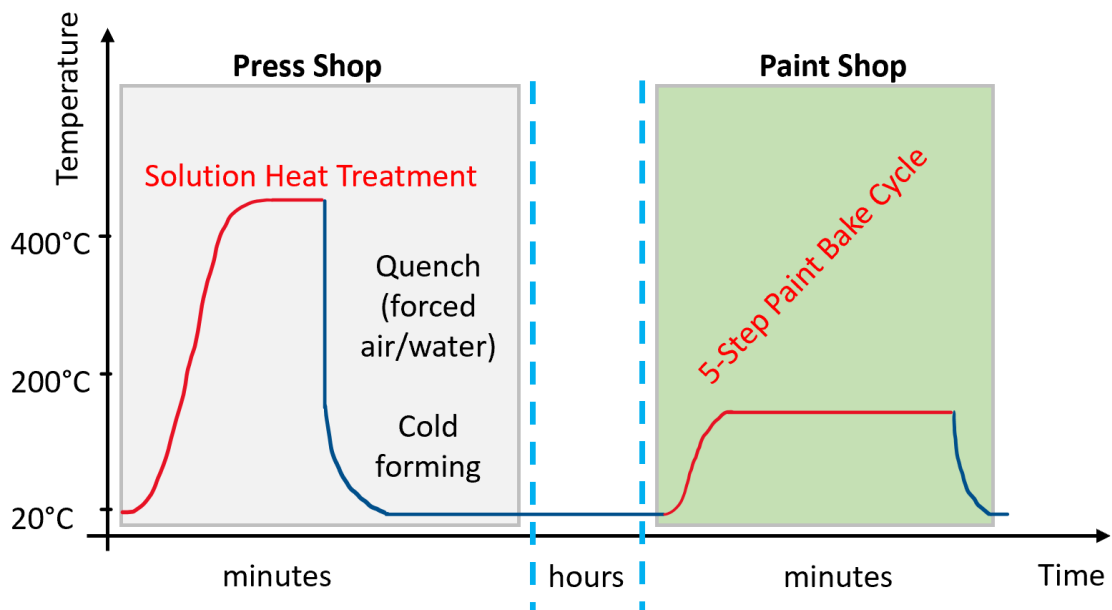


Figure 2-8: Temperature time diagram of press and paint shop (Grohmann 2016)

Example: B-pillar formed in the W-Temper process



Figure 2-9: W-Temper forming example: B-pillar component

2.2.5 Hotforming (HFQ®)

The term HFQ® (“solution **H**eat treatment, cold die **F**orming and **Q**uenching”) is a patented manufacturing technology by Imperial College. *“This is the first technology in the world enabling manufacture of high strength lightweight complex-shaped aluminium parts, through further developing 10 recently patented HFQ® related technologies aimed at improving cost efficiency and reducing environmental impact.”* (Lin 2016)

The HFQ® process (Figure 2-10) consists of heating aluminium sheet metal alloy to its solution annealing temperature (SHT) and transfer it to the press for quenching and forming. The formed part is held in the water-cooled tool for a few seconds to quench it and thus, to avoid the formation of precipitates.

As with the W-Temper process, the formed component undergoes a cutting process, either by laser or die, to finalise the geometry and an artificial ageing process to increase the strength and the corrosion resistance. In Figure 2-11 there is a schematic description of the temperature profile of the HFQ® process.

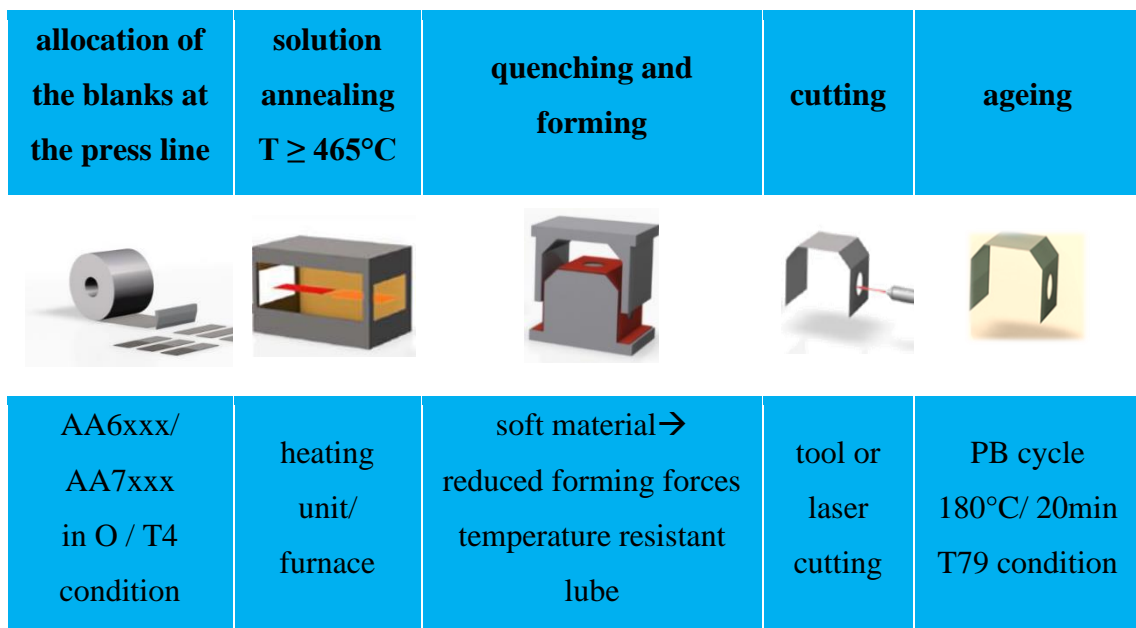


Figure 2-10: HFQ® process route

HFQ[®] Aluminium Hotforming aspects:

- **Initial sheet temper:** as-rolled (no temper)
- **Quench:** in the tool
- **Forming temperature:** hot
- **Time critical steps:** forming
- **Post-form artificial age:** yes
- **Suitable alloys:** 6xxx and 7xxx alloys
- **Formability:** very good
- **Final mechanical properties:** very good after paint baking

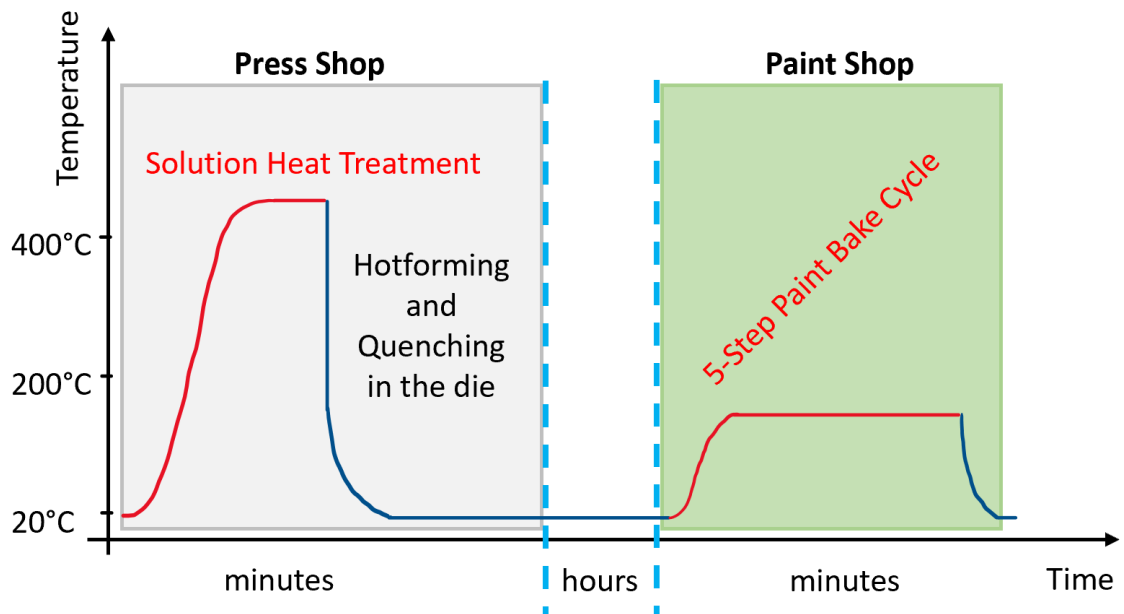


Figure 2-11: Temperature time diagram of press and paint shop (Grohmann 2016)

In the following figure (Figure 2-12) there is a B-pillar component formed using the Hotforming process. The drawing depth of this part is around 85 mm and no cracks or even notable localisations can be detected. The main problems in using this process for forming high- and ultra-high strength aluminium alloys are, for one thing the generation of severe grooves in the wall area of the formed component, and for another the galling effect onto the surface of the forming tool. This tribology problem is mainly attributed to the rather soft aluminium at this forming temperature.

In further investigation various anti-friction agents should be evaluated to avoid those unwanted effects.

Example: B-pillar formed using the Hotforming process (HFQ®)



Figure 2-12: Example of the Hotforming process (HFQ®) with a B-pillar component and its problems with adhesion and grooves

2.2.6 Concluding remarks

In the table below (Table 2-2) a comparison of each process against each other is carried out. The major aspects considered are the production rate, shape complexity, surface behaviour of the components and the industrial implementation of the process. In general, the forming process depends on the requirements of each customer.

The Warm-forming process is suitable for a high-volume production due to its short cycle time and it does not require any subsequent heat treatment. However, the major problem of this process is that complex-shaped components cannot be produced. In contrast, the W-Temper and the Hotforming process show a higher potential with regard to the formability. But those processes imply higher investments cost; e.g. fast heating and pre-cooling units are required.

Table 2-2: Aluminium forming process comparison

	Hot boron steel forming	Warm Forming	W-Temper	Hotforming HFQ®
lubrication	Not needed	Beruform STP152DL (water based)	Dry lube (E1) or Wisura ZO3373 (mineral oil based)	Boron nitride or similar Wisura ZO3373
Raw material	Special steel coating alloy	AA7075 T6	AA7075 O/ T4	AA7075 O/ T4
Production rate	Very high	Very high (no ageing required)	Low (solution annealing time, quenching separate & ageing time)	Low/ medium (solution annealing time, & ageing time)
Tool type	Complex cooling conditioned	Heated	Cold forming	Hotforming in a cold die with cooling
Shape complexity	Complex parts	Simple geometric shapes	Complex part	Complex part
Tool complexity	Complex shape tool /complex tool	Simple tool	Complex shape tool /complex tool Coating required	Complex shape tool /complex tool Coating required
Surface behaviour of stamped components	Very good	Very good	Medium	Insufficient, because of adhesion and groove effects

2.3 *Hardening mechanisms*

The most common hardening mechanisms for hardenable aluminium alloys are work hardening, solid solution hardening and precipitation hardening (Ostermann 2014). This chapter gives a brief introduction of the main hardening mechanisms.

Heat treatments can be used to improve the mechanical properties to produce a profile that is stronger, tougher and better suited to the requirements of the automotive or aerospace industries while maintaining the same appearance as before. To understand the advantages of heat treatment processes, one must first be aware of the metallic and alloyed structures (Zhang et al. 2017).

When a molten metal solidifies, the atoms arrange themselves into certain patterns called crystal structures. The two most common crystal structures in metals are body-centred cubic and face-centred cubic. These crystal structures grow uniformly in all directions within each evolving crystal. As the metal cools down, the crystals are held together by the neighbouring crystals and form a grain. The intersection lines between the grains are called the grain boundaries. Since the grains form independently of each other, their crystal structures develop in different directions and angles. All atoms in these crystal structures are held in place by electromagnetic effects to neighbouring atoms. If a force or stress is applied to a metal, these electromagnetic bonds expand to allow the atoms to move slightly. When the load is removed, the bonds pull the atoms back to their initial position. As the applied force exceeds the yield strength of the metal, these electromagnetic bonds are destroyed, resulting in plastic elongation or deformation (Zhang et al. 2017; Ostermann 2014).

2.3.1 Work hardening (Strain hardening)

Strengthening of aluminium alloys is achieved by work hardening or strain hardening. This is done by plastic deformation, intentionally or inadvertently. The process can include hammering, rolling, drawing or other physical processes. One of the most common methods of work hardening is cold rolling. As the degree of transformation increases, the longitudinal elongation of the precipitation structure and the grains in the rolling direction also increase. Through work hardening, which is based on the impediment and multiplication of dislocations, the concentration of dislocations can be raised from initially 10^7 cm^{-2} to 10^{12} cm^{-2} . In plastic deformation, the strain or ductility of the metal is the result of these atomic planes passing each other. Dislocations are inhibited by grain boundaries or obstacles (inclusions or stationary dislocation lines) during plastic deformation. Thereby, the dislocation will be blocked and a dislocation pile up, which increases the strength (Weißbach 2004; Kammer 2012). The moving of dislocations is shown in Figure 2-13.

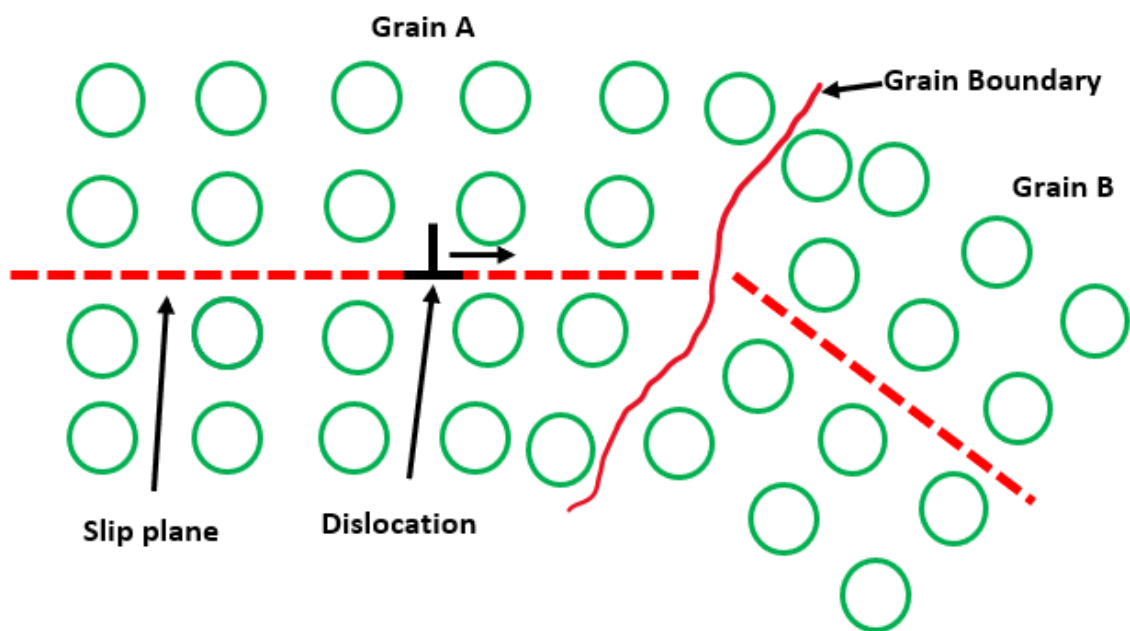


Figure 2-13: Movement of dislocation (Kammer 2012)

When plastic deformation begins, it generates more and more dislocations. For this reason, dislocations come into the path of other dislocations and they begin to obstruct each other in their movement. As there is disruption from other dislocations and the movement becomes difficult, the yield stress required to move them will increase and strengthening will take place. The degree of deformation and the composition of

aluminium alloy significantly determine the strengthening. The structural state before work hardening, the speed of deformation and the temperature have an influence too. Work hardening is done under recrystallisation temperature, usually at ambient temperature. Work hardening is limited. The yield strength limit increases faster than the tensile strength. At its peak, the material tends to brittle fracture and cracks can arise. This hardening can be reversed by heat (Kammer 2012).

2.3.2 Solid solution hardening

Solid solution hardening is carried out if alloying elements are added in the matrix of the basis material, which can be done substitutionally (replacing a solvent atom in the lattice) or interstitially (fitting into the vacancy of the lattice). The alloying element diffuses into the matrix and forms a solid solution. In most binary systems, a second phase occurs above a certain concentration in an alloy. The type of solid solution hardening depends on the size of the alloying element, which must have a sufficient difference in diameter to the aluminium atoms and adequate solubility in the aluminium matrix at room temperature. In both types, substitutional or interstitial, the overall crystal structure remains virtually unchanged and the solid solution has a higher yield strength than the pure element (Kammer 2012; Schneider 2015a).

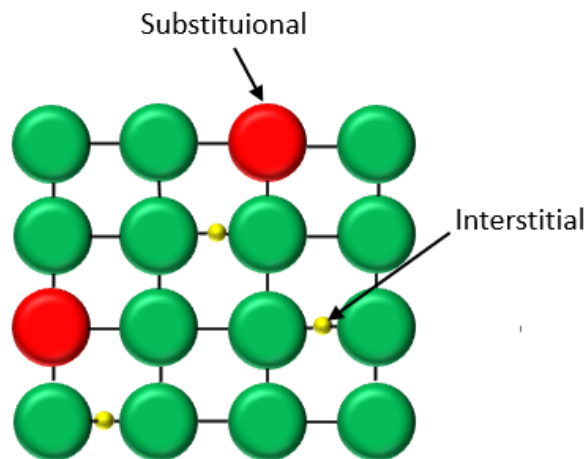


Figure 2-14: Solid solution with alloying element as substitutional (red) or interstitial (yellow) (Kammer 2012)

Figure 2-14 illustrates a solid solution with substitution and interstitial atoms. When a new atom (red colour), which is large enough, replaces the lattice position of the base

atom, this is called a substitution solution. Since both elements are in the same crystal lattice, they must have the same crystal structure in their pure form. In turn, an interstitial atom (yellow colour) fits into a cavity of the lattice.

These solid solution atoms affect the properties of the aluminium alloy by distorting the crystal lattice and interfering the homogeneity. This has the effect of obstructing the dislocation motion/slip and a deformation or strain field is generated around the solute atom (see Figure 2-15) (Kammer 2012; Schneider 2015a).

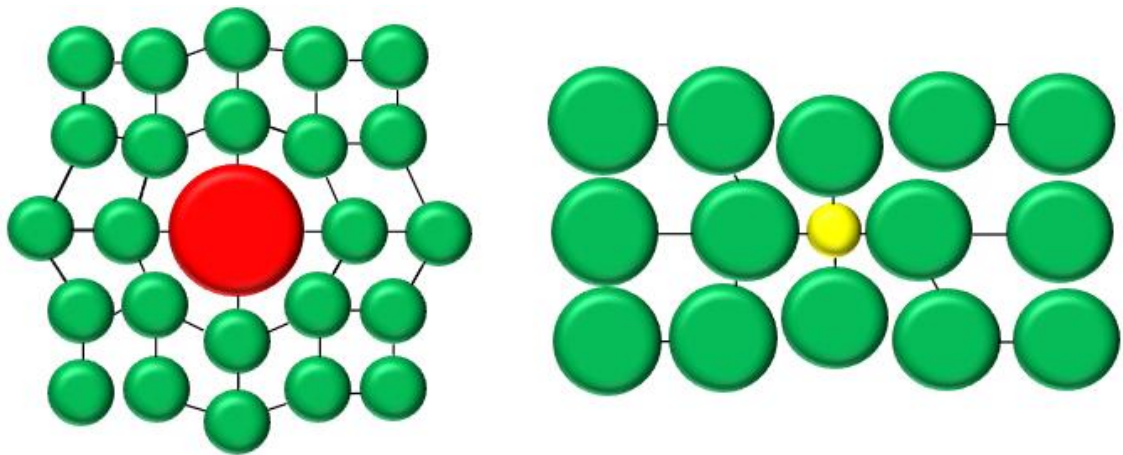


Figure 2-15: Distortion of the crystal lattice by a substitution atom (left) and an interstitial atom (right) (Schneider 2015a)

The strength of the material depends on how easily dislocations can propagate in its crystal lattice. These dislocations create stress fields within the material depending on their relative locations and sizes. When solute atoms are introduced, local stress fields are created, which interact with the dislocations, impeding their movement and causing an increase in the yield stress of the material, resulting in increased strength of the material. This gain is a result of both lattice distortion and the modulus effect. Solute atoms will either attract or repel dislocations in their vicinity. This is known as the size effect. It allows the solute atoms to relieve either tensile or compressive strain in the lattice, which in turn puts the dislocation in a lower energy state.

The energy density of a dislocation is dependent on its burgers vector as well as the modulus of the local atoms. When the modulus of solute atoms differs from that of the host element, the local energy around the dislocation is changed, increasing the amount of force necessary to move past this energy source. This is known as the modulus effect.

Meanwhile, in the specific case of a lattice distortion, the difference in lattice parameter leads to a high stress field around that solute atom that impedes dislocation movement. Surface carburising or case hardening is one example of solid solution strengthening. In addition, one should alloy with elements of different equilibrium lattice constants, increase the difference in lattice parameters, higher the local stress fields introduced by alloying with elements of higher shear modulus or very different lattice parameters to increase the stiffness and introduce local stress fields respectively. In either case, the dislocation propagation will be hindered at these sites impeding plasticity and increasing yield strength proportional to the solids concentration.

Solid solution strengthening depends on following aspects:

- Concentration of solute atoms
- Shear modulus of solute
- Atoms size of solute atoms
- Valency of solute atoms

Nevertheless, one should not add so much solute as to precipitate a new phase. This occurs if the concentration of the solute reaches a certain critical point given by the binary system phase diagram. This critical concentration therefore puts a limit to the amount of solid solution strengthening that can be achieved with a given material (Kammer 2012; Schneider 2015a).

2.3.3 Precipitation hardening

Precipitation hardening was discovered in 1906 by A. Wilm on Al-Cu-Mg alloys. Precipitation hardening is often referred to as age hardening, as a form of heat treatment used to increase the hardness and the yield strength of aluminium alloys. Precipitation hardening occurs by forming small precipitates in the initial phase of Al alloy. As shown in Figure 2-16 of the grain structure, the green dots represent how the precipitants will form evenly throughout the grains in a secondary phase. The general requirement for precipitation strengthening involves (Totten 2016):

- Formation of finely dispersed precipitates during ageing heat treatments (which may include either natural ageing or artificial ageing).
- The ageing must be accomplished not only below the equilibrium solvus temperature, but below a metastable miscibility gap called the Guinier-Preston (GP) zone solvus line.

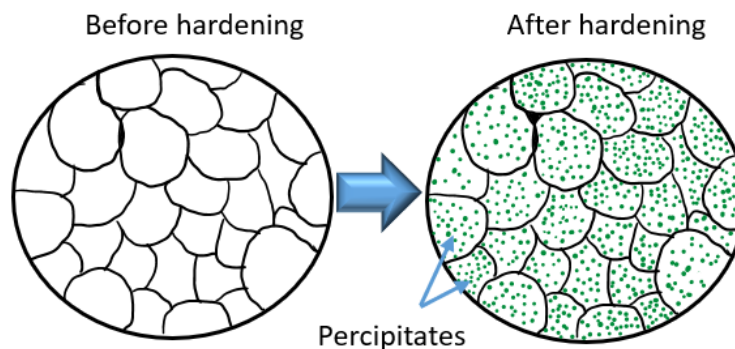


Figure 2-16: Changing of microstructure after precipitation hardening (Totten 2016)

The microstructural figure shows the precipitate generation in the base material. The precipitates are submicroscopic, so even under a regular light microscope, the precipitants would not be visible. Precipitation hardening is divided into three steps (Kammer 2012),

1. Solution heat treating
2. Quenching
3. Precipitation heat treating (ageing)

1. Solution heat treating

The aluminium alloy consists of solid solution and secondary phase particles. Through solution heating the solubility is increased so that the precipitations can move into the crystal lattice by diffusion. The temperature should be fairly high around 450°-480°C but below the melting temperature of the lowest melting phase. “The annealing time for wrought alloys is up to 30 minutes, for cast alloys it is up to three to six hours”. Depending on the Hotforming process, the annealing can be omitted (Kammer 2012).

2. Quenching

The next step is quenching, in which the alloy is rapidly cooled to room temperature to keep the alloying elements trapped in solution. The state of oversaturation can only be maintained if the quenching rate is high enough. The yield strength of the aluminium alloy has not risen. The quenching is done with e.g. water. Some alloys are only cooled by air or water mist (Kammer 2012; Totten 2016).

3. Ageing

Some aluminium alloys will harden after a few days at room temperature (natural ageing), which is designated as being in T4 condition (solution heat treated and naturally aged), while others are artificially aged by reheating to an intermediate temperature, which is designated as T6 (solution heat treated and artificially aged). Ageing increases the alloy strengthening because of the ultra-fine particles which precipitate from the supersaturated solid solution and act as obstacles to the dislocation movement (Totten 2016).

With ageing at room temperatures, the formation of precipitation occurs. The high density of dislocations is perfect for diffusion. Only an elastic distortion of the crystal lattice is the result.

Ageing at higher temperatures between 100°C and 200°C induces secondary phases/precipitations, which become larger at higher temperatures. The coherent phase that occurs at low temperature is slowly replaced by a partially incoherent phase. Higher temperature and longer ageing time have the effect of an incoherent phase (over ageing) and a decreasing of yield strength. This condition is designated as T7 (solution heat treated and overaged) and is used with some high strength alloys to improve fracture toughness and corrosion resistance (Kammer 2012; Totten 2016).

2.4 Tribology in sheet metal forming

Since Hotforming becomes a key technology to produce high strength aluminium components for the automotive industry, a detailed knowledge of the tribological behaviour and their related process boundaries in sheet metal forming is necessary (Kondratiuk & Kuhn 2011). It is of great importance for the process limits that the contact zone between sheet metal, tool die and lubricant is analysed in detail. The lubricant prevents abrasion and wear mechanisms that occur at the component and the tool surface and it is a main constituent to avoid cracks and grooves effects. Simultaneously, it is important for the washability of the sheet metal component to reduce the amount of applied lubrication to a minimum in order to reduce operating costs and to decrease the environmental impact (Ostermann 2014; Doege & Behrens 2010).

2.4.1 Friction mechanism

Tribological conditions for sheet metal forming are characterised by the following properties:

- large contact between workpiece and tool,
- low pressures in contact zone, and
- moderate velocities of the relative movement between workpiece- and tool surface
 - a low velocity of the relative movement does not fulfil the condition for the occurrence and the maintenance of hydrodynamic lubrication when using liquid lubricants

During the forming process, areas can be found that are separated by a thin lubricating film or areas with metal contact. The metallic contact depends on various factors, of which the finish roughness, surface texture and quantity of lubricant are the most important. At the beginning of the surface contact between the tool and the softer sheet surface the metallic contact is only limited to a few roughness peaks. These peaks are levelled because of the specific surface pressure and thereby hydrostatic pressure in the valleys is built up, which will be transferred onto the sheet metal. Simultaneously, the lubricant is squeezed out of the valley of the profile and forms a thin interfacial film, which consists of tribochemical reaction products and other substances e.g. metallic soaps. Due to the relative movement in the deep drawing process, shear stress occurs within the interfacial film, which is between the tool and the sheet metal surface.

If the pressure or the forming velocity is too high, the interfacial film can be teared up and a metallic contact occurs. If that happens, adhesion of the sheet material onto the tool surface will take place due to local pressure welding effects (galling). With further movement the metallic connections “bridging due to cold welding” are broken up and adhere onto the tool or they are loose abrasive particles in the metallic soap. At this moment the lubrication has collapsed (Ostermann 2014; Balbach 1988). These friction conditions are shown in Figure 2-17.

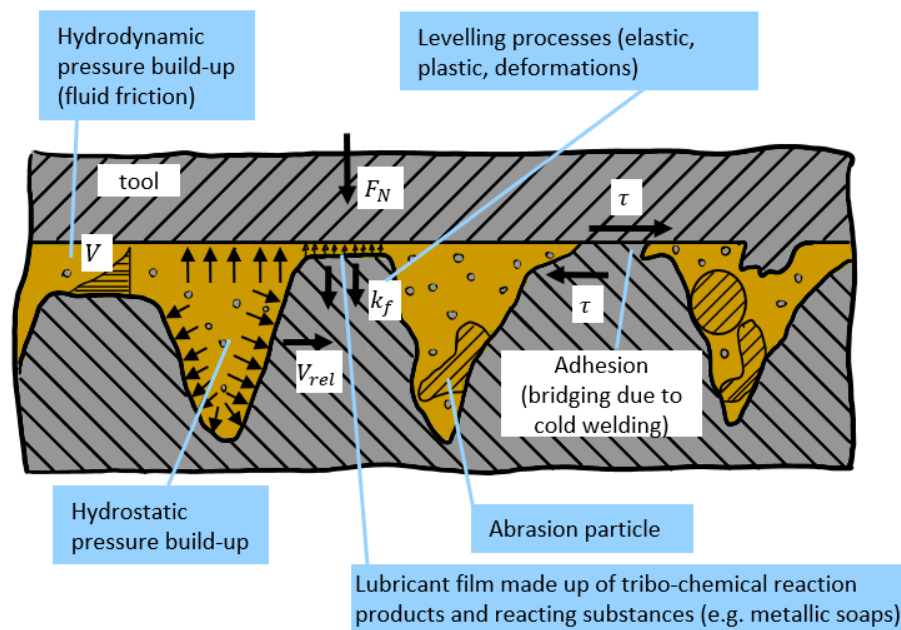


Figure 2-17: Mechanism of friction in a deep drawing process (Ostermann 2014)

In tribology, friction between areas of matter in contact with each other is divided into four friction states, depending on the aggregate state (Siegert 2015):

- a) Solid state friction is friction between areas of material with solid state properties in direct contact. If the friction takes place between solid boundary layers with modified properties, e.g. reaction layers, it is called boundary layer friction. If the boundary layer is a molecular film originating from the lubricant, this is also called boundary friction. The friction coefficient is between $0.1 < \mu < 0.3$.
- b) Fluid friction is a friction in a material area with fluid properties. This state of friction also applies to the liquid lubricant layer that completely separates the solids. The friction coefficient is lower than $\mu < 0.01$.

- c) Gas friction is a friction in a material area with gas properties. This state of friction also applies to a gaseous lubricant layer that completely separates the solids ($\mu \sim 0$).
- d) Mixed friction is any mixed form of the friction mentioned under a) to c). Mixed friction is primarily understood to be an intermediate form of solid body friction and fluid friction. The friction coefficient is between $0.01 < \mu < 0.1$.

Due to tribological conditions in sheet metal forming, mixed friction is the predominant lubrication condition. This is characterised above all by low relative speeds, low surface pressures and large contact surfaces between tool and workpiece.

Despite many attempts, it has not yet been possible to describe the mixed lubrication condition with physical accuracy. Therefore, tribological data, such as the coefficient of friction μ in models (strip drawing tests) or real tests must be determined experimentally (Siegert 2015).

2.4.2 Tribological system of sheet metal, tool die and lubricant

The complete tribological system consists of sheet metal surface, tool die surface and lubricant.

Friction behaviour of aluminium sheet metal

To model the friction behaviour and to determine the tribological parameter, many testing methods have been developed. The most commonly used is the strip-drawing test, where a sheet metal strip is drawn through two drawing brackets at a defined clamping force. The coefficient of friction can be calculated by means of the surface pressure and corresponding drawing force according to Coulomb's law.

$$F_F = \mu * F_N \quad (2.1)$$

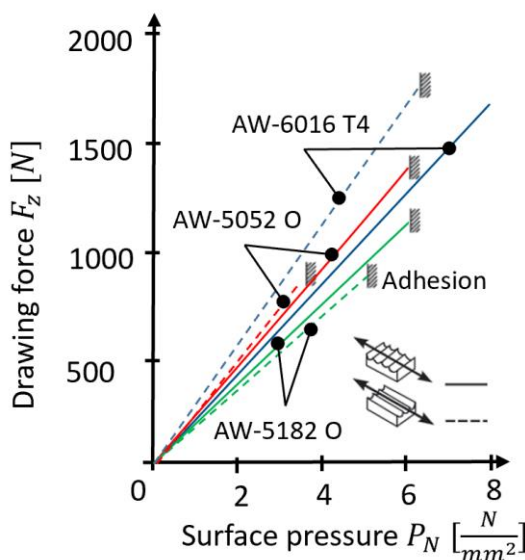


Figure 2-18: Friction behaviour and adhesion tendency of aluminium alloys in the strip drawing test (Mössle 1983)

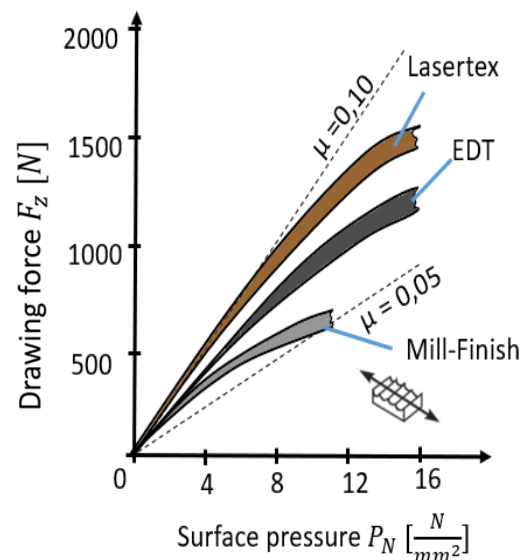


Figure 2-19: Influence of the surface structure on the friction behaviour (Ostermann 2014)

Figure 2-18 shows the results of a strip-drawing test. In this experiment the specimens consisting of various aluminium alloys (e.g. EN AW-6016-T4, EN AW-5052-O and EN AW-5182-O) with a “mill-finish” surface were tested (Mössle 1983). It is apparent that the friction is anisotropic as it depends on the direction of rolling. Furthermore, it can be seen that the adhesion or cold welding occurs at a relatively low blank holder pressure and it depends on the rolling direction too. Figure 2-19 indicates that the influence of

various surface structures, such as mill-finish (Figure 2-20 (A)), electrical discharge texturing (EDT) (Figure 2-20 (B)) or laser texturing, affect the friction behaviour to a certain extent. It is obvious that EDT surfaces are much better regarding the adhesion tendency (Nitzsche 2007; Kovalchenko et al. 2005; Zhou et al. 2011).

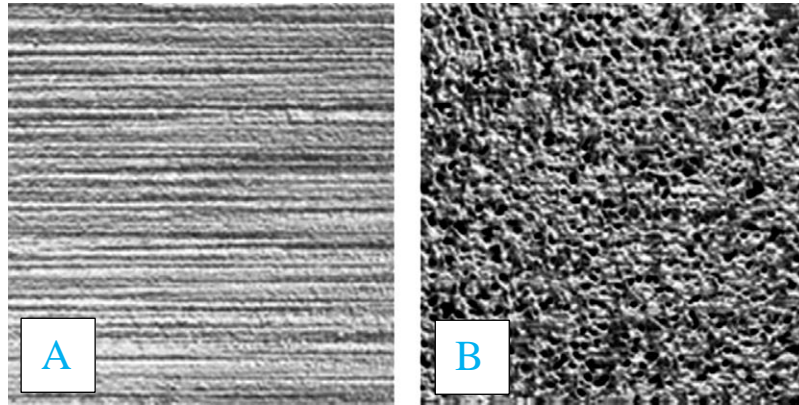


Figure 2-20: REM-recordings of surface structure of the aluminium alloy A) mill-finish; B) electrical discharge texturing (EDT) (source: (Zhou et al. 2011))

Tool surface

For the deep drawing process of aluminium the same tool materials are used as for the production of steel components such as tool steel 1.2311 or 1.2312 (Schuler GmbH 1998). However, due to the adhesion tendency, the tool surface should have an average roughness of $R_z \leq 1\mu m$ at critical contact zones. Through surface treatments of the forming tool the tendency to adhesion can be significantly affected. Plasma nitriding and physical vapour deposition (PVD) or chemical vapour deposition (CVD), coatings with Titanium nitride (TiN) and Vanadium nitride (VN) onto the tool steel are particularly suitable for aluminium processing (Podgornik et al. 2006). Moreover, Diamond-Like-Carbon (DLC) coatings also have very good anti-adhesion properties (Enke 1997; Sato et al. 2000). Which kind of surface treatment is useful depends on the technical and economic conditions, for example dimensions of the tool and number of pieces to be produced during a life of a forming tool.

2.4.3 Concluding remarks

Friction between the forming tool and the aluminium sheet is expected to be higher if compared to a forming operation using steel sheet because aluminium has a surface roughness (Ra) from 0.25 to 0.38 micron. In comparison, the Ra of steel sheet is about 0.63 to 0.88 micron. The smoother texture of aluminium requires dry, waxlike lubricants. When the die surface meets the generally rougher and softer surface of the sheet metal the area of direct metallic contact is, for a moment, relatively small and restricted to a few roughness peaks. Due to the high specific local pressure the peaks are levelled and the die surface sinks deeper into the sheet surface. The lubricant enclosed in the roughness valleys builds up a hydrostatic pressure and transmits the die pressure onto the sheet metal surface. At the same time the abundant lubricant is squeezed out of the valleys and pressed between the flattened roughness peaks. Whereby a thin boundary film (made up of tribochemical reaction products and reacting substances e.g., metallic soaps) is formed. To reduce and to avoid the metallic friction and the abrasion during the deep drawing process, a thin interfacial lubrication film is required. Furthermore, the hydrostatic pressure in roughness valleys of the sheet metal needs to be maintained throughout the whole process.

Surface texturing, in particular EDT surfaces, where micro dimples or micro channels in the metal sheet surface are included, improves the forming behaviour compared to mill-finish surfaces (cf. Figure 2-19). This reduction of friction is a result of the hollow and isotropic shape of the EDT surface of the aluminium sheet (Zhou et al. 2011). Through this technique there is sufficient lubricant reservoir and absorption capacity for abrasive particles (Ostermann 2014). Therefore, an EDT or laser surface texturing (Kovalchenko et al. 2005) behaviour is preferable to reduce and to avoid adhesion and abrasion effects onto the tool or component surface. However, it is currently not possible to obtain an AA7075 metal sheet with these surface conditions from a supplier. Therefore the following tests are carried out with a mill finish surface, which should also be used in the production process to reduce costs.

2.5 Fundamentals of simulation techniques for the forming process

The simulation of the forming process of complex shape sheet metal parts has become a standard approach in sheet metal processing. The objective is usually to ensure manufacturability, such as design of the drawing tools to avoid cracks, springback and delay. The consideration of initially available material directional deviation or the anisotropy occurring during the forming process must be given special importance in the forming simulation. A common assumption in sheet metal forming is the plane stress condition and anisotropic effect in plane. Depending on the material, this anisotropy can have a decisive effect on the material behaviour during a forming process.

In addition, the mechanical properties of the initial state of sheet metal cannot be used directly for crash simulation because the forming processes during production induced thinning and pre-damage. If necessary, heat treatments are also carried out after the forming process. As a result of the forming process, local flow stresses and fracture strains are not homogeneous. This inhomogeneity cannot be neglected and must be taken into account by means of a forming simulation. For this purpose, the stresses, strains, thicknesses and damages determined in the forming simulation are transferred to the crash simulation, which is illustrated in Figure 2-21 (Clees et al. 2010).

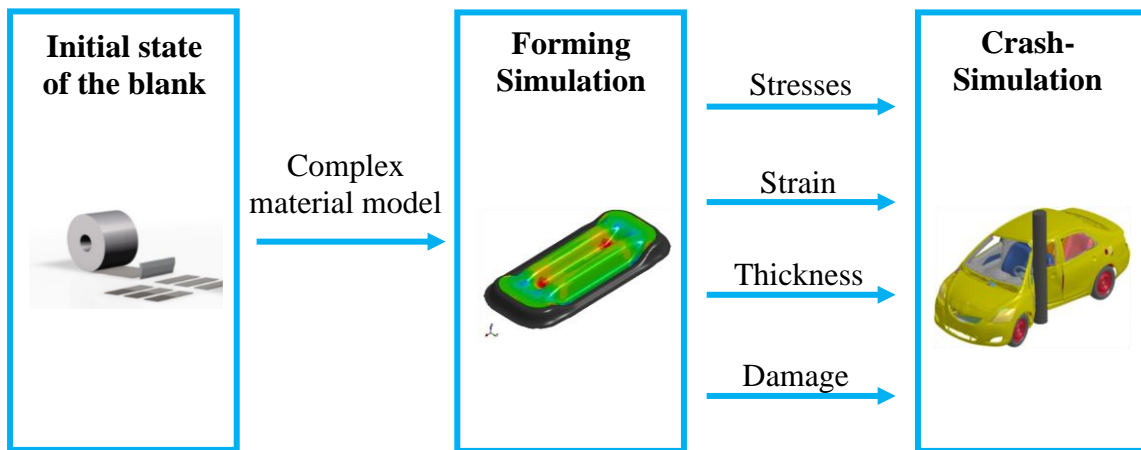


Figure 2-21: Crash simulation under consideration of the manufacturing process

The parameters required to describe the failure behaviour are determined by different tensile tests, which are illustrated in Table 2-3 in Chapter 2.5.3. These tensile tests cover different stress states and are simulated for the failure model. Using optimisation software, the parameters of the failure model are adjusted until the force-displacement or

stress-strain curves from the simulation match the experimentally determined curves for each individual tensile test. After the calibration of the failure model it can be used for further component simulations (see details in Chapter 2.5.4).

2.5.1 Material testing

To characterise the anisotropy, the use of the Lankford-Parameter or colloquial r-values is customary in the forming technique. These parameters can be determined by uniaxial tensile tests in different directions in the sheet plane, which is shown in Figure 2-22.

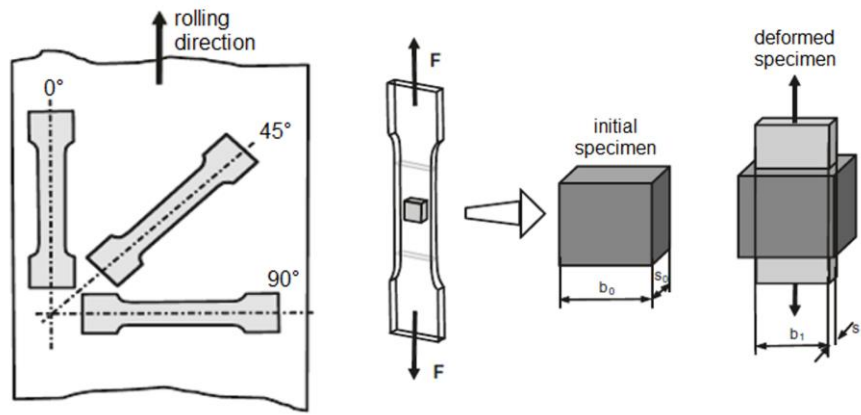


Figure 2-22: Determination of the Lankford-Parameter (0°/45°/90° rolling direction) after (DIN EN ISO 10113)

The r-value is defined by:

$$r = \frac{\varepsilon_2}{\varepsilon_3} = \frac{\ln\left(\frac{b_1}{b_0}\right)}{\ln\left(\frac{s_1}{s_0}\right)} \quad (2.2)$$

whereby ε_2 is referred to elongation in plane of the sheet perpendicular to the loading direction and ε_3 is the elongation in thickness direction of the sheet. Since the sheet thickness is usually smaller by orders of magnitude than the sheet width or length, a measurement of the sheet thickness during a tensile test would potentially be strongly affected by measurement errors. Therefore, taking advantage of the volume constancy (isochoric plastic flow), usually only a measurement of the longitudinal and transverse strain is made, then from the above assumption, the r-value is calculated by equation (2.3) (DIN EN ISO 10113).

$$r = \frac{\ln\left(\frac{b_1}{b_0}\right)}{-\ln\left(1 + \frac{\varepsilon_{pl}}{100\%}\right) - \ln\left(\frac{b_1}{b_0}\right)} \quad (2.3)$$

where ε_{pl} is the actual plastic strain:

$$\varepsilon_{pl} = \left[\frac{\Delta L}{L_e} - \frac{F}{S_0 * m_E} \right] * 100\% \quad (2.4)$$

The measurement is usually carried out at several different longitudinal strains below the uniform strain (for example, 2-15 %) and then averaged.

An r-value greater than one describes a material behaviour in which the material deforms more in the width than in the thickness. An r-value that is less than one describes a material behaviour in which the material deforms more in the thickness than in the width. An r-value of one describes an isotropic deformation behaviour in width and thickness (cf. Figure 2-23).

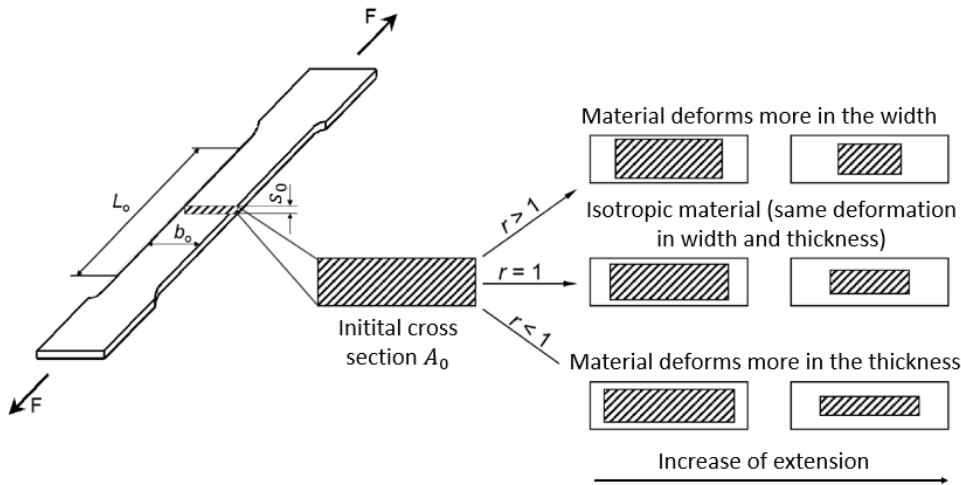


Figure 2-23: Illustration of the cross-section changes for different r-values (DIN EN ISO 10113)

From the r-values of the different orientations to the rolling direction, the normal anisotropy r_n can be determined after equation (2.5).

$$r_n = \frac{r_0 + 2r_{45} + r_{90}}{4} \quad (2.5)$$

This reflects the average ratio of the thinning to the transverse strain in the sheet metal plane and is thus a measure of the deep drawability. For deep drawn sheets, the highest

possible value for r_n is sought, since a lower thinning of the sheet during deep drawing means higher achievable degrees of deformation.

2.5.1.1 Uniaxial tension test

The tensile test is standardised after (DIN EN ISO 6892-1) and provides detailed information of the material properties required in sheet metal forming processes. Thus, the tensile test is used to determine the flow curve, which is then later used for e.g. FEM forming simulations. During the test the applied force versus length variation is measured (Birkert, Haage & Straub 2013). The data received (force-displacement diagram) is converted and plotted into a stress-strain diagram. In this diagram, the nominal stress σ_0 is plotted against the engineering strain ε_s . The nominal stress σ_0 is defined by applied force F related to the outlet cross-section A_0 (cf. Figure 2-24).

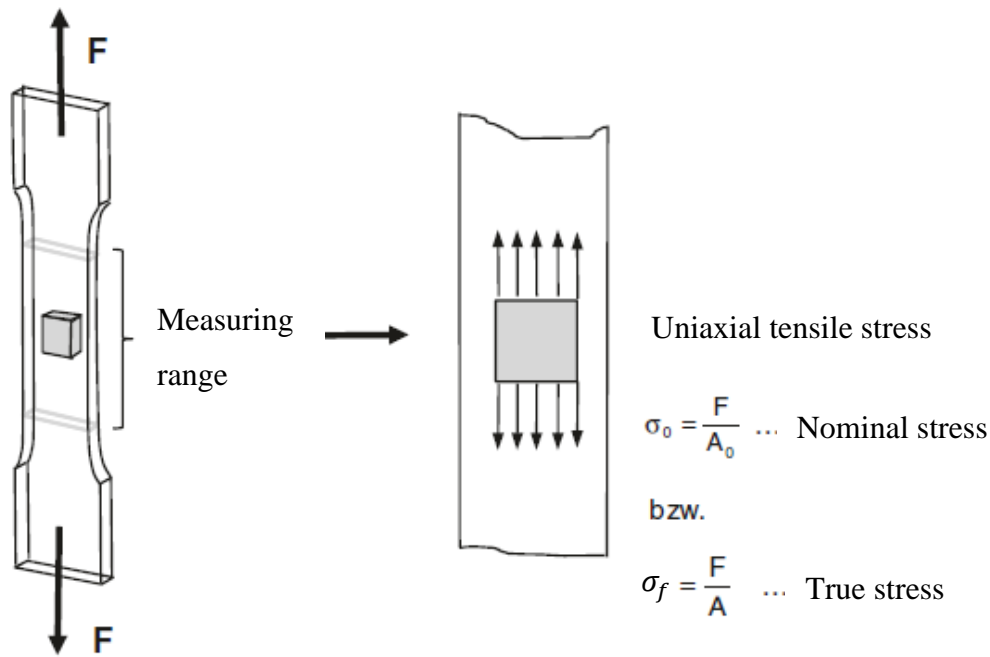


Figure 2-24: Tensile test on flat tensile specimen for flow curve recording according to DIN 6892-1

Due to the law of volume-constance and because the cross-section decreases during deformation, the nominal stress is not a common parameter to be used to describe stress conditions as it occurs in reality. Therefore, the true stress σ_t is used instead of the nominal stress. If the true stress exceeds the flow limit, it will be designated as flow stress σ_f (cf. Figure 2-25). This only applies until necking after achieving the uniform

elongation (Birkert et al. 2013). In the forming technique, the area between flow initiation and necking is important.

<p>(1)</p> $\sigma_0 = \frac{F}{A_0}, e_s = \frac{\Delta l}{l_0} \quad (2.6)$	<p>(2)</p> $\sigma_t = \frac{F}{A} = \sigma_0(1 + e_s), \quad (2.7)$ $\varepsilon = \ln(1 + e_s)$
<p>Continuous strain hardening results in an initially increasing course of the curve until e_u. As soon as the uniform elongation has been exceeded, the effect of necking of the cross-section predominates.</p>	<p>Since the force F is related to the true cross-section A, a continuously increasing curve profile is now obtained.</p>

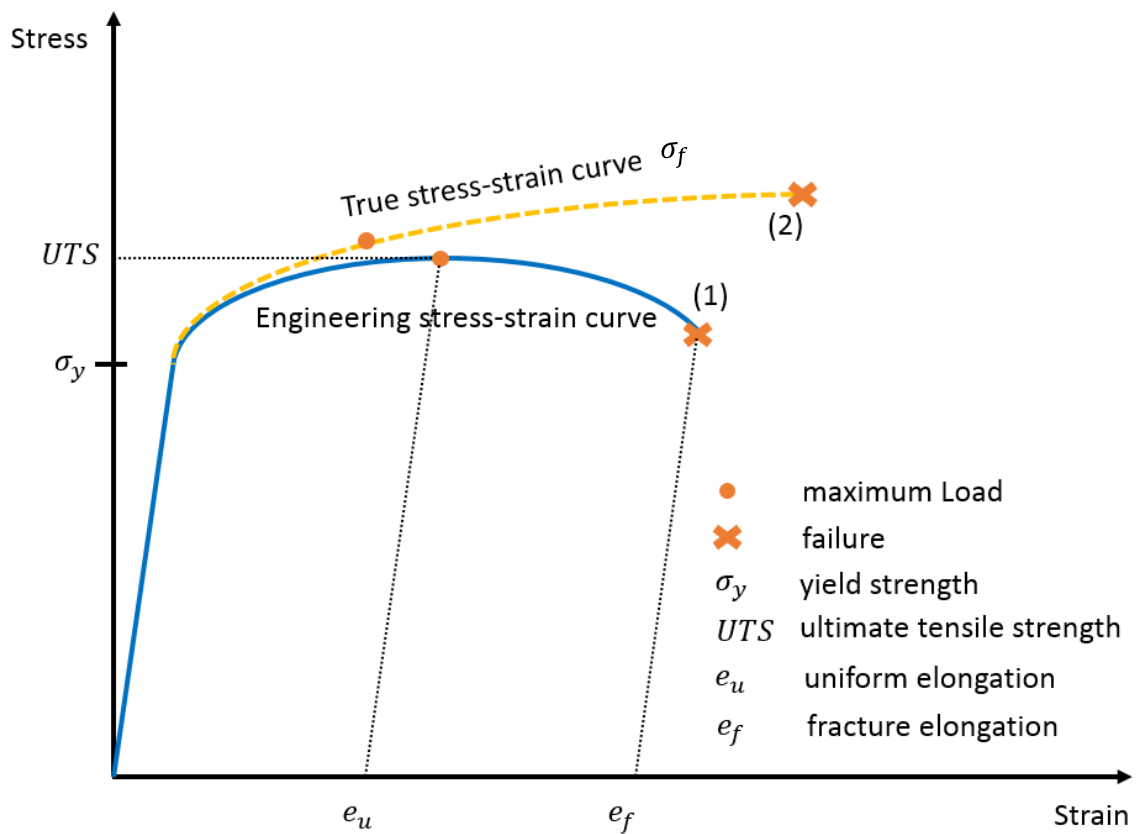


Figure 2-25: Schematic illustration of a stress-strain diagram

2.5.1.2 Erichsen testing

The Erichsen test is standardised after ISO 20482 and gives information of the stretch-formability of a material. A sheet metal specimen is clamped between a die and a blank holder by applying a blank holder force F_{BH} and, if necessary, the material is prevented from flowing on by additional clamping beads (blue circle Figure 2-26). A semicircular punch is pressed against the clamped specimen with a punching force F_p and the sheet is subjected to biaxial stretch forming until a crack appears at the tip. During the test the force-displacement curve is recorded and the final dome height D_h is measured. The thickness of the sheet metal plays an important role in relation to the height of the dome. Therefore, the Erichsen test is usually carried out to compare the stretch-formability of different materials with the same sheet thickness against each other (Ostermann 2014).

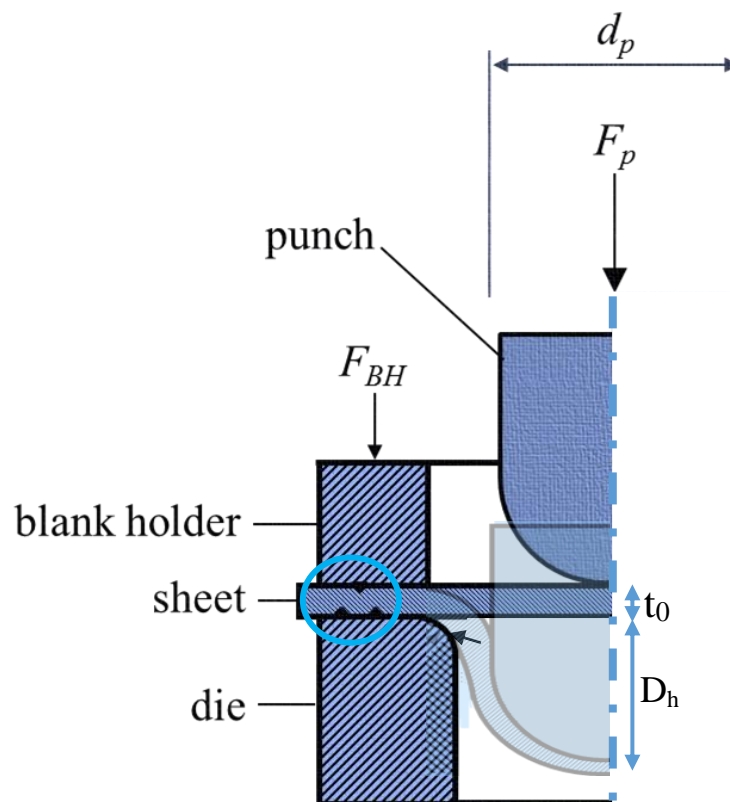


Figure 2-26: Schematic of an Erichsen testing set-up (Ostermann 2014)

F_p :	punch force	F_{BH} :	blank holder force
t_0 :	sheet thickness	D_h :	dome height
d_p :	punch diameter	r_d :	die radius

2.5.2 Stress measures

Material failure is dependent on the stress state. This was shown by (Bridgman 1952) and is useful to describe the stress state of different load cases using the first stress invariants of the stress tensor. In sheet metal forming it is a common assumption to use the plane stress case ($\sigma_3 = 0$). This simplification means that different stress states can be clearly determined with just one parameter. This parameter is called triaxiality η and it is defined as (Sandberg & Rydholm 2016):

$$\eta = \frac{I_1}{\sigma_{vm}} \quad (2.8)$$

where I_1 is the first stress invariant ($\sigma_3 = 0$):

$$I_1 = \frac{\sigma_1 + \sigma_2}{3} \quad (2.9)$$

and the von Mises stress (σ_{vm}) with the principal stresses (σ_1, σ_2 and σ_3):

$$\sigma_{vm} = \sqrt{\sigma_1^2 + \sigma_2^2 - \sigma_1 * \sigma_2} \quad (2.10)$$

Numerical practise is often the usage of strain-based failure criteria. The lower limit value of this equation results to $\eta = -2/3$ (pure pressure) and the upper limit value results to $\eta = 2/3$ (biaxial tension) for shell elements. In contrast to the three-dimensional view, whereas the lode angle ($-1 < \xi < 1$) is added. However, this is associated with a considerably long calculation time and is not a common assumption in sheet metal forming.

2.5.3 Constitutive models for forming simulation

The following section describes some common material models for forming simulation of metallic materials. These models are based on the assumption of an isochore plastic material behaviour and the independence of the yield criterion from the hydrostatic pressure. This common assumption is based on the results of (Bridgman 1952), which could not determine an independence of the plastic flow of an metallic material from the hydrostatic pressure. The description of plastic flow uses a yield criterion that represents an image of the stress tensor on a scalar. A simple distinction occurs between the so-called square and non-square flow surfaces. The best-known representative of quadratic flow conditions is the condition according to von Mises.

2.5.3.1 Flow criterion after Hill (1948)

The yield condition according to (Hill Rodney 1948) is given here as representative of the quadratic yield condition. It can be considered as a generalisation of the von Mises' yield criterion for orthotropic materials.

The yield criterion is given by:

$$\sigma = \sqrt{F(\sigma_{yy} - \sigma_{zz})^2 + G(\sigma_{zz} - \sigma_{xx})^2 + H(\sigma_{xx} - \sigma_{yy})^2 + 2L\sigma_{yz}^2 + 2M\sigma_{xz}^2 + 2N\sigma_{xy}^2} \quad (2.11)$$

In comparison to the von Mises formulation, the additional coefficients F, G, H, L, M and N are introduced, which allow a modelling of the anisotropy.

Under the assumption that orthotropic material behaviour is present, follows:

$$G + H = 1 \quad (2.12)$$

and the assumption of the plane stress state follows:

$$\sigma_{zz} = \sigma_{xz} = \sigma_{yz} = 0 \quad (2.13)$$

The requirements for the convexity of the yield surface place additional conditions on the coefficients:

$$\begin{aligned}
F + G &\geq 0 & L &\geq 0 \\
G + H &\geq 0 & M &\geq 0 \\
H + F &\geq 0 & N &\geq 0 \\
FG + GH + HF &\geq 0
\end{aligned} \tag{2.14}$$

The relation between the anisotropy coefficients r_0, r_{45} & r_{90} and the coefficients F, G, H, L, M, N may be easily obtained from the flow rule associated to the yield function.

$$F = \frac{r_0}{r_{90}(r_0 + 1)} \tag{2.15}$$

$$G = \frac{1}{r_0 + 1} \tag{2.16}$$

$$N = \frac{(1 + 2r_{45})(r_0 + r_{45})}{2r_{90}(1 + r_0)} \tag{2.17}$$

2.5.3.2 Flow criterion after Barlat89

A commonly used material model for modelling the plastic anisotropy is the Barlat89 or 3-parameter Barlat (Barlat & Lian 1989). The flow function is as follows:

$$\sigma = a|K_1 + K_2|^m + a|K_1 - K_2|^m + c|K_2|^m - 2\sigma_{yield}^m \tag{2.18}$$

Where K_1 and K_2 result from:

$$K_1 = \frac{\sigma_{xx} + h\sigma_{yy}}{2} \tag{2.19}$$

$$K_2 = \sqrt{\left(\frac{\sigma_{xx} - h\sigma_{yy}}{2}\right)^2 + p^2\sigma_{xy}^2} \tag{2.20}$$

The parameters a, c and h are dependent on the anisotropic parameters r_{00}, r_{45} & r_{90} and are defined as follows:

$$a = 2 - 2\sqrt{\frac{r_{00}}{1 + r_{00}}}\sqrt{\frac{r_{90}}{1 + r_{90}}} \tag{2.21}$$

$$h = \sqrt{\frac{r_{00}}{1 + r_{00}}} \sqrt{\frac{1 + r_{90}}{r_{90}}} \quad (2.22)$$

$$c = 2 - a \quad (2.23)$$

The parameter p , which has yet to be defined, is solved iteratively using the following equation:

$$\frac{2m\sigma_{yield}^m}{\left(\frac{\partial F}{\partial \sigma_{xx}} + \frac{\partial F}{\partial \sigma_{yy}}\right)\sigma_\varphi} - 1 - r_\varphi = 0 \quad (2.24)$$

Here φ is the angle of the respective Lankford parameter. The parameter $m=8$ should be used for face-centred cubic lattice structures and $m=6$ for body-centred cubic lattice structures.

2.5.3.3 Conclusion

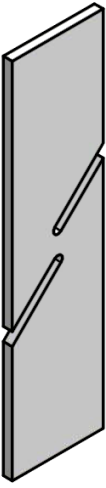
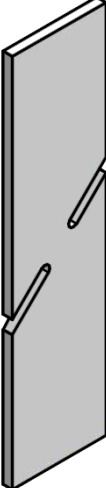
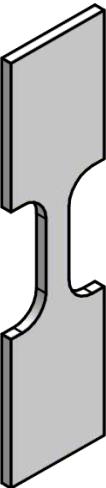

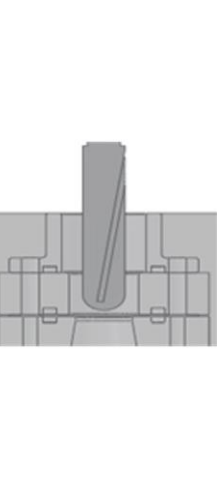
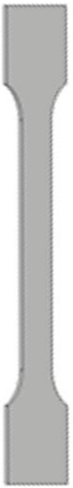
These yield conditions, like Hill48 or Barlat89, have the advantage of a simple structure and a limited number of parameters. Both material models can represent the flow behaviour of thin sheets with anisotropic properties under the assumption of orthotropic material behaviour. A disadvantage is the limitation to a given shape of the yield surface, which results from the square formulation. Experiments have shown that for certain classes of materials, such as aluminium alloys, the flexibility of the formulation is not sufficient to represent the behaviour (Barlat et al. 1997; Banabic et al. 2000). Because of these recent publications, Barlat, Yoon and Banabic have suggested a variety of especially non-quadratic flow criteria, for example Barlat YLD2000 or BBC2005 (Barlat et al. 2003; Yoon et al. 2004; Banabic 2010). These constitutive models require not only the anisotropic values r_{00} , r_{45} & r_{90} but also the yield stresses σ_{00} , σ_{45} & σ_{90} and the biaxial values r_b & σ_b .

Out of these values eight α -values are calculated, which are needed for the implementation of the Barlat YLD2000 model. A Matlab script, which has been developed in cooperation with the software producer Altair, is given in Appendix B to calculate these values out of the experimental results. This complex material model is used below to simulate the forming process.

2.5.4 Material failure

To understand how a material behaves under various load conditions, the material must be analysed under different stress states. At least five different tests (shear-, tensile-, notched and biaxial tensile test) are carried out to identify the damage and failure curve within a triaxiality of $0 < \eta < 0.66$, which means from pure shear up to biaxial stress condition. This area is of particular importance for sheet metal forming (Banabic 2010). The exact drawings of the specimens that are used to represent as many different triaxialities as possible, are shown in Appendix C and the schematic representation is given in Table 2-3.

Table 2-3: Schematic representation of the specimens (Feucht et al. 2017)

Shear test (shear angle 0°)	Shear test (shear angle 45°)	Small-tensile test	Notched test	Erichsen, Bulge or Nakajima test	Large-tensile test (only for element regularisation)
					
$\eta \sim 0$	$\eta \sim 0.25$	$\eta \sim 0.33$	$\eta \sim 0.5$	$\eta \sim 0.66$	$\eta \sim 0.33$

Furthermore, the failure strain depends on the load state, pre-damage and load path, which are described and validated in different publications (Haufe et al. 2011; Feucht et al. 2017). The influence is shown in Figure 2-27 and is illustrated by the following example.

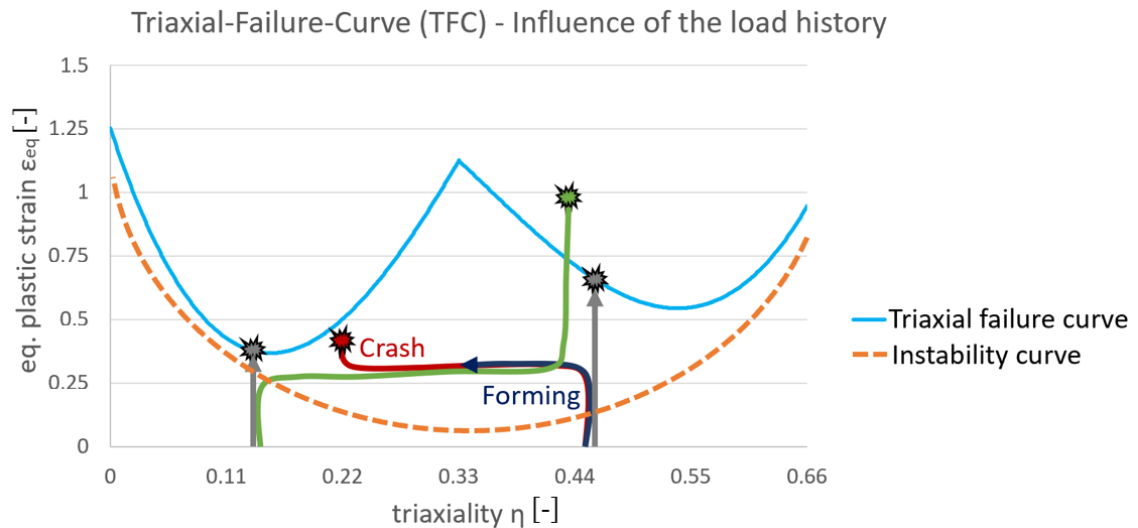


Figure 2-27: Influence of load state, pre-damage and load path (Feucht et al. 2017)

The green curve represents an element, which is loaded to an equivalent plastic strain of $\varepsilon_{eq} \sim 25\%$ at a triaxiality of $\eta \sim 0.11$ and then loaded directly to $\eta \sim 0.44$ until failure. Due to the damage accumulation and load path dependency, it can happen that the element fails only above or below the failure curve. The blue/red curve shows the pre-damage due to forming or other previous processes. In this process the element has a triaxiality for example of $\eta \sim 0.44$ and an equivalent plastic strain of $\varepsilon_{eq} \sim 25\%$. After the manufacturing process the damage parameter is transferred to the crash simulation. At this point, the element or rather damage accumulation started with a pre-damage of $\varepsilon_{eq} \sim 25\%$ until the element failed at a triaxiality of $\eta \sim 0.22$ and $\varepsilon_{eq} \sim 40\%$.

Furthermore, in Table 2-4 are different failure models that are commonly used in sheet metal forming and crash-simulations. In the further course of the thesis the “Generalised incremental stress state dependent damage model (GISSMO)” will be used and explained in detail.

Table 2-4: Failure Models (Feucht et al. 2017)

Name	Failure criterion	Dependency of		
		Load path	Strain rate	State of stress
Max. strain value	$\varepsilon_{pl} \leq \varepsilon_f$	no	no	no
FLD	$\varepsilon_1 = \varepsilon_{1, fld}(\varepsilon_2)$	no	no	yes
Johnson Cook	$\varepsilon_f = [D_1 + D_2^{D_3 \sigma^*}][1 + D_4 \ln \dot{\varepsilon}^*][1 + D_5 T^*]$ $T^* = \frac{T - T_{room}}{T_{melt} - T_{room}}$ $\sigma^* = \frac{I_1}{\sigma_{eff}}$ $\dot{\varepsilon}^* = \text{normalized effective strain rate}$ $\Delta D = \sum \frac{\Delta \varepsilon_p}{\varepsilon_f}$	yes	yes	no
GISSMO	$\Delta D = \frac{\Delta \varepsilon_p}{\varepsilon_f} n D^{(1 - \frac{1}{n})}$	yes	yes	yes
IDAM	$\varepsilon_f = f(\dot{\varepsilon}, \eta, \theta, \alpha)$	yes	yes	yes

2.5.5 Damage mechanics

Material damage is a central component of the material properties. The damage variable affects material stiffness and/or strength before final rupture occurs. The concept includes growing imperfections in the material. Figure 2-28 shows the section area with microstructural defects and the associated reduction of the effective cross-section.

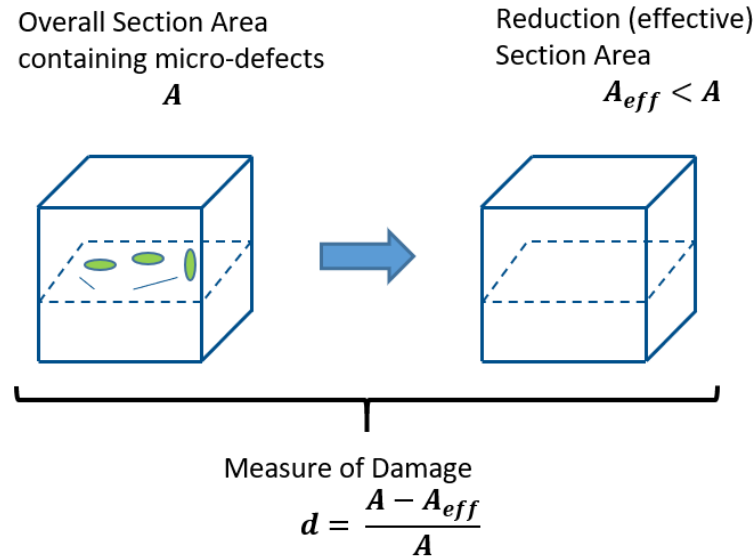


Figure 2-28: The current section area and the effective section area (Haufe et al. 2011)

The current section area A and the effective section area with microstructural defects A_{eff} define the damage parameter as follows:

$$d = \frac{A - A_{eff}}{A} \quad (2.25)$$

Therefore, the reduction of the effective cross-section leads to a reduction of tangential stiffness.

Table 2-5: Ductile damage (Feucht et al. 2017)

effective strain	effective geometry	effective stress	damaged modulus
$\varepsilon_p = \varepsilon_{p,eff}$	$A_{eff} = A(1 - d)$	$\sigma = \sigma_{eff}(1 - d)$	$E_d = E(1 - d)$
(2.26)	(2.27)	(2.28)	(2.29)

These equations (eq. (2.26)-eq.(2.29)) are basic relations and phenomenological descriptions to couple damage to the geometry, stress and modulus. Figure 2-29 illustrates

the relation between the equations in Table 2-5 and damaging of the material stiffness and strength.

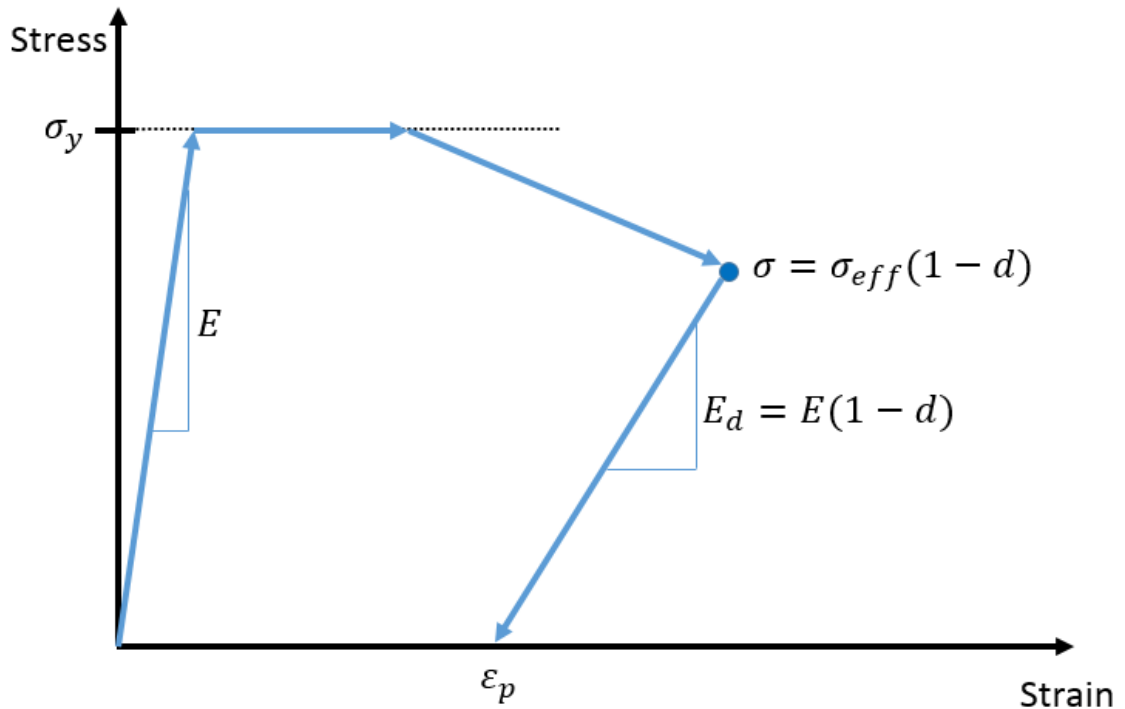


Figure 2-29: Ductile damage – illustration of damaging

In most damage models the damage variable also serves as a failure variable.

2.5.6 Generalised Incremental Stress-State dependent Damage Model (a.k.a. GISSMO)

Failure models can basically be divided into phenomenological and micromechanical models. The GISSMO (Generalised incremental stress state dependent damage model) is a phenomenological failure model and describes a strain failure model based on path-dependent damage accumulation using user-defined functions. This model is suitable for the failure of high strength aluminium and can be created using simple specimen geometries (see Table 2-3). It also offers various options for adjusting the material behaviour.

As input, the failure model requires the triaxial failure curve in tabular form (see Figure 2-27). The damage parameter D is introduced to describe the damage. The damage of each individual element is calculated at each calculation time step as follows:

$$\Delta D = \frac{\Delta \varepsilon_p}{\varepsilon_f} \cdot n \cdot D^{(1-\frac{1}{n})} \quad (2.30)$$

$$\sum \Delta D \geq 1 \quad (2.31)$$

The GISSMO model is evaluated and accumulated at every time step using the current value of damage (D), plastic strain increment ($\Delta \varepsilon_p$) and the equivalent fracture strain ($\varepsilon_f(\eta)$) as function of the triaxiality (cf. eq.(2.30) and (2.31)). A crack or element rupture occurs if the damage parameter D reached one, which is shown in equation (2.31). Then the element is deleted. Whereby removing the element is not physically correct, because it reduces the mass. However, this is negligible for finely meshed sheet metal parts.

According to the experience of DYNAmore, the GISSMO parameter n should be selected with $n = 2$ (see Figure 2-30). This reduces the initial damage mechanics and increases with further damage. In the Johnson-Cook failure model (see Table 2-4, $n = 1$), damage is already accumulated directly after the yield strength.

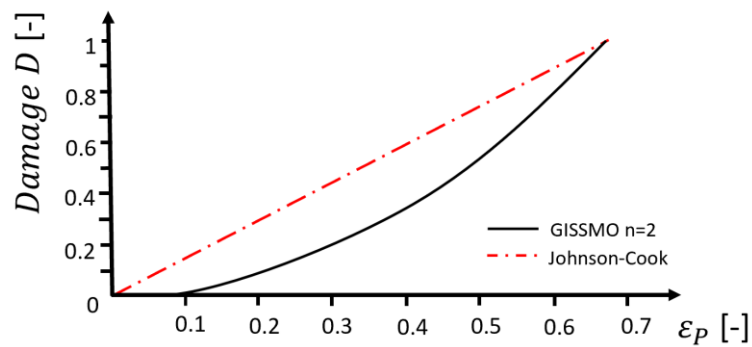


Figure 2-30: Damage accumulation (Feucht et al. 2017)

Once uniform elongation is reached, various instabilities occur, as diffuse necking. This is represented by a further curve of the so-called instability curve. It is based on the same formula as the damage accumulation described in the equation (2.30) and (2.31), where the D parameter is replaced by F . This curve is also adapted to the test data with the

parameter optimiser and is illustrated in Figure 2-27 too. Depending on the material instability, the behaviour or localisation depends on the element size. The finer a model is meshed, the greater the stress drop after uniform elongation. To take this into account, a regularisation with different element sizes should be carried out.

The parameters D_{crit} and $FADEXP$ offer a further possibility to control instabilities of the material behaviour. These enable the stress to be reduced from the specified damage D_{crit} according to the following equation (Feucht et al. 2017):

$$\sigma^* = \sigma \left[1 - \left(\frac{D - D_{crit}}{1 - D_{crit}} \right)^{FADEXP} \right] \quad (2.32)$$

In Figure 2-31 the $FADEXP$ is varied with constant parameter D_{crit} . This also shows that the stress reduction has no influence on the failure. The failure occurs for all parameters at the same strain (blue circle).

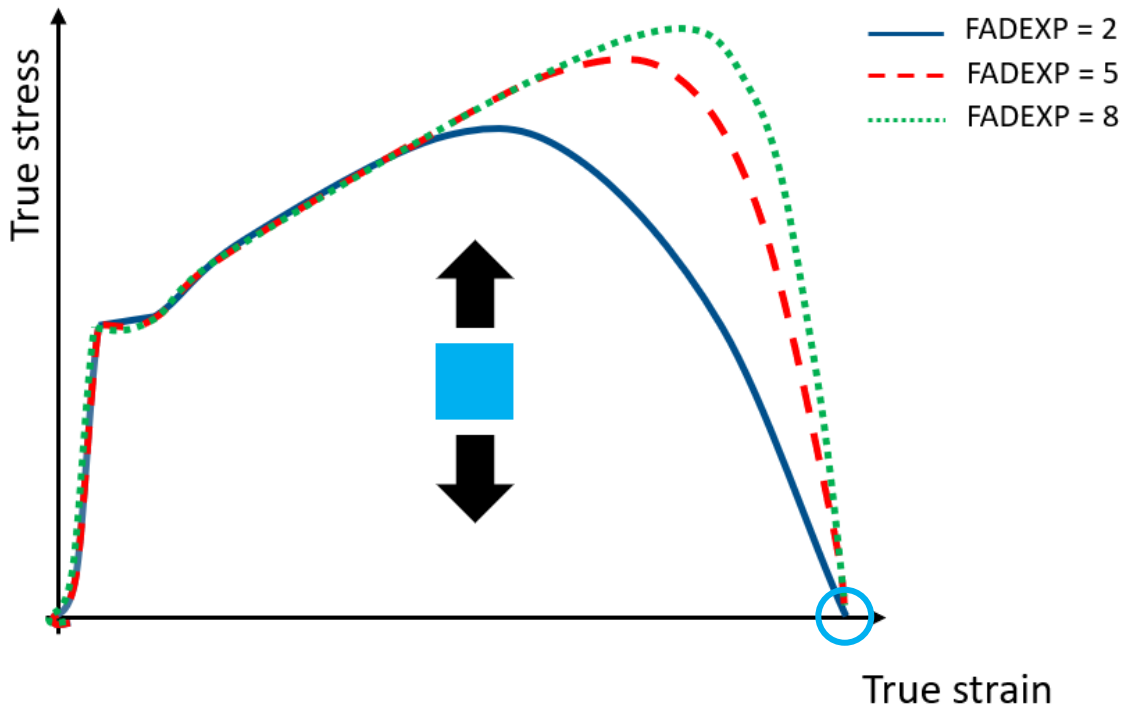


Figure 2-31: Influence of $FADEXP$ (Feucht et al. 2017)

Alternatively, the stress reduction can also be represented by the material instability curve. This is more accurate because the instability strain can be stored as a function of the triaxiality and is therefore not constant for all triaxialities, as D_{crit} is.

The failure of brittle or ductile material can be controlled by means of the element formulation. Shell elements consist of several layers or integration points. The more layers are created, the more accurate their calculation is, and the longer the calculation time. Five integration points are usually sufficient to calculate integration values.

If the material behaviour is brittle, the element is deleted as soon as one of the integration points fails. The higher the ductility, the more layers must fail for the element to be deleted. This allows the ductility to be adjusted (Feucht et al. 2017; Andrade et al. 2014).

Chapter 3 Experimental techniques and applied methods

This chapter presents a material investigation of the delivery condition of AA7075 T6 and the influence of the quenching rate on the strength during forming. Furthermore, a novel process called “Extended Hotforming” to produce hybrid material composites of high strength aluminium alloys and CFRP patches is presented. Detailed material models and failure models have been designed for an accurate simulation of the forming process and for the subsequent component simulation. Moreover, a friction test bench was designed and built for the selection of a suitable lubricant for forming at higher temperatures and the creation of a friction model for the forming simulation.

3.1 Material investigations of the delivery condition

In order to predict the material behaviour from the manufacturing process up to the event of a crash, the whole material “history” needs to be taken into account. While forming limit curves (FLC) are sufficient for forming simulations, they rather seem unsuitable for crash simulations due to co-occurring multiaxial loads. Thus, an accurate damage model is crucial for a robust numerical prediction of the crash behaviour of e.g. AA7075 component. Subsequently, material parameters and the mechanical behaviour of EN AW-7075 in T6 state are listed and fitted into a material card using the v. Mises flow rule hypothesis. To identify the fracture strain with optical measurement systems under various triaxiality states different tensile tests are carried out using various specimen geometries. Based on this experimental data, a triaxial failure curve (TFC) is determined and calibrated with parameter optimisation to obtain optimised input parameters for the failure model GISSMO.

3.1.1 Material and mechanical behaviour of AA7075 T6

For this study an aluminium alloy with the designation EN AW-7075 in T6 state was used. Table 3-1 illustrates the composition specification of tested aluminium alloy.

Table 3-1: Chemical composition (wt.-%) and mechanical properties
of AA 7075 T6 (Grohmann 2016)

Material	Si	Fe	Cu	Mn	Mg	Zn	Cr	Zr
AA 7075 T6	0.08	0.12	1.52	0.02	2.53	5.79	0.18	0.03

Material	σ_f [MPa]	UTS [MPa]	e_u [%]	e_f [%]
AA 7075 T6	500	565	8.2	12

The tensile test is standardised according to (DIN EN ISO 6892-1) and serves to evaluate the mechanical behaviour of metallic materials subjected to a uniaxial tensile force. The aluminium flow curve (see Figure 3-1), which is used for the FEM simulation, is extrapolated to a forming limit of $\varepsilon = 1$ using the Hockett & Sherby law, see equation (3.1).

This law is often used for high strength material and represents the strain hardening with increasing elongation well (Barlat et al. 2003; Yoon et al. 2004).

$$\sigma_f = a - be^{-c\epsilon_p^n} \quad (3.1)$$

Beyond the point of uniform elongation, the flow curve is iteratively adapted by adjusting the Hockett & Sherby parameters (a, b, c, n). The flow curve at room temperature of AA7075 T6 is given by the equation (3.2).

$$\sigma_f = 978 - 490e^{-1.18\epsilon_p^{0.48}} \quad (3.2)$$

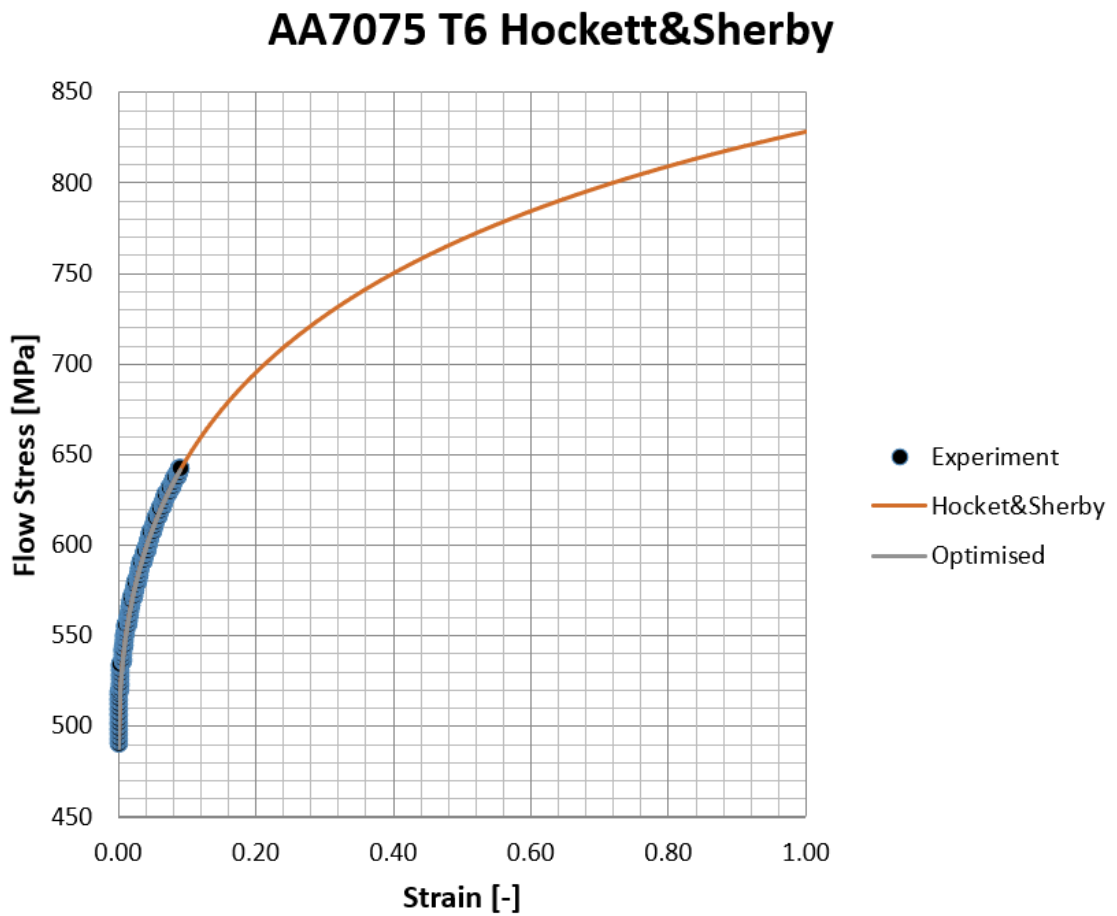


Figure 3-1: AA7075 T6 - Extrapolated flow curve after Hockett & Sherby

In order to define the failure curve in the biaxial area (see Chapter 2.5.4), an experimental test (biaxial state of the specimen) is usually needed. Thus, an existing Forming Limit Curve (FLC) of the AA7075 T6 material (Grohmann 2016) is used (see Table 3-2) and the respective value converted using following equations from (Li et al. 2010):

$$\text{plane stress: } \sigma_3 = 0 \quad (3.3)$$

$$\text{small elastic deformations: } \varepsilon_1 \sim \varepsilon_{p1} \text{ \& } \varepsilon_2 \sim \varepsilon_{p2} \quad (3.4)$$

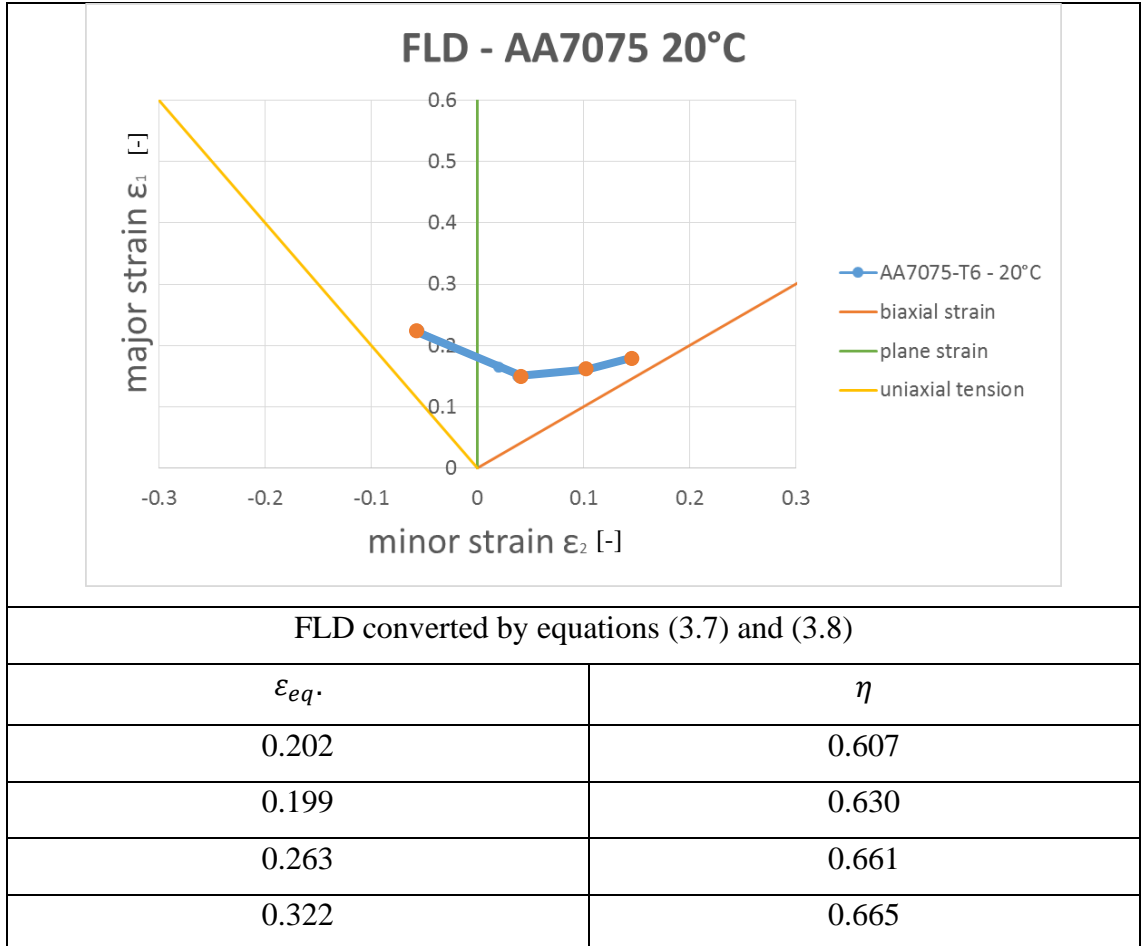
$$\text{isochoric plasticity: } \varepsilon_3 \sim \varepsilon_{p3} = -\varepsilon_{p1} - \varepsilon_{p2} \quad (3.5)$$

$$\text{proportional loading: } a = \frac{\varepsilon_2}{\varepsilon_1} \quad (3.6)$$

$$\text{equivalent plastic strain: } \varepsilon_{eq} = \frac{2}{\sqrt{3}} * \varepsilon_{p1} * \sqrt{1 + a + a^2} \quad (3.7)$$

$$\text{triaxiality } \eta = \frac{\sigma_m}{\sigma_{eq}} = \frac{1 + \alpha}{\sqrt{3} * \sqrt{1 + \alpha + \alpha^2}} \quad (3.8)$$

Table 3-2: Forming limit diagram AA 7075 T6 (Grohmann 2016)



3.1.2 Numerical calibration of a triaxial failure curve using parameter optimisation

The Aramis optical measuring system, which is illustrated in Figure 3-2, was adapted to the tensile testing machine to measure local strains. In order to measure the local strain, a stochastic pattern is applied onto the surface of the specimens. Based on this pattern the “GOM Correlate” software was used to calculate local distortions.

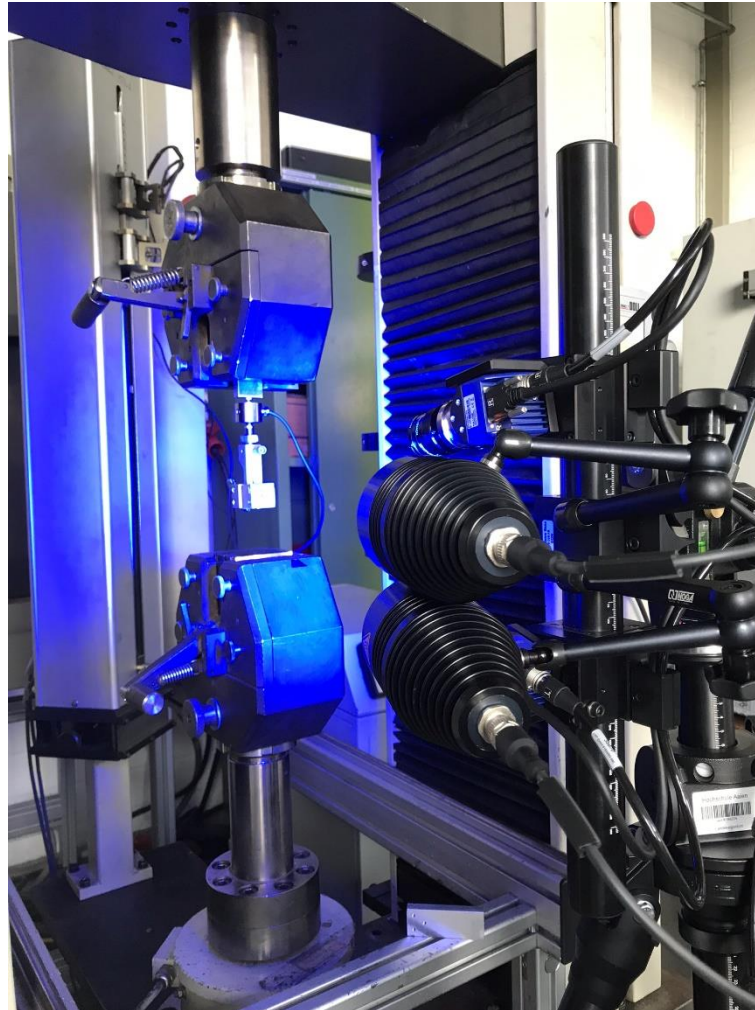


Figure 3-2: Tensile testing machine including GOM Aramis system to measure local strains

To achieve triaxiality-dependent failure strains, specimens with different geometries are needed (see Chapter 2.5.4). The specimens (shear 0°, shear 15°, tensile and notched) and a converted forming limit diagram (biaxial values) were used for this AA7075 T6 failure model. Table 3-3 shows the corresponding results (ϵ_{eq} and η) reached in the experiment, where the triaxialities started at nearly zero and rose to around $\eta = 0.5$.

Table 3-3: Test results of various specimens for TFC

	Shear 0°		Shear 15°		Tensile		Notched	
Test	ε_{eq}	η	ε_{eq}	η	ε_{eq}	η	ε_{eq}	η
results	0.287	0.089	0.277	0.240	0.377	0.384	0.253	0.496

Figure 3-3 shows the results of the optical measurement (blue curve) and the values of the converted FLD (blue circle) with individual standard deviations. The values of the standard deviations were also used as a restriction for parameter optimisation (upper and lower limit) in the LS-OPT version 6.0 software from LSTC. The orange line indicates the optimised failure curve within the pre-defined limits, which can further be used for any prediction of the force-displacement characteristic of the experiments.

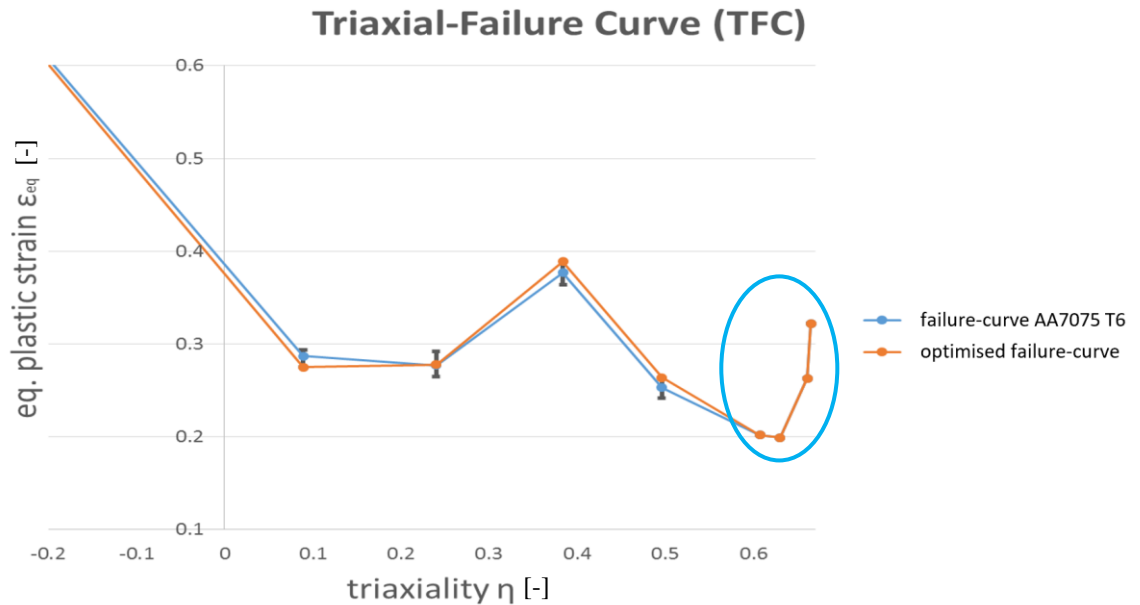
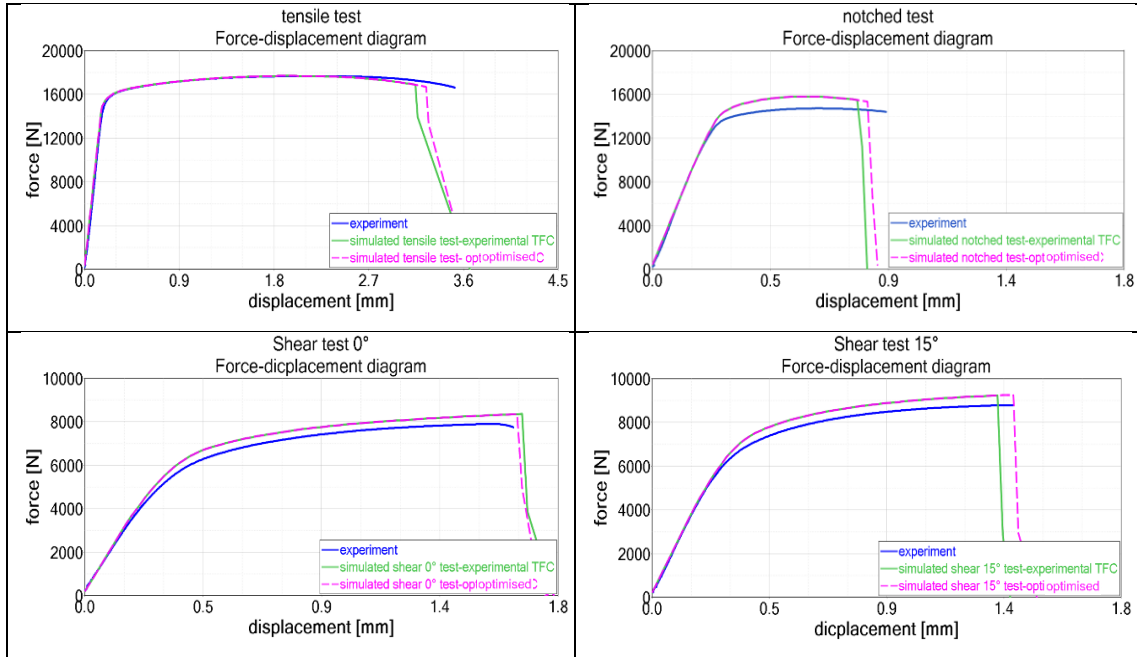


Figure 3-3: Triaxial-Failure Curve AA7075 T6

As optimisation basis, the experimental force-displacement curves were taken into account. During the optimisation process the equivalent plastic strain of each point (tensile, shear 0°, shear 15° and notched test) is varied among the lower and upper limits (which are the maximum deviation of the equivalent plastic strain measurement) in order to achieve the best fit between the experimental and simulated force-displacement curve. Table 3-4 indicates the experimental force-displacement curve (blue) and the optimised force displacement curves (green and purple), which are created on the one hand by the

initial TFC curve (blue) in Figure 3-3) and on the other hand by the optimised TFC curve (orange) in Figure 3-3. It is shown that the optimised TFCs are in good agreement with the experimental results.

Table 3-4: Force-displacement diagram; experiment-blue, average measurement values-green, optimised-purple



3.1.3 Concluding remarks

Experimental tests with various specimen geometries (shear 0°, shear 15°, tensile and notched) were carried out to determine the force-displacement characteristics of AA7075 T6 material. The local strains at fracture were monitored under different stress conditions ($-1/3 < \eta < 2/3$) using an adapted optical GOM Aramis measurement system. Corresponding values for biaxial area ($\eta = 2/3$) were taken from a forming limit diagram and converted. For the analysis, the v. Mises yield function was taken into account, and the Hockett & Sherby's law was used for the description of the materials hardening behaviour. Subsequently, a failure curve was optimised and fitted to experimental data using LS-OPT parameter optimisation. The predicted force-displacement data show a good correlation with experimental results for all loading states (compression, shear, tensile and biaxial). The developed material- and failure model can be applied for further assembly and components simulations using AA7075 T6 material.

3.2 Analysis of the strength behaviour at various quenching rates

It is known that especially the AA7075 alloy with its high copper content reacts very sensitively with regard to strength to variable quenching rates (Zhu et al. 2019). In order to ensure that a high strength is achieved after the Hotforming process, a test is now carried out with regard to strength as a function of the quenching rate. For this investigation tensile test specimens made of AA7075 T6 and 2.0 mm sheet thickness were equipped with thermocouples Type K and subjected to the complete Hotforming process with subsequent heat treatment. The procedure that the specimens go through are listed in Figure 3-4 (the layout used for this procedure will be further described in Chapter 3.3 Figure 3-8 and Table 3-5).

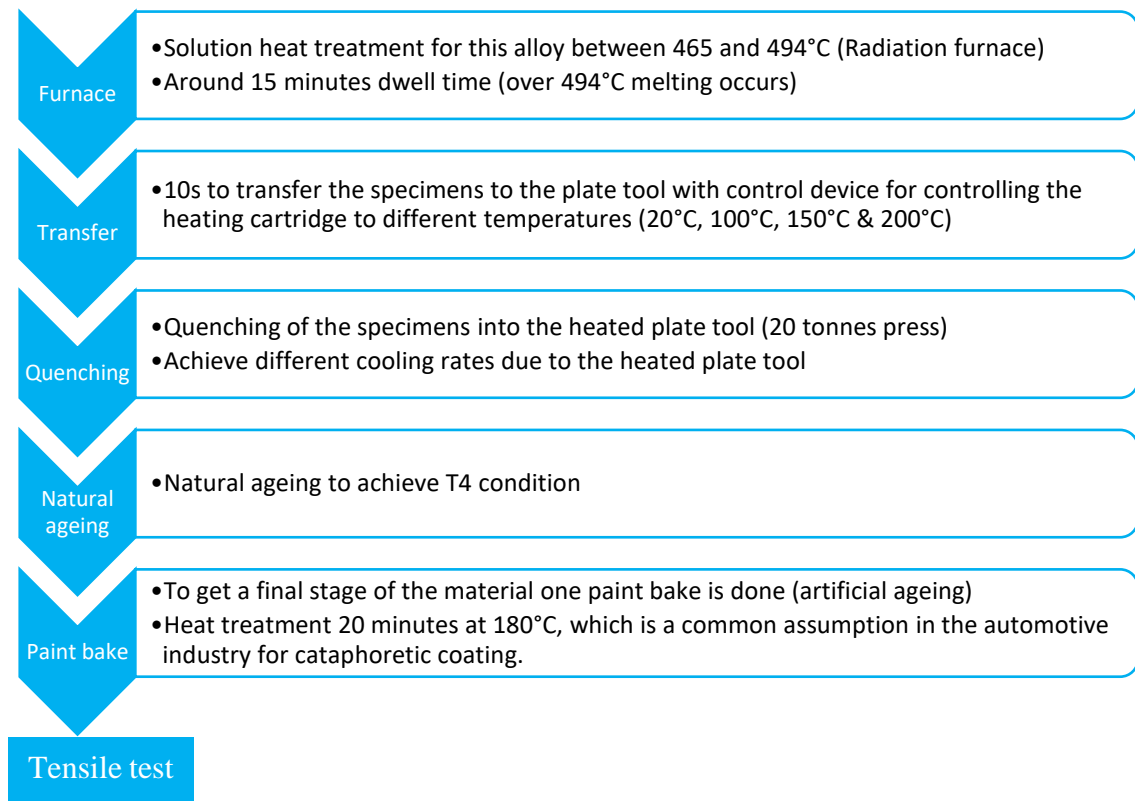


Figure 3-4: Procedure for the creation of test specimens (test setup see Chapter 3.3 Figure 3-8)

The influence of the die temperature, which corresponds to the plate tool in the model test, controls the quenching rate, that in turn controls the mechanical properties. Die temperatures of 20, 100, 150 and 200°C were used in the investigation, and the corresponding quenching rates were evaluated as a linear regression line between the temperatures of 400°C – 290°C. This range must be run through quickly to avoid premature segregation of the supersaturated α -solid solution, otherwise there is a deterioration of strength, ductility and corrosion resistance (Grohmann 2016; Liu et al. 2010). For a better reproducibility four specimens per temperature of the plate tool (see Chapter 3.3 Figure 3-8) were tested. Figure 3-5 and Figure 3-6 show the yield strength and ultimate tensile strength depending on the quenching rate for the AA7075 alloy. For a better interpretation of the results, the tendencies of the test points were approximated by a curve (blue). In both cases it can be seen that the strength is dependent on the cooling rate. Only after a cooling rate of ~80 K/s no significant increase in strength is noticeable.

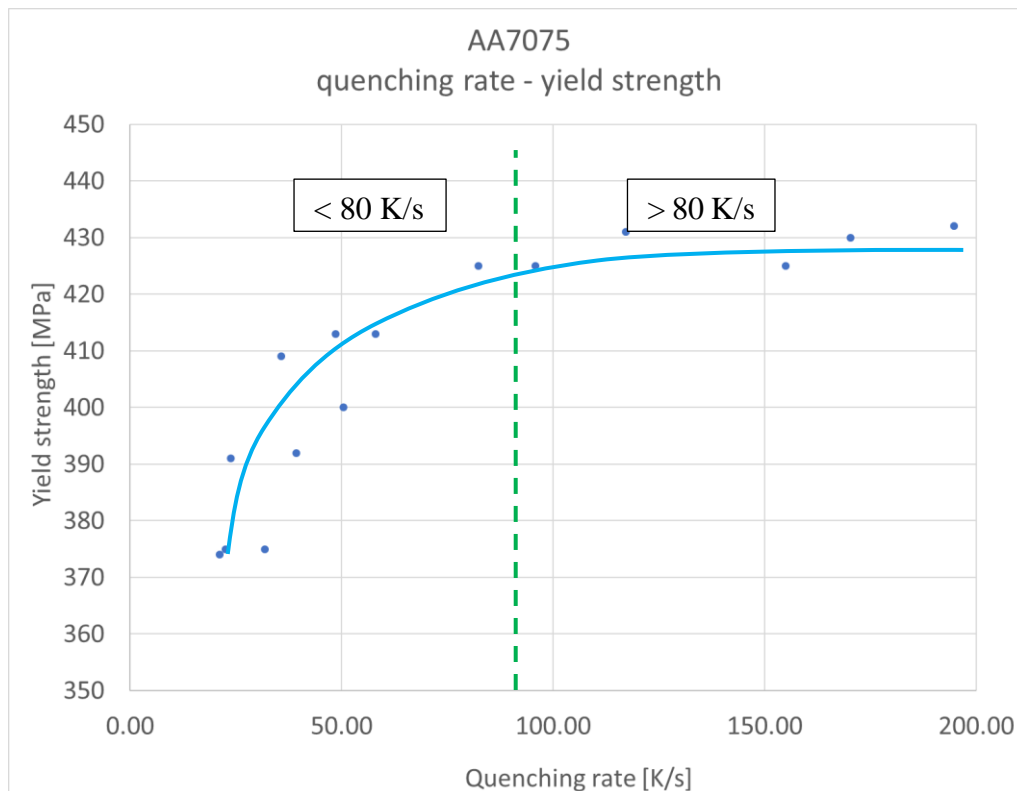


Figure 3-5: Dependence of the yield strength on the quenching rate

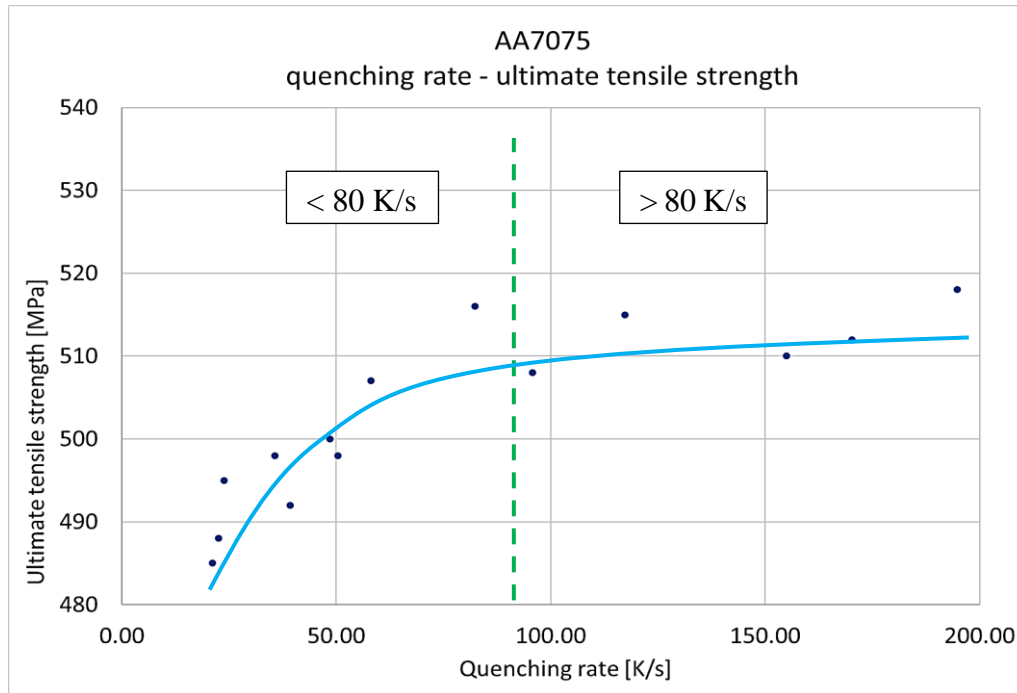


Figure 3-6: Dependence of the ultimate tensile strength on the quenching rate

3.2.1 Concluding remarks

The experiments conducted in this study show that the AA7075 alloy is very sensitive to the quenching rate during forming or respectively after solution heat treatment, which is shown by the results in Figure 3-5 and Figure 3-6 and comparable results in Liu et. al. (Liu et al. 2010). In both diagrams it is clearly visible that the final strength after forming and ageing is improved with increasing cooling rate during forming process, as shown in Figure 3-5 and Figure 3-6. On the one hand, a lower quenching rate (< 80 K/s) also leads to a lower solute precipitation and the loss of excess vacancies when the material is quenched to room temperature (Liu et al. 2010), which leads to a decrease in the later component strength after subsequent ageing. On the other hand, a high cooling rate, greater than 80 K/s, leads to high strength, where the difference between 80 K/s to 200 K/s is marginal. In this range the yield strength is around 425 MPa and the tensile strength around 515 MPa. Above the critical quenching rate of 80 K/s intergranular corrosion is avoided, which was shown by Grohmann (Grohmann 2016). In order to improve the overall performance of the AA7075 aluminium alloy in the manufacture of automotive parts with the Hotforming process it is essential to keep the transfer time low. The insert temperature in the forming tool should be above 400°C to reach a strength higher than 500 MPa, which is required for structural components.

3.3 *Extended Hotforming process*

At present, the Hotforming process (patented by Impression Tech Ltd. “WO2017/093767”) can be used to produce parts made out of high- and ultra-high strength aluminium alloys of the 7xxx group in more complex shapes than the other forming processes. This process is described in detail in Chapter 2.2.5 and serves as a basis for the novel “Extended Hotforming process”. Based on the standard Hotforming process, some modifications are made in order to generate crash components with local reinforcements via an “integrated thermal direct joining step” (see Figure 3-7).

The advantage of this “Extended Hotforming process” is that highly stressed areas of crash relevant components can be reinforced with a local patch made of CFRP or GFRP and thus, the sheet thickness of the base material can be further reduced. Another advantage of the Extended Hotforming process is the short cycle time due to the combination of the forming and joining process compared to the conventional manufacturing process of fibre reinforced parts.

The extension of the Hotforming process (cf. Figure 3-7) comprises several steps: laser structuring the blank (2) prior solution annealing at $T > 465^{\circ}\text{C}$ (3) to ensure a better adhesion of the patch. A subsequent cooling step of the blank (4) to $150\text{--}180^{\circ}\text{C}$ with a cooling rate greater than 80 K/s to avoid premature segregation of the supersaturated α -solid solution (see Chapter 2.3.2) and thus, to achieve highest strength values and to melt the matrix of the thermoplastic patch. This step is crucial since otherwise the patch would be destroyed at temperatures above 180°C . Further, the patch is positioned (5) on the sheet metal (incl. release agent) and put together into the forming press (6) which is also heated up to $150^{\circ}\text{--}180^{\circ}\text{C}$. This is followed by a forming process step at elevated temperature. At the same time, the thermal direct joining takes place just by using the residual heat of the sheet metal. Then the part is cut (7) by laser or directly in the die. The final step is the heat-treatment (8) to improve the strength and corrosion resistance of the 7xxx Al-alloy.

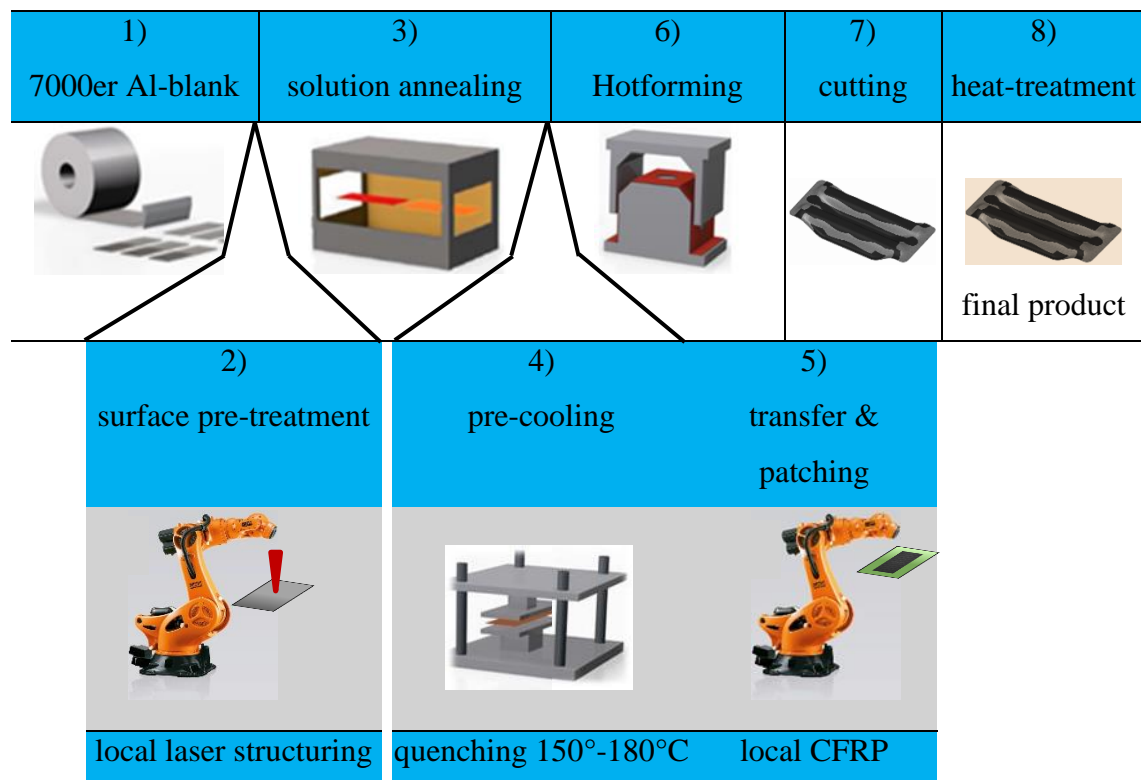


Figure 3-7: Novel Hotforming Process with integrated thermal direct joining

3.3.1 Layout of the test bench

To achieve high quality simulation results, the material must be described as accurately as possible. The material behaviour of rolled ultra-high strength aluminium alloys becomes anisotropic especially if exposed to multi-axial stress conditions. For this reason, anisotropic material models such as Barlat YLD2000 (Barlat et al. 2003) or Barlat89 (Barlat & Lian 1989) are used for the forming simulations (see Chapter 2.5.3).

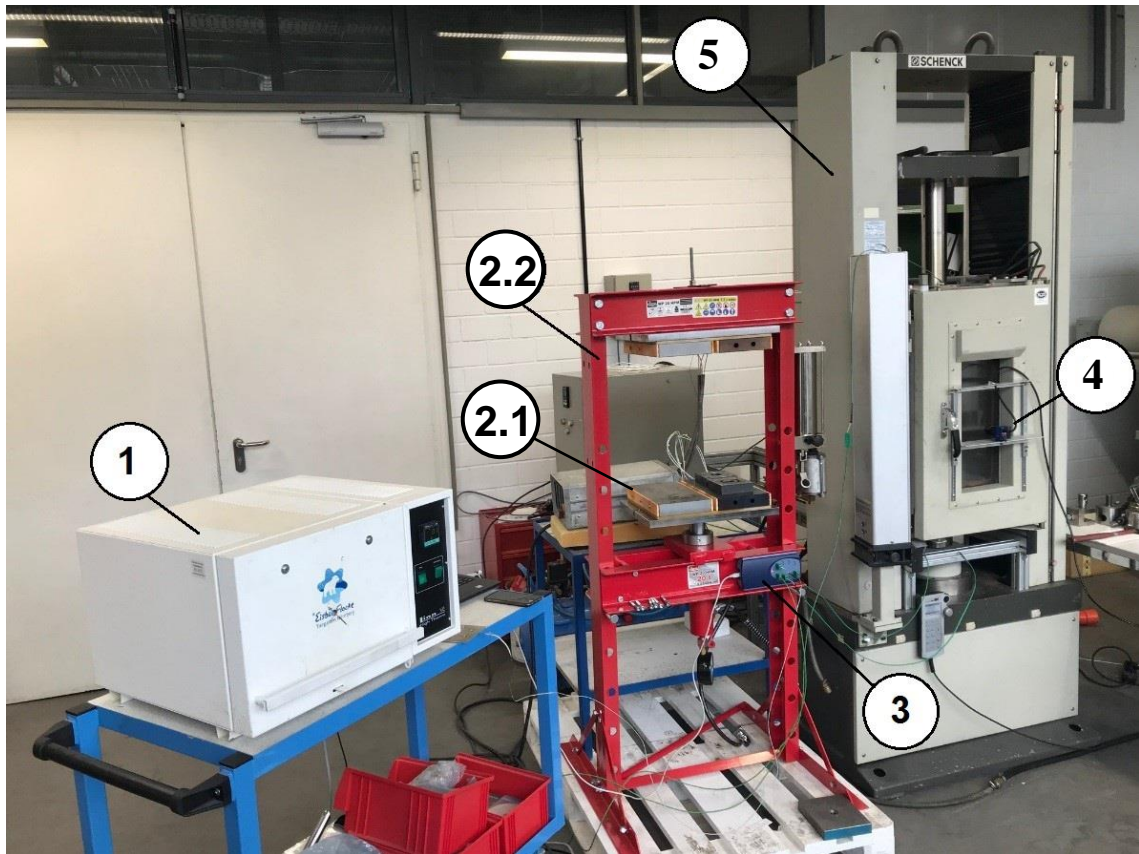

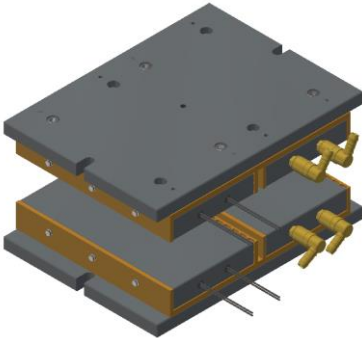
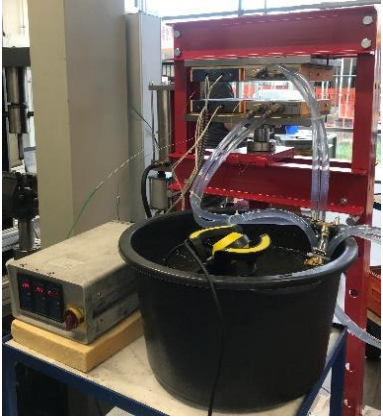




Figure 3-8: Test bench set-up for forming process at elevated temperature

In order to be able to characterise the material parameters under realistic conditions, an experimental test bench (see Figure 3-8) was developed and built up. The test bench consists of: a furnace (1), a heated and cooled plate tool integrated into a 20 tonnes press (2), a temperature data logger (3), an optical measuring system (GOM Aramis Adjustable – 2.3M) (4) and a tensile testing machine with climate chamber (5). A description of the individual components is given in Table 3-5 and for more details see Appendix D.

Table 3-5: Detailed overview of used testing equipment (for further detail see Appendix D)

Position	Image	Description
1. Radiation furnace		<ul style="list-style-type: none"> Furnace for solution annealing Solution annealing temperature between 465°C and 490°C.
2.1 Plate tool		<ul style="list-style-type: none"> Plate tool with heating and cooling plates. Heating plates with four heating cartridges (630watt) Cooling plates include water cooling channels
2.2 Forming press and Control device		<ul style="list-style-type: none"> 20 tonnes forming press Control device for controlling the heating cartridge (2-Zones) Water container with water pump for the cooling plates
3. Temperature logger (sample time 1s)		<ul style="list-style-type: none"> Temperature data logger to monitor the temperature of the furnace, specimens and tensile testing machine
4. Aramis (GOM) Adjustable – 2.3M		<ul style="list-style-type: none"> Deformation and strain measurement 2.3 MPixel (1936x1216) 130 frames per second

Test procedure:

1. First, the specimens are heated to 465°C in the furnace, which takes about 8 minutes. To ensure that all alloying elements are in solution the temperature of the specimen is maintained for 5 minutes.
2. In the next step the specimens are transferred within 7 seconds to the plate tool, which is preheated to 150°C. The specimens are pressed for 15 seconds applying 5 tonnes. This time corresponds to the industrial requirements for a reasonable cycle time of 15 seconds. This step allows the insertion of a CFRP/GFRP patch, which will be bonded by direct thermal joining. At this stage the matrix of the patch acts like an adhesive.
3. Finally, the specimens are tested in a uniaxial tensile testing machine with a climate chamber. The climate chamber is heated up to 150°C to prevent any cooling of the specimen during the test. In addition to the force-displacement measurement an optical measurement of the surface of the specimens is carried out. This is necessary to determine the local equivalent strain at fracture and the anisotropic Lankford-parameters (r-values).

The temperature of the furnace, specimens, heating/ cooling plates and climate chamber is recorded and monitored by a data logger throughout the whole process and regularly checked with the set temperatures of the control device. The equipment used for the tests is regularly checked and calibrated by qualified personnel.

3.3.2 Mechanical behaviour at elevated temperatures

All specimens consisting off shear (0° , 15° , 30° and 45°), tensile (0° , 45° and 90°), notched and Erichsen tests, which are described in Chapter 2.5.3 (see Appendix C in detail), are tested via the test procedure of the Extended Hotforming process as described in Chapter 3.3.1. The temperature profile during the test procedure is shown in Figure 3-9.

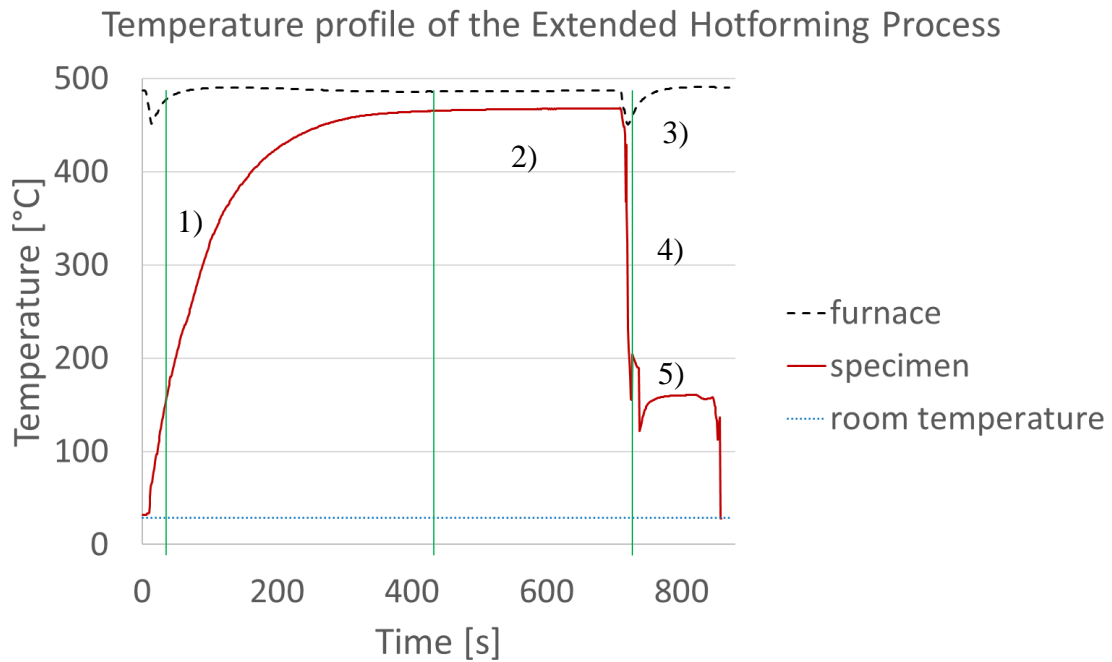


Figure 3-9: Temperature profile during Extended Hotforming process

The temperature-time curve in Figure 3-9 can be divided into five sections (cf. in detail Chapter 3.3.1):

- 1) In the first area the specimens are heated up within ~7-8 minutes to 465°C (solution annealing temperature),
- 2) Then the specimen is kept at the temperature level of 465°C - 480°C for ~5 minutes,
- 3) Transfer from the furnace into the heated plate tool (150°C),
- 4) Quenching in the plate tool at approx. 150°C (quenching rate from 400°C to 290°C should be greater than 80°K/s), and
- 5) Insertion of the specimens into the tensile testing machine and start testing with optical strain measurement.

3.3.2.1 Material model of the Extended Hotforming process

Now an anisotropic material model called Barlat YLD2000 for the Extended Hotforming process is calibrated. All specimens consisting of shear (0°, 15°, 30° and 45°), tensile (0°, 45° and 90°), notched and Erichsen testing geometries, which are subjected to the Extended Hotforming process, are now used to create the material model. The experiments provide stress-strain-diagrams and for the Erichsen test a force-displacement-diagram. From the tensile tests the Lankford parameters, yield stresses (Table 3-6) and flow curves (Figure 3-10) were determined using sheet metal specimens with different rolling directions.

Table 3-6: Anisotropic parameters

	0°-direction	45°-direction	90°-direction
Lankford-Parameter	$r_0 = 0.44$	$r_{45} = 0.87$	$r_{90} = 0.36$
Yield stress [MPa]	$\sigma_{f0^\circ} = 203$	$\sigma_{f45^\circ} = 194$	$\sigma_{f90^\circ} = 204$
Flow curve after Hockett-Sherby	$434 - 203e^{-4.18\varepsilon_p^{0.78}}$	$395 - 194e^{-5.14\varepsilon_p^{0.83}}$	$415 - 204e^{-5.12\varepsilon_p^{0.84}}$

The extrapolation of the flow curves was performed using the Hockett-Sherby equation (3.1). Thereby, the flow curves of the specimens with different rolling directions were approximated and extrapolated as illustrated in Figure 3-10.

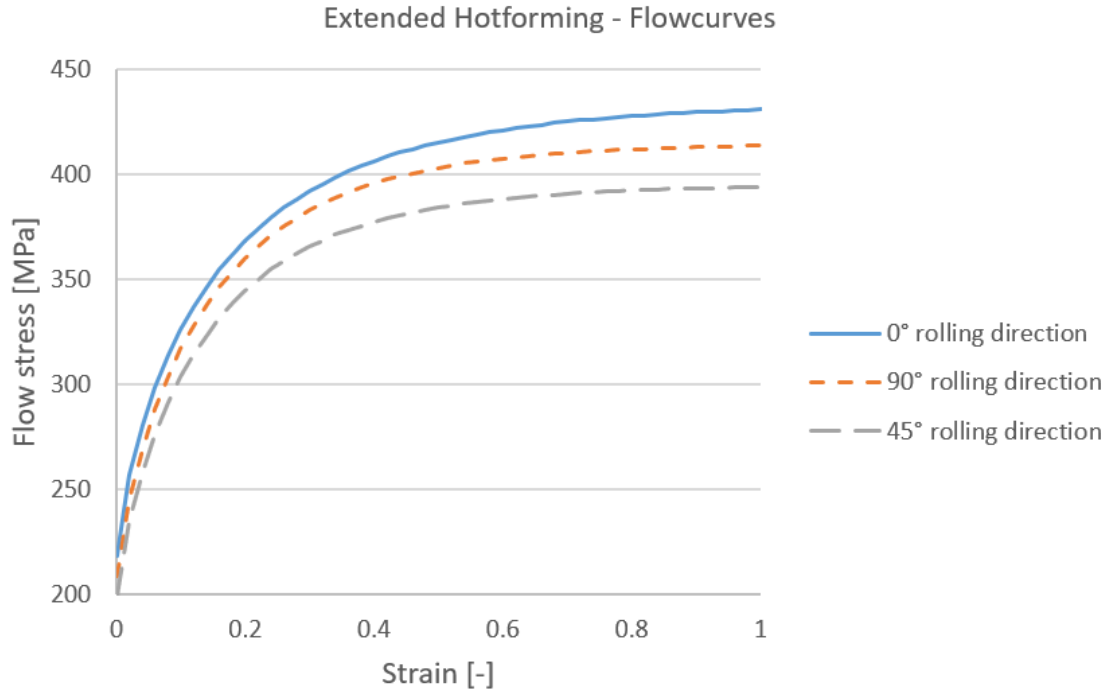


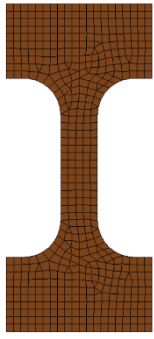
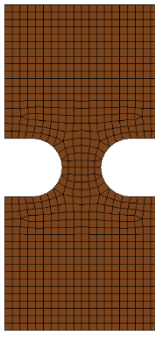
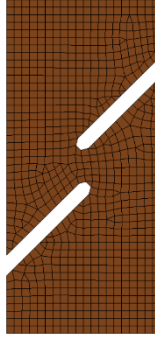
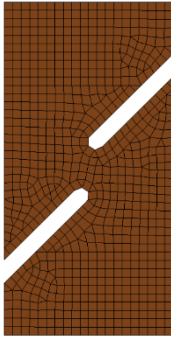
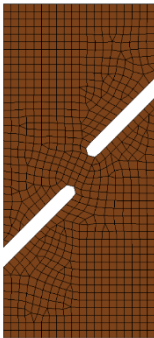
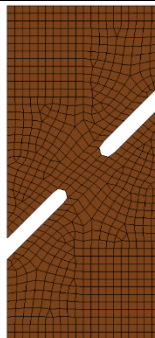
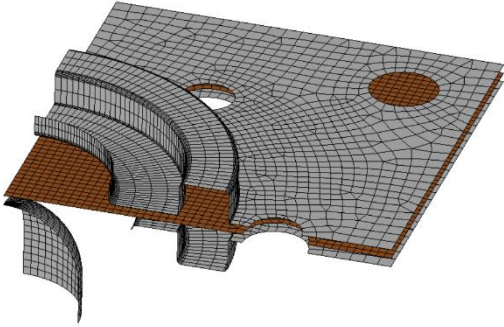
Figure 3-10: Extrapolated flow-curves after Hockett-Sherby in different rolling directions of the Extended Hotforming process

The material behaviour during the Extended Hotforming process can be described with the Barlat YLD2000 (Barlat et al. 2003) material model (LS-DYNA MAT_133), which allows a good illustration of the anisotropy of high strength aluminium alloys. This model requires eight α -values as input variables, which are described by the following test values:

- Lankford Parameter: r_0, r_{45}, r_{90}, r_b
- Yield stress: $\sigma_0, \sigma_{45}, \sigma_{90}, \sigma_b$

The parameters are listed in Table 3-6. The biaxial parameters r_b and σ_b are determined by reverse engineering / parameter optimisation. The aim of the optimisation is to adapt the stress-strain curves from the simulation to the experimentally determined stress-strain curves. The force-displacement curve is used in the Erichsen test. The material model is calibrated with the Software LS-OPT from LSTC. The created simulation models of the specimens are illustrated in Table 3-7. The specimens were meshed by shell elements with an element edge length of 1 mm.

Table 3-7: Overview of the simulation models for material and damage/failure model calibration

			
<i>Tensile test</i>	<i>Notched test</i>	<i>Shear test 0°</i>	<i>Shear test 15°</i>
			
<i>Shear test 30°</i>	<i>Shear test 45°</i>	<i>Erichsen test</i>	

In each of these simulation models the eight α -values of the Barlat YLD2000 material model are parameterised. In addition, a Matlab script (see Appendix B) is created for the conversion of the experimental data ($r_0, r_{45}, r_{90}, r_b, \sigma_0, \sigma_{45}, \sigma_{90}, \sigma_b$) into the Barlat α -values, where σ_b and r_b are used as optimisation parameters.

The procedure of the optimisation can be described as follows (see numbers in Figure 3-11):

- 1) The input values $r_0, r_{45}, r_{90}, r_b, \sigma_0, \sigma_{45}, \sigma_{90}$ and σ_b are transferred into Matlab where the yield strengths are normalised to σ_0 .
- 2) Those input values are used to calculate the eight α -values of the Barlat YLD2000 material model with the Matlab script in Appendix B. This material model is implemented to the seven simulation models (as shown in Table 3-7).
- 3) After successful simulation the stress-strain curves are evaluated. From the Erichsen test, the force-displacement characteristics are analysed (see Table 3-9). The deviation between the predicted curve and the experimentally determined curve is determined for each test.

The r_b and σ_b values are optimised by the optimisation software minimising the corresponding deviation value by means of curve fitting.

The optimised stress-strain curves and force-displacement curves are shown in Table 3-9. The black curves are the experimental data and the green curves are the numerically predicted curves using the Barlat YLD2000 material model, which is listed in Table 3-8 for the Extended Hotforming process.

Table 3-8: Parameters for the calibrated Barlat YLD2000 material model of AA7075 Hotforming material

r_b	σ_b	α_1	α_2	α_3	α_4	α_5	α_6	α_7	α_8
1.496	0.663	0.861	1.080	2.292	1.318	0.959	0.656	1.030	0.781

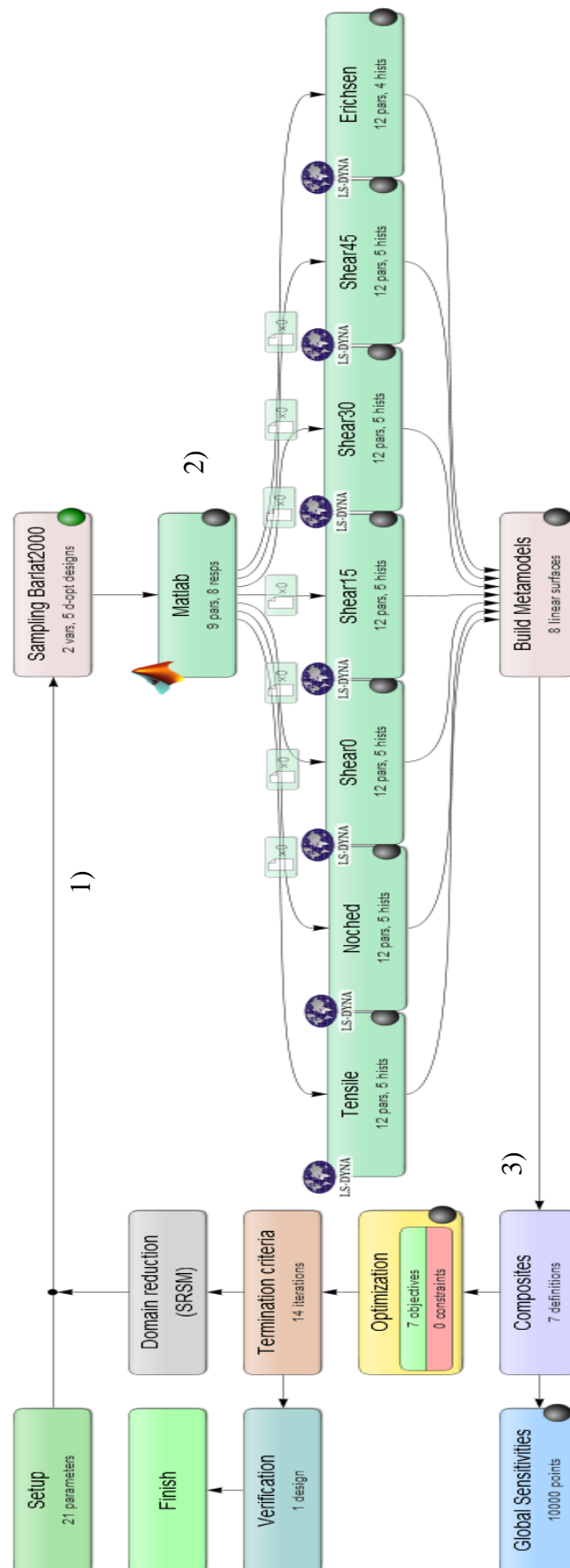
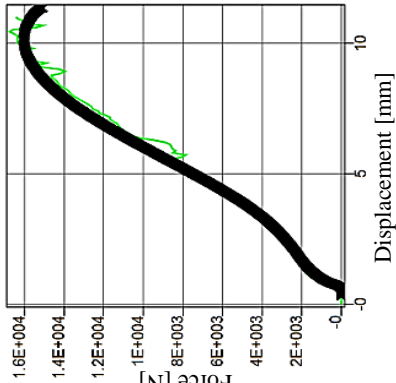
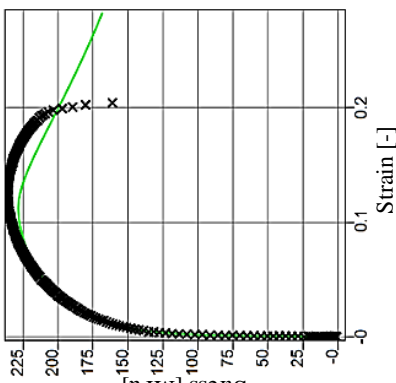
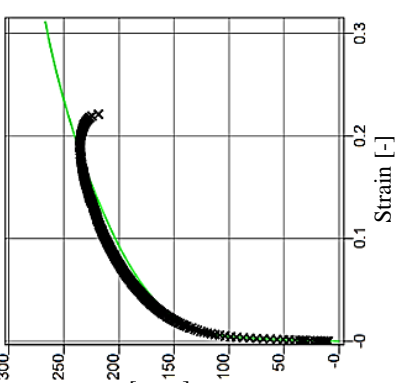
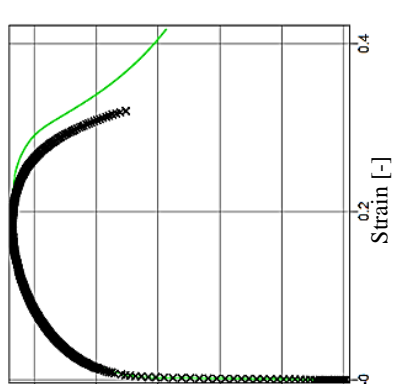
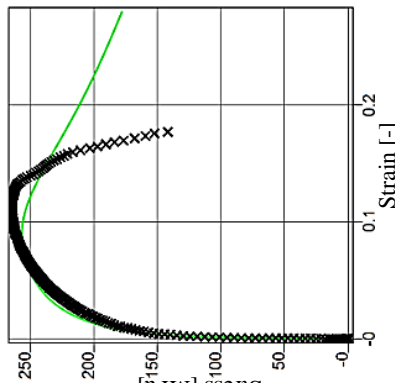
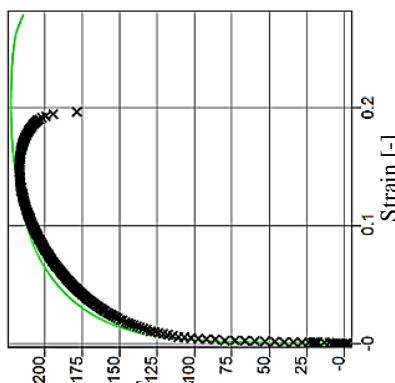
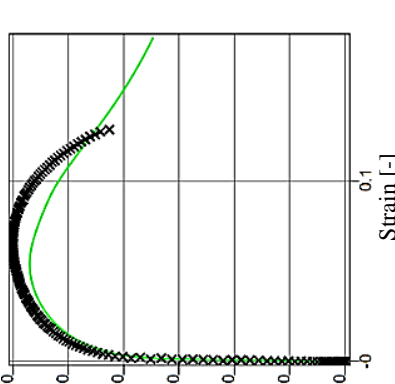


Figure 3-11: LS-OPT structure of the material and damage/failure calibration

Table 3-9: Comparison of experimentally and numerically determined stress-strain curves and force-displacement diagrams using Barlat YLD2000 model

<p>Erichsen test</p> 	<p>Shear 30° test</p> 	<p>Shear 0° test</p> 	<p>Tensile test</p> 
	<p>Shear 45° test</p> 	<p>Shear 15° test</p> 	<p>Notched test</p> 

3.3.2.2 Damage and failure model of the Extended Hotforming process

The calibration of the failure model is carried out in the same manner as the calibration of the material model, as shown in Figure 3-11. For this purpose, the same simulation models are used, which are illustrated in Table 3-7. In addition, the damage/ failure model GISSMO is parameterised. For this, the triaxial-failure-curve (TFC) and material-instability-curve, also called E_{crit} , is adjusted according to the existing experimental data. The previously optimised Barlat YLD2000 is used for the Extended Hotforming material model. The damage/ failure model GISSMO, which is described in detail in Chapter 2.5.3, is used for the prediction of necking and fracture of the material when exposed to the Extended Hotforming process. For further crash investigations it is possible to map the plastic strain, thinning and damage to the crash simulation model in order to reach higher quality of results. To describe the failure and instability curve, three distinctive triaxialities are chosen:

- Pure shear stress ($\eta = 0$)
- Pure tensile stress ($\eta = 0.333$)
- Pure biaxial stress ($\eta = 0.666$)

The associated failure and instability strain are parameterised as shown in Table 3-10.

Table 3-10: Parameterisation and results of the failure and instability curve of the
Extended Hotforming process

Triaxiality	Failure strain		Instability strain	
	Parameter TFC	Optimised value	Parameter E_{crit}	Optimised value
0	TR0	1.252	ECR0	0.950
0.111	TR1	0.426	-	-
0.222	TR2	0.502	-	-
0.333	TR3	1.125	ECR3	0.249
0.444	TR4	0.714	-	-
0.555	TR5	0.548	-	-
0.666	TR6	0.855	ECR6	0.855

The TFC- and E_{crit} -parameters (TR0 to TR6 and ECR0 to ECR6), as shown in Table 3-10, are varied by the optimisation software until necking and fracture of each specimen correspond to the experiment as illustrated in Table 3-11. The black curves are the experimental data and the green curves are the numerically predicted curves using the Barlat YLD2000 material model for the Extended Hotforming process.

Table 3-11: Optimisation results for damage/ failure model stress-strain and
force-displacement diagrams

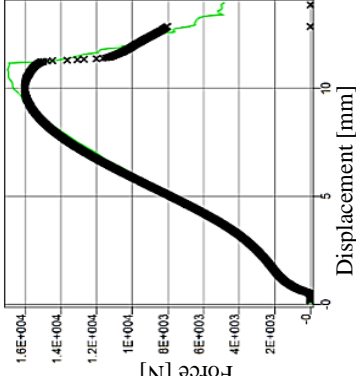
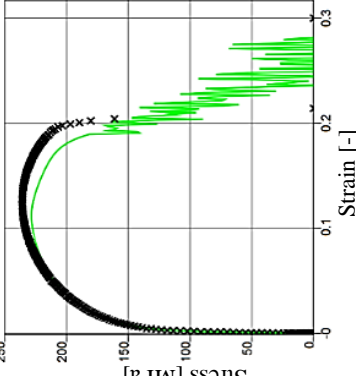
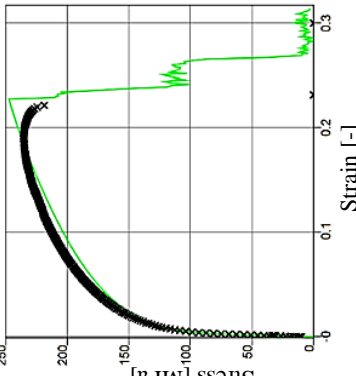
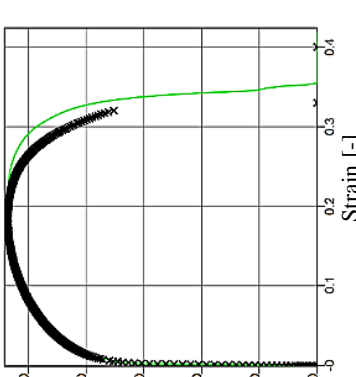
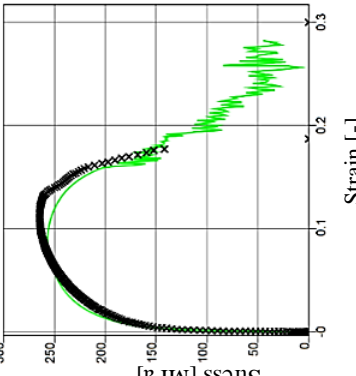
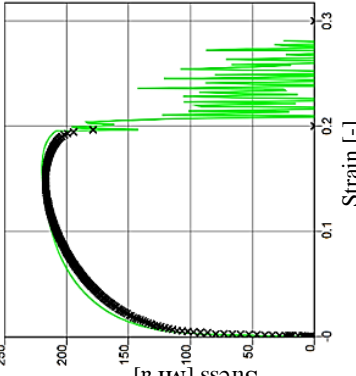
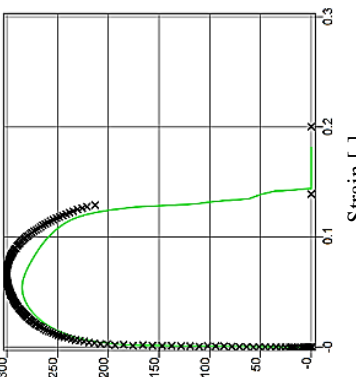
Erichsen test	Shear 30° test	Shear 0° test	Tensile test
			
	Shear 45° test	Shear 15° test	Notched test
			

Figure 3-12 shows the triaxial failure curve (TFC) and the instability curve (E_{crit}) of an AA7075 material applied to the Extended Hotforming process, which are generated using the optimised values listed in Table 3-10. For a more distinct triaxiality failure curve, two second-order polynomials with the same point ($\eta = 0.33$; green circle) were determined and implemented into the simulation models. Only a second-order polynomial was defined for the instability curve (orange curve).

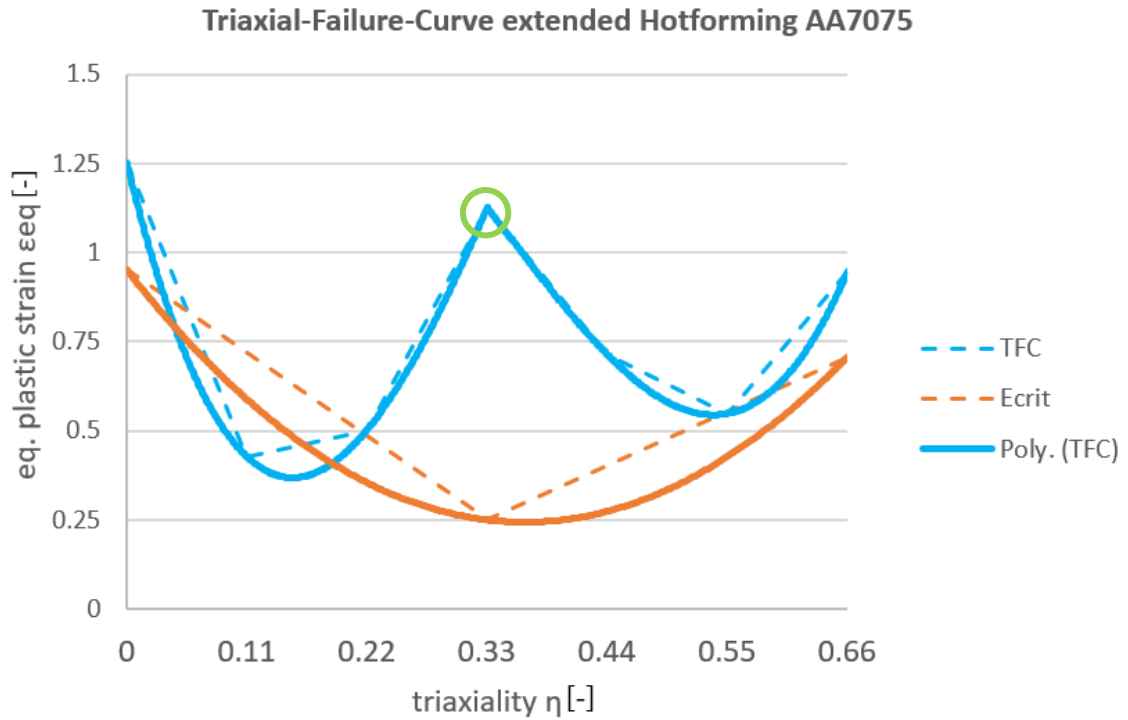


Figure 3-12: Triaxial failure curve and instability curve of the Extended Hotforming process AA7075

3.3.3 Concluding remarks

This work shows the calibration of a material model Barlat YLD2000 with a damage/failure model (GISSMO) for the Extended Hotforming process. It is shown that no biaxial values (r_b & σ_b) are required for the calibration of the complex material model. This can be solved via a parameter optimiser and a Matlab script, where the eight alpha values for the material model can be calculated using the experimental data.

On the one hand, it is clear that the more test values are available, the more the optimisation or the models are improved. On the other hand, the quality of the material model is sufficient to calibrate it to the different specimen geometries required for the damage- and failure model (GISSMO).

Due to the parameter optimisation, the eight alpha values required for the material model Barlat YLD2000 were adjusted. These values are based on the anisotropy values or Lankford parameters (r_0, r_{45}, r_{90}, r_b) and the flow stresses $\sigma_0, \sigma_{45}, \sigma_{90}, \sigma_b$ in different directions. This material model was then used to calibrate the instability curve and triaxial failure curve. It is noticeable that the triaxial failure curve looks like a double-u, if two second degree polynomial functions are fitted into the optimised points. In literature, it is a common shape of the triaxial failure curve (Haufe et al. 2011).

The comparison of the test and simulation results (see Table 3-11), which includes the material model Barlat YLD2000 and damage/failure model GISSMO, shows a very good agreement regarding the stress and strain values. The range between the triaxialities $\eta = 0.33$ and $\eta = 0.66$ is of particular interest for the forming process, which is represented by the specimens' notch tension, unidirectional tension and Erichsen. These curves also show a very good agreement.

This model can now be used for realistic forming simulation for Extended Hotforming, in order to detect cracks and thinning at an early stage during component and tool design. It is also meaningful for the “normal” Hotforming process, which in turn is based on the same solution heat treatment material condition. Another important variable in forming is friction, which is dependent on many factors (see Chapter 2.4). Therefore, for an even better forming simulation, a friction value model is created and integrated into the forming simulation.

Afterwards it is possible to transfer the thinning, plastic elongation, stresses and damage from the forming simulation to a realistic crash model that has very good accuracy.

3.4 *Final state of the material after one paint bake*

In order to create a crash simulation model for the final state of the material after forming and paint bake, first the specimens are solution annealed and formed at 150°C in the heated plate tool.

These steps and specimens' geometries are similar to the Extended Hotforming process, which is explained in the previously Chapter 3.3. Instead of drawing the specimens as before, they are now stored at room temperature for a period of four days (swap-out duration). During this time, natural ageing process takes place, which raises the specimens to a temper state T4 due to growing segregations. In this state, the condition is stable at room temperature again. Now the specimens get a heat treatment at 180°C for 20 minutes in a furnace and are then cooled down to room temperature. This results in artificial ageing and increases the strength due to further separation mechanisms (see Chapter 2.3). In the industry this one paint bake (180°C, 20 min), which is the minimum of heat treatment for aluminium alloys, corresponds to the cathodic dip coating for corrosion protection. The mechanical properties and the local failure elongation of the treated specimens are then determined in order to create a material model and a damage/failure model.

3.4.1 Material model of the final state

In contrast to the forming simulation, a simple material model without anisotropic effects is now assumed for crash simulation due to the long calculation time.

For this reason, the material model according to von Mises, which is an isotropic material model and similar to Hill (cf. Chapter 2.5.3.1 equation (2.11)) only without the anisotropic coefficients, was selected (LS-DYNA MAT_24). In addition to the density, modulus of elasticity, Poisson's ratio and the yield strength, the material model requires a flow curve in tabular form. The extrapolation method according to Hockett & Sherby (equation (3.1)) is a common assumption for generating the flow curve for high strength aluminium alloys (Barlat et al. 2003; Yoon et al. 2004).

The calibration of the material behaviour by means of parameter optimisation is described below. A simulation model of the tensile test is created for this purpose. In this model the flow curve is parameterised after Hockett & Sherby (equation (3.1)) in Matlab (see Appendix E), and is output in tabular form and integrated into the simulation of the tensile test as a material model.

The goal of this optimisation is to adapt the stress-strain curve from the simulation to the experimentally determined curve. For this purpose, an optimisation is set up with the LS-OPT optimisation software. The overview of the optimisation is shown in Figure 3-13.

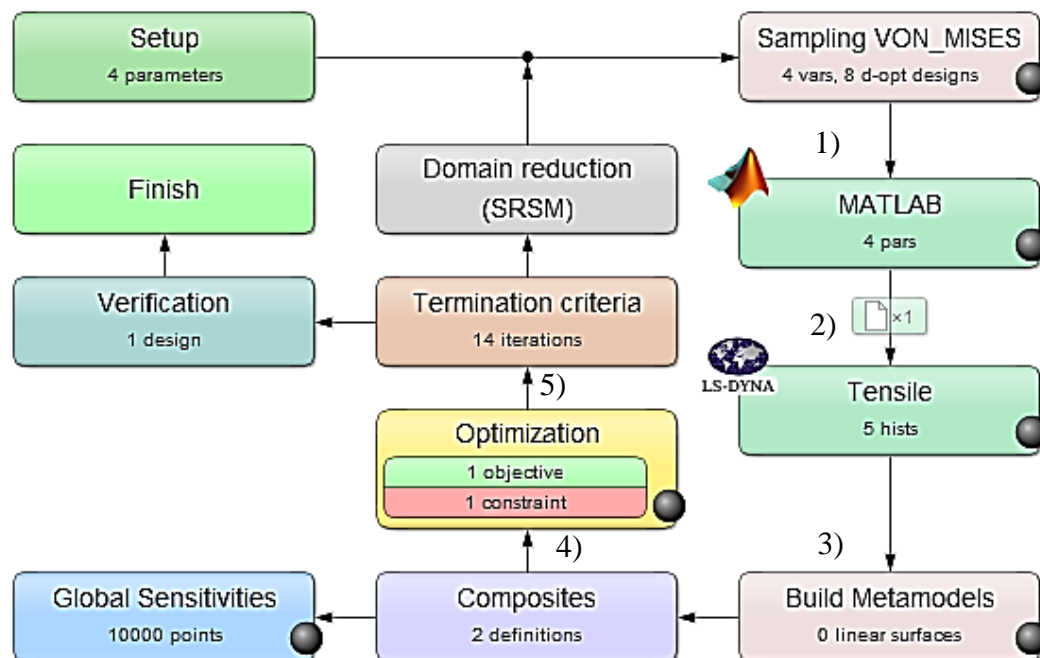


Figure 3-13: LS-OPT Overview (von Mises) calibration

The parameter optimisation procedure can be described as follows:

- 1) In the first step, the parameters are determined using the optimisation algorithm and transferred to Matlab version 2018b.
- 2) Matlab calculates a flow curve using the Hockett & Sherby parameters a, b, c and n (cf. equation (3.1)) and outputs this in tabular form as MatlabOutput.k file. This file is passed on to LS-DYNA simulation (solver version R10) and integrated into the simulation model as *INCLUDE command.
- 3) In the third step the tensile test is simulated. After finishing the calculation, the stress-strain curve from the simulation is evaluated.
- 4) In the next step the y-distance, i.e. the stress difference between the simulation and the experimental curve is determined. This function is called "Curve Matching" in LS-OPT.
- 5) Finally, the stress difference is minimised.

Calibration of the material model for the final state of the AA7075 after forming process and paint bake is given by the following flow curve function:

$$\sigma_f = 723.96 - 296.96e^{-3.08\varepsilon_p^{0.65}} \quad (3.9)$$

The comparison of the experimental curve (black) and the simulation (blue) shows a very good agreement (see Figure 3-14). Now the failure curve for a GISSMO model is created:

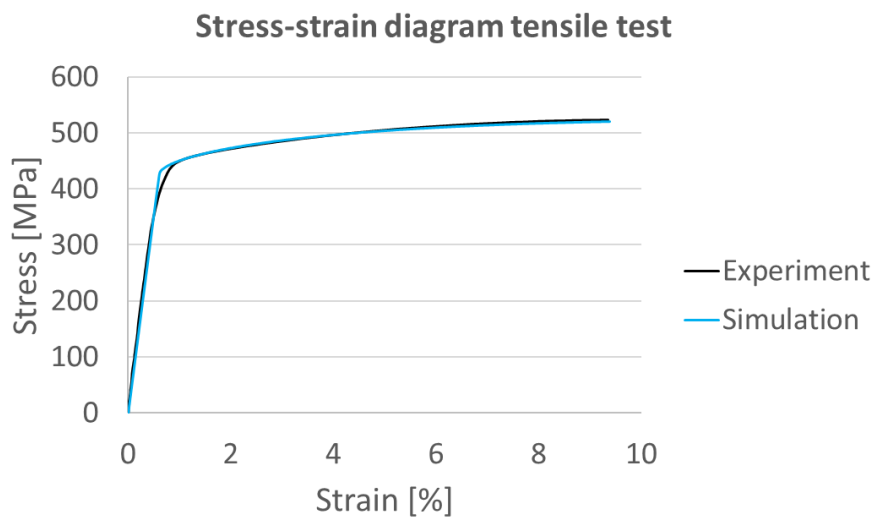


Figure 3-14: Stress-strain diagram, tensile test experimental curve and simulation curve

3.4.2 Damage and failure model of the final state (GISSMO)

After calibrating the material model for the finale state of the aluminium alloy, the failure model is now calibrated with the same specimens and in the same way as in the Extended Hotforming process (cf. Chapter 3.3). The LS-OPT optimisation software is also used here.

For the calibration of the failure model, all specimens are included in the optimisation (see Figure 3-11). In contrast to the material calibration, where the experimentally determined stress-strain curves are used up to uniform elongation, for the failure model the entire stress-strain data are implemented. The adaptation of the stress-strain curves from the simulation to the experiments is done with the "Curve fitting" function in LS-OPT. The optimisation comprises 10 parameters to be optimised, the same as in Chapter 3.3.2 (Table 3-10), where 7 parameters (TR0-TR6) are for the failure curve and three for the instability curve (ECR0, ECR3 & ECR6) at different triaxiality states.

The calibration of the failure model provides the optimised parameters as illustrated in Table 3-12:

Table 3-12: Parameterisation and results of the failure and instability curve of the finale state AA7075

Triaxiality	Failure strain		Instability strain	
	Parameter TFC	Optimised value	Parameter E _{crit}	Optimised value
0	TR0	0.367	ECR0	0.293
0.111	TR1	0.295	-	-
0.222	TR2	0.241	-	-
0.333	TR3	0.161	ECR3	0.087
0.444	TR4	0.473	-	-
0.555	TR5	0.328	-	-
0.666	TR6	0.493	ECR6	0.431

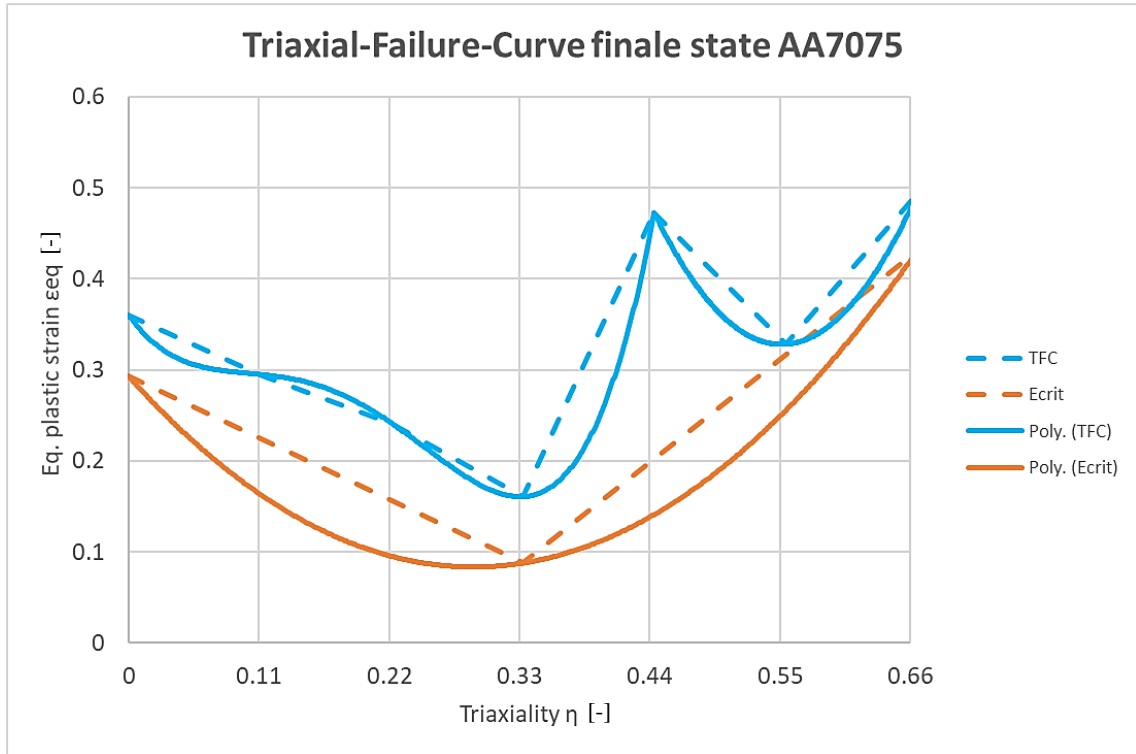


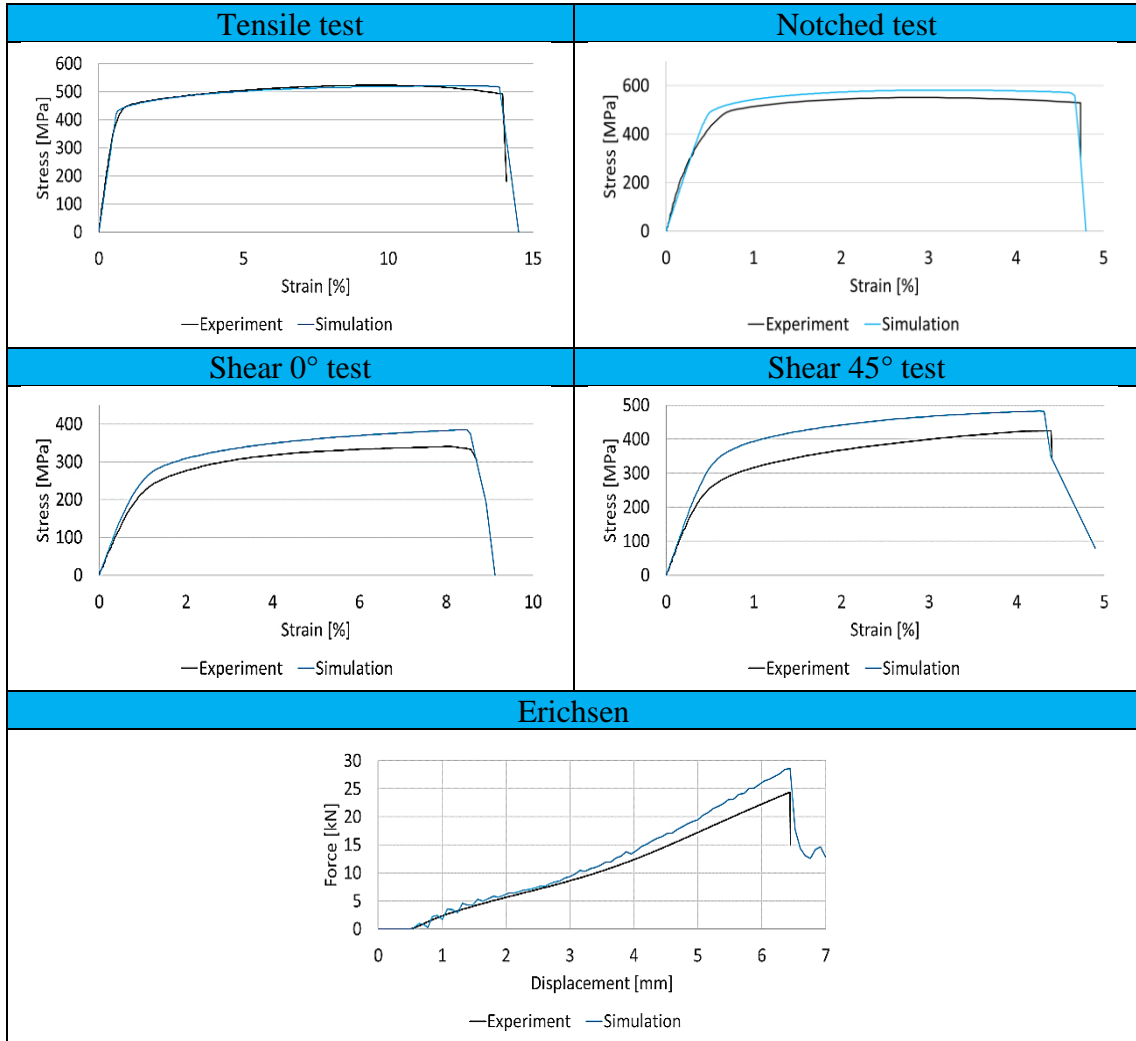
Figure 3-15: Triaxial failure curve and instability curve of the final state of AA7075

In contrast to the failure model of the Hotforming process, the specimens of shear test 15° and shear test 30° are not considered for the final state GISSMO model. This leads to a considerable reduction of the calibration effort and is sufficient for the calculation, due to the simple material model of von Mises.

Figure 3-15 shows the triaxial failure curve and the instability curve for the AA7075 in the final state. The curves were shown linear on one side and polynomial on the other side, which results in a smoother characteristic. If the calibrated GISSMO model is implemented into the simulation, a good agreement (less than 0.5 % deviation in elongation at fracture) between the stress-strain curve of the tensile test and notched test can be determined, which is illustrated in Table 3-13. Furthermore, there is a slight deviation in the shear test and the Erichsen test, which is due to the missing anisotropy in the material model.

Nevertheless, the material model (von Mises) including the failure model (GISSMO) can now be used for further crash calculations.

Table 3-13: Optimisation results for damage/ failure model at finale state - stress-strain and
force-displacement diagrams



3.4.3 Concluding remarks

In this study, a material and damage/ failure model for the final state of AA7075 after 180°C 20 minutes of artificial ageing, which corresponds to the cathodic dip coating (KTL), was created. In the industry, a simple isotropic material model is often used for crash calculations in order to keep the calculation times acceptable. Therefore, the yield curve of a von Mises material model was extrapolated according to Hockett & Sherby and the damage/ failure model was adapted to the experimental stress-strain/ force-displacement curves of the shear, tensile, notched and Erichsen tests with the help of a LS-OPT parameter optimiser. The comparison of the curves from the experiments with the simulation curves shows a good agreement and the models can be used for further component simulations.

3.5 *Friction analysis*

In sheet metal forming the lubrication is one of key element concerning the surface quality of the formed component and the process stability. Common lubricants in sheet metal forming are mineral oils, synthetic oils and soaps. For difficult applications, such as forming operations at higher temperatures, colloidal or molybdenum sulphide mixtures may be used.

In order to obtain an accurate forming simulation and a relation to the predictability of cracks and defects, the friction between die, blank and blank holder are of great importance. A pioneer in this field is “TriboForm”, which is a software for simulation of friction and lubrication conditions from the company AutoForm (AutoForm Engineering GmbH). The software enables the user to simulate the effects of tool coatings, lubrications, surface conditions or new sheet metals. This software is not available to the university, but a comprehensive friction coefficient model is created, which can be used in further forming simulations in LS-DYNA.

3.5.1 **Tribometry in sheet metal forming**

The term tribometry refers to tribological measuring and testing technology and ranges from investigations of complete technical systems under real operating conditions to laboratory model tests with simple test specimens. The aim of tribometry in sheet metal forming is the measurement and testing of the quantities influencing friction and wear. The extensive test field of tribometry can be divided into 6 categories, which is illustrated in Figure 3-16. A higher category always means a simplification of the system to be tested. In sheet metal forming, categories I - III correspond to the operational or operation-like tests. However, determining the coefficients of friction directly in the forming tool is technically very complex. Tribological investigations in sheet metal forming are therefore carried out almost exclusively with the aid of model procedures, which corresponds to categories IV and VI (Czichos & Habig 2015).


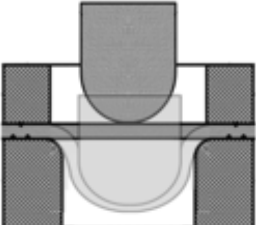
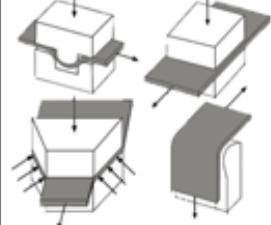

Test principle			
Category I-III	Category IV	Category V	Category VI
			
Field test	Model experiment		
<div><div>←</div><div>Transferable to real process</div><div>→</div></div>			
<div><div></div><div>Accessibility of measurement</div><div></div></div>			

Figure 3-16: Categories of tribological testing technology (Staeves 1998)

A deep-drawing part can be divided into several tribological areas. These areas are simulated by different model procedures of the strip drawing test. The strip drawing processes can be subdivided as follows (cf. Figure 3-17): Draw bead test, wedge drawing test, draw edge test and strip drawing test or flat strip drawing test.

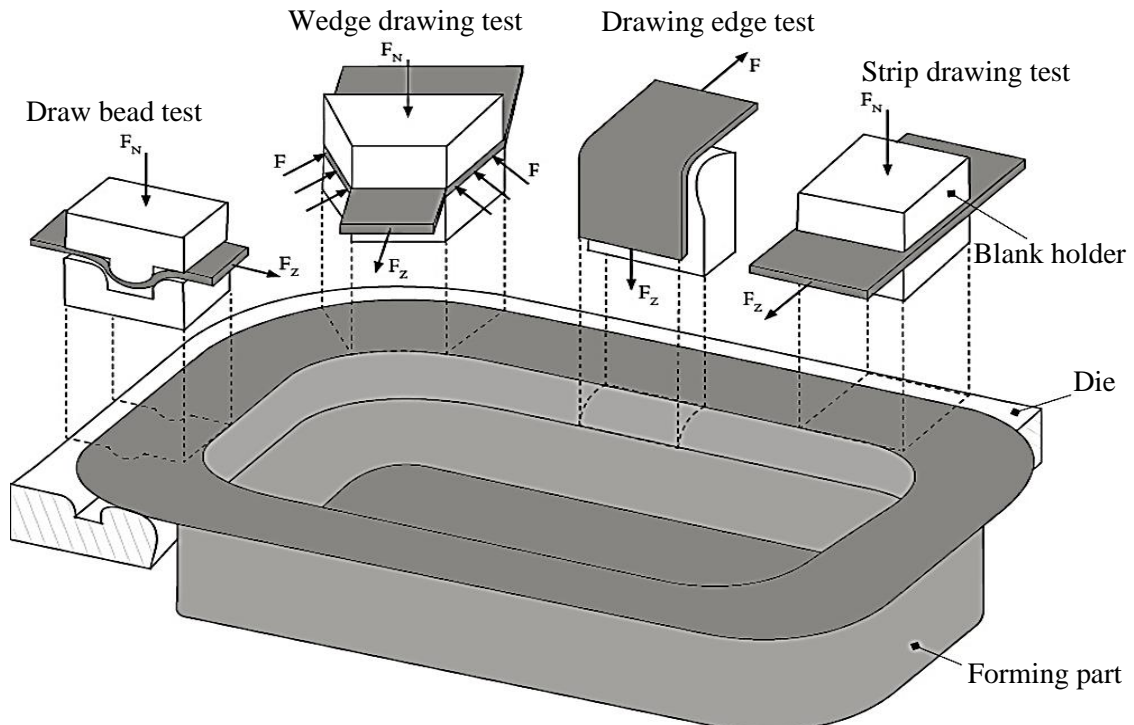


Figure 3-17: The test variants of the strip drawing test (Hoffmann et al. 2012)

The flat strip drawing test has the greatest significance in the field of deep-drawing and is regarded as the standard test for determining the friction parameters. A sheet metal strip is drawn through between flat drawing jaws with a defined normal force at constant speed. The coefficient of friction is determined from the pull-out force and the normal force according to this relationship:

$$\mu = \frac{F_Z}{2P_N A} = \frac{F_Z}{2F_N} \quad (3.10)$$

The coefficient of friction is a meaningful parameter and is used to compare tribological systems with different influencing parameters such as lubricant, temperature, drawing speed, blankholder force, sheet material, tool material and surface (Hoffmann et al. 2012). The pull-out force curves over the pull-out displacement can look different depending on the influencing parameters.

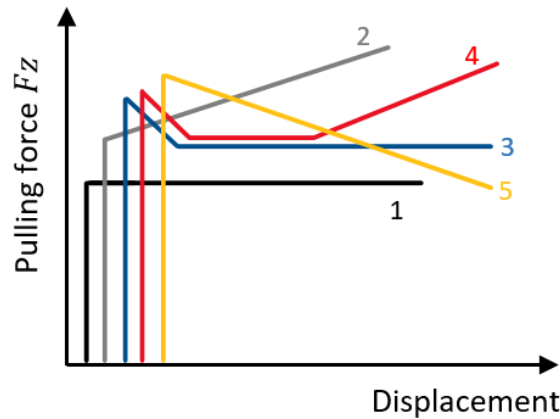


Figure 3-18: Possible force-displacement curves for strip drawing (Lange 1990)

The force-displacement diagrams shown in Figure 3-18 may be interpreted as follows (Lange 1990):

1. No cold welding, intact lubricating film
2. Cold welding (adhesion), collapse of the lubricating film
3. High static friction with subsequent sliding friction
4. High static friction with subsequent cold welding (adhesion)
5. Reduction of drawing force due to formation of intermediate layers of lubricant additives

Depending on the test conditions and the influencing variables to be investigated the results from the strip drawing tests can be compared with the force-displacement curves from Figure 3-18 to know which condition is present.

3.5.2 Development of a flat strip drawing tool for the tensile testing machine

In this work, a flat strip drawing test for friction tests is developed. Due to the constellation of the uniaxial tensile stress, the developed tool can also be used to carry out draw bead and wedge drawing tests (see Figure 3-17). Strip drawing test with deflection is not integrated and will not be followed up.

The conception and construction of the tool is based on VDI 2221. The guideline shows a procedure for methodical development and construction of a technical product. From the task definition to the constructive solution, the guideline offers a structured solution process according to iterative working methodology.

3.5.2.1 List of requirements

According to VDI 2221 the first step is to clarify and specify the task. In the requirements list, all available information and requirements of the task are clarified, specified and checked. The requirements list is a continuous document, which can be adapted and supplemented during the entire construction process.

The specifications in the requirements list, which were created through literature research, are subdivided into fixed requirements (f) and wish requirements (w). Fixed requirements are quantitative or qualitative information that must be fulfilled in any case. If a requirement is not met the concept lapses. On the other hand, the wish requirements do not have to be fulfilled but ideally bring added value to the product. Most of the requirements were defined by a competitive analysis of different friction test benches.

Table 3-14: Requirements of the flat strip drawing tool

No.	f/w	Requirement	Value	Comment
1	f	Normal force Clamping force	Max. 50 kN	Surface pressure between 1- 40 MPa should be possible
2	f	Test surface	2000 mm ²	Friction jaw surface
3	f	Test stroke	Min. 100 mm	Pulling out the specimen
4	f	Operating temperature	Max. 200 °C	Climate chamber temperature of the tensile testing machine
5	f	Readability of the clamping force	Yes	Sensor or measuring scale
6	f	Interchangeability of the drawing jaws	Yes	Test surface, shape, material
7	w	Quick change of the drawing jaws	Yes	
8	f	Sheet thicknesses of the specimens	1-8 mm	
9	f	Application on the Schenck tensile testing machine	Yes	
10	f	Installation space restriction to climate camera dimensions	W: 330 mm H: 348 mm D: 320 mm	Width x height x depth
11	f	Design suitable for installation	Yes	
12	f	Tooling costs	Max. 2000€	

3.5.2.2 Analysis of the installation space of the tensile testing machine

The construction environment of the strip drawing tool is limited to the climate chamber dimensions. A long tool holder is used for tensile tests due to climate chambers. The tool extension is designed in such a way that the traverse moves up to the limit switch and prevents a collision between the clamping jaws of the tensile testing machine and the climate chamber ceiling. The pull-out stroke of the strip drawing tool is thus limited to the traverse stroke up to the limit switch. The internal dimensions (see Figure 3-19) of the climate chamber and the axis position of the tool holder were taken from old drawings of the tensile testing machine. The climate chamber is 330 mm wide and 320 mm deep when the door protrudes into the installation space. The pull-out axis of the tensile testing machine is located exactly in the centre of the climate chamber. Other dimensions, such as the tool holder, were taken directly from the machine.

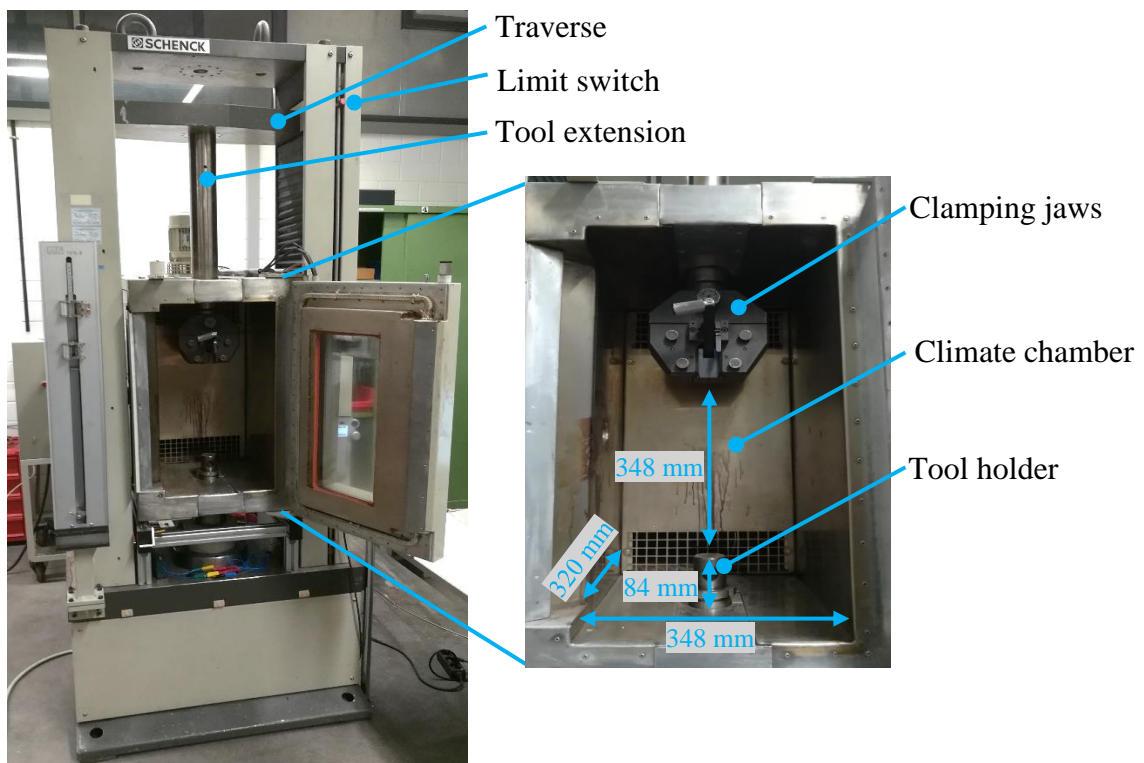
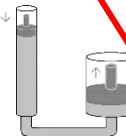


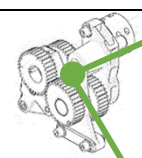
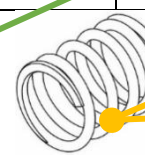
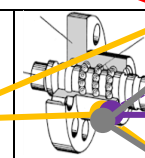
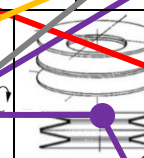
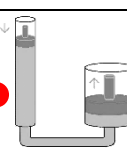
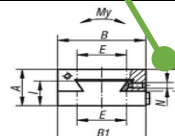
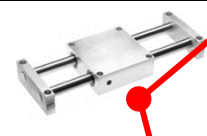
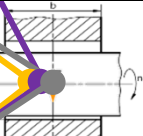
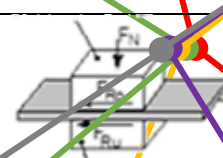
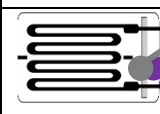
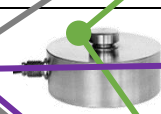
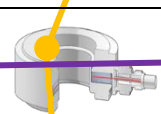
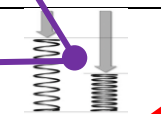
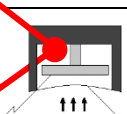
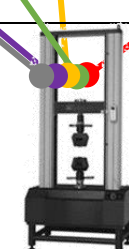


Figure 3-19: Tensile testing machine with climate chamber

3.5.2.3 Morphological box

Creativity techniques are often used in construction to search for different solution principles. The morphological box is particularly suitable for the systematic combination of solution principles to a total solution variant.

Table 3-15: Morphological box

Function	Variant 1	Variant 2	Variant 3	Variant 4	Variant 5
Generate normal force	 Hydraulic	 Electric motor	 Human force		
Normal force transmitted	 Gear	 Springs	 Spindle	 Disc Springs	 Hydraulic
Guides/ bearing	 Dovetail guide		 Cylindrical guide	 Clearance fit	
Clamp sheet metal	 friction jaws				
Measurement of normal force	 Strain gauge	 Load cell	 Piezo load cell	 Spring deflection	 Pressure sensor
Draw sheet metal	 Tensile testing machine				

Five variants have been developed for the overall strip drawing tool system.

Variant 1

In variant 1, the force is generated hydraulically and transferred to the strip drawing jaws by means of a piston. The moving parts are guided and supported by a cylinder guide. The normal force is determined with a pressure sensor.

Variant 2

The force is generated by an electric motor and transmitted via a gear due to high normal force requirements. The parts are guided and stored via a dovetail-, flat- or cylindrical guide. The normal force is determined using a "force transducer" based on strain gauges.

Variant 3

In the third variant, the force is generated by muscle power, which is increased with the aid of a lever in order to set the required normal force. The spindle transmits the rotary motion with interposed compression springs into translatory force transmission. The parts are guided and supported in a housing via a clearance fit. According to Hooke's law, the normal force is determined by the spring deflection.

Variant 4

The fourth variant is similar to the third. The normal force transmission, however, takes place via disc springs. Since disc springs have a non-linear spring characteristic curve the normal force is determined by means of strain gauge attached to a component or loading cell.

Variant 5

In the fifth variant, the springs are not interposed and the required force is introduced directly into the tool via a lever arm through the spindle. In this variant, too, the guidance and bearings are provided by a clearance fit in the housing. The force to be set is determined by means of a strain gauge attached to a component through which the force is measured. The morphological box offers far more than five total solution variants. In order to limit the possible variations a team meeting was held for decision making. The decision was made for variant 4, which offers the advantage of cost efficiency (no motor, gearbox or hydraulics required) and the normal force can be read analogously via the spring travel as well as via the strain gauge.

3.5.2.4 Construction of the flat strip drawing tool

Initially, a general functional principle was designed, which is shown in Figure 3-20. The changeable friction jaws are fixed in a friction jaw holder. The required normal force is applied to one side of the tool. This divides the tool into a fixed and a movable half. The fixed side of the tool is closed by a housing cover. In order to test different sheet thicknesses, a distance plate is required. This ensures that the friction jaw on the fixed side is positioned evenly to the sheet specimen.

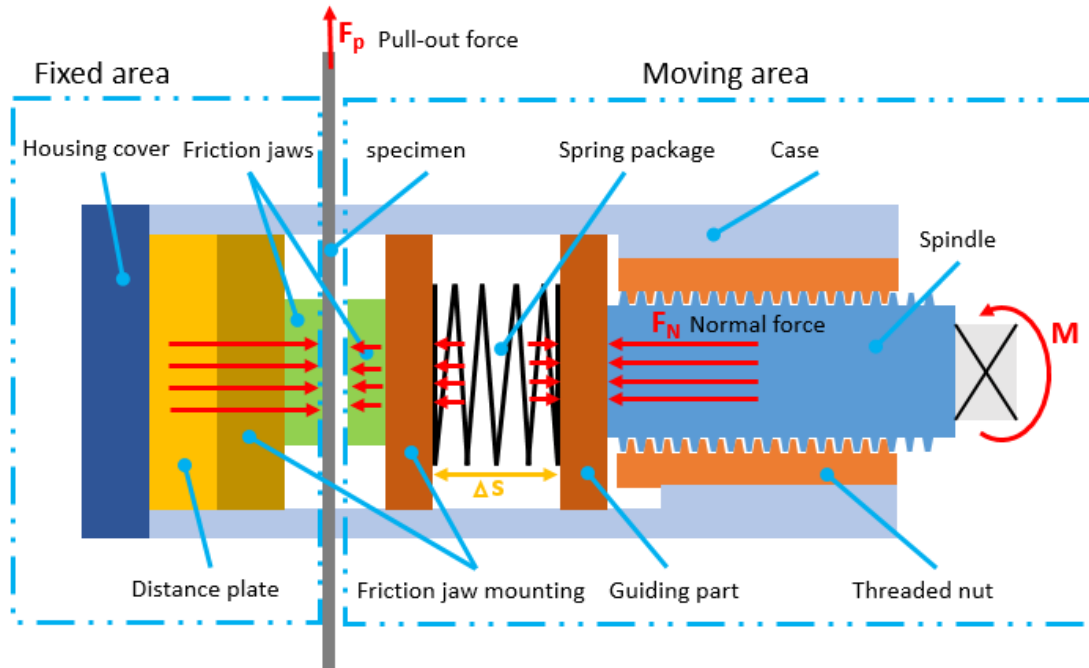


Figure 3-20: Functional principle of the strip drawing tool

By turning the spindle, the spring package is compressed between the friction jaw holder and the guiding part. The spring package applies a normal force on both sides of the tool, which is measured by a strain gauge or spring deflection. The force is transmitted to the clamped sheet metal by the self-locking mechanism in the thread and the firmly screwed housing cover.

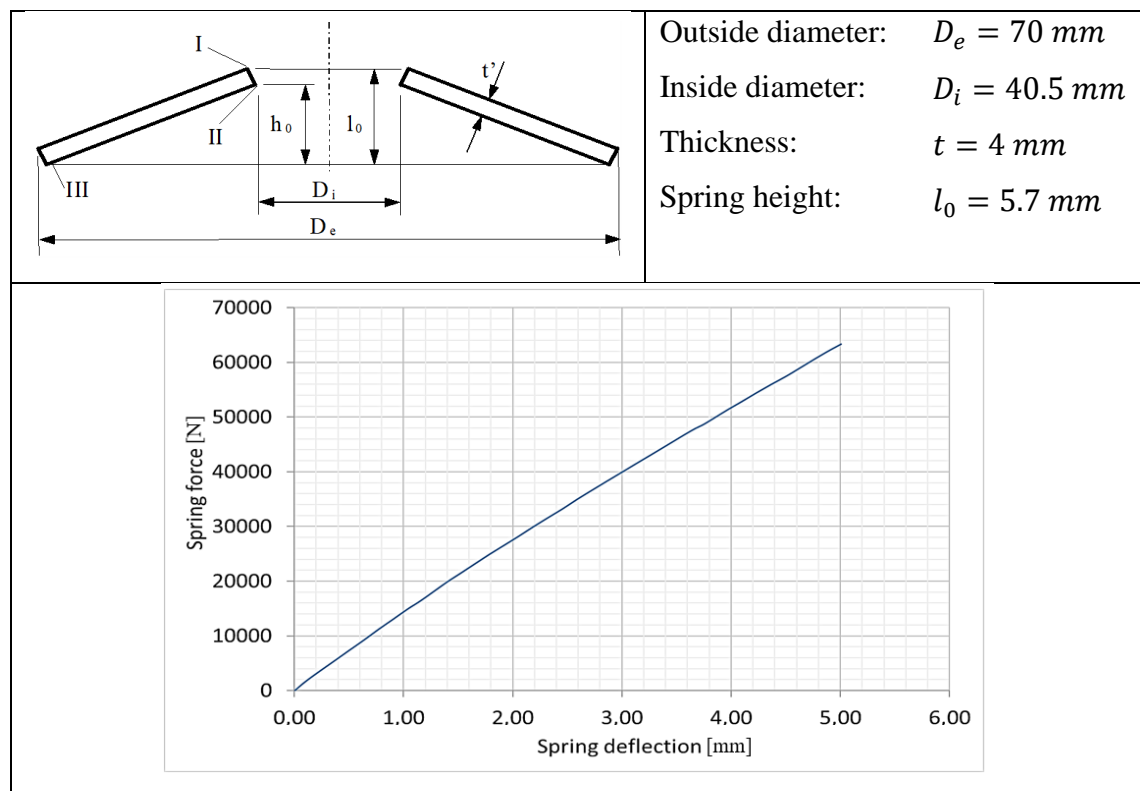
In the fourth variant, disc springs are used for force transmission. The required normal force of 50 kN can already be transmitted by a cup spring. Due to its flat geometric shape, the spring deflection of a single spring is too short for force determination.

Disc springs are normally used as a modular element by layering the disc springs to form a spring package or spring column. Disc springs layered in the same direction are called spring packages. Single springs or packages with alternating layers are called spring

columns. In the case of a layering in the same direction the spring deflection of the package is equal to the spring deflection of the individual spring. The spring force is proportional to the number of individual springs used in the package.

To read the force over the spring deflection, a spring column was selected from three alternately stacked packages with two individual springs each. This combination results in a three-fold spring deflection and a two-fold force. The spring characteristic curve of the spring column of six-cup springs is almost linear. Further characteristic values are contained in Table 3-16. On the basis of the force-deflection curve, the spring travel is determined, and the force is read off from the spring travel in the diagram.

Table 3-16: Technical data of disc springs



The design of the strip drawing tool corresponds exactly to the general functional principle and is illustrated in Figure 3-21.

The inner parts of the tool are cylindrical in order to place the disc springs precisely. Due to the cylindrical design, both friction jaw holders are fixed against twisting with an anti-twist device, which is screwed onto the housing. This ensures the horizontal position of the friction jaws.

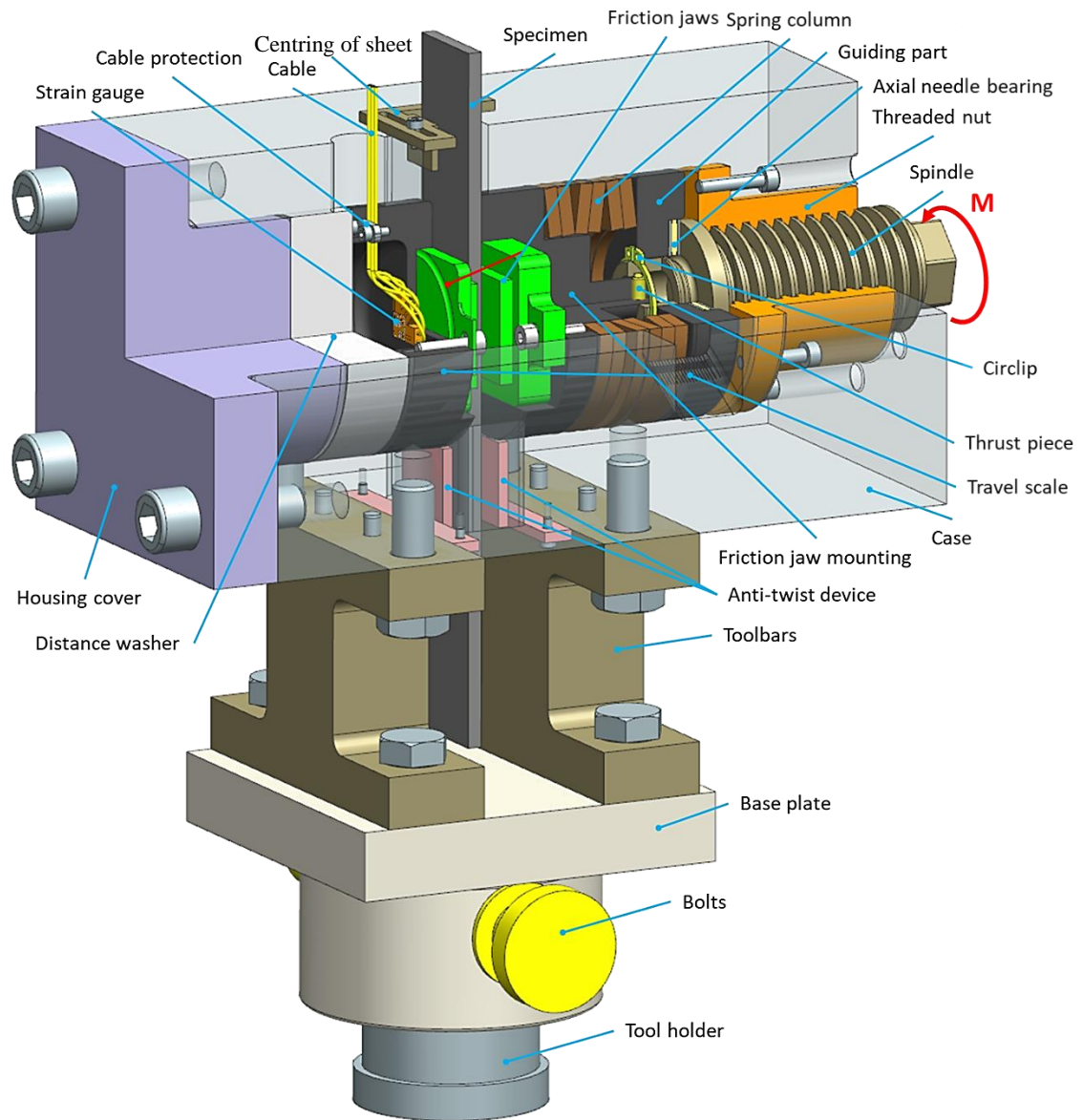


Figure 3-21: Strip drawing tool in $\frac{3}{4}$ sectional view

The strain gauge was mounted centrally on the back of the friction jaw holder on the fixed side of the tool. The geometry of the friction jaw, as well as of the holder, was specially optimised and designed for the application of the strain gauge (cf. Chapter 3.5.2.6). In order to prevent the strain gauge cables from tearing off they are firmly screwed to the friction jaw holder with a small plate. The cables are led out through a hole in the housing and connected to a measuring amplifier.

The friction jaws are screwed to the friction jaw holders on both sides of the tool. The screws are only used to fix the friction jaws and are not loaded during strip drawing. When pulling out the sheet metal sample the friction jaws are supported by the upper side of the friction jaw holders mounted in the housing via positive locking.

An axial needle bearing was used to reduce friction on the contact surface between the trapezoidal spindle and guide component. In order to achieve a backward movement of the components on the moving side a circlip and a thrust piece were used.

The rectangular housing at the top and bottom is cut out for the insertion of the sheet specimens. The upper recess is equipped with a sliding centring device. Distance washers of different thicknesses are provided for flush mounting of the pull-out specimen of different thickness on the fixed side of the tool. A distance washer was manufactured for each specimen thickness of 1-5 mm (see Table 3-17).

Table 3-17: Specimen thickness with the respective distance washer

Specimen thickness [mm]	Thickness of the distance washer [mm]
1	23
1.5	22.75
2	22.5
2.5	22.25
3	22
3.5	21.75
4	21.5
4.5	21.25
5	21

The minimum requirement of the friction jaw test surface of 2000 mm^2 is fulfilled and can be designed as required up to a maximum of 2042 mm^2 (cf. Figure 3-22)

The connection to the tool holder of the tensile testing machine is made via a base plate and toolbars.

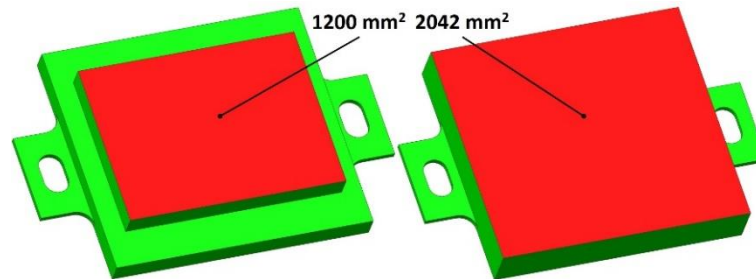


Figure 3-22: Friction jawplates geometry with different test surface sizes

The length and width of the strip drawing tool are 226.6 mm and 110 mm respectively (see Figure 3-23). The maximum strip pull-out length, measured from the lower friction jaw edge to the base plate, is 108.5 mm and meets to the requirements list. With a weight of approx. 25 kg, the tool can be easily mounted into the tensile testing machine by one person.

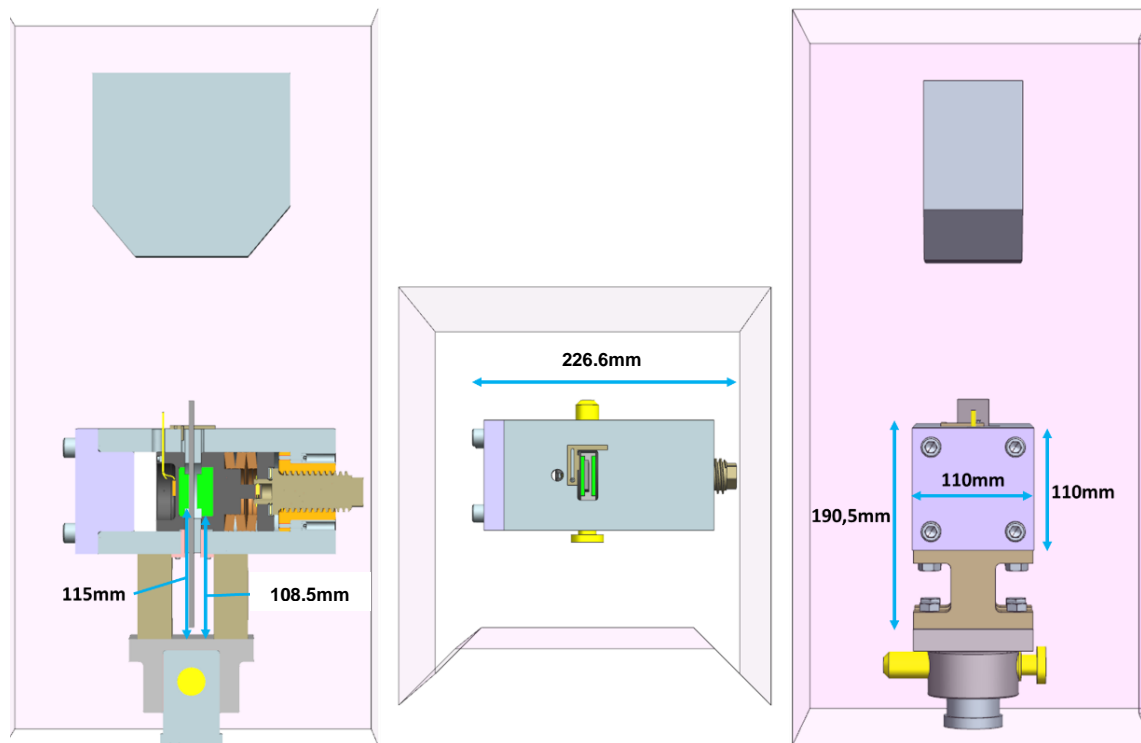


Figure 3-23: External dimensions of the strip drawing tool

A complete assembly instruction of the strip drawing tool as well as images of the finished test bench can be found in Appendix F.

3.5.2.5 Material selection

The material for the strip drawing tool must fulfil high thermal requirements as well as mechanical requirements. A Q&T (Quenched and Tempered steel) steel made of 42CrMo4 was selected for the tool. The steel is mainly used in automotive and mechanical engineering applications. High strengths combined with high ductility enables the material to be used for highly stressed components such as steering knuckles, connecting rods, crankshafts and gear shafts, gear wheels or pinions. The mechanical properties of this steel grade are pointed out in Table 3-18 and are used in further FE-simulations.

Table 3-18: Mechanical properties of 42CrMo4 in tempered condition (Saarstahl AG 2017)

Yield strength σ_f	Ultimate tensile strength UTS	Fracture elongation e_f	Young's modulus E
750 – 900 [MPa]	1000-1300 [MPa]	Min. 10 [%]	210 GPa

3.5.2.6 Application of the strain gauge

Due to the geometry of the friction jaw holder, the surface on which the strain gauge is placed will deform to the inside when force is applied. The specification of the strain gauge is in Appendix F.

As the deformation is not exactly symmetrical a strain gauge rosette with 3 measuring grids in 0°, 45° and 90° was attached to determine the strains. The position of the strain gauge, the dimension and the schematic deformation of the friction jaw holder are shown in Figure 3-24. The strain gauge that is used can be applied for temperatures up to 200°C.

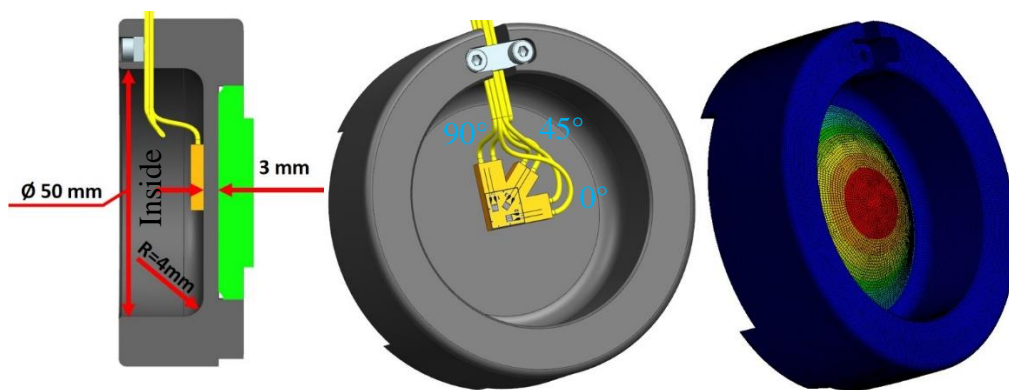
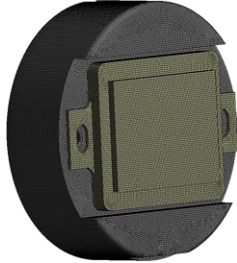
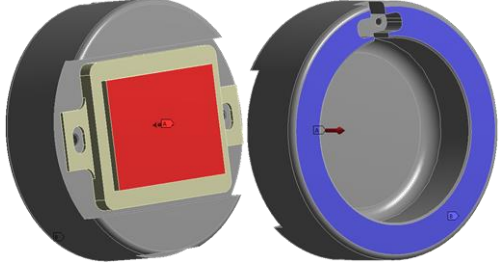
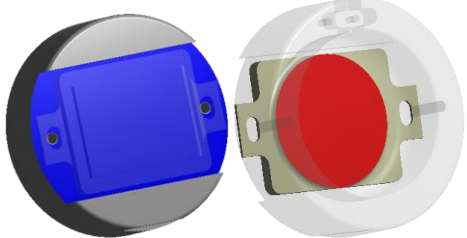


Figure 3-24: Dimensions of the friction jaw holder, positioning of the strain gauge rosette, deformation of the friction jaw holder and image from FEM simulation

In order to measure the strains, the friction jaw holder and the friction jaw plates were designed by FE-analysis. With the generated FE-model (see Table 3-19) the design of the

friction jaw plates and the friction jaw holder were dimensioned in a way that no plastic deformation occurs (a safety factor of 2 was considered to avoid plastification of the tool) but still an adequate elastic deflection that can be measured.

Table 3-19: Boundary conditions for the numerical simulation

Mesh with Hex – Dominant Method Element size: 0.5 mm	
Variable force (0.2kN – 65.5kN) on the surface of the friction jaw (red). Fixed clamping on the rear side of the friction jaw holder (blue).	
Contact between friction jaw and holder with friction coefficient $\mu=0.15$.	

Three different friction jaw plates were designed in order not to plastically deform the radius at the friction jaw holder at high forces. The plates are equally thick and have the same front side. But on the rear, there are different diameters (circular elevations) for different loading conditions, which are shown in Figure 3-25.

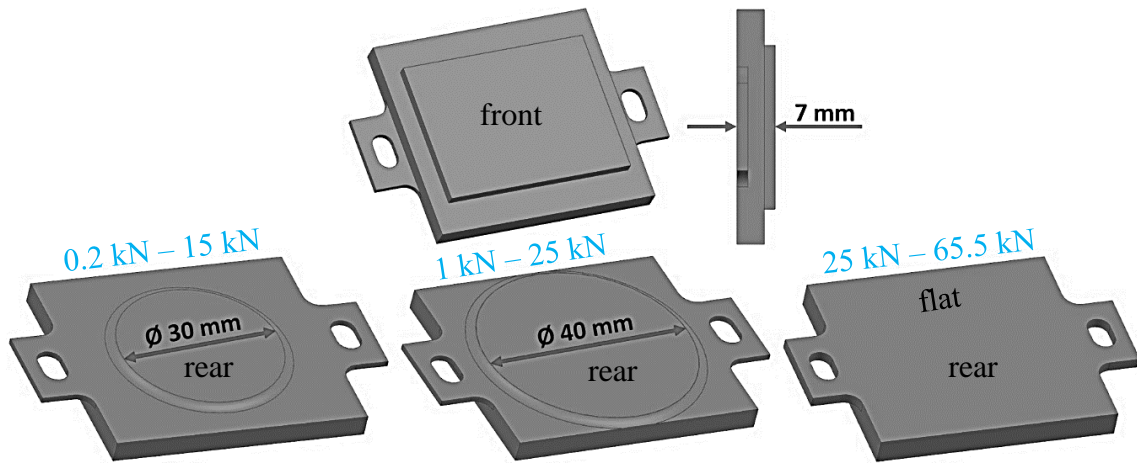


Figure 3-25: Friction jaw plates geometries

The v. Mises stresses in the friction jaw holder at different loads (0.2 kN-65.5 kN) and the diameters of the friction jaw plates were analysed by FE-analysis. Furthermore, the strain at the position of the strain gauge on the friction jaw holder is determined and it is important that the elongation is high enough, greater than 5 $\mu\text{m/m}$, to be measured in the measuring force amplifier.

The simulation results, which are listed in Appendix F, show an equivalent to the v. Mises stress between 326 MPa – 477 MPa, therefore the jaw holder is only loaded up to half of its yield strength value (representing a safety factor of around two) and thus plastic deformations of the component are excluded.

In the technique the elongation is indicated with $\mu\text{m/m}$. Therefore, the simulation results of the strains are given in $\mu\text{m/m}$ and are also listed in Appendix F. Depending on load (0.2 kN-65.5 kN) and diameter ($\varnothing 30$, $\varnothing 40$, *flat*) of the friction jaw, the elongations in the middle of the friction jaw holder, where the strain gauge measures, are between 5.3 $\mu\text{m/m}$ up to 590 $\mu\text{m/m}$. Those values can be measured well with the force amplifier from the company HBM (*Hottinger Baldwin Messtechnik GmbH*).

3.5.2.7 Calibration of the friction test bench

In order to get the friction coefficient μ over the draw path during the tests, the strain gauge is first calibrated. For further friction investigations, the friction jaw with a diameter of 40 mm was chosen, which allows a surface pressure from ~ 1 MPa up to 28 MPa.

The measured main strain is converted into surface pressure by means of a force-strain curve. First, the screws on the housing cover were removed and the strip drawing tool

was placed on the base plate and adjusted (see Figure 3-26). The screws of the threaded nut were also unscrewed so that the body, threaded nut and spindle can move freely in the housing. Subsequently, the strain gauge is connected to a calibrated measuring force amplifier MGCplus from the company HBM (*Hottinger Baldwin Messtechnik GmbH*), which transmits the strains to the recording and evaluating "EVIDAS version 1.4" software via Ethernet cable.

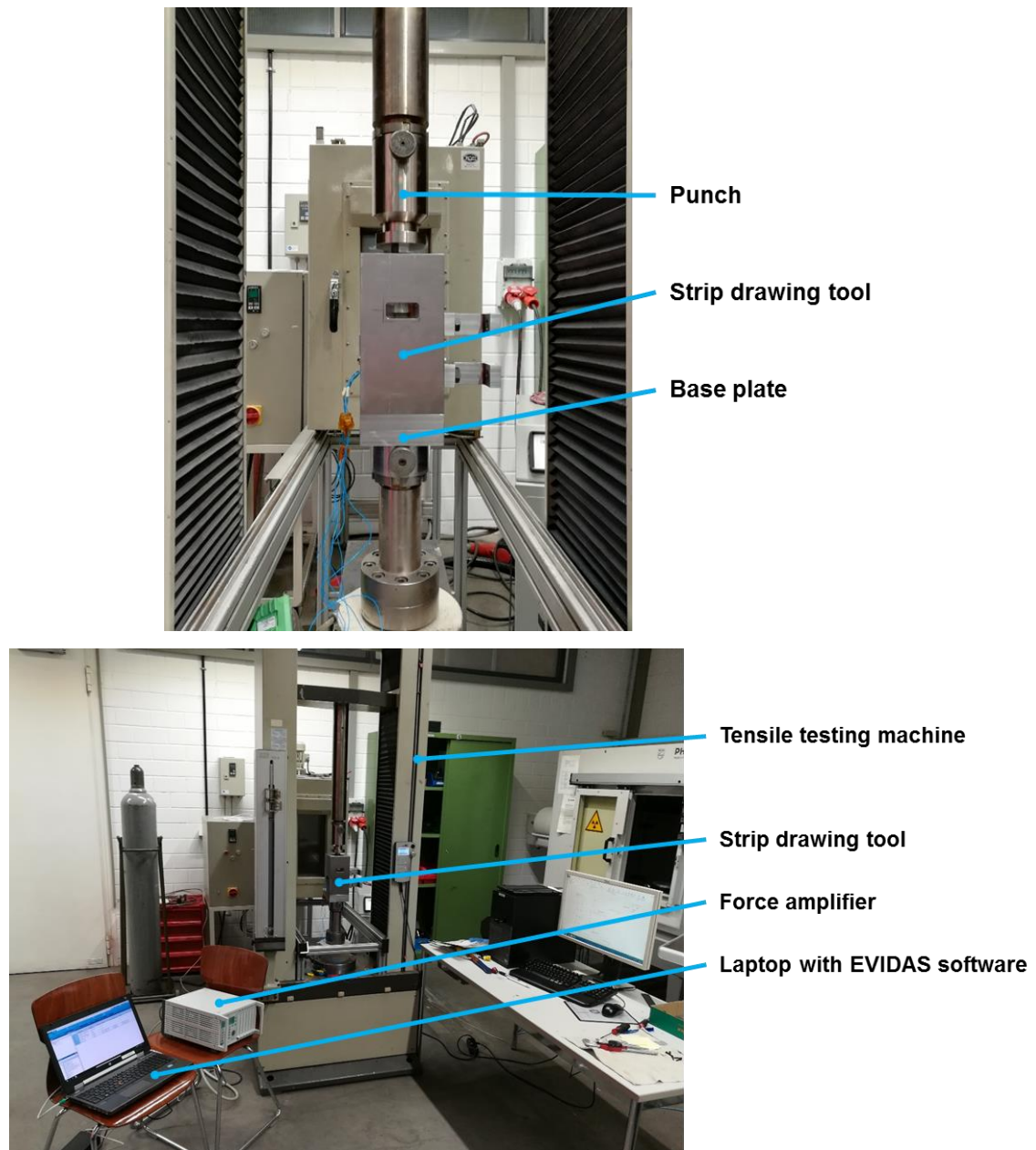


Figure 3-26: Setup for strain gauge calibration

During calibration the compression force on the tensile testing machine is incrementally increased. The software determines the strain in $\varepsilon_1 = 0^\circ$, $\varepsilon_2 = 45^\circ$ and $\varepsilon_3 = 90^\circ$ direction from the three measuring grids and calculates the main strain by the equation (3.11).

$$\varepsilon_{I,II} = \frac{\varepsilon_1 + \varepsilon_2}{2} \pm \frac{1}{2} \sqrt{2} \sqrt{(\varepsilon_1 - \varepsilon_3)^2 + (\varepsilon_2 - \varepsilon_3)^2} \quad (3.11)$$

The main strain and the force from the tensile testing machine are transferred into the Excel table and a mathematical function is fitted into the measuring points (cf. Figure 3-27).

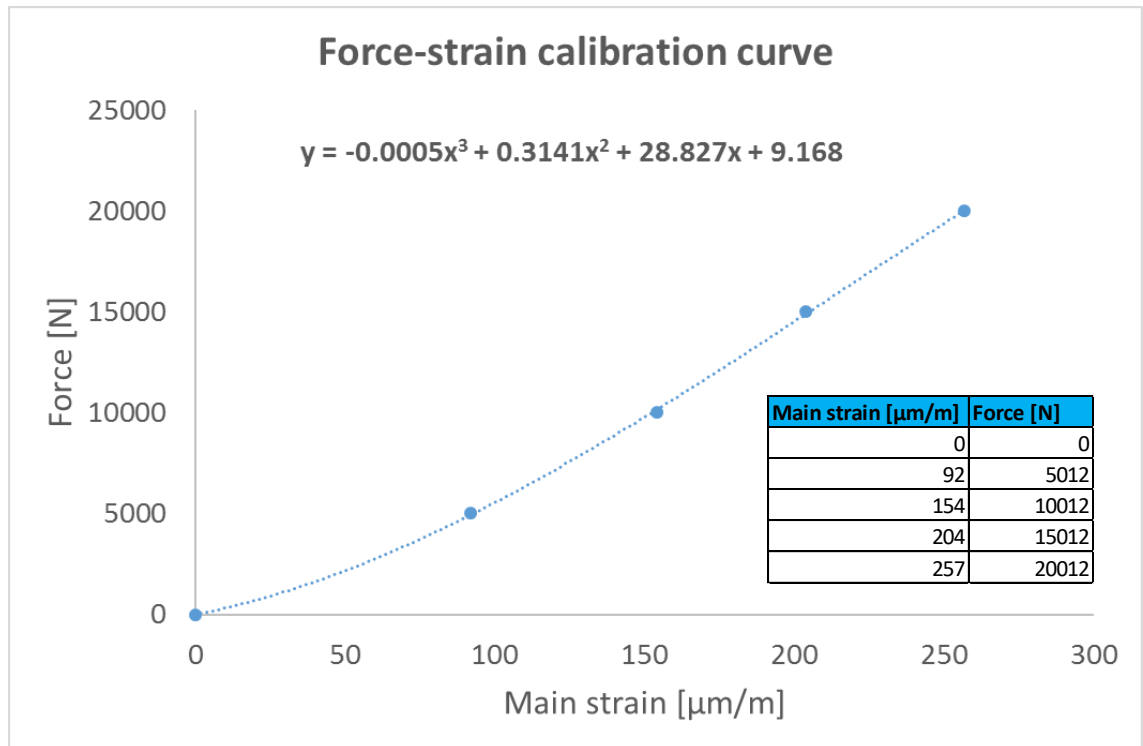


Figure 3-27: Calibration force-strain curve and mathematical function

The mathematical function used to calculate the normal force, is now integrated into the tensile testing software called “Test and Motion from Doli”.

Using equation (3.10) the friction coefficient can now be derived by using the normal force F_N , which is set by the spindle prior testing, and the pull-out force F_Z which is received as response signal of the loading cell of the tensile testing machine.

3.5.3 Pre-tests and measurements

Before the actual trials were conducted the hardness of the steel jaws (made out of steel 1.2311) was measured in hardened and unhardened condition. The drawing strips were also measured in the “as-delivered” T6 condition and in the solution annealed condition. Although better friction conditions can be achieved using EDT (electrical discharge texturing) or laser textured sheet metal surfaces (Chapter 2.4.1), the tests were carried out with mill finish conditioned sheets. This was due to the material supplier who could not deliver such a material at this stage. The hardness was measured on a hardness tester from EMCO-TEST GmbH with the type designation DuraVision 30G5 using the Brinell test method (HBW2.5/6.25).

The condition of the drawing strips, which are solution annealed, corresponds to the sheet metal used for the Hotforming process. Further, the same steel grade, as it is considered for the forming tool, was used for the hardened steel jaws. Figure 3-28 shows the hardness measurements of the pull-out strips and friction jaws in different conditions. The T6 condition strip serves as a reference measurement, with a strength of 170 HB (560-575 MPa). This corresponds to the T6 strength values from the material manufacturer (Grohmann 2016).

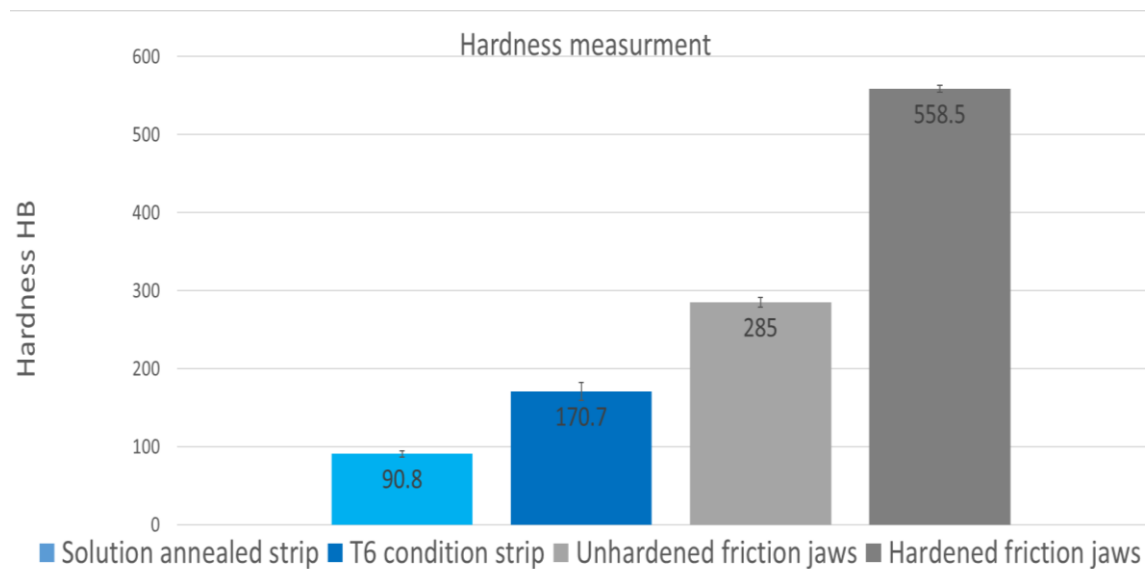


Figure 3-28: Hardness measurement of pull-out strips and friction jaws in different conditions

Generally, it can be noticed that the difference in hardness of the solution annealed pull-out strip compared to unhardened friction jaws is more than 195 HB (which is an equivalent of 660 N/mm²). If the hardened friction jaws and the solution annealed pull-

out strip are compared, a difference of the hardness values of ~468 HB can be seen. The high hardness for the forming tool is essential in order to avoid wear mechanisms during forming (see Chapter 2.4).

The surfaces of the individual strips and friction jaws were checked for deep scratches, damage, etc., so that any influences on the measurement result could be excluded. To avoid burr formation the corners and edges were ground by hand with sandpaper.

The surface roughness of the strips, which is measured by a White-light interferometer (Zygo GPI XP), indicated a Ra (average roughness) value of 2 μm , which corresponds to a mill finish condition. The friction jaws showed a surface roughness of Ra = 2.3 before polishing and Ra = 0.062 μm after polishing. In order to make a selection of suitable lubricants that can withstand the high temperatures and the forming process conditions, BECHEM Lubrication (*Hundertmark 2019*) Technology and HumanTec (*Kirberich 2019*), which are specialised in lubricant technologies, have been contacted. In discussions with these companies, four different lubricants were selected for further investigations.

Various anti-friction agents, as illustrated in Table 3-20, were tested to make an assessment of their applicability at high temperatures and lubrication properties.

Table 3-20: Overview of tested anti-friction agents

Supplier	Identification	Basis	Application temperature
Bechem	XP 10	Liquid lubricants	+950°C max.
Bechem	Beruforge 120 D	Liquid lubricants	+320° max.
Bechem	Berulit 935 H	Liquid lubricants	+950°C max.
HumanTec	Omega 35	Dry lubricant	+700°C max.




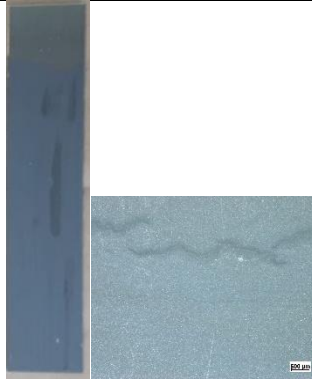




Before the actual strip drawing test was carried out, the lubricants were applied to the specimens and examined. First a defined amount of lubrication ($200\text{--}300\text{ g/m}^2$) was put onto an aluminium strip (width 30 mm and length 150 mm) and distributed equally over the surface by a brush (see Figure 3-29).



Figure 3-29: Dry lubrication strip

Then the surface was analysed with a microscope after the strip was put in the furnace for 15 minutes at 200°C and cooled down to room temperature. Table 3-21 shows the comparison of the lubricants. There are no abnormalities at room temperature, but it is noticeable that the “Berulit 935 H” lubricant has slight cracks in the lubrication layer, and after heating, the “Beruforge 120D” no longer covers the whole surface of the specimen (see Table 3-21 green box), which is due to the so-called “Leidenfrost-Effect” (Ostermann 2014). For this reason, the “Beruforge 120D” lubricant becomes unsuitable for Hotforming and is no longer considered in further investigations.

Table 3-21: Microscopic examination of lubricants

Lubrication	Applied and dried	After 180°C 15 minutes
XP 10 (18020)		
Berulit 935 H		
Beruforge 120D		
Omega 35		

3.5.4 Investigation of the friction properties of various lubricants and temperatures

To determine the friction coefficient occurring between the aluminium sheet and the forming tool a modification of a strip-drawing test was carried out at different pressures and temperatures. The test setup is shown in Figure 3-30. First of all, the specimen with a mill finish surface was solution annealed in the furnace (1), which is the initial state of the Hotforming process. Subsequently the specimen is put into a water bath (2), dried and covered with various lubricants (3), which are shown in Table 3-21. Finally, the specimen was clamped in the friction test bench (4) at a defined pressure between 0.5 MPa and 16 MPa and pulled by means of the tensile testing machine. If necessary, the climate chamber was additionally used for higher temperatures (5).

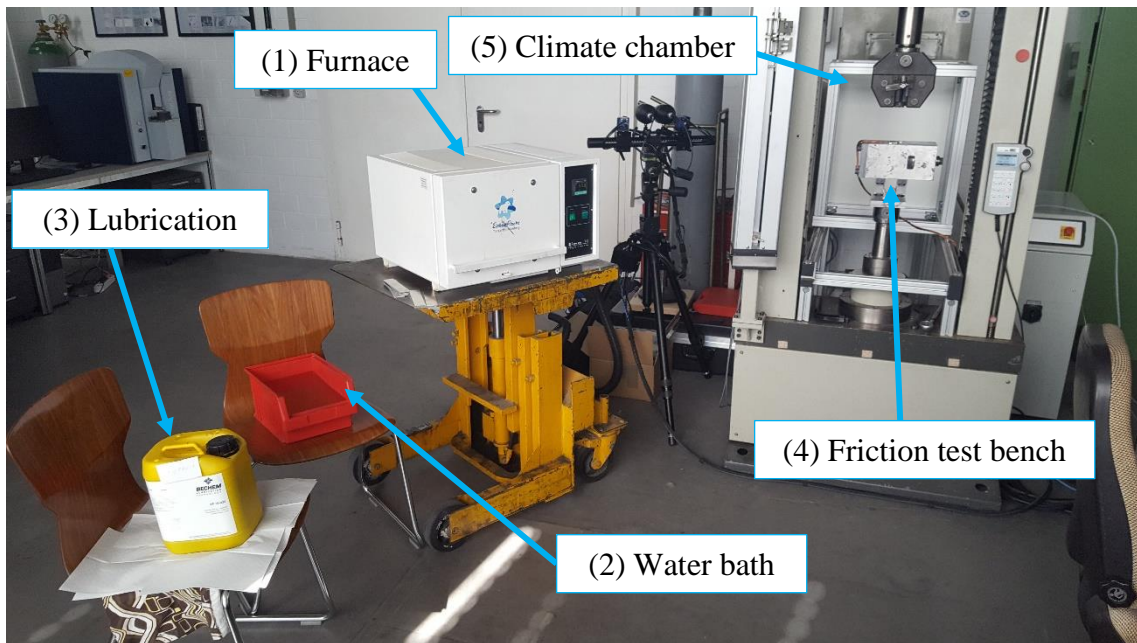


Figure 3-30: Test set-up for the evaluation of the friction coefficient

For the evaluation of the friction coefficient μ_{2-8} the average value between 2 mm and 8 mm of the specimen's pull-out distance (see Figure 3-31) was determined. Due to the length of the strip two tests could be carried out per specimen. The standard deviation was calculated from six average values of each pressure. The static friction coefficient (μ_{peak}), which is also shown in Figure 3-31, will not be considered further, as the friction value models in the simulation, in particular in the forming simulation, are based on dynamic friction values.

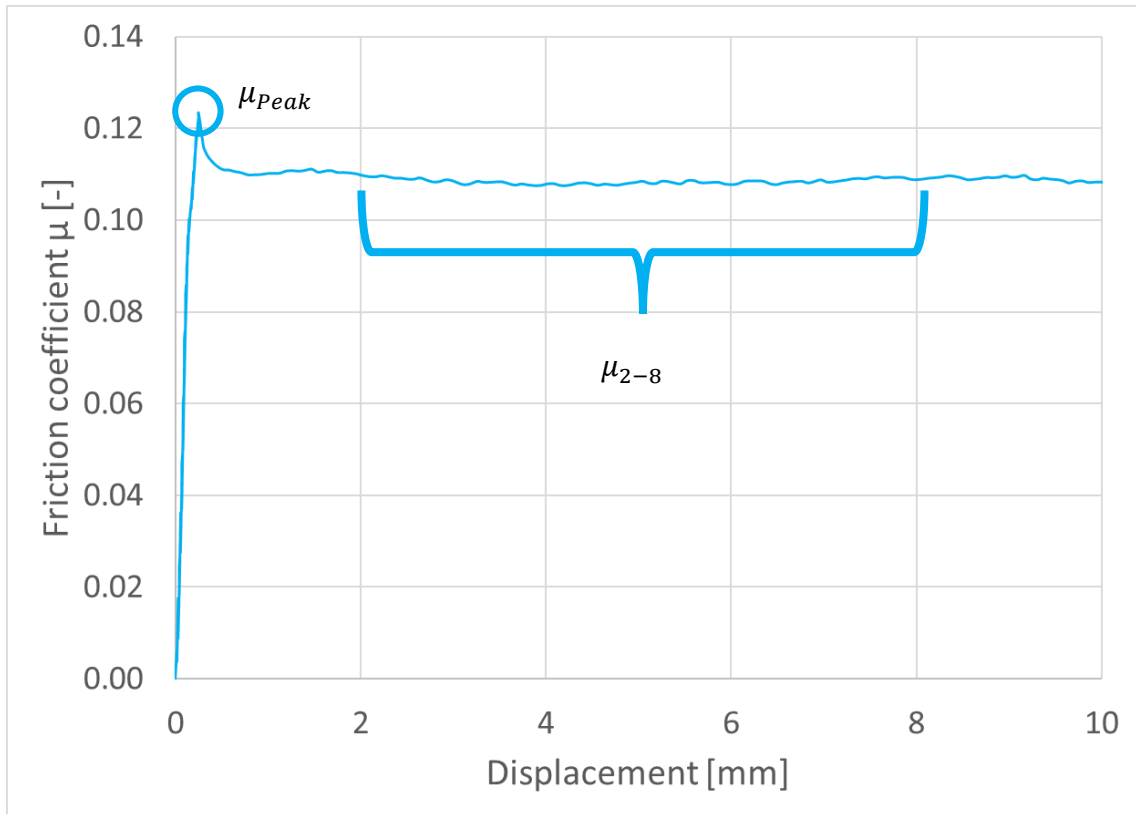


Figure 3-31: Exemplary representation of a friction coefficient-displacement curve

Figure 3-32 shows the results of a comparative study of different lubricants at various pressures. It is noticeable that the lubrication called “Beruforge 120D” is not suitable for forming, due to the high friction values ($\mu > 0.25$) even at low pressures (0.5 MPa and 2 MPa), which is due to solid state friction (see Chapter 2.4.1 a). Therefore, this lubricant was not considered any further. In contrast, the other three lubricants show friction values between 0.1 and 0.6 at low pressure (0.5 MPa, 2 MPa and 4 MPa), which represents mixed friction (see Chapter 2.4.1 d). At higher pressures (8 MPa and 16 MPa) it is remarkable that the two lubricants called “XP 10” and “Berulit 935H” become clearly worse and move towards solid state friction ($0.1 < \mu < 0.3$), whereby the “Omega 35” lubricant improves significantly and remains in the mixed friction state even at higher pressures. Thus, “Omega 35” is used for further investigations, on the one hand for the production of the demonstrators (see Chapter 5.2) and on the other hand for the friction coefficient model in the simulation.

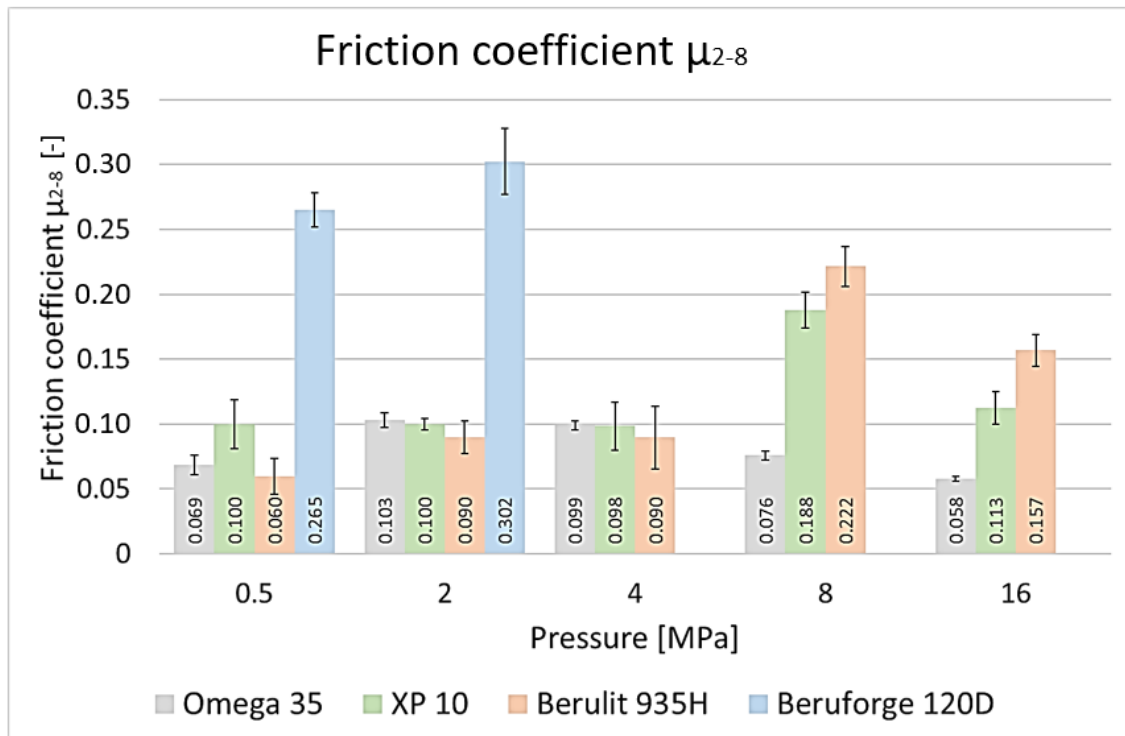


Figure 3-32: Comparative study of different lubricants at room temperature

To create a friction model depending on pressure and temperature for an accurate forming simulation the climate chamber was used now. After applying the “Omega 35” lubricant, the strip was clamped, and the temperature measured. As soon as the strip had reached the temperature between 180°C - 200°C, the pull-out test was performed. The strip drawing tool was also measured and kept within the same temperature range.

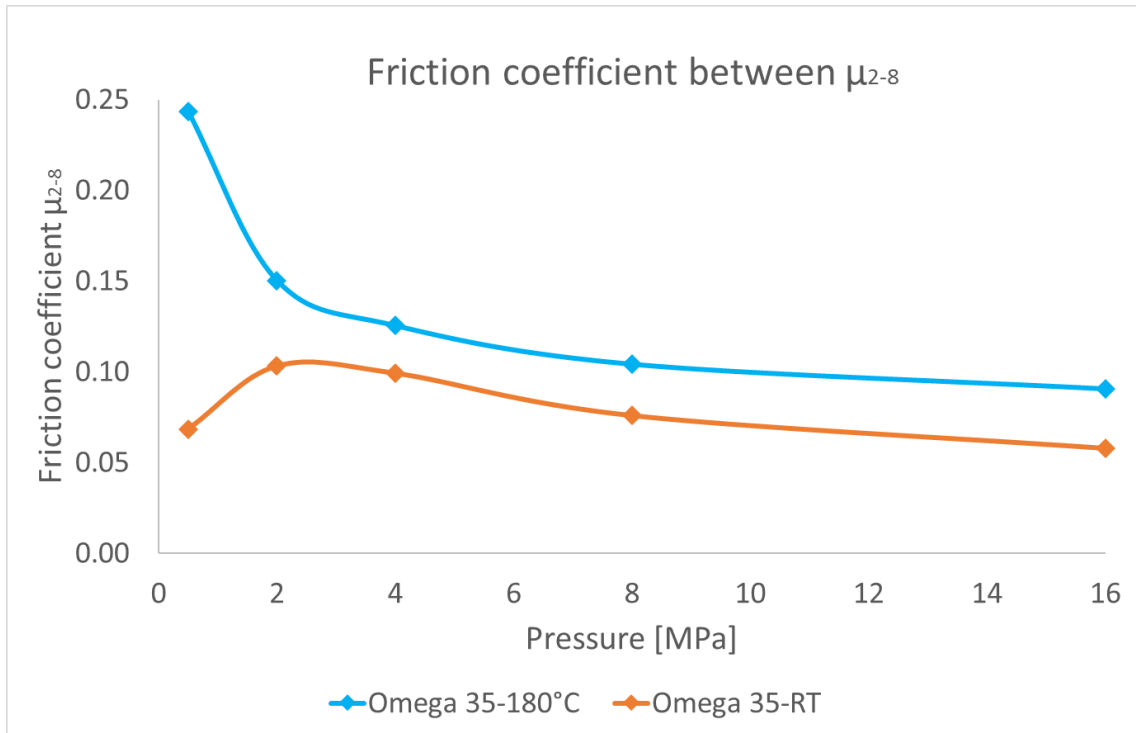


Figure 3-33: Friction as a function of temperature and pressure for the Omega 35 lubricant

Figure 3-33 shows two curves of “Omega 35” lubricant, one at room temperature (orange curve) and the other at 180°C (blue curve). It is noticeable that the friction coefficient at 180°C is higher than at room temperature, which is caused by the reduction of viscosity of the lubricant. It is assumed that the lubricant partially evaporates and is squeezed too much out of the valley of the profile. Thus, the roughness peaks are more levelled because of the specific surface pressure and the reduction of the lubricant (see Chapter 2.4.1). This leads to an increase of friction. Furthermore, the friction coefficient also decreases with increasing pressure independent of the temperature (see Figure 3-33), which indicates an improvement of the tribological system and hydrodynamic pressure (see Chapter 2.4.1). This reduction of the friction value at higher pressures is very noticeable with the Omega 35 lubricant compared to the rest of the lubricants. However, the friction value determined at room temperature and at a pressure of 0.5 MPa is noticeable, which is about $\mu_{2-8} = 0.069$. This is mainly due to the waxy lubricant that better separates the friction pairs at low temperatures and pressures (Hundertmark 2019).

In order to achieve accurate forming simulations in the following these two curves are implemented as a friction value model which should significantly improve the accuracy of the simulation in contrast to a global friction coefficient.

3.5.5 Concluding remarks

First, a test bench was developed and built up to determine friction coefficients as a function of temperature, pressure and lubricant. For this purpose, a list of requirements was defined and the existing tensile testing machine including climate chamber was adapted and used for the tests. For the design of the friction test bench different principles and variants were shown. To measure the normal force a strain gauge was used, which was calibrated by the tensile testing machine. For the selection of different lubricants suitable at elevated temperatures two companies were contacted (Bechem and Human Tec). Based on their expertise four different lubricants (Omega 35, XP 10, Berulit 935H and Beruforge 120D) were chosen and examined. The lubricant Omega 35 was identified to be the most suitable for the Hotforming process because of its low friction coefficient at high contact pressures at room and elevated temperatures. The friction coefficients at room temperature and higher pressures correspond to a mixed friction state ($\mu < 0.1$). If temperature is elevated the friction coefficient rises to slightly higher values ($0.1 < \mu < 0.15$) at elevated temperatures. Finally, the friction values determined as a function of temperature and pressure were used for a friction value model in the FEM-simulation of the forming process.

Chapter 4 Production of a car body part

First a car body part is selected, and a comparison study is presented, which shows the lightweight construction potential of high strength aluminium alloys using a side impact beam as an example. A dedicated side impact beam is then developed using the Toyota Yaris press hardening steel tube as industrial design guidelines and the EURO NCAP pole impact test as a crash standard for the boundary conditions. Based on topology optimisation, a functional side impact beam model is designed in CAD. Some optimisation loops are carried out, which include a simulation of the producibility and the evaluation of the crash performance to obtain an optimal design of a lightweight side impact beam made of AA7075. In order to increase the lightweight potential, a local CFRP patch was developed using fibre optimisation.

Subsequently a forming tool was developed and designed to produce the side impact beam with the various forming processes at elevated temperatures, such as Warm-forming, W-Temper and Hotforming/ Extended Hotforming.

4.1 Selection of a car body part and industrial requirements

First and foremost, this is intended to identify a structural component that can be produced using all aluminium forming processes at elevated temperatures, which are listed in Chapter 2.2. This prototype allows further investigations to be carried out on the finished component. Figure 4-1 shows some structural components selected from a car body. Most of these components are made of different types of steel. Because of some restrictions of aluminium forming at elevated temperatures, in particular the formability in the Warm-forming process, there is no possibility to produce components with complex shape and high draw depth (see Chapter 2.2.3). Furthermore, industrial requirements are needed such as crash conditions, connectivity to other parts and design specifications. These are taken from the Toyota Yaris and the EURO NCAP pole impact test (Euro NCAP 2015). The open source FE-model Toyota Yaris was developed through a reverse engineering process by Center for Collision Safety and Analysis researchers under a contract with the Federal Highway Administration (Center for Collision Safety and Analysis 2010) and is used for further investigation on industrial scale.

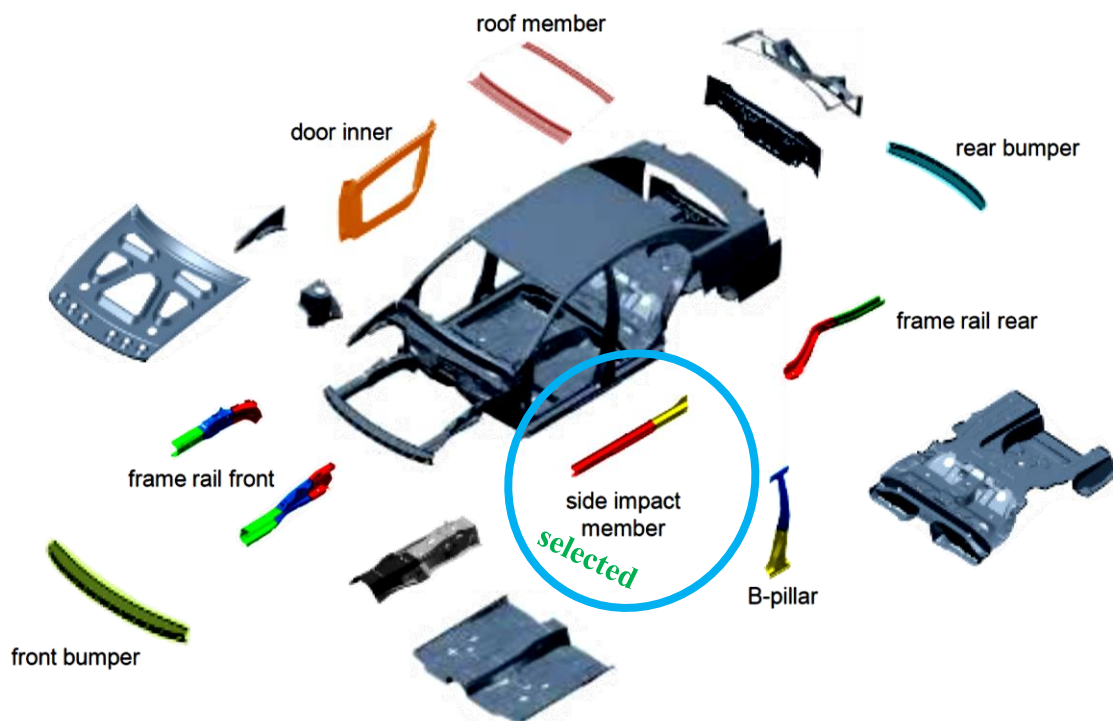


Figure 4-1: Potential structural component for forming at elevated temperatures (Schneider 2015a)

4.2 *Pre-investigation of a crash-beam – a comparison study showing the potential for weight saving using warm-formed ultra-high strength aluminium alloys*

4.2.1 Experimental

In this pre-investigation study aluminium alloys with the designation EN AW-6082, EN AW-7021 and EN AW-7075 were used and benchmarked against each other. In addition, a press hardening steel (PHS) was taken for comparison and to demonstrate the lightweight design potential of each material. Table 4-1 illustrates the composition of tested materials.

Table 4-1: Chemical composition of used material

	Si	Fe	Cu	Mn	Mg	Cr	Ni	Zn	Ti
AA7075	0.05	0.12	1.53	0.01	2.65	0.18	0.01	5.86	0.05
AA7021	0.25	0.40	0.16	0.10	2.10	0.05	6.80	6.00	0.10
AA6082	1.30	0.50	0.25	1.00	1.20	0.25	-	0.20	0.10
	C	Si	Mn	P	S	Al	Cr	Ti+Nb	B
PHS	0.35	0.50	2.00	0.02	0.005	0.10	0.50	0.10	0.005

4.2.1.1 Mechanical behaviour for various materials

The tensile test is standardised according to (DIN EN ISO 6892-1) and is for the purpose of evaluating the mechanical behaviour of metallic materials subjected to a uniaxial tensile force. The tensile testing specimens were taken from a warm-formed crash beam (see Figure 2-4, for the forming process route) to consider any effects of material ageing. During testing the applied force versus length variation is measured with a specific sampling rate. For comparison, Table 4-2 shows the typical mechanical properties that are important for further investigations. The aluminium flow curves, which are used for the FEM simulation, are extrapolated to a forming limit of $\varepsilon = 1$ using Voce's law (Voce 1948) 'equation (4.1)'. The flow curve used for the press hardening steel (PHS) material is extrapolated using Hollomon's law (Hollomon 1945) 'equation (4.2)'.

$$\sigma_f = b - (b - a) \times e^{-m \times \varepsilon} \quad (4.1)$$

$$\sigma_f = C_0 \varepsilon^n \dot{\varepsilon}^m \quad (4.2)$$

b = steady state stress

a = variable for the onset of yielding

m = strain rate sensitivity parameter

C_0 = material constant

n = strain hardening coefficient

Table 4-2: Mechanical behaviour of various materials

	σ_f [MPa]	UTS [MPa]	e [%]	Flow curve
AA7075	460	540	12	<p>AA7075-flow curve</p>
AA7021	360	420	5	<p>AA7021-flow curve</p>
AA6082	260	310	6	<p>AA6082-flow curve</p>
PHS	1200	1900	5	<p>PHS-flow curve</p>

4.2.1.2 Laboratory

The experiment is performed at a partner institute using a drop tower test (Figure 4-2). In this test setup the side impact beam is welded on adapter plates and screwed to hinge joints. The distance between the hinge joints is $w = 1370 \text{ mm}$ and the distance of the beam to the ground is $l = 275 \text{ mm}$.

Drop tower test

Throughout the test a mass of 40 kg is released from a height (h_0) of one metre in order to crash into the reference side impact beam made out of AA7075. This energy corresponds to the EURO NCAP pole test (Euro NCAP 2015) which is further described in Chapter 4.3.1. The velocity of the mass (v_0) is calculated using the principle of conservation of energy as given in ‘equation (4.3)’.

$$v_0 = \sqrt{2gh_0} \quad (4.3)$$

During the crash a set of various parameters (e.g. reaction forces, deformations, deceleration time) are measured and analysed afterwards.

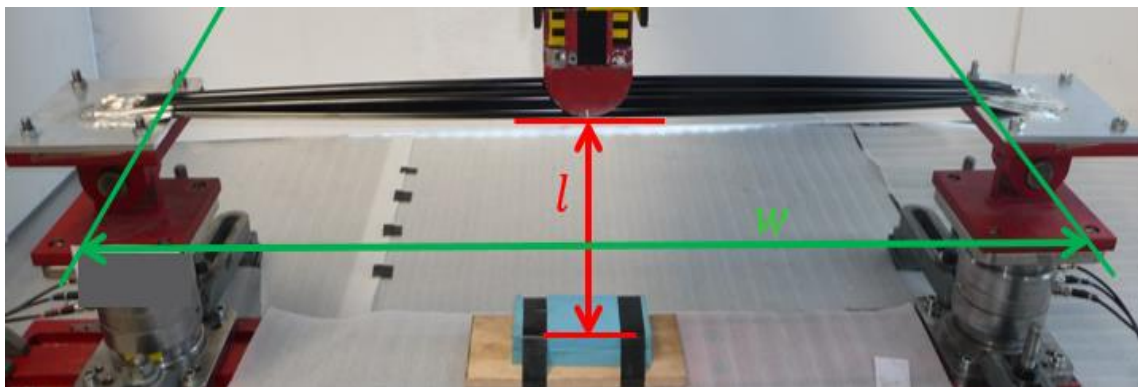


Figure 4-2: Test setup drop tower test (front view)

4.2.2 Simulation and optimisation of a crash-beam

4.2.2.1 Modelling and crash characteristics

Analogous to the experiment, a model of the drop test is designed and implemented into the FEM simulation software. To minimise the computational time, the complexity of the hinge joint is simplified (see Figure 4-3). Thus, the hinge joint is modelled with a rigid body and one degree of freedom around the z-axis. The adapter plate, hinge joint and some elements of the side impact beam (uniform shell elements) are fixed. In addition, the initial velocity of the impactor (uniform shell elements), also defined as a rigid body, is set to $v_0 = \sim 4430 \frac{\text{mm}}{\text{s}}$.

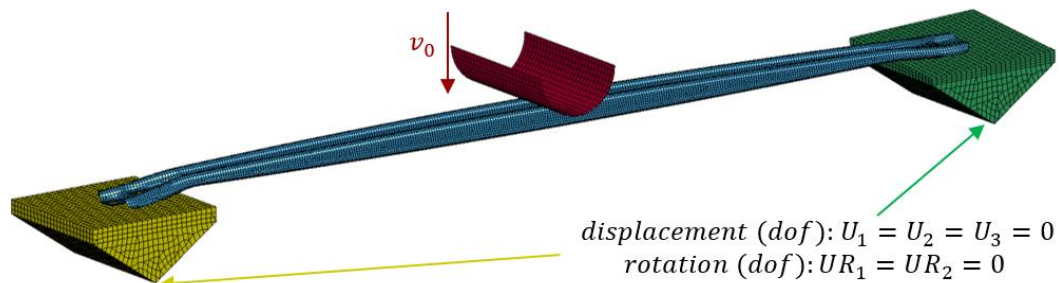


Figure 4-3: Simulation model of a drop tower test

4.2.2.2 FE-Analysis (FEA) of the reference crash-beam made out of AA7075

After modelling the drop test the necessary material parameters (e.g. elastic-plastic material behaviour) and the thickness of the reference beam 1.6 mm are implemented into the FE-Modell. Figure 4-4 illustrates a comparison of the predicted and the real deflection of the reference side impact protection beam. The results of the FEM simulation (Figure 4-5 and Figure 4-6) seem to be in good agreement with the experimental results.



Figure 4-4: Validation of the simulation model compared to the experiment (reference crash-beam)

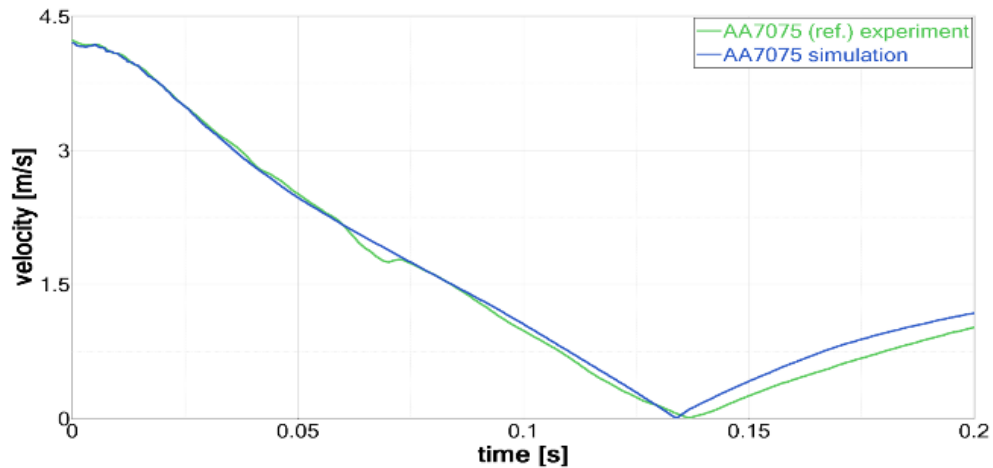


Figure 4-5: Predicted and real deflection of the side impact protection beam during deformation.

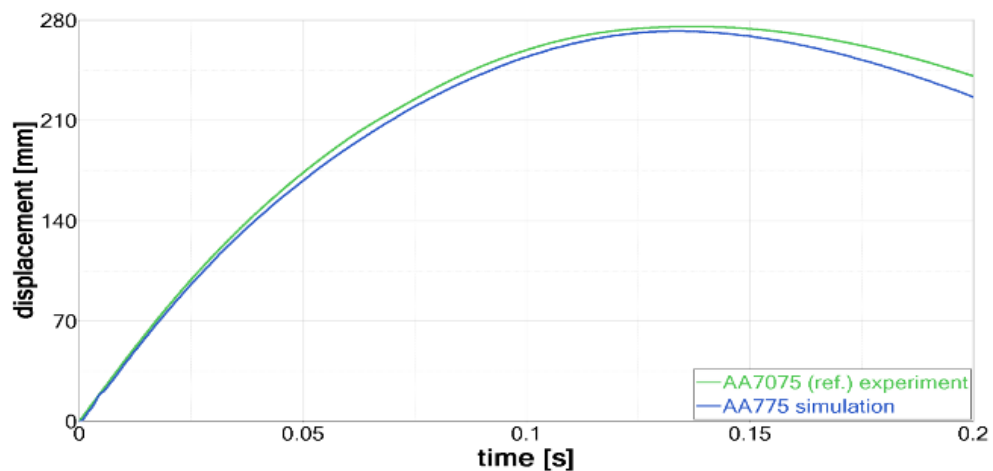


Figure 4-6: Predicted and real velocity of the side impact protection beam during deformation.

4.2.2.3 Sizing optimisation by thickness adjustment for various materials

After the validation of the FE-Model with the experiment of the reference side impact beam (Figure 4-5 and Figure 4-6) the material parameters, as described in Table 4-2, are varied and the thicknesses are adjusted by sizing optimisation to reach the same performance indicated by the reference side impact beam. To avoid too many simulation loops, a static equivalent load is adopted to carry out a sizing optimisation with a rough estimation of the thickness values. The aim of this numerical simulation is to adapt the thicknesses of the side impact beam to obtain the same performance as indicated by the reference beam. To achieve the same deflection of each other an object function, like min/max sheet thicknesses and a displacement constraint of 275 mm, was configured. According to the pre-defined thickness values of the optimisation results, the precision adjustment is made by explicit finite element analysis with an elastic-plastic material model using the flow curves given in Table 4-2.

4.2.2.4 Simulation based comparison of various materials with same crash performance

The resulting deflections and velocities using different materials for the side impact protection beam are shown in Figure 4-7 and Figure 4-8. The maximum deflection of approximately 275 mm is reached after 0.14 seconds for all tested beams. It can be seen that the side impact beam made out of AA7075 has a much smaller permanent plastic deformation than the other tested materials (Figure 4-7). This is due to the relatively high residual fracture elongation, which is approximately 12 % (Table 4-2).

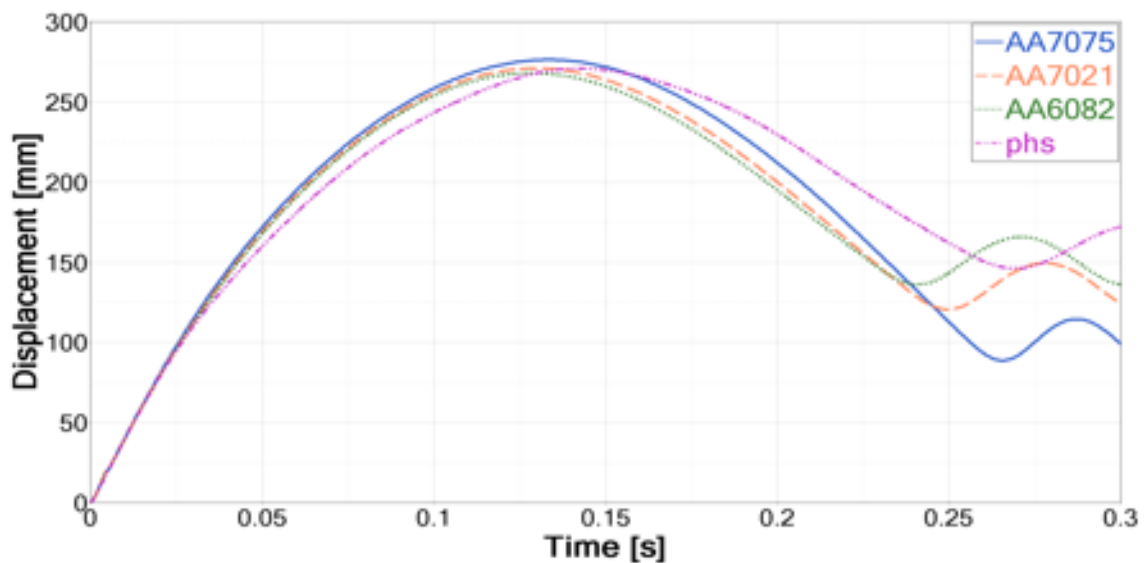


Figure 4-7: Deflection curves of side impact protection beams using different materials in the 3-point bending simulation.

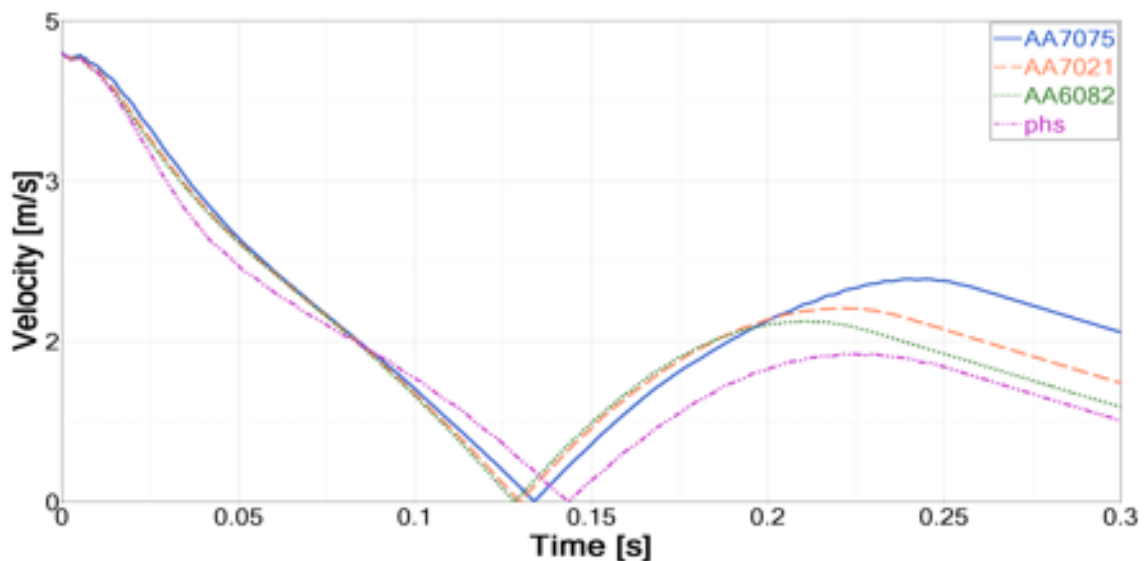


Figure 4-8: Velocity curves of side impact protection beams using different materials in the simulation.

4.2.2.5 Lightweight design potential of ultra-high strength aluminium alloys

After the adjustments of the thicknesses of the side impact protection beams (indicating an equivalent crash performance) using individual materials, the weight of all beams are compared against the reference beam made out of AA7075. Figure 4-9 indicates the weight saving potential of high and ultra-high strength aluminium alloys. It can be seen that the weight saving potential of a side impact beam made out of AA7075 is over 20 %, if compared with a press hardening steel material. This corresponds to a weight reduction of about 240 g.

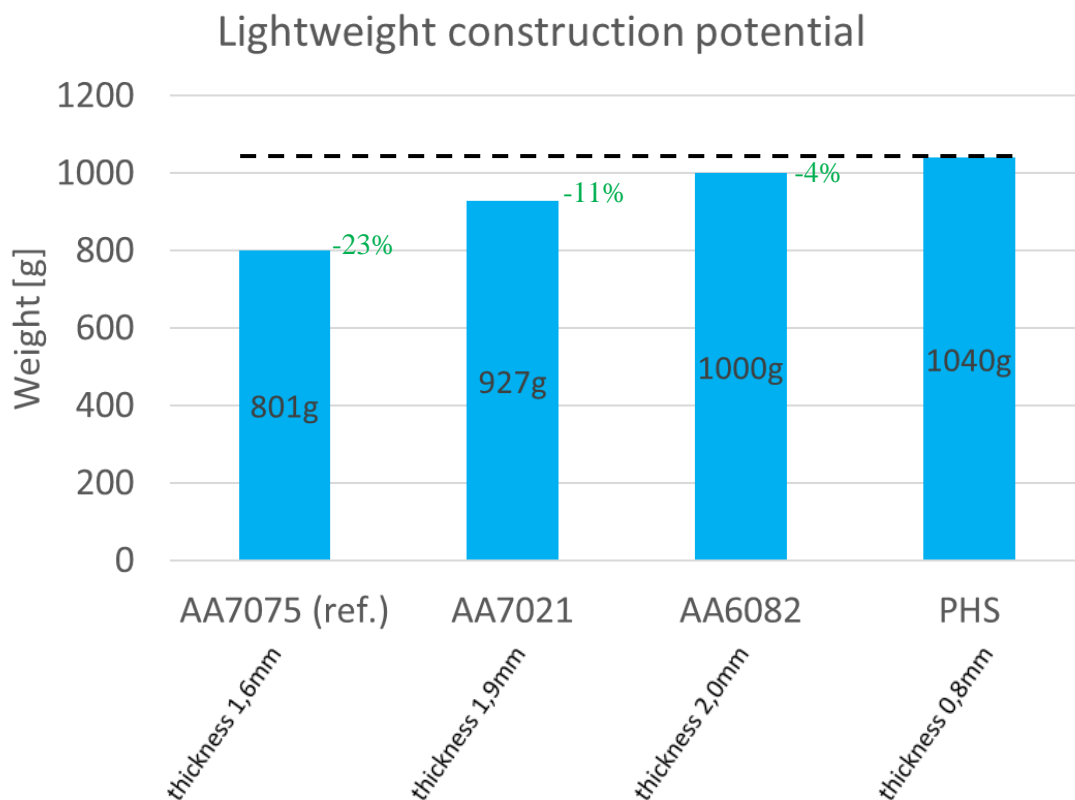


Figure 4-9: Lightweight design potential of crash beams using different materials

4.2.3 Concluding remarks

The FEA simulation results of drop tests using side impact protection beam geometries are shown to be in good agreement with the corresponding experimental results. The simulation model is validated and can be used for further investigations with various materials. By means of sizing optimisation, the thicknesses of the different side impact beams, including various materials such as AA7021, AA6082 and a press hardening steel grade, can be adjusted to obtain equivalent crash performances. The precision adjustment (calibration) is made by explicit finite element analysis with an elastic-plastic material model with the various flow curves.

The weight comparison shows that by using an ultra-high strength aluminium alloy, such as the AA7075 instead of a press hardened steel material, a weight saving of more than 20 % can be achieved. Thus, to exploit the entire lightweight potential of a crash relevant component it is essential to adjust any geometry dependent on the specific material behaviour.

4.3 Conception of a demonstration part

The side impact beam is selected to demonstrate the feasibility of manufacturing in various forming processes at elevated temperatures (Warm-forming, W-temper and Hotforming processes). The geometry of the side impact beam is scalable, so that the component can be produced using the existing equipment (forming press, dynamic bending and drop testing apparatus).

4.3.1 Determination of loads and boundary condition

A side impact beam is of great importance in the event of a side impact in a car accident where the vehicle is thrown sideways against rigid objects (e.g. trees). Such accidents often result in serious or fatal injuries. Therefore, passenger cars are subjected to the EURO NCAP pole impact test (Euro NCAP 2015). Due to the localised load, the deformation of the side impact beam can be very high, and the counterpart can penetrate deep into the passenger compartment. As shown in Figure 4-10, the vehicle is driven against a pole at a speed of 32 km/h (8.89 m/s) and at an angle of 15°. The point of impact is at the height of the driver's centre of gravity.



Figure 4-10: Side impact of a car against a pole with a speed of 32 km/h - NCAP test (Euro NCAP 2015)

In order to determine the loads and boundary conditions of the side impact beam, an existing and freely available simulation model of a Toyota Yaris (cf. Figure 4-11) is used.

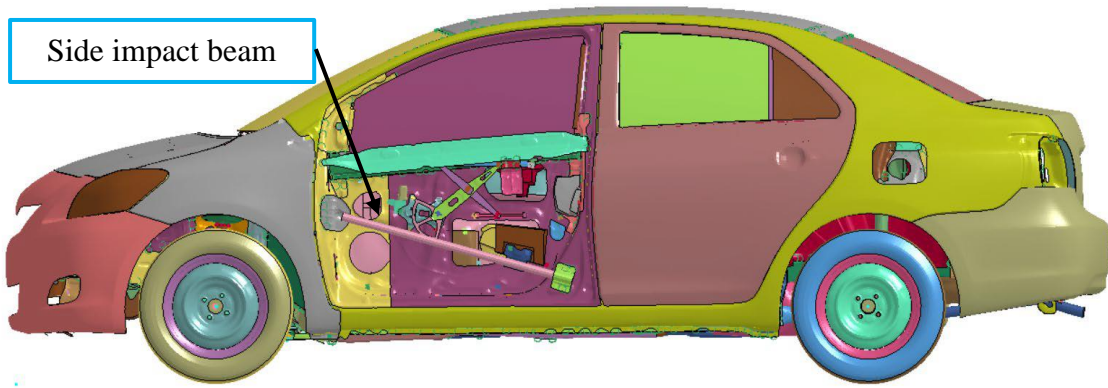


Figure 4-11: Side impact beam of a Toyota Yaris (U.S. Department of Transportation 2018)

Analogous to the EURO NCAP pole impact test, a simplified model of a drop test is designed and implemented into the FEM simulation software. After analysing the deformation of the press hardened steel side impact beam, which is set as default in the full Toyota Yaris FE-model, it can be seen that the deformation behaviour is equal as shown in a dynamic three-point bending. The connection points to the door behave like hinges. To minimise the computational time, the complexity of the hinge joint is simplified (cf. Figure 4-12). Thus, the hinge joint (height 50 mm) is defined as a rigid body with one degree of freedom around the y-axis and a distance of 980 mm, which is given by the original Toyota Yaris model. But the length will be scaled down later to ~ 300 mm for the construction of the SIB, because of manufacturing and testing restrictions. The adapter plate, hinge joint and some elements of the side impact beam (uniform shell elements) are fixed together (tied contact). In addition, the initial velocity and mass of the impactor (uniform shell elements), also defined as a rigid body, is set to $v_0 = \sim 4430 \frac{\text{mm}}{\text{s}}$ and $m = 40 \text{ kg}$, having the same internal energy as the original full Toyota Yaris side impact beam.

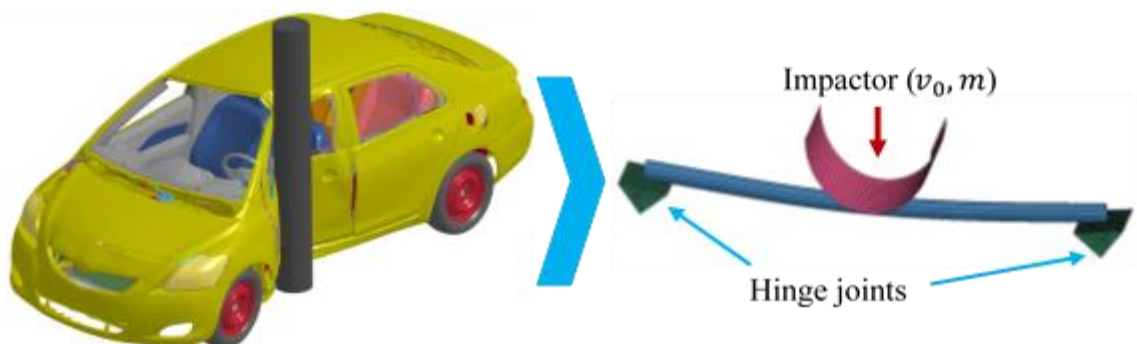


Figure 4-12: Full Toyota Yaris FE-model - NCAP pole test and simplify FE-Model

4.3.1.1 Design guidelines for the side impact beam

Figure 4-13 shows the dimensions of the initial side impact beam (press-hardened steel (PHS) tube $\varnothing 30$ mm). From the design guidelines (U.S. Department of Transportation 2018) a minimum distance of the beam from the glass (25 mm) and from the door interior (4 mm) is specified. The design space for the new beam is set to the following dimensions:

- Length of 980 mm (later to be scaled down to 300 mm due to restriction of the test bench and forming press)
- Width 105 mm
- Depth of 30 mm
- Thickness 2.0 mm
- 25 mm distance from the glass
- 4 mm distance from the door interior

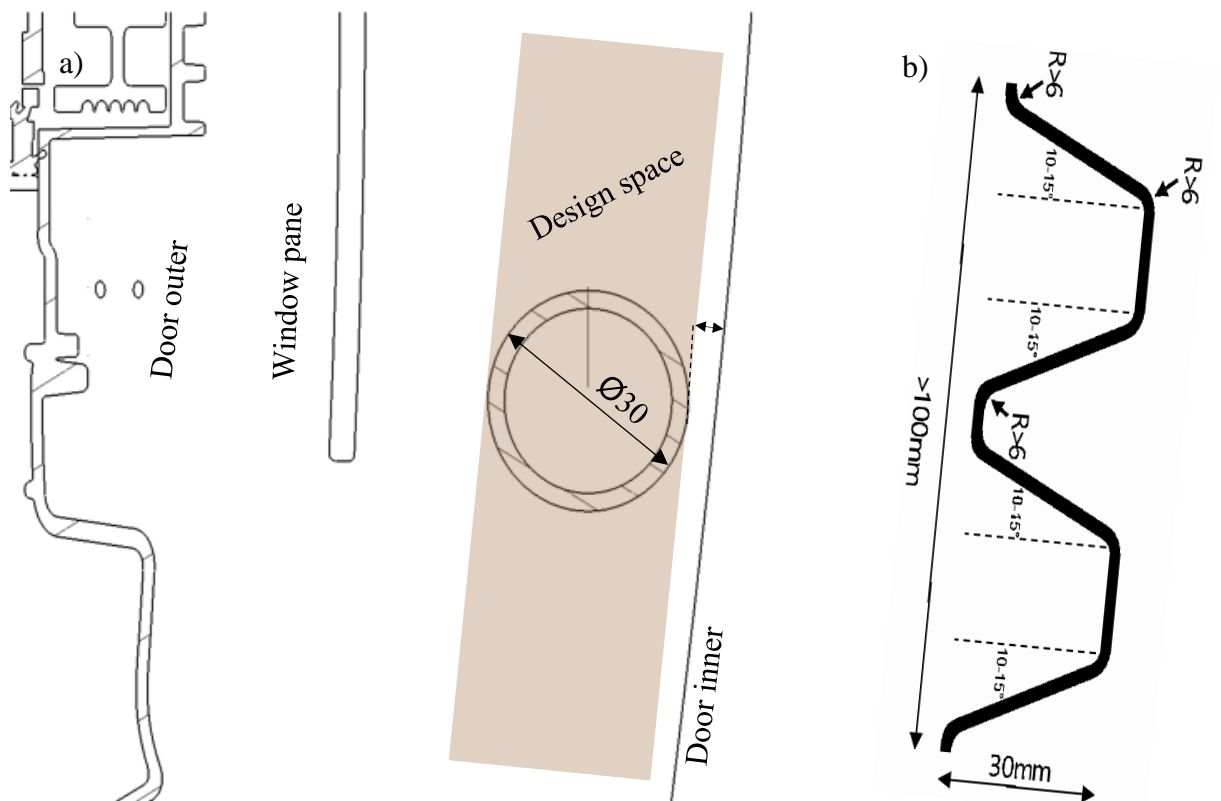


Figure 4-13: Design space for topology optimisation (a) and forming guidelines (b)

Due to the manufacturability of the functional model with all forming processes at elevated temperatures, some design restriction, which are based on practical experience from the industry (see Figure 4-13 b), are considered in the construction of the beam.

4.3.2 Topology optimisation

To determine a cross-section with a high energy absorption when substituting the press hardened steel with AA7075 material, a topology optimisation is carried out. The topology optimisation is performed using the static optimisation method with the OptiStruct optimisation software from the software developer Altair.

4.3.2.1 Simulation model and optimisation task

The topology optimisation requires the specification of a design space that describes the maximum possible space (see Figure 4-13 – brown rectangle) of the component. Figure 4-14 shows the simulation model with its loads and boundary conditions. In order to reduce the optimisation time, a half model with symmetrical boundary conditions is used. The hinge and impactor are modelled with shell elements and are defined as rigid bodies. Their support is in their centre of gravity. These are connected to the shell elements with connectors. A mass of 40 kg is applied to the impactor. Their support is in their centre of gravity. These are connected to the shell elements with connectors. A mass of 40 kg is applied to the impactor.

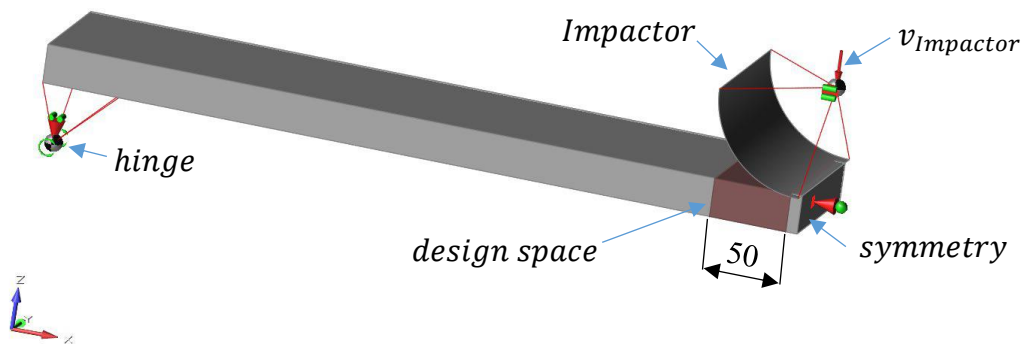


Figure 4-14: Simulation model for topology optimisation

To find a suitable cross-section and to minimise the computational time, a small design space was defined near the impactor where the largest deformation takes place. This also avoids defining boundaries and loads in the design space. As shown in Figure 4-14, the design space is defined with a length of 50 mm and height of 30 mm. Due to different forming processes certain design restrictions, which are mainly based on practical experience, are considered for the beam design.

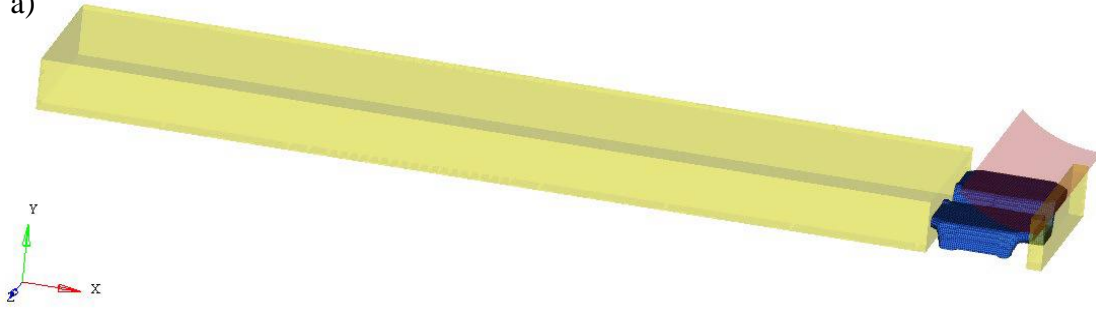
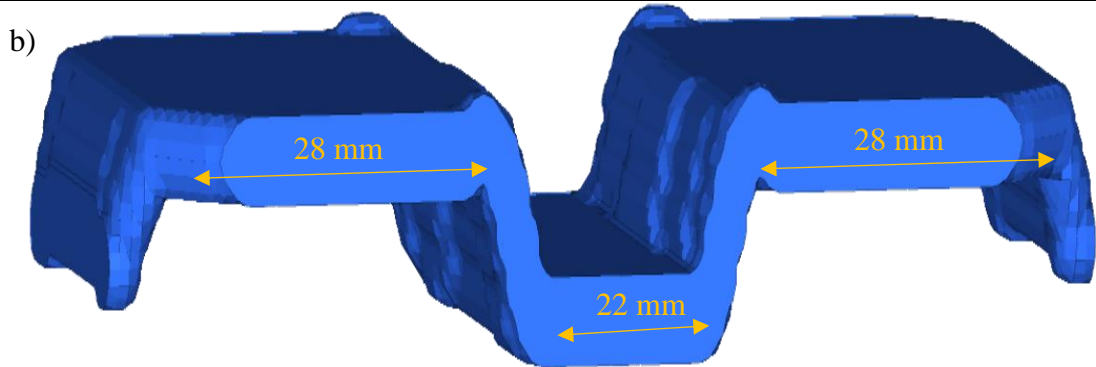
For this purpose, the following restrictions are incorporated into the optimisation:

- The objective function is to maximise the stiffness of the part and to reduce the mass of the part to 15 %,
- Double-sided demoulding (split draw) with the option “no hole” as a production restriction, and
- Minimum material thickness of 2 mm, which corresponds to a sheet thickness of the AA7075 blank.

4.3.2.2 Optimisation results

The result of the static topology optimisation is shown in Table 4-3, whereby the predicted cross-section corresponds to a W-profile (Table 4-3 b).

Table 4-3: Input parameter and results of the topology optimisation

<ul style="list-style-type: none"> • The objective function is to maximise the stiffness of the part and to reduce the mass of the part to 15 %, which gets good results for metal forming. • Double-sided demoulding (split draw) with the option “no hole” as a production restriction. The direction of demoulding is in $\pm y$- direction. • Minimum material thickness of 2 mm. This corresponds to sheet thickness of the sheet to be formed.
<p>a)</p>  <p>b)</p> 

4.3.3 Design of the demonstrator (functional model) and the tooling

Based on the topology optimisation and the design guidelines, which are described in detail in Chapter 4.3.1.1, a new lightweight side impact beam made out of AA7075 is designed. For further scientific considerations it is not necessary to produce the full length of the side impact beam, because essentially a relatively small part is sufficient for strength investigations and springback behaviour of the various forming processes, which are compared with each other. Therefore, the length of the beam is set to 300 mm, which can be produced with the existing forming press (see Chapter 5.1). For further details regarding the dimensions see Appendix G.

In order to manufacture the lightweight side impact beam, some design optimisation loops were carried out. The schematic approach, which is shown in Figure 4-15, clarifies the procedure for a suitable design.

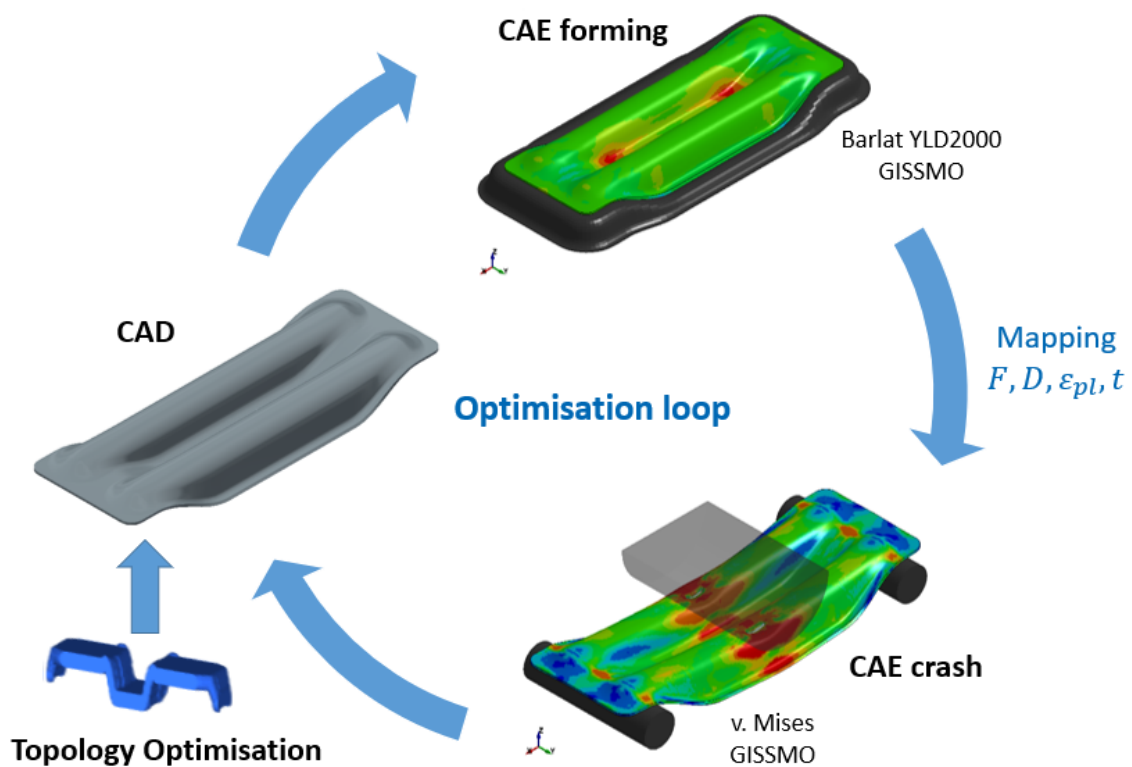


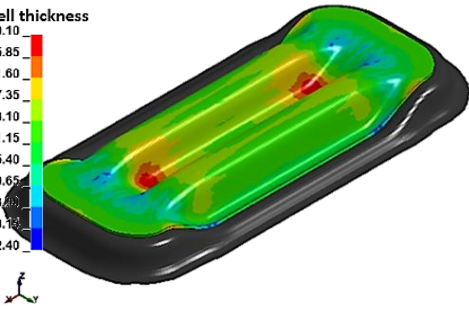
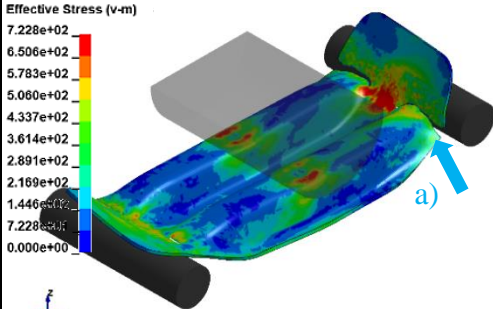
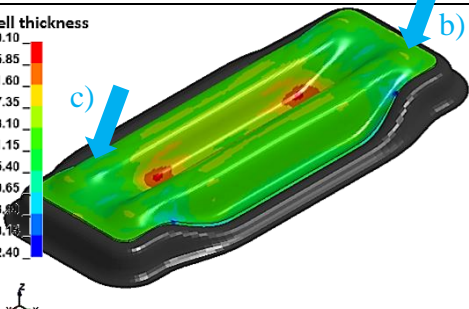
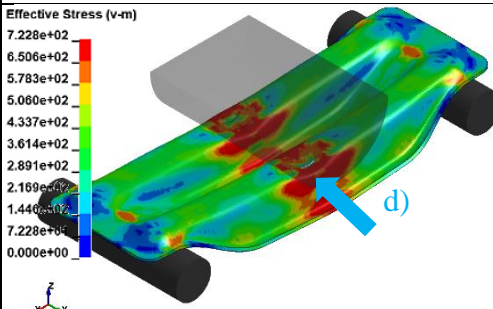
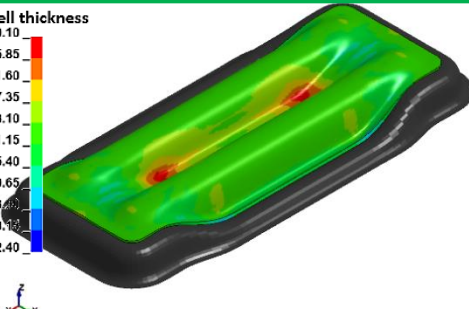
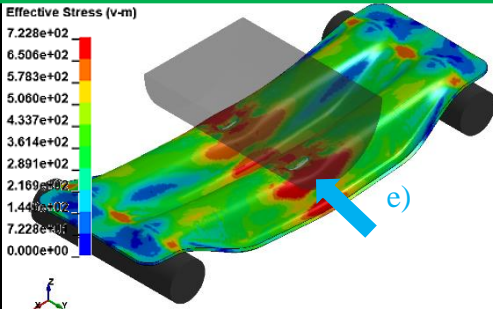
Figure 4-15: Schematic procedure to find a suitable design that is manufacturable and has a good crash performance

First, a topology optimisation is carried out to find a cross-section that is as rigid as possible and can be produced by sheet metal forming. The result of this optimisation (see Chapter 4.3.2) was a cross-sectional W-profile for the side impact beam. A CAD-model was then created from the predicted profile. Subsequently, a forming and crash simulation was carried out to check any manufacturing problems like wrinkling, thinning and cracks and to ensure the crash performance. Good performance requires a high energy absorption and a sufficient stiffness so as not to endanger the occupant. After this, a new optimisation loop can be initiated if the values are not equivalent to a reference side impact beam taken from a Toyota Yaris model (U.S. Department of Transportation 2018).

Table 4-4 illustrates the procedure and the individual stages of development of different side impact beam geometries. For the simulation, the die and the punch are modelled as rigid bodies with shell elements. The blank is provided with the parameter of the previously calibrated Hotforming process material and failure model, which is given in Chapter 3.3. In addition, the friction value model from Chapter 3.5 was used.

To calculate the crash simulation, the thicknesses, strains and pre-damages of the side impact beam are transferred from the forming simulation to the crash model. Subsequently, the material and failure model of the final state of the material (see Chapter 3.4) and an adapted dynamic three-point bending design were used.

Table 4-4: Comparison of different developmental stages of the side impact beam

CAE	Forming simulation	Crash simulation
Vers. 1	 <ul style="list-style-type: none"> Max. thinning: 20.1 % Max. thickening: 18.0 % 	 <ul style="list-style-type: none"> Unsatisfactory stiffness
Vers. 2	 <ul style="list-style-type: none"> Max. thinning: 17.9 % Max. thickening: 22.4 % → formation of wrinkles 	 <ul style="list-style-type: none"> Highest stiffness
Vers. 3	 <ul style="list-style-type: none"> Max. thinning: 19.4 % Max. thickening: 11.3 % 	 <ul style="list-style-type: none"> Satisfactory stiffness

The first version of the side impact beam has 20.1 % thinning, 18.0 % thickening and no cracks, which is acceptable in regard of formability. But considering the crash simulation this beam shows insufficient stiffness (see a) in the area of the hinges. In contrast, the second version indicates an enhanced crash performance in the event of a crash.

This is due to the redesign of the humps, which reach to the two ends of the hinges now (see b). There are slight cracks in the middle of the side impact beam (see d). Furthermore, some formation of wrinkles on the top can be seen (see c). In the final (third) design also slight wrinkles occur but the stiffness of the beam corresponds to the reference press hardened steel side impact tube (see Figure 4-16).

In the event of a crash, it is important to have sufficient stiffness and minimum intrusion with high energy absorption. If the internal energy-intrusion diagram of the different versions of the side impact beams are illustrated, it can be noticed that version three with a 2 mm sheet thickness has not enough stiffness compared to the original press hardened steel (PHS) tube (Figure 4-16). But if the sheet thickness is increased to 3 mm, version three shows the same crash performance as the original tube. In this case a weight saving of 18.1 % can be achieved, while maintaining the same stiffness and energy absorption compared to the PHS tube.

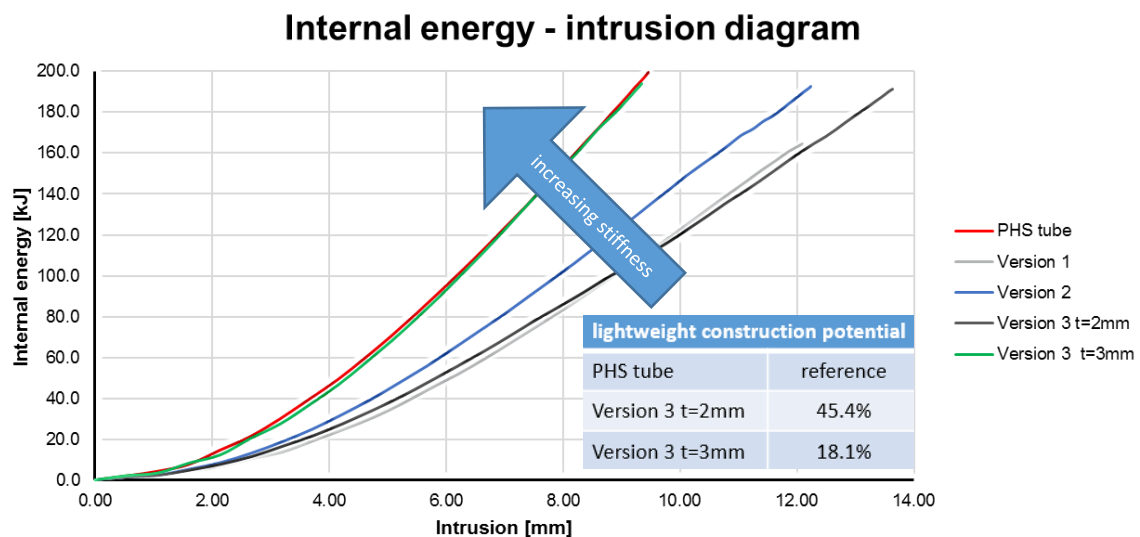


Figure 4-16: Comparison of crash performance of various versions of the side impact beam - dynamic three-point bending test

In order to get a higher lightweight potential, a sheet thickness of 2 mm is used for further investigations and the stiffness will be increased by applying CFRP or GFRP patches on the side impact beam at critical locations. This will be produced by using the Extended Hotforming process (see Chapter 3.3). For the design of the patch a fibre optimisation is carried out (Chapter 4.4).

4.4 *Optimisation of a carbon fibre reinforcement patch*

In order to increase the lightweight construction potential, a CFRP patch is now being designed to further improve the stiffness. The fibre optimisation includes the optimisation of shape, thickness and layer orientation of the CFRP patch. The aim of this optimisation is to design a hybrid side impact beam made out of AA7075 2 mm sheet thickness and CRFP that has the same intrusion as the reference side impact tube made of PHS.

4.4.1 The challenge of optimisation

Before the fibre optimisation can be carried out, preliminary tests are required. So far, the simulations have been performed explicitly dynamically, but the optimisation is based on the implicit quasi-static method (Altair Engineering). In this case no initial speed can be assigned to the impactor of the simplify FE-Model of the dynamic three-point bending test (cf. Figure 4-12). Alternatively, this can be loaded with a force, acceleration or displacement.

Furthermore, fibre optimisation is based on the theory of small deformations. In this case, plastic strains up to a maximum of 5% are allowed. In the event of larger deformations the theory is no longer valid and does not provide meaningful results (Altair Engineering). Another conflict of the quasi-static method is that the failure behaviour cannot be taken into account in fibre optimisation. Although parameters describing the failure of the material can be calculated, the failure behaviour during the simulation is not included in the material behaviour. Thus, no failure or breakage is represented in the simulation (Altair Engineering).

4.4.2 Setup of the simulation model

The symmetry of the side impact beam is used to reduce the modelling effort and the calculation time. For this purpose, a quarter minor of the side impact beam is created in Optistruct and stored symmetrically in the xy- and yz-plane. The overview of the simulation model is shown in Figure 4-17. The hinge joint is fixed, and the impactor has a displacement of 2 mm. This is determined based on preliminary tests in which the plastic strains remain below 5 % at different displacements (theory of small displacements). Both are modelled as rigid bodies.

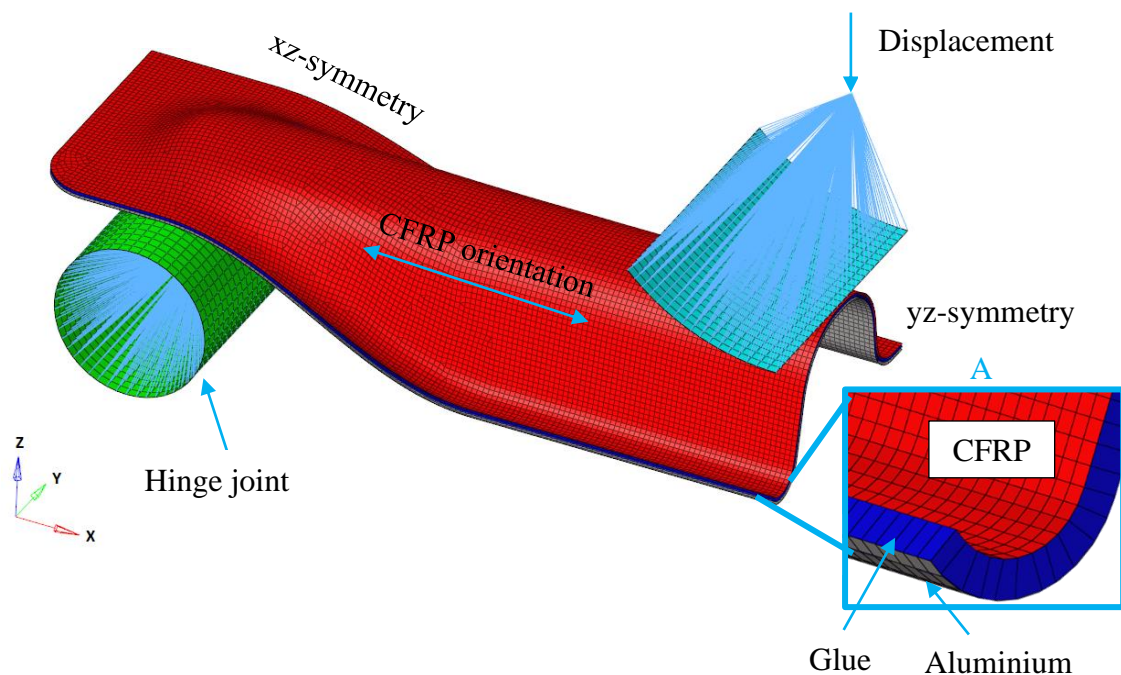
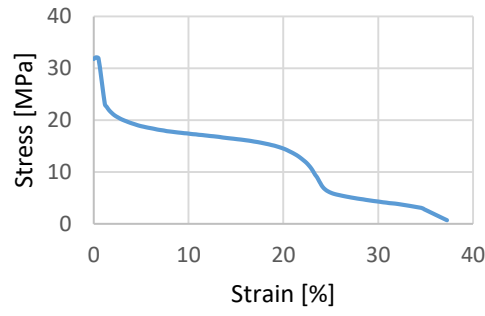
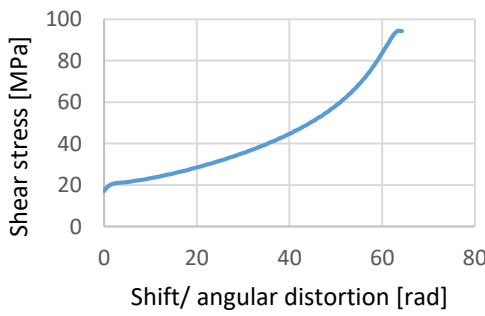


Figure 4-17: Simulation model hybrid side impact beam and layer layout (A)

The model consists of three layers (see Figure 4-17 A). The lowest layer is the high strength aluminium AA7075, which was previously optimised and designed with an element thicknesses, which is transferred from the Hotforming simulation to the hybrid side impact beam. The top layer is the CFRP with a fibre orientation of 0° to the longitudinal direction of the carrier (x-axis), which is showed in Figure 4-17 and a thickness of 0.2 mm. An adhesive layer is modelled by cohesive volume elements between the aluminium and the CFRP with a fixed thickness of 0.1 mm. Figure 4-17 (A) shows the layered structure.

For fibre optimisation, a suitable CFRP material (CFRP – IM7/8552) is selected or an existing CFRP material model is taken from the literature for crash simulation (Cherniaev et al. 2018), in order to avoid extensive investigations for the initial design to determine material data. In addition to the mechanical parameters for describing the elasticity behaviour, this model also includes failure stresses for various types of load. The adhesive used is Teroson EP 5065 from the manufacturer Loctite. It is based on epoxy resin and is used in car body construction for structural bonding. The overview of both material parameters used in the simulation is shown in Table 4-5.

Table 4-5: Material data for CFRP and glue (Cherniaev et al. 2018)

CFK – IM7/8552		Teroson EP 5065	
Density	1.58 g/cm ³	Density	1.03 g/cm ³
Poisson's ratio	0.5	Young's modulus	3491 MPa
Young's modulus longitudinal direction E_{11}	165 000 MPa	Shear modulus	512 MPa
Young's modulus transverse direction E_{22}	9000 MPa	<p>True stress-strain curve</p>  <p>True stress strain curve</p> 	
Shear modulus G_{12}	2800 MPa		
Shear modulus G_{23}	5600 MPa		
Max. longitudinal compressive strength	1590 MPa		
Max. longitudinal tensile strength	2560 MPa		
Max. transverse compressive strength	185 MPa		
Max. transverse tensile strength	73 MPa		
Shear strength	90 MPa		

4.4.3 Free-Size optimisation

The objective function of optimisation is to maximize the stiffness of the overall system. The reduction of the CFRP layer by 50 % is defined as volume constrain. A maximum total thickness of the layer CFRP of 0.2 mm is specified as a manufacturing restriction. This corresponds to layers with a thickness of 0.2 mm. During the Free-Size many layers with different thicknesses were created. The result of the optimisation is shown in Figure 4-18. The individual layers are shown in different colours and consist of 118 individual layers of different thicknesses.

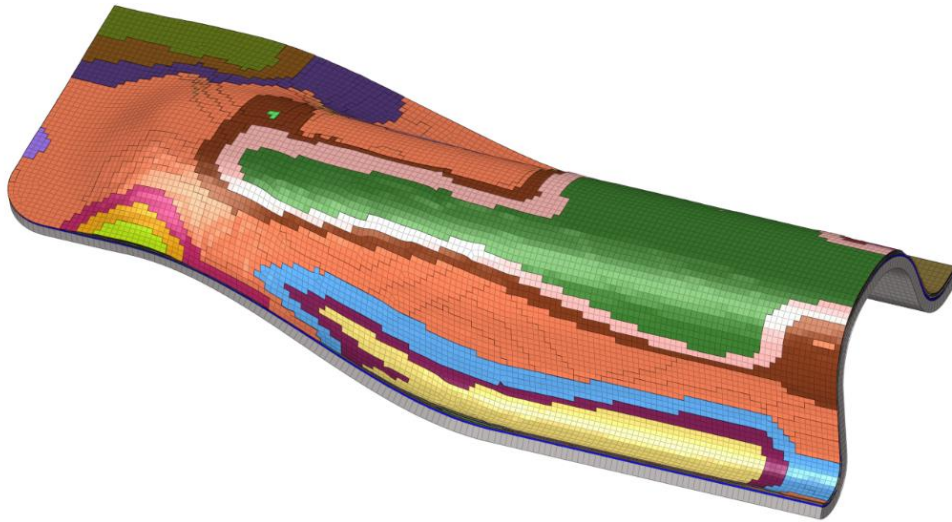


Figure 4-18: Result of the Free-Size optimisation of the hybrid side impact beam

Since the aim of the hybrid SAT is to apply a local CFRP patch, the next step is to remove cluster areas of Free-Size optimised CFRP thinner than 0.2 mm from the model. This leads to the following shape and cut of the patch (Figure 4-19).



Figure 4-19: CFRP Patch cut of the hybrid side impact beam

Now the optimised hybrid side impact beam is compared to the original one made of PHS and the one without CFRP patch with regard to crash performance and weight. To evaluate the crash performance, the internal energy of the beam over the intrusion of the impactor is shown in the diagram Figure 4-20 for the different variants.

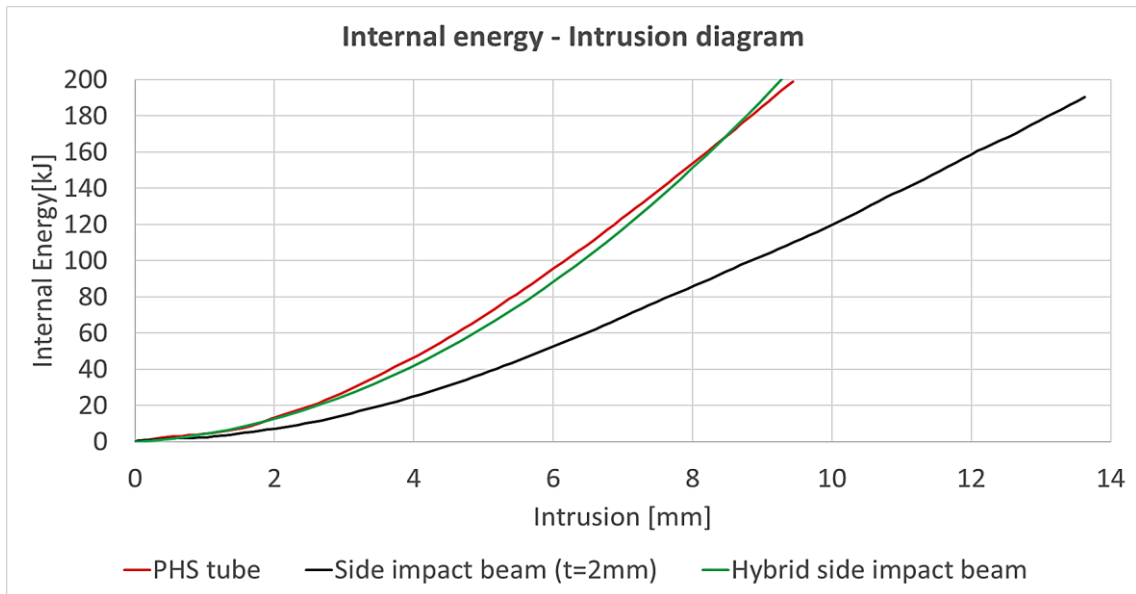


Figure 4-20: Comparison of crash performance of various versions of the side impact beam - dynamic three-point bending test

The hybrid SIB has the same crash performance as the PHS tube. This weight ~276 g includes CFRP and adhesive layer (cf. Figure 4-21). If this is compared with the reference component made of PHS, it represents a weight saving of 36.38 %

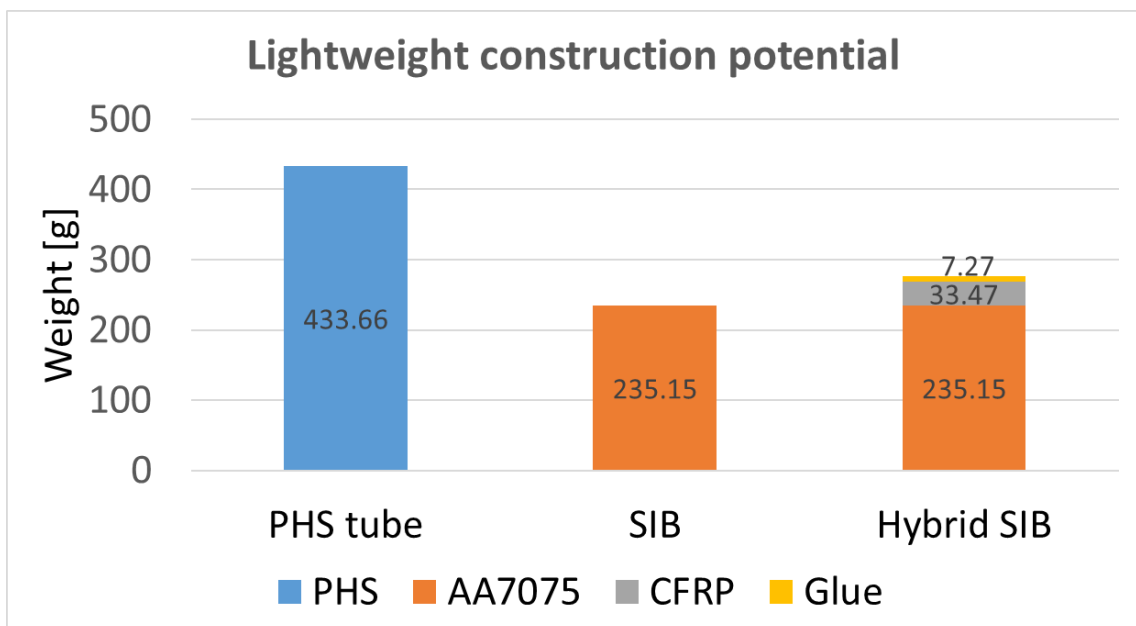


Figure 4-21: Lightweight construction potential of the hybrid side impact beam

4.5 Design layout of the forming tool

The aim is to design a tool which enables the manufacturing of the side impact beam with the different forming processes at elevated temperatures such as (Extended) Hotforming, W-Temper and Warm-forming. Therefore, the two stages of heating and forming must be heated up to 150°C-250°C separately.

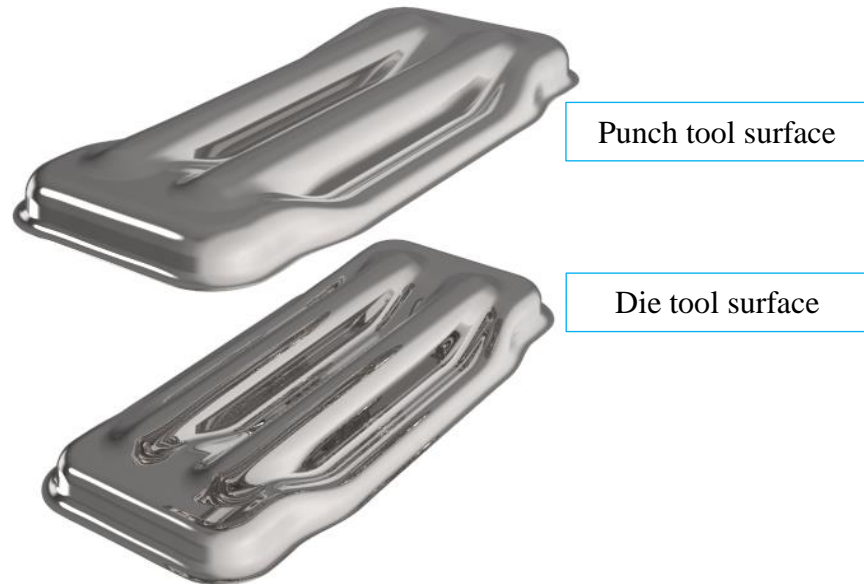


Figure 4-22: Tool surfaces

Based on the forming simulation, tool surfaces were derived (see Figure 4-22). These surfaces are used to create the solid body of the punch and die. In order to make a rough calculation of the output for heating cartridges, the equation (4.4) from the supplier, which takes into account an addition factor of 1.5 for energy losses, is used for the design of the heating cartridges. To heat one stage of the forming tool, which is about 80 kg of steel to 250 degrees in one hour, 3527 Watts are needed. One of the heating cartridges has 630 Watt, therefore six of them per stage are at least needed to reach 250°C in one hour with 3.78 kW. An insulating plate is installed between the forming stages and the base plate to avoid heating up of the press.

$$P = \left(\frac{m * c * \Delta T}{t} \right) * 1.5 \quad (4.4)$$

$$P = \left(\frac{80 \text{ kg} * 460 \frac{\text{J}}{\text{kg} * \text{K}} * (250 - 20) \text{ K}}{3600 \text{ s}} \right) * 1.5 = 3526.7 \text{ W}$$

Furthermore, fixed stops are designed for the precise positioning of the specimens, steel guides and distances for the minimum gap of the closed forming tool are constructed. A detailed overview of the forming tool is shown in Figure 4-23 and technical drawings are given in Appendix G

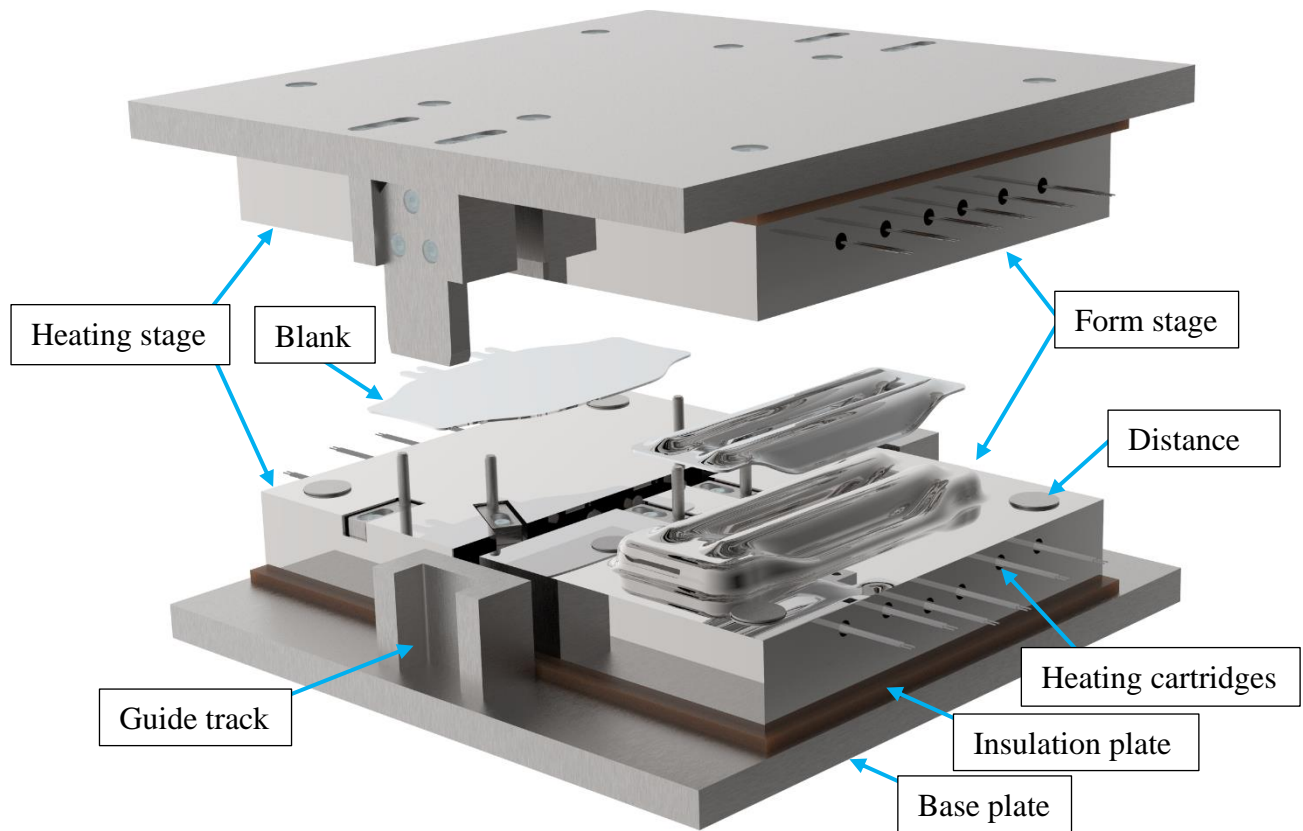


Figure 4-23: Side impact forming tool

Inspire form, an Altair software, was used to obtain the sheet metal unfolding. The CAD model of the side impact beam was imported into the software and pressed flat using one step solver. Figure 4-24 shows the schematic evolution from the side impact beam to the flat blank with two stops for centring.

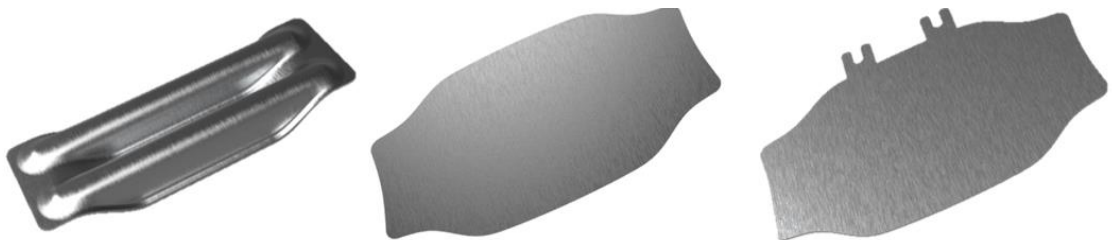


Figure 4-24: Schematic representation of the sheet metal unfolding

4.5.1 Heating layout of the forming tool - Temperature field simulation

The heating of the side impact beam components was again conducted by integrated heating cartridges. Figure 4-25 show the individual heating channels (highlighted in blue) for die and heating stage. The heating channels were positioned with a uniform spacing within the tool surface to avoid and minimise any temperature gradients onto the tool surface. The heating cartridges diameter were chosen with 12.5 mm and each of them has 630 Watt, thus a total output per stage of 3.78 kW (see equation (4.4)).

Now two analyses are carried out, one thermal-transient to estimate the heating time and one thermal-stationary at 200°C to show the temperature distribution, which is important for springback in the Warm-forming process.

The model was built in Ansys. The thermal properties of the tooling steel and isolation plate are illustrated in Table 4-6. Furthermore, free convection was defined at each surface.

Table 4-6: Thermal properties of the material

	Density ρ $\left[\frac{k * g}{m^3}\right]$	specific heat capacity c $\left[\frac{J}{kg * K}\right]$	thermal conductivity λ $\left[\frac{W}{mK}\right]$
Insulation plate	1400	1150	0.17
Tooling steel	7872	448	35

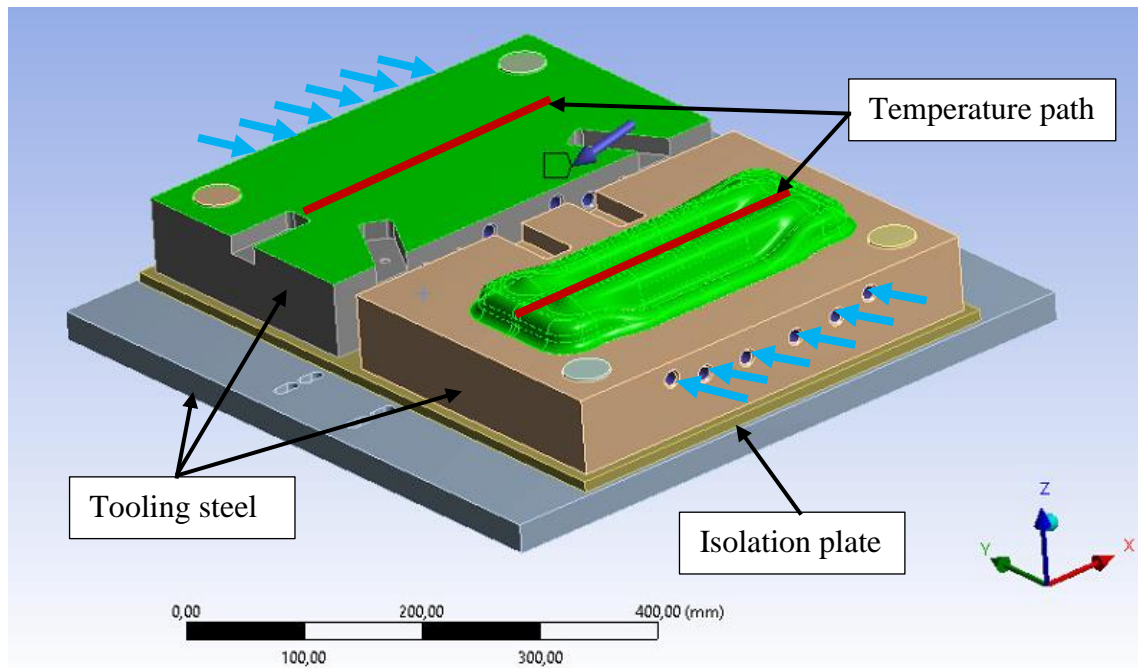


Figure 4-25: Die and heating stage - heating channel (blue arrows)

For the thermal-transient analysis, the heating channels are charged with 630 Watt each (see Figure 4-25 blue arrows) and the heating time is evaluated, where the minimum of the green area was evaluated. This ensures that the entire forming area and heating surface (see Figure 4-25 green area) is over 200 degrees after the heating time.

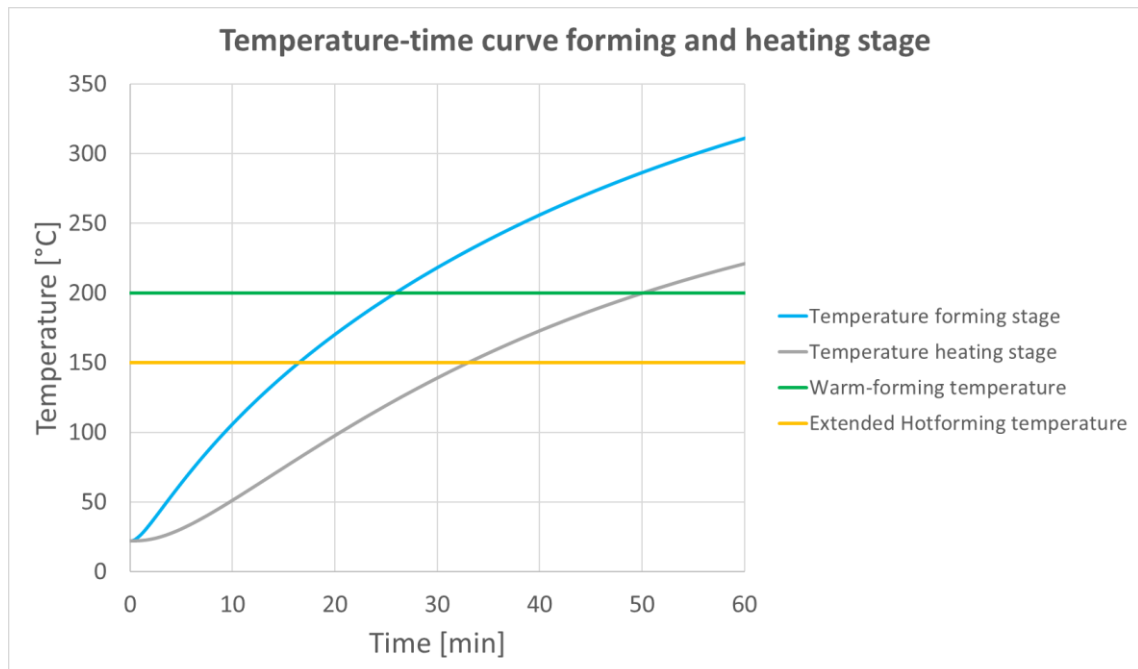


Figure 4-26: Heating time of forming and heating stage of the tooling

The heating time for the forming stage is much faster than for the heating stage. The forming stage takes about 27 minutes and the heating stage needs 50 minutes to reach 200°C, which is the Warm-forming temperature. For the Extended Hotforming the heating time is 10-15 minutes faster.

In the thermal-stationary simulation, which is important due to the temperature distribution, 200°C are applied to the heating channels of the tooling. In the experiment this corresponds to the steady state after a longer regulation period by the control unit. The evaluation of the two paths (see an overview in Figure 4-26 and in detail Figure 4-27) shows that the temperature varies only slightly between 50 and 250 mm. It can therefore be assumed that over this distance the temperature is constantly and homogeneously distributed, which prevents distortion in the component. Only in the rear of the heating station the temperature curve drops. Later in the experiment care must be taken that the blanks are not placed too far out.

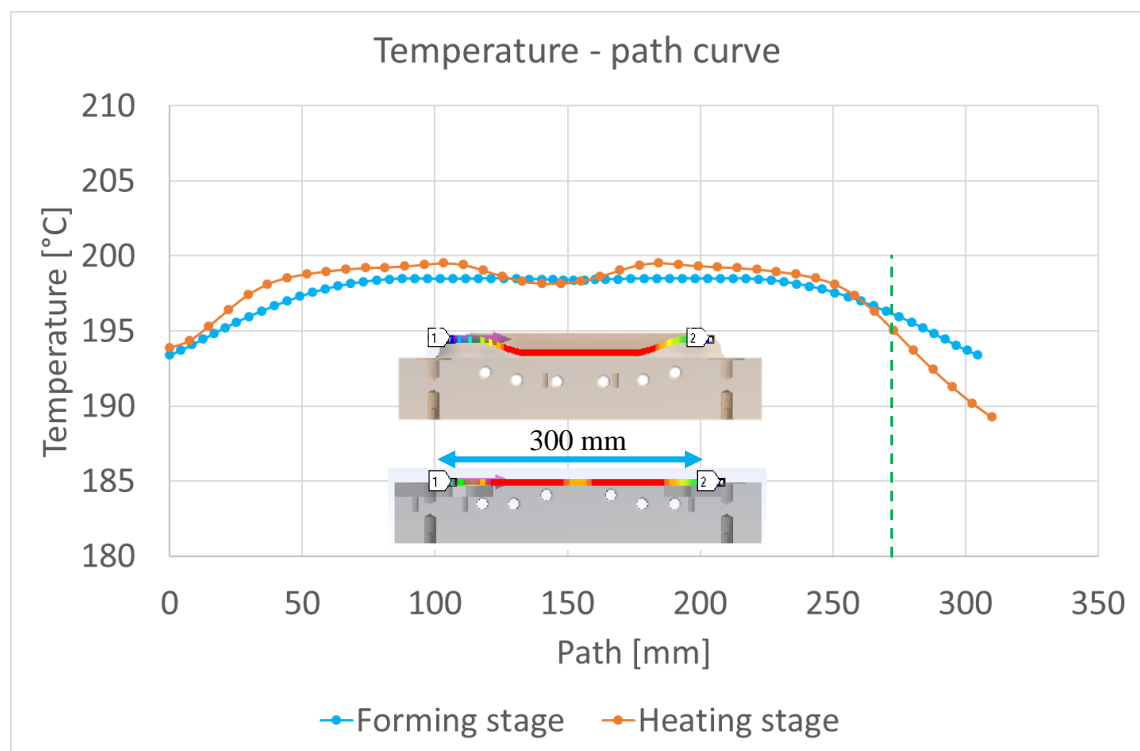


Figure 4-27: Temperature - path curve for forming and heating station

4.5.2 Quality inspection of the tool

After the production of the individual components, the form stage (die and punch) was measured on a coordinate measuring machine to ensure a gap width of 2 mm for the sheet metal in order to avoid a collision during forming. For the measurement, the tool was fixed clamped on the coordinate measuring machine, which is shown in Figure 4-28, and a program was written, which compares different positions with the CAD data.



Figure 4-28: Zeiss-DuraMax RT coordinate measuring machine with forming stage

For the comparison with the CAD geometry data four frames and six lines were programmed for both parts (die and punch). This is highlighted in Figure 4-29. The levelness was also checked.

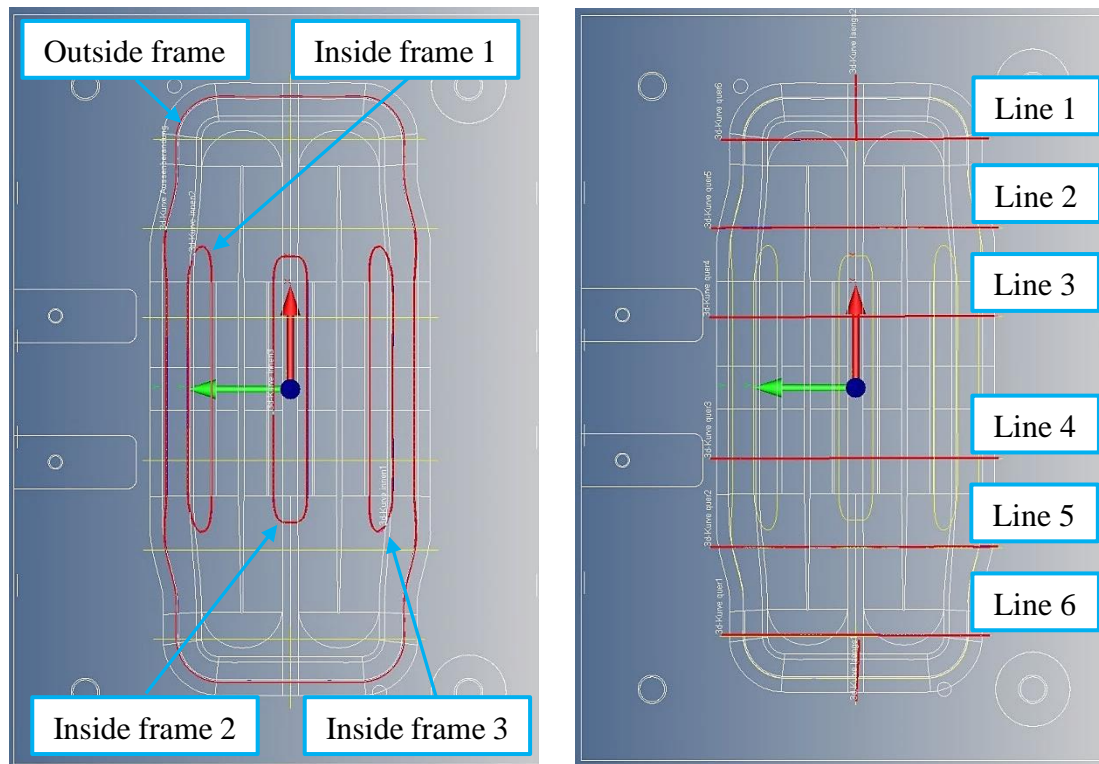
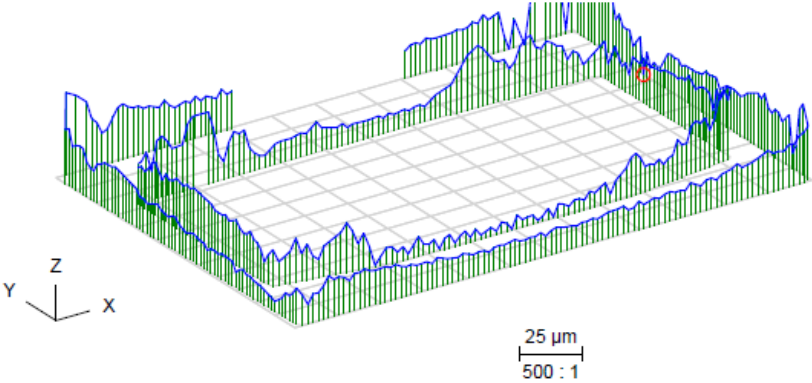
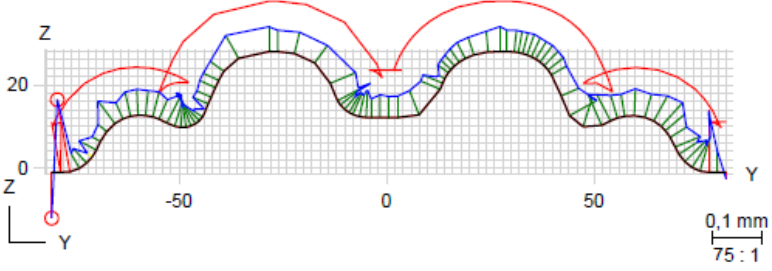


Figure 4-29: Illustration of the programmed inspection lines

The results of the coordinate measuring machine are shown in the Table 4-7. It is noticeable that the oversize of the punch is much lower than of the die. This is due to the three axis milling, because the ball cutter used for finishing is better to mill the elevations of the punch as the depressions of the die. The maximum oversize of the punch is around 0.068 mm and of the die 0.201 mm, which is adjusted on the one hand by light polishing and on the other hand by readjusting the distances (cf. Figure 4-23 position of distances) of the forming tool.

Table 4-7: Oversize measurement of the forming stage

	Die	Punch
	Oversize	Oversize
	Schematic illustration of the measured levelness & frames	
		
Levelness	0.0332	0.0229
Outside frame	0.0980	0.0519
Inside frame 1	0.1547	0.0382
Inside frame 2	0.2013	0.0457
Inside frame 3	0.0930	0.0437
	Schematic illustration of the measured lines	
		
Line 1	0.1419	0.0519
Line 2	0.0772	0.0685
Line 3	0.1079	0.0667
Line 4	0.1450	0.0565
Line 5	0.1453	0.0562
Line 6	0.0959	0.0447

4.6 Summary

First, a structural component was selected as a demonstrator, which can be made of high strength aluminium and offers a high lightweight construction potential (>30%) compared to the steel material (PHS) to be substituted. The manufacturability of the demonstrator was taken into account, so that it can be produced at elevated temperatures with all forming processes. The selected side impact beam was designed using structural optimisation methods, in particular topology optimisation, and improved in several iterative loops. The loops included a Hotforming simulation using a complex anisotropic material model and a crash calculation of the final state with the mapped data (thickness, plastic strains and pre-damage) from the forming simulation. For the boundary conditions a standardised side impact test (Euro NCAP 2015) was used and transformed into a simplified dynamic three-point bending test. For the dimensioning and as a reference for the evaluation of the crash behaviour an open source Toyota Yaris vehicle model (Center for Collision Safety and Analysis 2010) was used. During the crash calculation and comparison of different versions of the side impact beam with the original high strength steel (PHS) tube, it was noticed that for the same crash performance, a high strength aluminium beam needs about 3 mm sheet thickness, which results in a weight reduction of ~18 %. To increase the lightweight potential, a local reinforcement was applied. The shape and position were determined by a “Free-Size” optimisation. With this CFRP patch, the base material AA7075 of the side impact beam can be reduced to 2 mm, which results in a weight saving of ~36 % while maintaining the same crash performance. This beam will also be tried to be produced by the Hotforming process with a thermal direct joining step, called “Extended Hotforming”, later on. The newly designed side impact beam made out of AA7075 and the forming simulation were used to create the surfaces of the punch, die and forming blank. For the design of the separately heatable tool stages, a thermodynamic equation was used for the number of the heating cartridges and then checked with the aid of a transient and a stationary temperature simulation to ensure homogeneous temperature distribution on the surface of the tool. Furthermore, various attachments such as guide tracks, distances and centring pins were provided. For the subsequent production of the tool, technical drawings were created. Photos of the processing and production of the tool are in Appendix H.

Chapter 5 Manufacturing

and investigations of the

demonstrator with each forming

process at elevated temperatures

This chapter illustrates the application of the previously evaluated tool design on a sheet metal forming tool. Demonstration parts are also produced using different forming processes and evaluated in terms of mechanical behaviour and springback. The influence of the supplier on the mechanical properties were also illustrated. For the validation of the FE-simulation, a drop tower test (dynamic three-point bending test) was carried out and compared to the simulation results. Finally, industrial layouts were developed for each forming process at elevated temperature.

5.1 Experimental forming set-up

For the experimental forming test of the side impact beam, the designed heatable forming tool and hydraulic press (Rapp & Seidt) were used, indicating a maximum tappet force of 1200 kN. Further, heating cartridges and a corresponding control system were provided in order to examine the Warm-forming process. Figure 5-1 shows the forming press with ancillary equipment and a detailed overview of the devices is given in Table 5-1. For the forming tests the anti-friction agent Omega 35 (Section 3.5 Friction analysis) was used due to its temperature resistance and good friction properties. Further, the sheet metal forming was carried out as a 1-stage process with a forming speed of 10 mm/s.

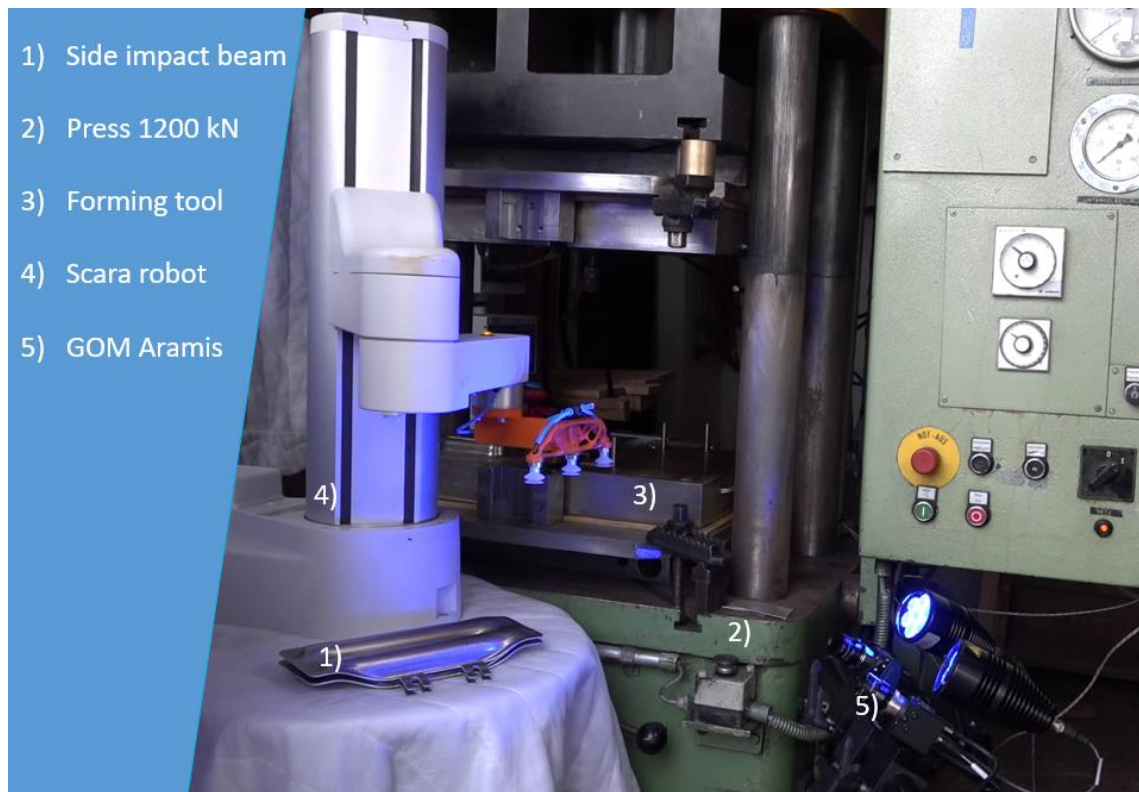



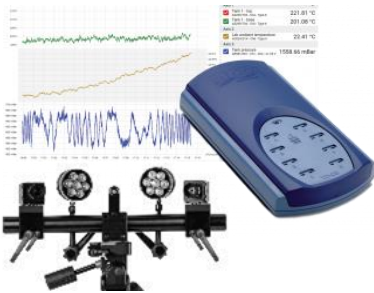


Figure 5-1: Experimental forming set-up

Table 5-1: Detail overview of the set-up

Detailed overview	Image	Description
1) Side impact beam		<ul style="list-style-type: none"> Stacked side impactors
2) / 3) Press including side impact forming tool		<ul style="list-style-type: none"> Side impact forming tool with heating (a) and forming station (b). Maximum stamping force of 1200 kN 10 mm/s forming velocity Integrated control unit for adjustable heating cartridges (two zones, between RT and 400 °C)
4) Scara robot radiation furnace Type: Heraeus VT 5050		<ul style="list-style-type: none"> Furnace for solution heat treatment Furnace temperature is recorded via separate thermocouples in the furnace and in the blank Robot for transfer
5). GOM Aramis and Temperature logger (sample time 0.1s)		<ul style="list-style-type: none"> Temperature data logger in order to monitor the temperature of the furnace and specimens. GOM Aramis for optical process monitoring

5.2 Production of the demonstrator

All forming processes at elevated temperature were used to produce the side impact beam. Figure 5-2 shows the qualitative temperature profile of the mentioned forming processes.

In the Warm-forming process (blue curve), the AA7xxx blank in T6 temper is heated to about 180°C (T_{WF}) by contact heating in the heating stage of the forming tool. After maintaining the temperature for 5 - 10s, the blank is formed in the heated forming stage, which is also heated to approximately 180°C. Previous studies have shown that AA7075 shows a decrease in stress and an increase in elongation at temperatures between 140°C and 220°C. At temperatures above 260°C both strength and elongation decrease significantly due to its overage condition (see Chapter 2.3.3). In addition, AA7075 shows the best deep drawability at 180°C. The limiting drawing ratio (LDR) reaches a value of 2.0 and is therefore equivalent to e.g. AA6181 in T4 temper at room temperature (Wang et al. 2012)

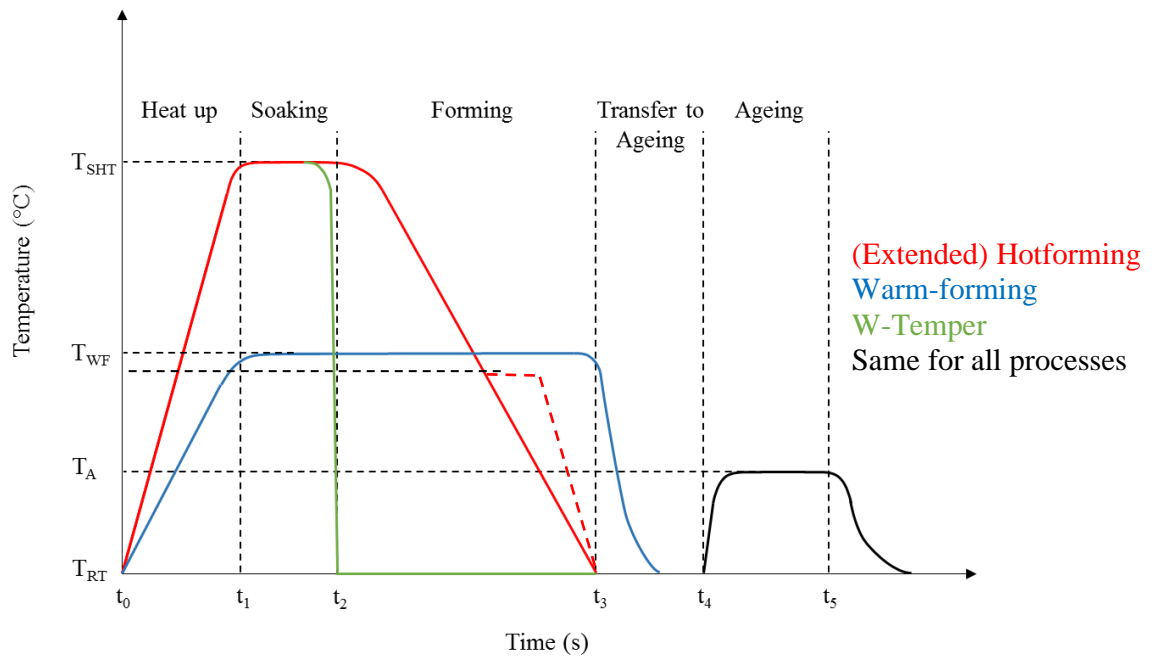


Figure 5-2: Temperature curve of the (Extended) Hotforming, Warm-forming and W-Temper process

In the Hotforming process (red curve), the AA7xxx blank in T4 temper is heated up in a furnace to its solution heat treatment temperature ($t_0 - t_1$, $465^{\circ}\text{C} < T_{SHT} < 494^{\circ}\text{C}$). The temperature is then maintained for a specific period of time in order to dissolve the coarse precipitates and soluble inclusions ($t_1 - t_2$) (Oberhauser et al. 2013).

Afterwards, the blank is quickly transferred to the forming unit, where it is formed and held between the cold dies to quench the material to lower temperatures ($t_2 - t_3$). As a deviation from this process, it is also possible to quench the blank down to $\sim 150 - 180^\circ\text{C}$ (T_{EHF}) in a heated plate station and form the blank at the same temperature. This process, called Extended Hotforming, allows the direct thermal joining of CFRP or GFRP patches. The W-Temper process (green curve) is a thermally decoupled forming technique. The blank in T4 temper is first heated in the furnace, kept at solution annealing temperature and then quenched in a water bath, flat plates, spray cooling or high-pressure air, depending on the desired cooling rate. Afterwards, the cold blank is formed at ambient temperature and cut by laser or directly in the tool before the natural ageing of the material takes place. Previous studies on AA7075 have shown that the material begins to harden after approximately 10 minutes. This therefore represents the maximum time allowed before forming (Sáenz de Argandoña et al. 2015).

After the forming process, heat treatable aluminium alloys such as the 7000 series can be aged naturally (at T_{RT}) or artificially (at T_{A}) in order to restore the microstructure and mechanical properties of the T6 temper. In contrast to the other forming processes described above, Warm-forming requires no further heat treatment due to the high strength of the initial T6 temper. Components for the automotive industry are a special feature in this context. They can be heat treated by the curing time of the cathodic dip painting, which takes place after the forming process ($t_4 - t_5$). The typical conditions for this type of artificial ageing are 170°C to 180°C for about 20 minutes.

The following Table 5-2 offers a summary of the processes in the test series.

Table 5-2: Procedure of the test series

Process	Heating in	Heating Temp. [$^\circ\text{C}$]	Holding time	Quenching and forming	Ageing (see Chapter 5.3 & 5.4)
Hotforming	Furnace	465 - 490	10 – 15 min	Forming tool at RT	1 Week natural ageing, then heat treatment
W-Temper	Furnace	465 - 490	10 – 15 min	Water bath and forming tool	1 Week natural ageing, then heat treatment
Warm-forming	Heating station in press	180 - 210	10 s	Heated forming tool (180°C)	1 Week natural ageing, then heat treatment

In order to monitor the temperature curve during the forming processes, the blank was equipped with two thermocouples (see Figure 5-3 S1 & S2).

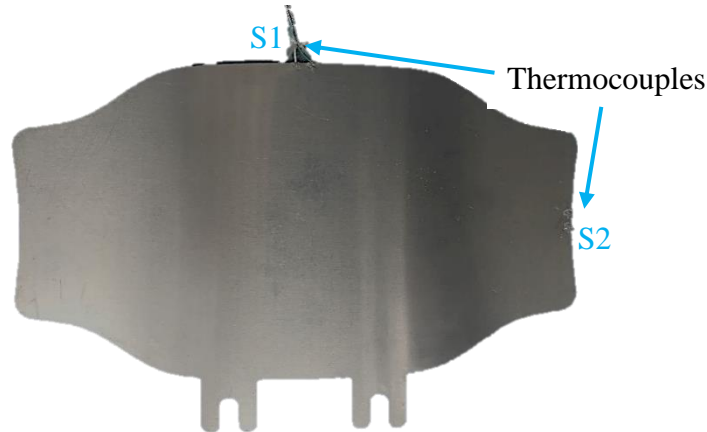


Figure 5-3: Blank with two thermocouples

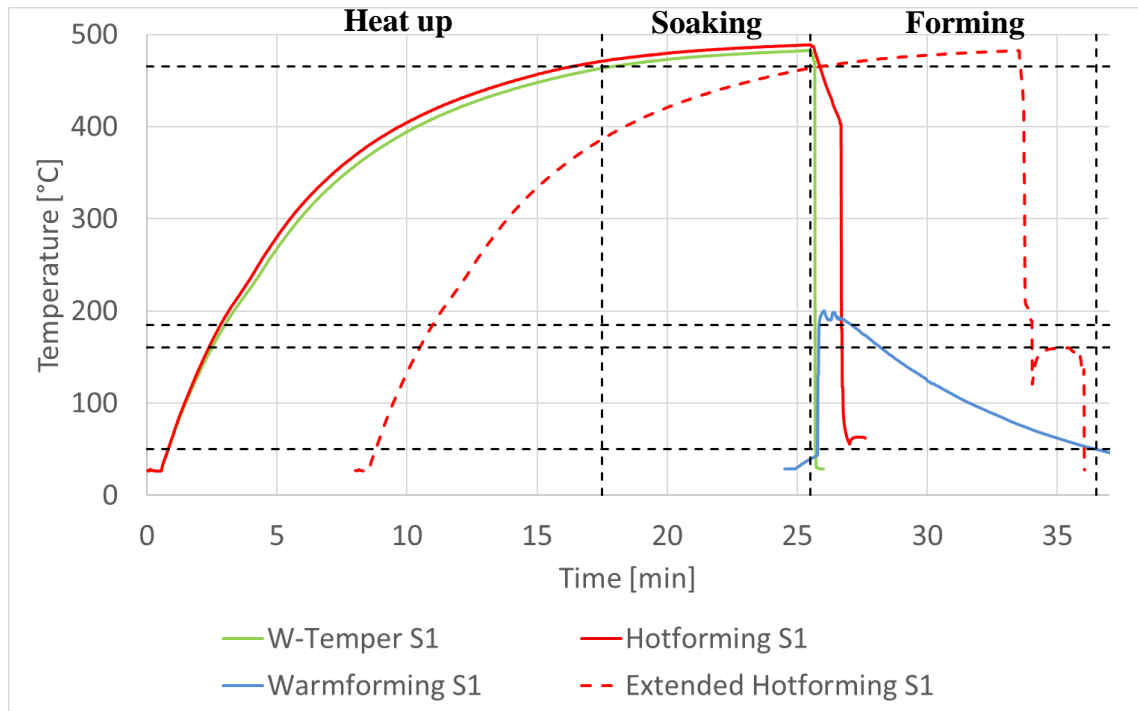


Figure 5-4: Measured temperature curve of each process at elevated temperature using thermocouple S1

For reasons of clarity, the temperature curves measured during the various forming processes were plotted for thermocouple S1 only (see Figure 5-4). For the W-Temper process and Hotforming process a quenching rate of 211 K/s and 95 K/s is achieved, which is greater than 80 K/s and therefore no strength is lost (cf. Chapter 3.2). The Extended Hotforming process is slightly below with 73 K/s, due to the heated tool.

The finished contour is cut from the AA7075 blank and formed into the demonstrator side impact beams. Afterwards, tensile specimens are extracted from areas as shown on the right illustration in Figure 5-5.



Figure 5-5: Forming of the side impact beam and position of the specimens for the tensile tests

Numerous investigations have focused on the influence of pre-strain on the mechanical properties of high strength aluminium alloys. In general, the test results agree that pre-strain before heat treatment can result in a variation of strength depending on the temperature used (Kilic et al. 2019). In order to evaluate an influence on the investigation, a forming simulation of the described component was carried out. The following Figure 5-6 shows the true von Mises strain of the elements after forming.

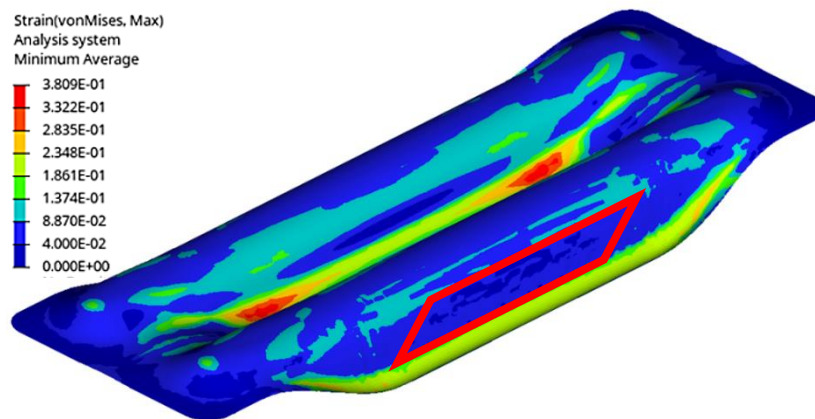


Figure 5-6: True von Mises strain of the elements after forming

As shown in Figure 5-6, the true strain in the relevant area (red box) is approximately 0.04 or 4 %. In relation to results of already published studies, a slight decrease in yield strength and tensile strength is expected when using an ageing temperature of 200 °C (Kilic et al. 2019). As these values change only slightly the influence of pre-strain is not further considered in the course of this test series.

The choice of the forming process, the material supplier and the subsequent heat treatment is carried out depending on the objectives of investigation. These are described separately in the following Chapters 5.3 and 5.4. A period of one week was observed between forming and heat treatment in order to achieve a stable T4 condition by natural ageing. The following Figure 5-7 shows the demonstrators, which were produced with the different processes.

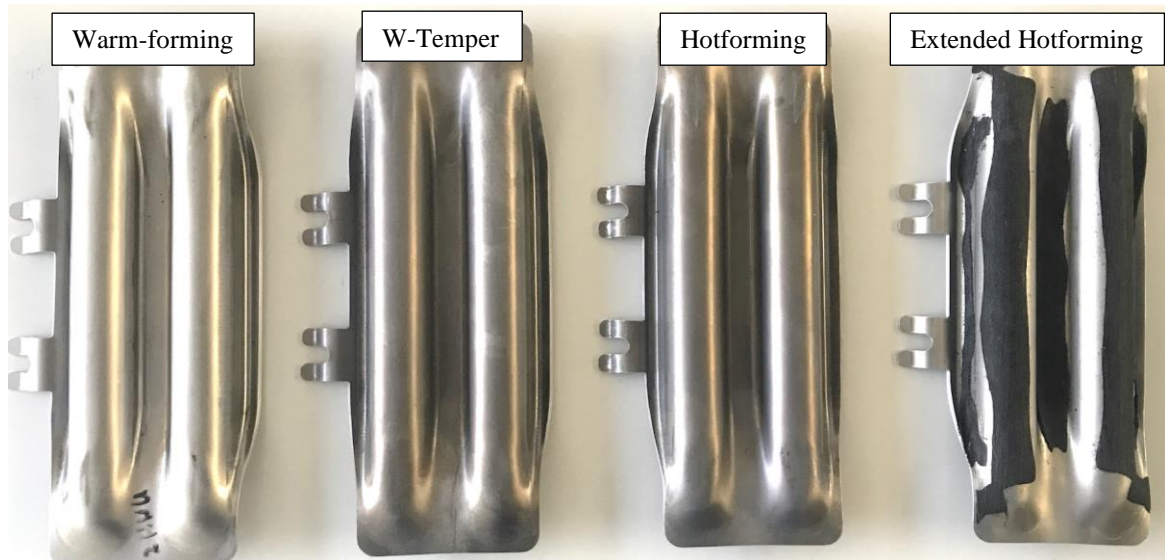


Figure 5-7: Manufactured demonstrators with Warm-forming, W-Temper, Hotforming and Extended Hotforming processes

5.3 Investigations of the material suppliers

In this study, aluminium alloys with the designation EN AW-7075 (state T6) from different suppliers are compared to each other. Table 5-3 illustrates the chemical composition and characteristic material parameters. All stated values are based on the specifications provided by the manufacturers.

Table 5-3: Comparison of the chemical and mechanical properties of the aluminium alloys from different suppliers

EN AW-7075 T6 temper	Si [%]	Fe [%]	Cu [%]	Mn [%]	Mg [%]	Cr [%]	Ni [%]	Zn [%]	Ti [%]
Supplier									
• Alcoa	0-0.4	0-0.5	1.2-2.0	0-0.3	2.1-2.9	0.18- 0.28	-	5.1-6.1	0-0.2
• Constellium									
• Novelis									
Supplier									
• AMAG	0.05	0.11	1.7	0.02	2.7	0.19	-	5.8	0.05
DIN EN 485-1	0-0.4	0-0.5	1.2-2.0	0-0.3	2.1-2.9	0.18- 0.28	-	5.1-6.1	0-0.2

EN AW-7075 T6 temper	Nominal thickness [mm]	Hardness [HBW]	Min. yield stress [MPa]	Min. tensile strength [MPa]	Min. fracture elongation [%]
Supplier Alcoa	2	150	455	530	7
Supplier AMAG	2	-	500	565	12
Supplier Constellium	2	150	500	560	7
Supplier Novelis	2	-	480	540	10
DIN EN 485-1	1.5-3.0	161	470	540	7

The influence of the supplier is investigated by carrying out two forming processes with different materials (with and without subsequent heat treatment). Only the Hotforming and W-Temper process are performed, as these are not influenced by the delivery condition of the material due to solution heat treatment. This guarantees the comparability of the material properties, since other influences are excluded. The heat treatment is carried out at 180°C for 20 min after one week of natural ageing and thus corresponds to the industrial standard of one paint-bake-cycle for 6xxx car body materials.

5.3.1 Results of supplier comparison

The following results are based on the mean value of three components and show the variations of the material parameters ultimate tensile strength (UTS), yield strength and fracture elongation determined in the tensile test.

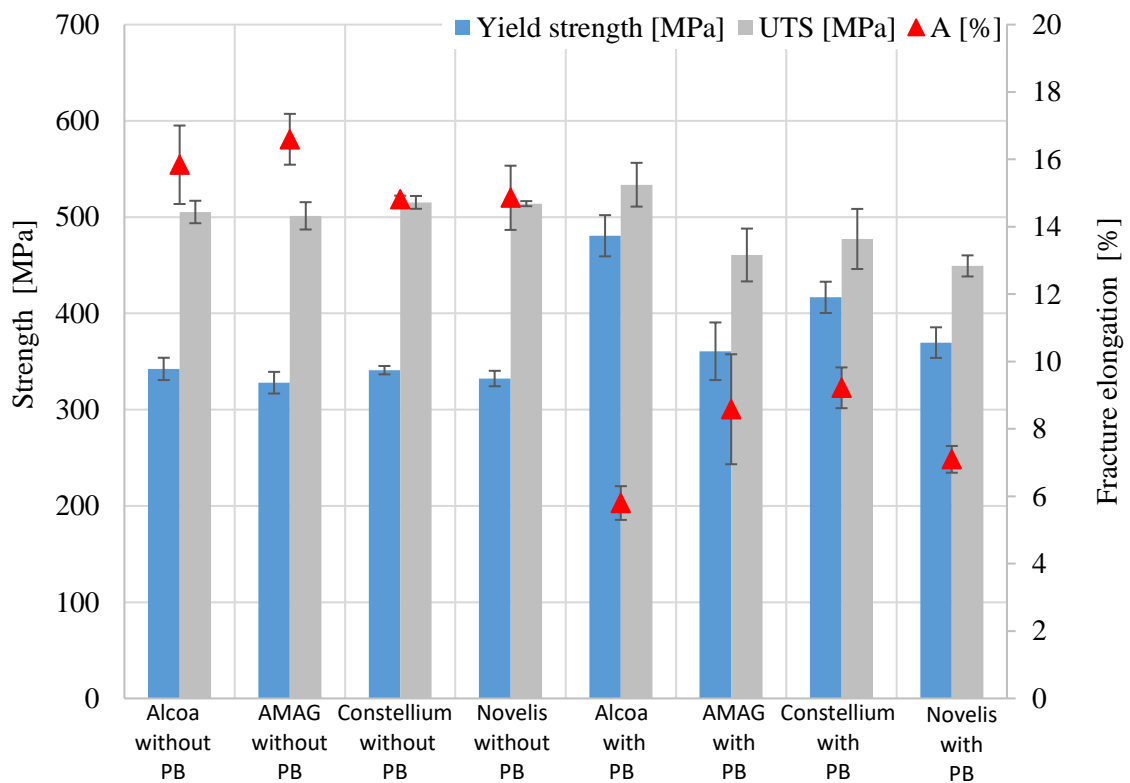


Figure 5-8: Test results of the supplier influence in the Hotforming process

When using the Hotforming process, the parts produced without subsequent heat treatment show no influence concerning the suppliers, since the strength and elongation values vary only within a small range of 15 MPa and 1.8 %. Constellium shows the highest strength value with a UTS of 515 MPa. Compared to the minimum strength specified by the supplier, this material achieves 92% of the strength in T6 condition. A significant difference of the material behaviour can be seen if one paint bake cycle is applied. Here, the UTS values and those for yield strength vary up to 73 MPa (~ 14 %) and 120 MPa (~ 25 %) respectively. The material from Alcoa has an average ultimate tensile strength of 533 MPa. In relation to the specified ultimate tensile strength of 530 MPa, the material reaches 100 % of the minimum strength of the T6 condition.

Figure 5-8 also shows that with subsequent heat treatment the yield strength increases and the elongation at break decreases for each supplier material. The greatest increase in yield strength is seen in the material from supplier Alcoa with an increase of 140 MPa. At the same time, the elongation at break decreases most significantly by 10 %. The ultimate tensile strength values decrease for suppliers AMAG and Novelis, while it increases slightly for Alcoa. The increased standard deviation and variance of values can be explained by the material influence and the varying cooling rate, since the transfer of the blank from furnace to press was performed manually.

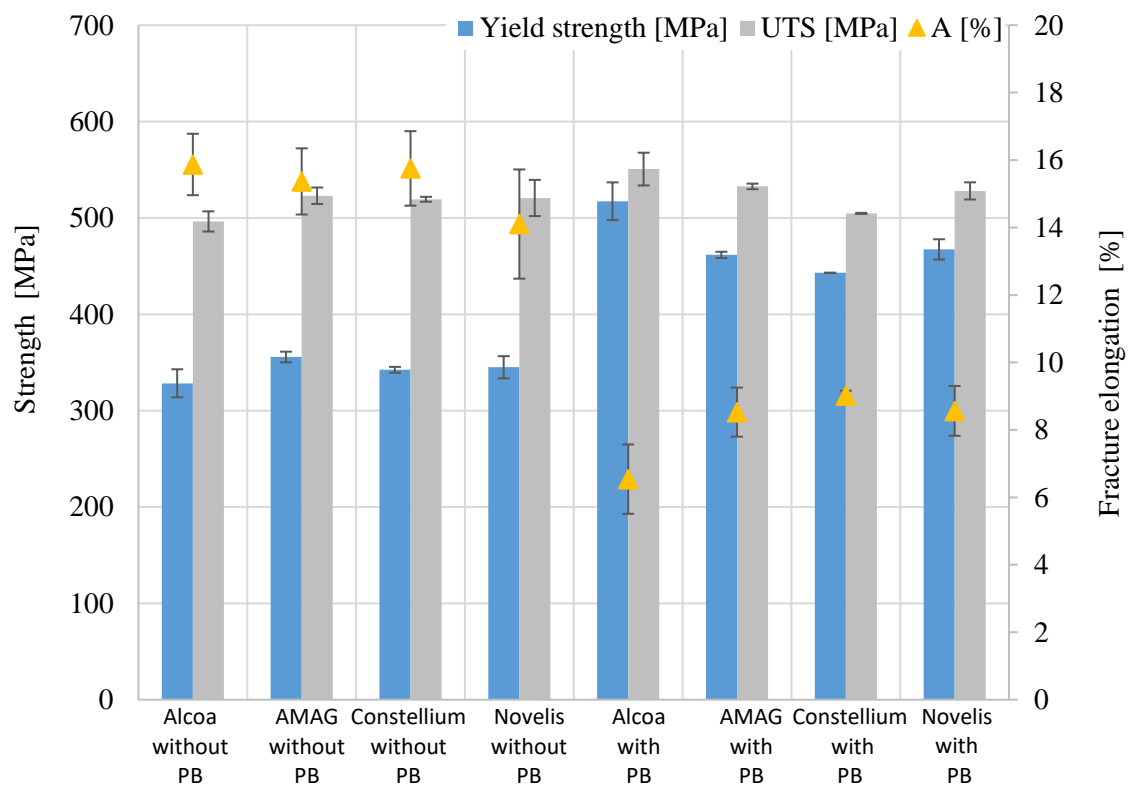


Figure 5-9: Test results of the supplier influence in the W-Temper process

When using the W-Temper process (see Figure 5-9), the parts produced without subsequent heat treatment show no supplier influence, as the values recorded remain almost constant. The strength and elongation values vary only by 27 MPa and 1.7 %. The material from supplier AMAG has the highest tensile strength value with an average of 523 MPa. In relation to the minimum tensile strength specified by the supplier, a strength of 93 % of the T6 condition is achieved. If one paint bake cycle is applied, the same trends as in the Hotforming process can be detected. The UTS values and those for yield strength

vary within a range of 46 MPa (~9 %) and 74 MPa (~15 %) respectively. The material from Alcoa shows the highest average UTS of 550 MPa. Compared to the minimum strength specified by the supplier, the heat-treated material achieves 100 % of the strength in T6 condition.

In addition, it can be seen from the preceding Figure 5-9 that after heat treatment the yield strength increases while the fracture elongation decreases. The greatest increase in yield strength (189 MPa) and decrease in fracture elongation (9.3 %) can be observed in the material from Alcoa. The tensile strength of this supplier increases by 50 MPa after heat treatment, while it remains almost constant for suppliers AMAG and Novelis. The values here only vary by a maximum of 15 MPa and can therefore be regarded as constant within the context of the measuring accuracy. Compared to the Hotforming process, the strength values are higher while the variation of values is lower. This is caused by the cooling rate, which is higher and can be kept more constant.

5.4 Investigations of forming processes at elevated temperatures

5.4.1 Mechanical behaviour under different heat treatment conditions

Based on the test results obtained so far, the material behaviour under different heat treatment conditions will be investigated now. Due to the sufficient availability of sheet material, AMAG was selected for further experiments. A trial plan was also created for the execution, which is listed in Table 5-4.

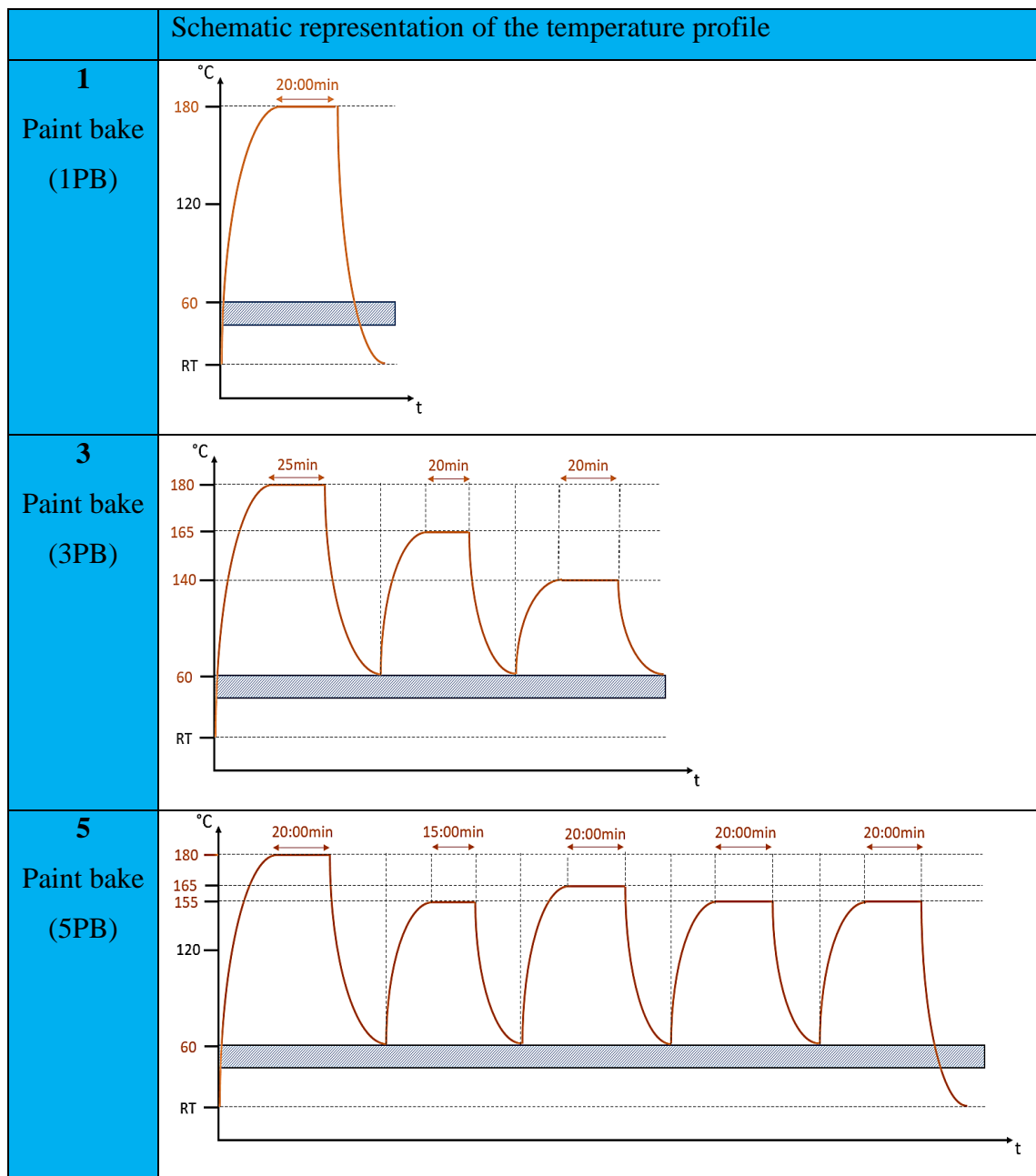
Table 5-4: Trial plan for mechanical properties investigations of different forming processes and paint bakes

Forming-process / Name of treatment	Warm-forming	W-Temper	Hotforming
Without Paint bake (W)	5 specimens (index X WF W)	5 specimens (index X WT W)	5 specimens (index X HT W)
1 Step Paint bake (1PB)	5 specimens (index X WF 1PB)	5 specimens (index X WT 1PB)	5 specimens (index X HT 1PB)
3 Step Paint bake (3PB)	5 specimens (index X WF 3PB)	5 specimens (index X WT 3PB)	5 specimens (index X HT 3PB)
5 Step Paint bake (5PB)	5 specimens (index X WF 5PB)	5 specimens (index X WT 5PB)	5 specimens (index X HT 5PB)

*X –specimen number

In order to imitate the final component heat treatment in the automobile painting shop, three different paint bake cycles were carried out, which are commonly used and discussed directly with an OEM in the automotive industry. The schematic representations of the paint bake cycles are listed in Table 5-5.

Table 5-5: Heat treatments - schematic representation of the temperature profile



First, the specimens are taken by sawing and milling on the sidewall of the side impact beam as shown in Chapter 5.2 Figure 5-5 and naturally aged for one week. Five specimens for each artificial heat treatment and forming process were then placed in a preheated oven and various paint baking cycles (PB) were performed. One of the specimens has two thermocouples. The set furnace temperature was measured and controlled both with a thermocouple in an additional blank and in the furnace itself. Between the individual temperature steps, samples were taken out and cooled down at air (below 60 °C). During

this time the furnace was adjusted to the new temperature. The measured temperature profiles of the two thermocouples in the specimen for each paint bake cycle are presented in Table 5-6. It is noticeable that the temperature curves vary slightly when the target temperature is reached. This is due to the regulation of the furnace.

Table 5-6: Measured temperature profiles of each paint bake cycle

	Measured temperature profiles in the specimens
1 – Paint bake (1PB)	<p>1 Paint bake cycle - Simple KTL</p>
3 – Paint bake (3PB)	<p>3 Paint bake cycles</p>
5 - Paint bake (5PB)	<p>5 Paint bake cycles</p>

In this study, the influence of the different processes and the different heat treatment on the strength is examined. The five tensile test specimens of each process were drawn to standard (DIN EN ISO 6892-1). The mean value and standard deviation of ultimate tensile strength, yield strength (Figure 5-10 a & b) and fracture elongation (Figure 5-11) are compared for each process. For a different representation see Appendix I.

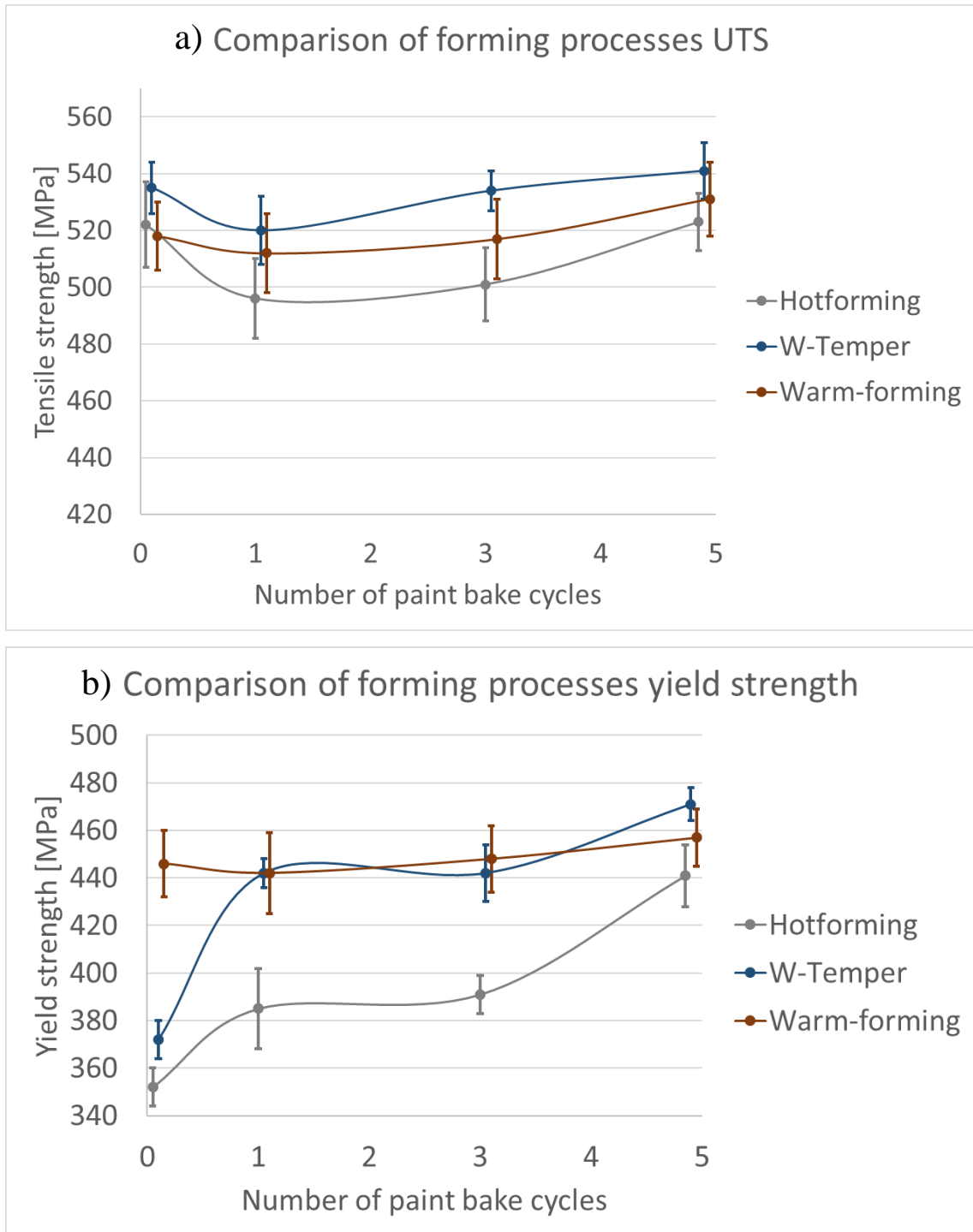


Figure 5-10: Strength comparison of forming processes and heat treatment

In the Hotforming process, the tensile strength decreases slightly between 1 and 3 paint bake cycles, reaching its maximum of 523 MPa at 5 PB, which is approx. 93% of UTS at T6 condition. This effect is similar to the W-Temper process, although the absolute values are slightly higher and reach a tensile strength of 541 MPa at five PB. The results correspond to those published in (Grohmann 2016), which show the difference in strength between Hotforming and W-Temper for 5 PB cycles.

In contrast, the increase in yield strength is similar for both the Hotforming and W-Temper process. Depending on the paint bake cycle, the tensile strength and yield strength in the W-Temper process is about 40-70 MPa higher, which is due to the increased quenching rate in the water bath.

This effect is similar to the investigations carried out by AMAG, which have shown that the cooling rate is a decisive factor for strength (Oberhauser et al. 2013) and should be greater than 80 K/s for AA7075 (see Chapter 3.2). Due to the same hardening mechanism of the two processes, namely precipitation hardening (et. Chapter 2.3.3), the strength curves are very similar over the artificial ageing cycles. The reason for the increase in strength is the formation of secondary phases that occur at temperatures between 100 and 200°C (Totten 2016).

In contrast to the other forming processes, the tensile strength and yield strength in the Warm-forming process remain almost constant over the number of heat treatments. The slight increase in strength between PB1 and PB5 is known as re-ageing and occurs at forming temperatures of just over 200 °C (Oberhauser et al. 2013).

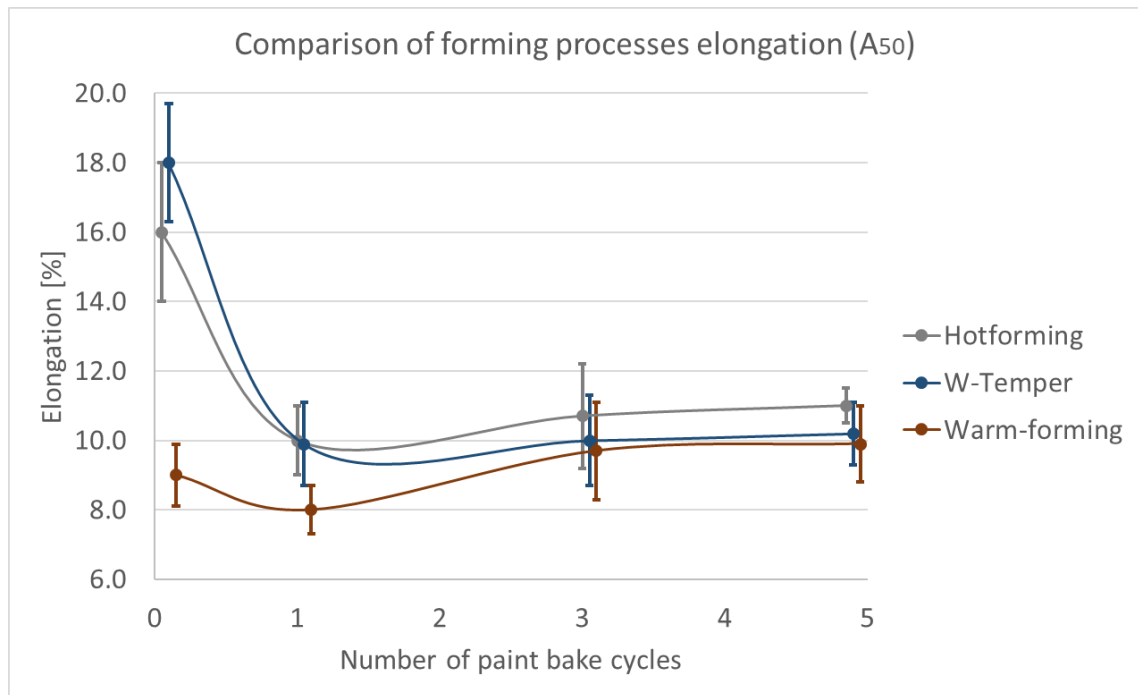


Figure 5-11: fracture elongation comparison of forming processes and heat treatment

The two curves of the Hotforming and the W-Temper process (see Figure 5-10 and Figure 5-11) are comparable since the elongation at break of both processes is between 16 – 18 % after forming. Then it decreases to about 10 % and remains almost constant at this level. This is a typical effect of artificial ageing, in which strength increases and elongation decreases. The values at 5PB are almost the same as in the publication (Grohmann 2016).

The elongation at break during Warm-forming is significantly lower after forming and remains almost constant over the PB cycles at around 8 - 10 %. This is due to the ageing condition of the AA7075 material, which is in T6 state prior to forming and overaged (T7) due to the heating time in the paint bake cycles, where incoherent phases take place (Totten 2016).

5.4.1.1 Concluding remarks

With regard to the further investigations, it becomes clear that the quenching rate has a high influence on the achievable strength in the Hotforming and W-Temper processes. During precipitation hardening, this is characterised by the same curve but differing absolute values. The cooling rate during quenching in the Hotforming process was determined to be 60 - 90 K/s and in the W-Temper process more than 100 K/s.

The results from Figure 5-10 show that using the Hotforming process, the AA7075 alloy achieves 92 % of tensile strength and 88 % of yield strength compared to the T6 state. This level was achieved after five paint bake cycles and is similar to the strength achieved in the other two processes. If a lower number of paint bake cycles is used, a significant difference between the processes could be observed, especially in terms of yield strength. In addition, the W-Temper process achieved the best values with 96 % of UTS compared to the initial state (T6) of the material. However, the strength is almost constant over the heat treatment using the Warm-forming process (~ 94 %, see Table 5-7).

Table 5-7: Potential of different forming processes at elevated temperatures using artificial ageing (5 PB)

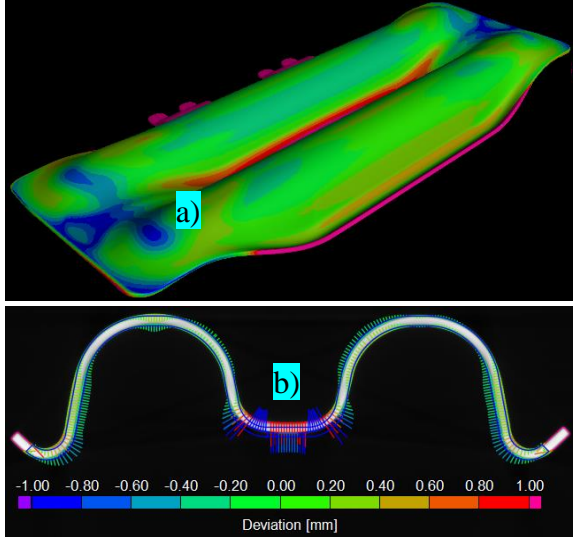
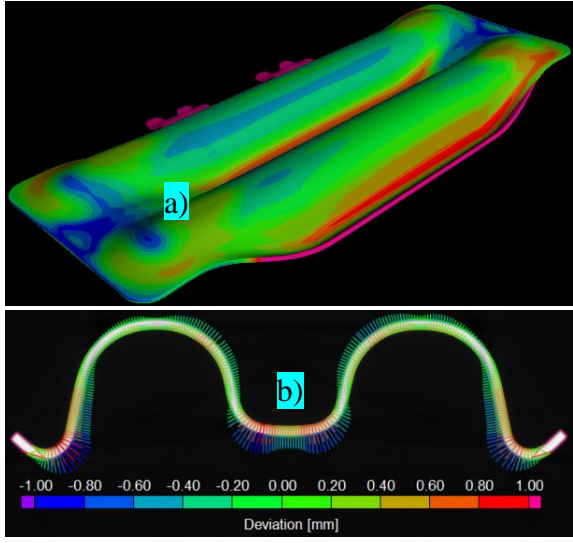
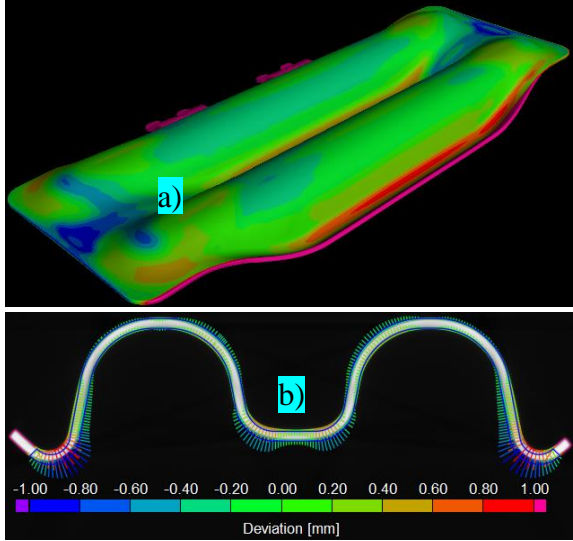
	T6 condition	Hotforming	W-Temper	Warm-forming
UTS	565 MPa	92 %	96 %	94 %
Yield strength	500 MPa	88 %	94 %	92 %
Fracture Elongation	12 %	92 %	83.0 %	83 %

5.4.2 Analysis of the springback of various forming processes

Now, the springback behaviour of the corresponding processes has to be evaluated. After forming (without paint bake) one side impact beam per process was examined and then compared to the CAD geometry to obtain the production dimensions. For these investigations, the demonstrators produced with the Warm-forming, W-Temper and Hotforming processes, were measured using computer tomography (CT - Zeiss Metrotom 1500). The measurement of the component from Extended Hotforming process is not conducted due to the similarity to the standard Hotforming process and the additional patch, which would significantly falsify the result of deviation.

The target-actual-comparison in Table 5-8 clearly shows that all processes have different springback behaviour. It is noticeable that the Warm-forming is the worst in terms of dimensional accuracy. This process deviates more from the CAD contour at point a) and point b) compared to the others, which is due to increased internal stresses and springback caused by the high strength condition of the material during forming. On the other hand, the deviation compared to the CAD geometry is better in the Hotforming and W-temper processes, as forming takes place in the solution annealed condition. In the comparison of points a) and b), the Hotforming process shows the highest accuracy.

Table 5-8: Target-actual-comparison of Warm-forming, W-Temper & Hotforming processes with
CAD geometry

<p>Warm-forming</p>	
<p>W-Temper</p>	
<p>Hotforming</p>	

5.4.3 Analysis of the thickness of various forming processes

In a further computer tomography study, the thicknesses of the different demonstrators produced with different forming processes (Warm-forming, W-Temper and Hotforming) are compared with each other and with the forming simulation results. The thicknesses, which were also measured by computer tomography (CT - Zeiss Metrotom 1500), were shown in Table 5-9. Three significant points were marked with the letters a), b) and c) and compared with each other.

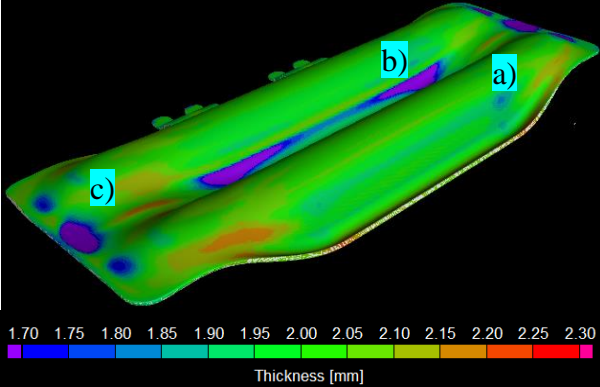
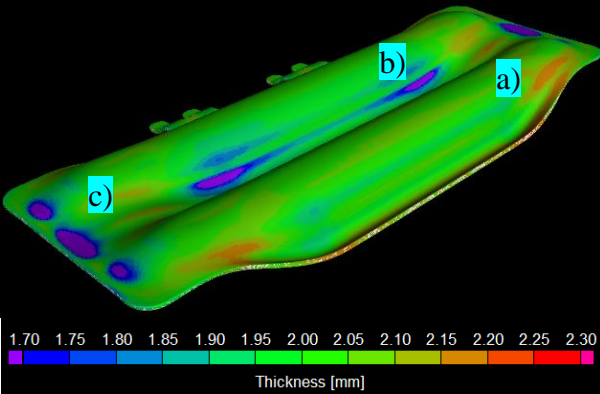
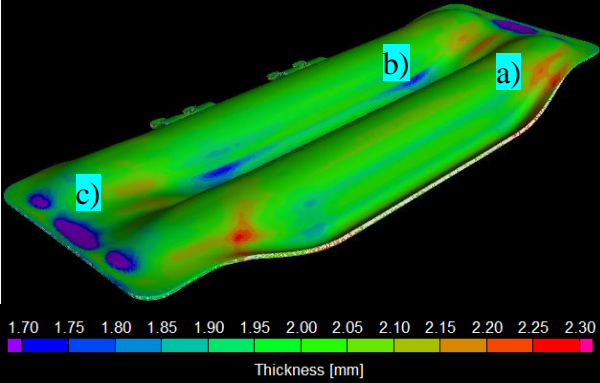
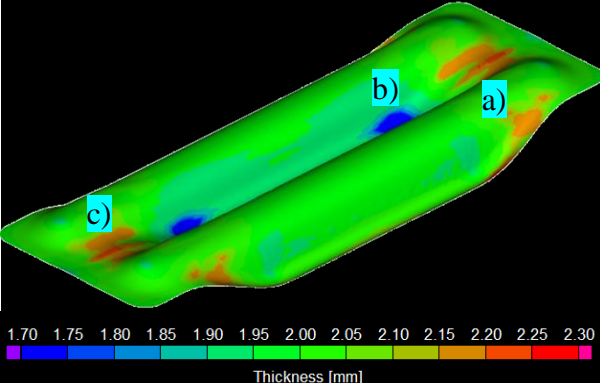
When first comparing the side impact beam thicknesses of each forming processes, it is noticeable that at point a) all three forming processes have nearly the same thickening, which is:

- Warm-forming < 2.15 mm
- W-Temper < 2.25 mm
- Hotforming < 2.30 mm

At point b) the Warm-forming and W-Temper processes have approximately the same thinning (less than < 1.70 mm). However, the SIB produced with the Hotforming process has the lowest thinning at this place.

In comparison to the Hotforming simulation, a very good agreement can be observed at all points. Except at point c), there is a worse agreement between the simulation result and the Hotforming demonstrator SIB, which is due to the tolerances of the forming tool. Nevertheless, the forming simulation, which is based on the complex material-, failure- and friction models, allows a very good prediction of the thickness and shape of the component.

Table 5-9: Comparison of Warm-forming, W-Temper and Hotforming processes with forming simulation

<p>Warm-forming</p>	
<p>W-Temper</p>	
<p>Hotforming</p>	
<p>Simulation Hotforming</p>	

5.5 Drop-Tower test – dynamic three-point bending test

To validate the simulation model for the final state of the SIB, a dynamic drop test is carried out using a drop tower setup. The acceleration of the impactor and the reaction force at the bottom of the tower are measured here. The test is then compared with the simulation. Only the side impact beam made of AA7075 in the final state (after Hotforming and one paint bake) is considered, since the original PHS tube from the Toyota Yaris model is not available. However, this component test is sufficient for the validation of the implemented simulation models, as these have already been adapted and validated to the experimental data of the material and failure specimens (shear-, tensile-, notched-, and Erichsen test).

5.5.1 Test setup Drop-Tower test

An overview of the test setup is shown in Figure 5-12. Due to the downscaled SIB and the limit of the Drop-tower test bench at Aalen University, the energy, which can be adjusted by the drop height and weight of the impactor, is set to ~193J. This is about half as much as in the large-scale component test, see Figure 4-4 and Figure 4-12. This corresponds to a height of fall of 1.4 m and a mass of 14 kg. The side impact beam is placed in the middle of the hinge joints, which have the same size and distance as the simulation model. Furthermore, the simulation model was adapted to the same experiment conditions in order to make a comparison afterwards and to validate the simulation model.

During the test, measurement data is recorded, wherein the acceleration is measured by an acceleration sensor in the impactor and the reaction force is measured by a force sensor on the base plate. An overview of the test bench including a detailed view is given in Figure 5-12.



Figure 5-12: Drop-Tower test bench at Aalen university – overview and detail

5.5.2 Test execution and comparison with the simulation results

Three tests of the side impact beam in the final state, after Hotforming and paint bake, are performed. The following two diagrams (Figure 5-13) show the results of such a measurement. For a comparison between experimental and simulation dynamic three-point bending test, only the first impact of the impactor is used. In both cases, acceleration and reaction force, there is a very good agreement of the simulation and experimental curve.

The two maxima are on the one hand at an acceleration of $\sim 1300 \text{ m/s}^2$ and on the other hand at a reaction force of 18 kN .

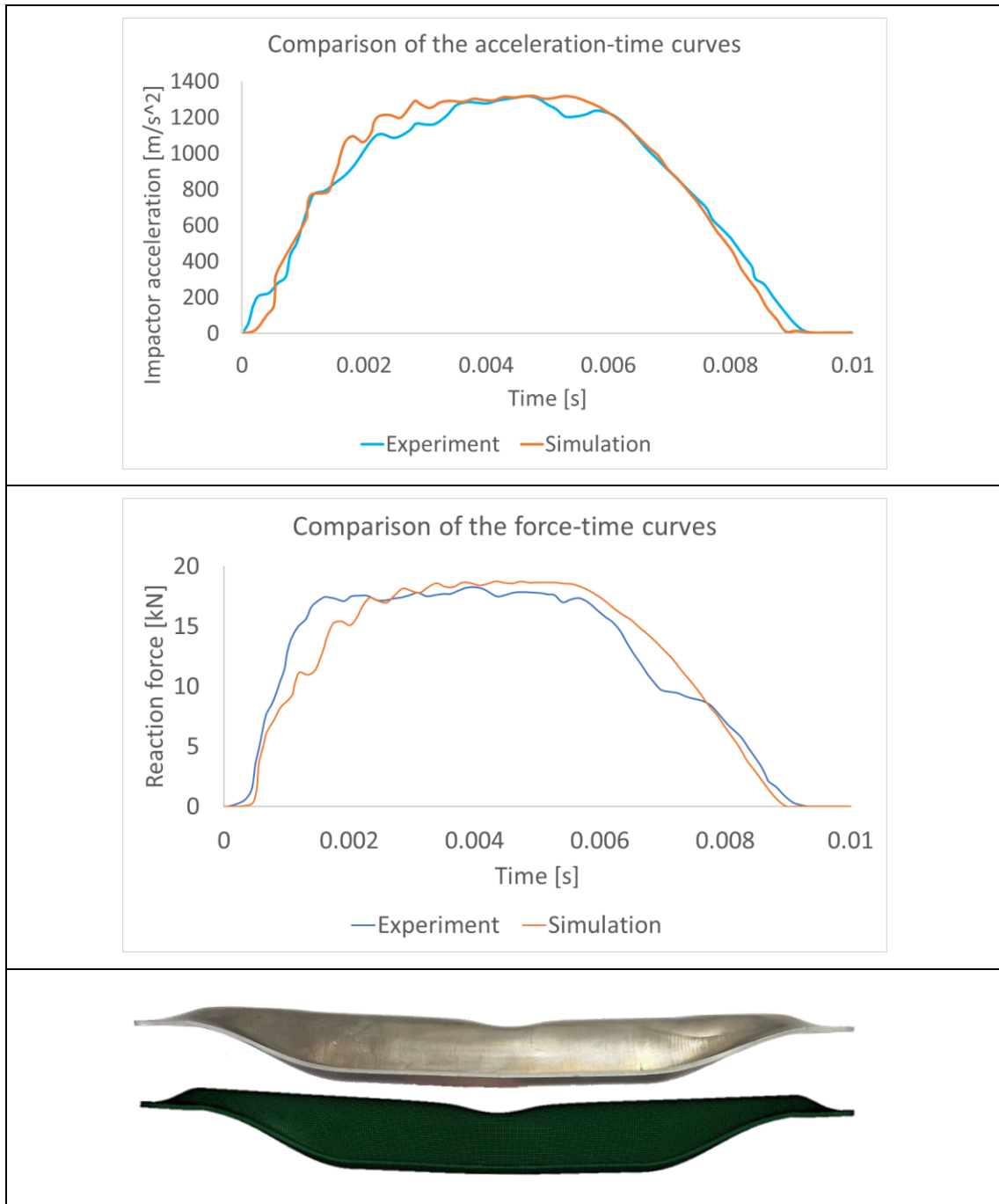


Figure 5-13: Acceleration-time curve, Force-time curve and optical comparison of the simulation with experimental component test

By optical comparison of both crashed components, the same dent in the middle of the SIB and the consistency of acceleration and force curves can be seen. The comparison ensures that the simulation model including material model, damage model and mapped data from the previously forming simulation, leads to a very good agreement in the component test. This means that the models can continue to be used in complete vehicle tests.

5.6 Development of an industrial scaled layout for each forming process

For a better implementation in the industry, a mass production layout is now being created. Those schematic layouts allow short cycle times and a simple implementation in the industry, because of the existing press hardened steel facilities.

The Warm-forming process, which is described in Chapter 2.2.3, enables a compact design of the production system (see Figure 5-14). First, the blank is allocated at the press line and transferred with a robot to the heating station in the press tool. The blank is heated to over 180°C and placed into the heated forming tool and formed. Then the die-cutting is carried out and the finished component is placed onto the discharge conveyor for optical quality assurance. Finally the components are put into a storage box and brought to an assembly or coating plant.

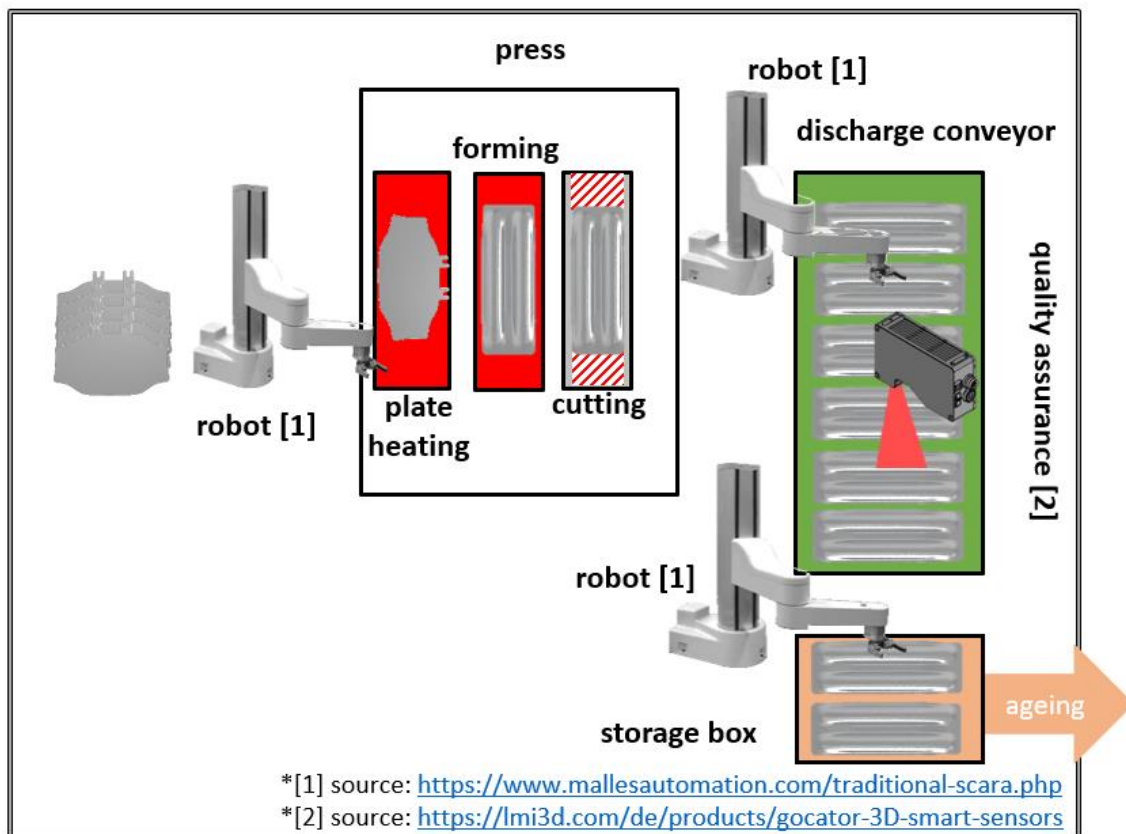


Figure 5-14: Schematic industrial layout of Warm-forming process

Compared to the other forming processes at elevated temperatures, W-Temper (see also Chapter 2.2.4) is the largest process with the most intermediate steps (et. Figure 5-15). First, the blank is placed by a robot to a plate heating station ($T > 465^{\circ}\text{C}$ solution annealing temperature) and then it passes through a continuous furnace for solution annealing. After that, the next robot takes the blank, quenches it in a water bath and transfers it to the forming press. After forming and trimming the finished component is placed on the discharge conveyor and passes the quality assurance. Finally, the component is placed into a storage box and brought to an assembly or coating plant.

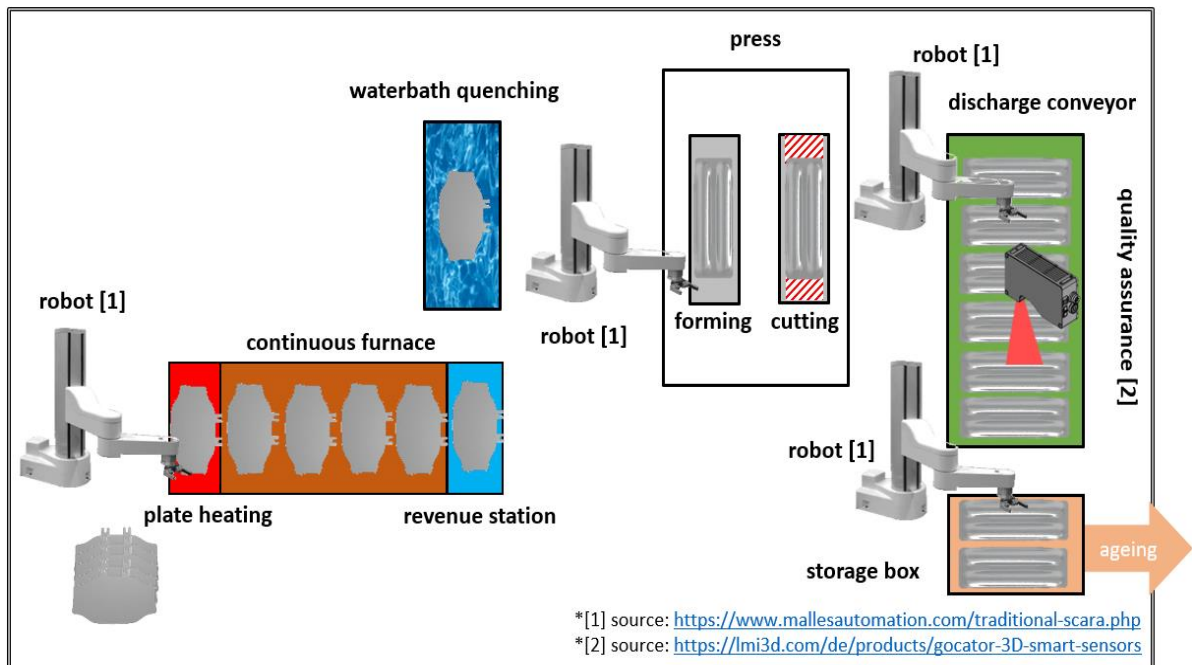


Figure 5-15: Schematic industrial layout of W-Temper process

The next layout (see Figure 5-16) shows the Hotforming or the Extended Hotforming process, which is also possible. This process is most similar to the press hardening process and therefore the cheapest and easiest to implement. First a robot transfers the blank to the plate heating station, which heats the blank above the solution annealing temperature. If the Extended Hotforming process is carried out, the area where the CFRP/ GFRP patch is to be placed must be laser structured. After passing through the continuous furnace, the next robot picks up the blank and inserts it into the quenching stage to lower the temperature to the melting temperature of the resin matrix of the patch, or if only Hotforming is carried out, directly into the forming/ quenching station. The CFRP/ GFRP patch is then applied and formed in a thermal direct joining step and cut in the die. The component is then placed on a conveyor belt and inspected using optical methods. Finally, the components are stacked and brought to an assembly or coating plant.

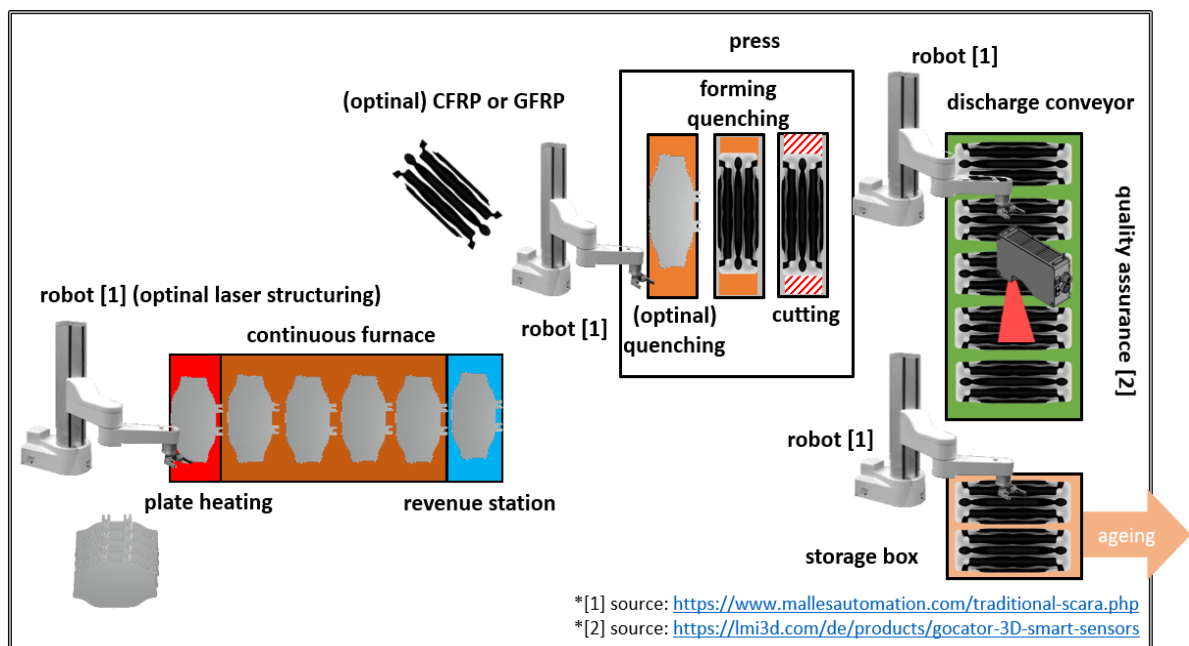


Figure 5-16: Schematic industrial layout of (Extended) Hotforming

5.7 Summary

First, a simplified industrial setup for the production of side impact beams with the various forming processes at elevated temperatures was established. Therefore a 120 tonnes press including a heated forming unit, an oven for solution annealing, a robot for the transfer of the blank and several measurement equipment were installed. Afterwards, the demonstrators were produced and strength, springback and thickness distribution values compared to each other. On that point, the influence of different AA7075 sheets, supplied by different material suppliers, could be demonstrated.

In particular, the mechanical properties of the AA7075 alloy from the material suppliers Alcoa, AMAG, Constellium and Novelis were exposed to the Hotforming and W-Temper processes and the mechanical parameters determined were then compared. For this purpose, tensile specimens were taken from the sidewall of the side impact beams, which exhibit low pre-stressing (low strain hardening). The results show that the Hotforming and W-temper processes, without heat treatment, have no influence concerning the different materials, since the strength and elongation values vary only within a small range of 15 MPa and 1.8 %. A significant difference of the material behaviour can be seen if one paint bake cycle (180°C for 20 min) is applied. Using the Hotforming process the UTS values and those for yield strength vary up to 73 MPa (~14 %) and 120 MPa (~25 %) respectively. The same trends can be detected for the W-Temper forming process. In this regard, further investigations were conducted to simulate the final component heat treatment in the automotive paint shop with three different paint baking cycles. The results show that using the Hotforming process and five paint bake cycles, the AA7075 alloy achieves 92 % of tensile strength and 88 % of yield strength compared to the strength values which can be obtained in the T6 state. If a lower number of paint bake cycles is used, a significant difference between the processes could be observed, especially in terms of yield strength.

For the springback and thickness distribution analysis, the demonstrators were measured and compared using computer tomography after the forming process without heat treatment. An increased springback behaviour could be determined on the components applied to the Warm-forming process. Further, a similar thickness distribution could be seen if all forming processes are considered and compared to each other.

Furthermore, the results of the Hotforming simulation were also compared with the corresponding CT-Scan and show a very good agreement (see Table 5-9). To evaluate the simulation for the final state component (after forming and one paint bake), a dynamic three-point bending test was carried out in the drop tower. Here, the reaction forces of the hinge joints and the acceleration of the impactor were compared.

Finally, industrial application process layouts were created of the forming process at elevated temperatures. These can be used both cost-effectively and on existing equipment of press hardened steels plants.

Chapter 6 Discussion, Conclusions and Further Work

This chapter provides a discussion and conclusion of this research. It is shown how the aims and objectives have been achieved, and the final results are listed. At the end of this chapter an outlook and suggestions for further work are given.

6.1 Discussion

In this thesis, the forming behaviour of high strength aluminium sheet alloy of the series 7000, in particular AA7075, is analysed in different forming processes. The focus is on the Hotforming process, and predictive models for the simulation are developed. Besides the determination of the material properties during the forming process and the final state of the component after paint bake, complex material and failure models were designed, which can also be used in the future for the design of structural components.

The analysis of the strength behaviour at various quenching rates shows that the AA7075 alloy is very sensitive to the quenching rate after solution annealing. This results in some limitations regarding forming at higher temperatures, including the transfer time and the furnace insertion temperature. The temperature just before forming should be above 400°C and the quenching rate should be not lower than 80 K/s in order not to lose strength. Quenching rates far above 80 K/s provide only marginal improvements in strength. It becomes clear that the quenching rate has a high influence on the achievable strength in the Hotforming and W-Temper process.

Based on these results, the conventional Hotforming process serves as a basis for a novel process called Extended Hotforming. For this process some modifications are made to generate crash relevant components with local reinforcements via an integrated thermal direct joining step. The advantage of this process is that highly stressed areas can be reinforced with a local patch made of CFRP or GFRP and produced in a short cycle time due to the combination of a forming and a joining process in the same step. Preliminary studies have shown that a structural component such as a side impact beam, which is substituted by high strength aluminium, has a lightweight construction potential of about 18 % with the same crash performance. Whereas a locally reinforced side impact beam has a weight saving of about 30 % to 40 % with constant stiffness and energy absorption. These values depend on individual design and material usage.

In order to develop a demonstrator component and to make the process predictable for the industry, complex material and failure models (Barlat YLD2000 and GISSMO) were developed and implemented for the forming process as well as for the final state of the material after cathodic dip painting. For this purpose, a test bench was built up to produce the material conditions during and after forming and to determine the material properties. Subsequently, optimisation strategies and Matlab scripts were created to generate these

complex material and damage models from experimental tests. In order to further improve the quality of the forming simulation, a suitable lubricant for the forming processes at elevated temperature was determined to avoid adhesion effects. Therefore, a friction test bench was designed and friction tests with different lubricants, temperatures and pressures were carried out. Afterwards a friction value model was created for the simulation. It has been shown that the Omega 35 lubricant offers the best lubrication conditions in comparison to the remainder lubricants that were tested. The results showed that the friction conditions improved at higher pressures, with continuous mixed friction condition ($0.05 < \mu < 0.1$). Furthermore, a deterioration of the friction conditions at elevated temperatures (180°C) has been observed, due to the reduction of the viscosity of the Omega 35 lubricant.

The generated material-, failure- and friction models were then used for the design and optimisation of a demonstrator part, a side impact beam. The boundary conditions and a simplified component test for this crash relevant component were derived from an open source model of a Toyota Yaris model and the Euro NCAP pole test. For an optimal shape, a topology optimisation was carried out, which was then transferred into a CAD-model of the side impact beam. Some optimisation loops were carried out to investigate and improve the forming and crash behaviour via FEM-simulation. In order to further increase the lightweight construction potential, a hybrid side impact beam was created using further structural optimisation methods such as fibre optimisation.

The final predicted component geometry was then used to design the die, punch and blank of the forming tool. Special attention was paid to the production of the demonstrator with all forming processes at elevated temperatures (Warm-forming, W-Temper and “Extended” Hotforming) and therefore, a heating concept close to the contour was developed and verified by means of a thermal transient and thermal steady state calculation. The tool was manufactured and measured with a coordinate measuring machine. Deviations of up to 0.2 mm were found, which could be compensated by spacer discs in the tool.

The tool was then installed in a 120 tonnes press and demonstrator side impact beams were produced by applying the different forming processes (Warm-forming, W-Temper and “Extended” Hotforming) and, if necessary, subjected to a paint bake at 180° for 20 minutes. The mechanical properties of the EN AW-7075 alloy from different material

suppliers were compared after applying the Hotforming and W-Temper processes. For this purpose, tensile specimens were taken from the sidewalls of the SIB, which exhibit low pre-stressing (low strain hardening). The results show that the Hotforming and W-Temper processes, without heat treatment, have no influence on the material properties of tested EN AW-7075 alloys (supplier-independent). However, a clear difference is noticeable after performing one paint bake cycle at 180°C for 20 minutes after forming. The Alcoa material achieves the highest values and is significantly better than those of the other suppliers. The yield strength is 517 MPa and the tensile strength 550 MPa, which is 100 % of the T6 condition compared to the data sheet. In this regard, further investigations were carried out to simulate the final component heat treatment in the automobile paint shop. Three different paint baking cycles were carried out with AMAG material due to the material availability and good strength values in the W-Temper process.

CT-Scans were carried out for a comparison regarding springback behaviour, thickness distribution and thinning of the demonstrator produced by different forming processes at elevated temperatures (without heat treatment). Furthermore, the Hotforming simulation was compared and verified with the corresponding CT-Scan. To validate the FEM-simulation of the component (after forming and one paint bake cycle), a dynamic three-point bending test was carried out in the drop tower test bench. Here, the reaction forces of the hinge joints and the acceleration of the impactor were compared. The high correlation between experiment and simulation is noticeable, which is due to the good quality of the previously calibrated material and failure models. These models can now be used for the simulation of the Hotforming process as well as for the component simulation.

For industrial application, process layouts of the forming process at elevated temperatures were created, which can be used on existing equipment from press hardened steel plants.

6.2 Conclusions

This thesis offers a new perspective regarding aluminium sheet metal forming. It was demonstrated that complex material models, such as Barlat YLD2000 and GISSMO offer a very good possibility to simulate and predict realistic forming processes and crash applications. For the calibration, different tensile tests, such as shear-, tensile-, notched and Erichsen are necessary, which have to be carried out experimentally and simulatively, and the mathematical models can be adapted with the help of a parameter optimiser.

To avoid adhesion effects, the graphite-containing Omega 35 lubricant was used for the production of a demonstration component, and a friction model, which is dependent on pressure and temperature, was implemented for the forming simulation.

A side impact beam made of high strength EN AW-7075 alloy and a heated forming tool were developed to produce the component using the Warm-forming, W-Temper and Hotforming processes. Intensive investigations regarding strength, quenching rate, ageing, supplier differences, thickness reduction and springback of the different processes were carried out and compared. On this basis, a layout for industrial implementation was developed that is both cost-effective and suitable for mass production.

However, there are still some process-related limitations such as:

- Accessible anti-friction agents that are suitable for forming high strength aluminium alloys at elevated temperature and which are approved by the OEMs.
- The dependence of quenching rate and the transfer times on strength.

It turned out that for crash-relevant components, such as a side impact beam, the lightweight construction potential is about 18 % weight reduction. In order to increase the lightweight potential even further, a concept and first investigations for a novel process called Extended Hotforming was developed, whereby the previously developed EN AW-7075 side impact beam is reinforced locally with a patch made of CFRP or GFRP using structural optimisation methods. With this Extended Hotforming process, which consists of the common Hotforming process including a thermal direct joining step, a patch can be applied during forming. By combining such hybrid material composites it is now possible to raise the lightweight construction potential to about 30 % - 40 %.

Forming of aluminium alloys at elevated temperature offers an interesting forming technique for the sheet metal processing industry and this thesis offers a basis for further research in that field.

6.3 Further Work

Related to this work, further investigations and developments have to be carried out:

- 1.) Further analyses are required for a more precise specification of the microstructural mechanisms of aluminium alloys during forming at higher temperatures. Depending on the degree of deformation and heat treatment, a dislocation density determination using a transmission electroscope would be valuable.
- 2.) Further material testing, particularly on a component formed at elevated temperature, must be carried out. Thereby, the crash behaviour of a component formed conventionally and formed at higher temperatures in combination with post-heat-treatments should be examined and compared.
- 3.) To further improve the adhesion effects during the forming of high strength aluminium alloys at high temperatures, further temperature dependent lubricant tests in combination with coatings should be carried out. Special attention should be paid to the applicability of lubrication in automation processes and that the OEM's standards are met. The washability of potential lubricants when applied to aluminium sheets is also of great importance. In this context, statements must be made about possible cathodic dip coating processes of the lubrication and the aluminium alloys.
- 4.) For a more detailed forming simulation, further temperature dependent material models should be created. Especially more detailed friction coefficient models, which are based on different lubricants, temperatures, pressures and strain conditions, should be implemented to improve the accuracy. In addition, forming limit curves should be generated, which are important for the design of the tool geometries and the evaluation of the components. For this purpose, a heated Nakajima tool was already developed and is now being built.

- 5.) Studies on adhesion, corrosion and strength should be carried out for the continuation and investigation of the Extended Hotforming process. Furthermore, the industrial suitability should be proven and a demonstration process should be established. For this purpose, a research application with the acronym “Serialform” must now be submitted to the Ministry of Education and Research (improved crash safety of high strength aluminium components through series production of thermal direct joining of local fibre reinforcements in the Hotforming process).

References

Altair Engineering (2017): "HyperWorks OptiStruct /RADIOSS User Guide", www.connect.altair.com/CP/documentation.html, last accessed May 2019

Andrade F., Feucht M., Haufe A. (2014): "On the Prediction of Material Failure in LS-DYNA- A Comparison Between GISSMO and DIEM", Wiley-Interscience, Bamberg, 2014

AutoForm Engineering GmbH (2019): "Software development", www.autoform.com, last accessed December 2019

Balbach R. (1988): "Optimierung der Oberflächenmikrogeometrie von Aluminiumfeinblech für das Karosserieziehen", (engl. Optimisation of the surface microgeometry of aluminium sheet for car body drawing), Vol. 97 of IFU - Berichte aus dem Institut für Umformtechnik der Universität Stuttgart, Springer Verlag, Berlin, Heidelberg, 2013, ISBN 978-3-642-83574-2, DOI 10.1007/978-3-642-83574-2

Banabic D. (2010): "Sheet Metal Forming Processes", Constitutive modelling and numerical simulation, Springer Verlag, Berlin, Heidelberg, 2010, ISBN 978-3-540-88113-1, DOI 10.1007/978-3-540-88113-1

Banabic D., Bunge H.-J., Pöhlandt K., Tekkaya A. E. (2000): "Formability of Metallic Materials - Plastic anisotropy, formability testing, forming limits" Springer Verlag, Berlin, Heidelberg, ISBN 978-3-540-67906-6, DOI 10.1007 / 978-3-662-04013-3

Barlat F., Brem J. C., Yoon J. W., Chung K., Dick R. E., Lege D. J., Pourboghrat F., Choi S.-H., Chu E. (2003): "Plane Stress Yield Function For Aluminum Alloy Sheets—Part 1: Theory", In International Journal of Plasticity, Vol. 19, No. 9, pp. 1297–1319, 2003, DOI 10.1016/S0749-6419(02)00019-0

- Barlat F. & Lian J. (1989): "Plastic Behaviour and Stretchability of Sheet Metals Part 1: A Yield Function For Orthotropic Sheet Under Plane Stress Conditions", International Journal of Plasticity, Vol. 5, pp. 51-66, Pergamon Press Inc., New York, USA, 1989 DOI 10.1016/0749-6419(89)90019-3
- Barlat F., Maeda Y., Chung K., Yanagawa M., Brem J. C., Hayashida Y., Lege D. J., Matsui K., Murtha S. J., Hattori S., Becker R. C., & Makosey. S. (1997): "Yield Function Development For Aluminum Alloy Sheets", Journal of the Mechanics and Physics of Solids, Vol. 45, No. 11-12, pp. 1727–1763, 1997, DOI 10.1016/S0022-5096(97)00034-3
- Birkert, A., Haage S., Straub M. (2013): "Umformtechnische Herstellung komplexer Karosserieteile - Auslegung von Ziehanlagen", (engl. Forming production of complex car body parts - Design of drawing plants), Springer Verlag, Berlin, Heidelberg, 2013, ISBN 978-3-642-34669-9, DOI 10.1007/978-3-642-34670-5
- Bridgman P. W. (1964): "Studies in Large Plastic Flow and Fracture - With special emphasis on the effects of hydrostatic pressure", Harvard University Press, 1964 ISBN 978-0-674-73133-2, DOI 10.4159/harvard.9780674731349
- Center for Collision Safety and Analysis (2010): "2010 Toyota Yaris Detailed Finite Element Model", commerce Building 4087 University Drive, Suite 2100, Fairfax, VX 22030, www.ccsa.gmu.edu/models/2010-toyota-yaris/, last accessed April 1019
- Cherniaev A., Montesano J., Butcher C. (2018): "Modeling The Axial Crush Response of CFRP Tubes Using Mat054 Mat058 and Mat262 In LS - DYNA", 15th International LS-DYNA User Conference, Detroit, 2018
- Hundertmark C. (2019): "Bechem - Lubriaction Solutions for Industry", Hagen, www.bechem.de/en/imprint.html, last accessed December 2019
- Clees T., Steffes-Iai D., Helbig M., Roll K., Feucht M. (2010): "Process Chain Forming to Crash: Efficient Stochastic Analysis", www.dynamore.de/de/download/papers/papers/konferenz09/papers-depr/F-IV-03.pdf, last accessed December 2019

- Czichos H.& Habig K.-H. (2015): "Tribologie-Handbuch - Tribometrie, Tribomaterialien, Tribotechnik" (engl. Tribology Handbook - Tribometry, Tribomaterials, Tribology), Springer Vieweg, Wiesbaden, 2015, ISBN 978-3-83481810-2, DOI 10.1007/978-3-8348-2236-9
- DIN EN ISO 10113 (2006): "Metallic Materials - Sheet And Strips - Determination Of Plastic Strain Ratio", Beuth Verlag GmbH, 2006
- DIN EN ISO 6892-1 (2017): "Metallic materials - Tensile testing - Part 1: Method of test at room temperature", Beuth Verlag GmbH, 2017
- Doege E. & Behrens B.-A. (2010): "Handbuch Umformtechnik - Grundlagen, Technologien, Maschinen", (engl. Forming Technology Handbook - Basics, Technologies, Machines), Springer Vieweg (VDI-Buch), Berlin, 2010, ISBN 3-642-04248-1
- Domke W. (1994): "Werkstoffkunde und Werkstoffprüfung", (engl. Materials science and materials testing), Cornelsen, Düsseldorf, Berlin, 1994, ISBN 3-590-81220-6
- Enke K. (1997): "Minderung von Reibung und Verschleiß von Bauteilen aus Aluminium mit diamantähnlichen Kohlenstoffschichten (DLC)", (engl. Reduction of friction and wear of aluminium components with diamond-like carbon layers - DLC), Materialwissenschaft und Werkstofftechnik, 1997, Vol 28, No. 11, pp. 520–523, DOI 10.1002/mawe.19970281108
- Euro NCAP (2015): "Side Pole Euro NCAP - For safety cars", www.euroncap.com/en/vehicle-safety/the-ratings-explained/adult-occupant-protection/lateral-impact/side-pole, last accessed May 2019
- Fan X., He Z., Yuan S., Lin P. (2013): "Investigation On Strengthening Of 6A02 Aluminum Alloy Sheet In Hot Forming-Quenching Integrated Process With Warm Forming-Dies", In Materials Science and Engineering, Vol. 587, pp. 221–227, 2013, DOI 10.1016/j.msea.2013.08.059

- Fan X., He Z., Zheng K., Yuan S. (2015): "Strengthening Behavior Of Al–Cu–Mg Alloy Sheet In Hot Forming–Quenching Integrated Process With Cold–Hot Dies", In *Materials & Design* 83, pp. 557–565, 2015, DOI 10.1016/j.matdes.2015.06.058
- Feucht M., Haufe A., Andrade F. (2017): "Damage and Failure Models in LS-Dyna", training course and documents, DYNAmore Gmbh, Daimler AG, 2017
- Grohmann T. (2016): "Forming of AMAG 7xxx Series Aluminium Sheet Alloys", *New Developments in Sheet Metal Forming*, Stuttgart, 2016
- Haufe A., DuBois P., Neukamm F., Feucht M. (2011): "GISSMO – Material Modeling With A Sophisticated Failure Criteria", *LS-DYNA Developer Forum*, Filderstadt, 2011
- Heine B. (2017): "Eigenschaften Metallischer Konstruktionswerkstoffe - Vorlesungsskript)", (engl. Properties of metallic structural materials - lecture notes), Aalen, 2018
- Hill R. (1948): "A Theory of the Yielding and Plastic Flow of Anisotropic Metals", *Proceedings of the Royal Society of London. Series A, Mathematical and Physical Sciences*, the Royal Society, Vol. 193, No. 1033, pp. 281-297, London, UK, 1948, ISSN 0080-4630
- Hoffmann H., Spur G., Neugebauer R. (2012): "Edition Handbuch der Fertigungstechnik" (engl. Edition handbook of production engineering), Hanser, München, 2012, ISBN 3-446-42778-3
- Hollomon J. H. (1945): "Tensile Deformation", *Transactions of the Metallurgical Society of AIME*, Vol. 162, 1945, pp. 268-290, 1945
- Ilchner B., Singer R. F. (2016): "Werkstoffwissenschaften und Fertigungstechnik - Eigenschaften, Vorgänge, Technologien (engl. Materials science and production engineering - Properties, processes, technologies)", Springer Vieweg, Berlin, Heidelberg ISBN 978-3-642-53891-9, DOI 10.1007/978-3-642-53891-9

- Josef K. (2019): "HumanTec GmbH - Lubricants", Leopoldshoehe www.humantec-schmierstoffe.de/impressum.html, last accessed January 2020
- Kammer C. (2012): "Aluminium-Taschenbuch", (engl. Aluminium pocketbook), Beuth, Berlin, 2012, ISBN 978-3-410-22028-2
- Kilic S., Kacar I., Sahin M., Ozturk F., Erdem O. (2019): "Effects of Aging Temperature, Time, and Pre-Strain on Mechanical Properties of AA7075", In Mat. Res., Vol 22, No. 5, pp. 4273, 2019, DOI 10.1590/1980-5373-mr-2019-0006
- Kondratiuk J. & Kuhn P. (2011): "Tribological Investigation On Friction And Wear Behaviour Of Coatings For Hot Sheet Metal Forming", Dortmunder Oberflächencentrum GmbH, Dortmund, Vol. 270 No. 11-12, pp. 839–849, 2011, DOI 10.1016/j.wear.2011.02.011
- Kovalchenko A., Ajayi O., Erdemir A., Fenske G., Etsion I. (2005): "The Effect Of Laser Surface Texturing On Transitions In Lubrication Regimes During Unidirectional Sliding Contact", In Tribology International, Vol. 38, No. 3, pp. 219–225, 2005, DOI 10.1016/j.triboint.2004.08.004
- Lange K. (1990): "Umformtechnik - Handbuch für Industrie und Wissenschaft", (engl. Forming technology - Handbook for industry and science), Springer Verlag, Berlin, Heidelberg, 1990, ISBN 978-3-662-10687-7, DOI 10.1007/978-3-662-10686-0
- Li Y., Luo M., Gerlach J., Wierzbicki T. (2010): "Prediction Of Shear-Induced Fracture In Sheet Metal Forming", In Journal of Materials Processing Technology, Vol. 210, No. 14, pp. 1858–1869, 2010, DOI 10.1016/j.jmatprotec.2010.06.021
- Lin J. (2016): "Low Cost Material Processing Technologies for Mass Production of Lightweight Vehicles - LoCoMaTech" European Union funded project, Imperial College of Science, Technology and Medicine, 2016

Liu S., Zhong Q., Zhang Y., Liu W., Zhang X., Deng Y. (2010): "Investigation Of Quench Sensitivity Of High Strength Al–Zn–Mg–Cu Alloys By Time–Temperature–Properties Diagrams", In *Materials & Design*, Vol. 31, No. 6, pp. 3116–3120
DOI 10.1016/j.matdes.2009.12.038

McKinsey & Company (2017): "CO₂-Regulierung sorgt bis 2030 für dreistelliges Milliardenwachstum im Leichtbau", (engl. CO₂-regulation ensures triple-digit billion growth in lightweight construction by 2030), www.mckinsey.de/co2-regulierung-sorgt-bis-2030-f%C3%BCr-dreistelliges-milliardenwachstum-im-leichtbau, 2017, last accessed April 2017

Mössle Erhard (1983): "Einfluß der Blechoberfläche beim Ziehen von Blechteilen aus Aluminiumlegierungen", (engl. Influence of the sheet surface during sheet metal forming of aluminium alloys), Springer Verlag, Berlin, Heidelberg, 1983, ISBN 978-3-642-52233-8

Nilmani M. (1997): "Aluminium Cast House Technology", Minerals Metals & Materials Society, Australian, Asian, Pacific Course and Conference Aluminium Cast House Technology Warrendale, 1997, ISBN 0-87339-378-3

Nitzsche G. (2007): "Reduzierung des Adhäsionsverschleißes beim Umformen von Aluminiumblechen", (engl. Reduction of adhesive wear during forming of aluminium sheets), *Berichte aus Produktion und Umformtechnik*, Ptu Darmstadt, Aachen, 2007 ISBN 978-3-8322-6719-3.

Oberhauser P., Sotirov N., Grohmann T., Schulz P. (2013): "Performance Of High Strength Alznmg(Cu) Aluminium Alloys After W-Temper And Warm Forming", TTP2013 - Tools and Technologies for Forming Ultra High Strength Materials, Graz, 2013

Ostermann F (2014): "Anwendungstechnologie Aluminium", (engl. Application Technology Aluminium), Springer Verlag, Berlin, Heidelberg, 2014, ISBN 978-3-662-43806-0, DOI 10.1007/978-3-662-43807-7

- Podgornik B., Hogmark S., Sandberg O. (2006): "Proper Coating Selection for Improved Galling Performance Of Forming Tool Steel", In *Wear*, Vol. 261, No. 1, pp. 15–21, 2006, DOI 10.1016/j.wear.2005.09.005
- Saarstahl AG (2017): "Werkstoff-Datenblatt: 42CrMo4", (engl. Material data sheet: 42CrMo4), www.saarstahl.de/sag/de/produkte/stahl-loesungen/maschinenbau/stahl-massivumformung/index.shtml, last accessed June 2019
- Sáenz de Argandoña E., Galdos L., Ortubay R., Mendiguren J., Agirretxe X. (2015): "Room Temperature Forming of AA7075 Aluminum Alloys: W-Temper Process", In *Key Engineering Materials*, Vol. 651-653, pp. 199–204, 2015, DOI 10.4028/www.scientific.net/KEM.651-653.199
- Sandberg H., Rydholm O. (2016): "Evaluation of Material Models to Predict Material Failure in LS-DYNA", Nordic LS-DYNA Users Conference 2016, Division of Solid Mechanics, Lund University, Sweden, 2016
- Sato T., Besshi T., Tsutsui I., Morimoto T. (2000): "Anti-Galling Property Of A Diamond-Like Carbon Coated Tool In Aluminum Sheet Forming", In *Journal of Materials Processing Technology*, Vol. 104 (1-2), pp. 21–24, 2000, DOI 10.1016/S0924-0136(00)00581-1
- Schneider R. (2015a): "An Analysis of Aluminium Sheet Metal Alloys on their Formability Behaviour at Cryogenic Temperatures", Dissertation, Department of Engineering and Applied Physics, University of Wales, Aalen University, 2015
- Schneider R., Heine B., Grant R. J., Zouaoui Z. (2015): "Aluminium Sheet Metal Forming at Low Temperatures", In *IOP Conference Series, Material Science and Engineering*, Vol. 74, pp. 12014, 2015, DOI: 10.1088/1757-899X/74/1/012014
- Schuler GmbH (1998): "Handbuch der Umformtechnik", (engl. Metal forming handbook), Springer Verlag, Berlin, 1998, Heidelberg ISBN 3-540-14760-8

- Siegert K. (2015): "Blechumformung. Verfahren, Werkzeuge und Maschinen", (engl. sheet metal forming, Springer Verlag, Berlin, Heidelberg, 2015, ISBN 978-3-540-02488-0 DOI 10.1007/978-3-540-68418-3
- Staeves J. (1998): "Beurteilung der Topografie von Blechen im Hinblick auf die Reibung bei der Umformung", (engl. Assessment of the topography of sheet metal with regard to friction during forming), Aachen, 1998, ISBN 3-826-54379-3
- Tingting M. & Taylan A. (2013): "Aluminium Sheet Forming for Automotive Applications, Part 1. Material Properties and Design Guidelines", www.StampingJournal.com, last accessed June 2019
- Totten G. (2016): "Heat Treating of Nonferrous Alloys", ASM International, Materials Park, OH. ASM handbook, Vol. 4E, 2016, ISBN 978-1-627-08113-9.
- U.S. Department of Transportation (2018): "Crash Simulation Vehicle Models", National Highway Traffic Safety Administration, www.nhtsa.gov/crash-simulation-vehicle-models, last accessed June 2019
- Voce E. (1948): "The Relationship Between Stress and Strain for Homogeneous Deformation" J. Int. Metals, Vol. 74 pp. 537–562, 1948
- Vogt U. (2009): "Near-Series Design Of Aluminum Tailored Heat Treated Blanks", Bamberg, Meisenbach (Fertigungstechnik - Erlangen), 2009, ISBN 3-875-25296-9
- Wang H., Chen M.-h., Friedman P., Gao L., & Luo Y.-b. (2012): "Warm Forming Behaviour of High Strength Aluminum Alloy AA7075", In Transaction of Nonferrous Metals Society of China Vol. 22, No. 1, pp. 1–7, 2012, DOI 10.1016/S1003-6326(11)61131-X
- Weißbach W. (2004): "Werkstoffkunde und Werkstoffprüfung", (engl. Materials science and testing), Vieweg & Teubner Verlag, Wiesbaden, 2004, ISBN 978-3-528-11119-9, DOI 10.1007/978-3-322-93987-6

Yoon J.-W., Barlat F., Dick R.E., Chung K., Kang T.J. (2004): "Plane Stress Yield Function For Aluminum Alloy Sheets—Part II: FE Formulation And Its Implementation", *International Journal of Plasticity*, Vol. 20, No. 3, pp. 495–522, 2004, DOI 10.1016/S0749-6419(03)00099-8

Zhang Y., Yi Y., Huang S., He H. (2017): "Influence of Temperature-Dependent Properties of Aluminum Alloy on Evolution of Plastic Strain and Residual Stress during Quenching Process", *In Metals*, Vol. 7, No. 6, pp. 228, 2017, DOI 10.3390/met7060228

Zhou R., Cao J., Wang Q.J., Meng F., Zimowski K., Xia Z.C. (2011): "Effect Of EDT Surface Texturing On Tribological Behavior Of Aluminum Sheet", *In Journal of Materials Processing Technology*, Vol. 211, No. 10, pp. 1643–1649, 2011, DOI 10.1016/j.jmatprotec.2011.05.004

Zhu M. Y., Zhu B., Liu Y., Zhang Y. S. (2019): "Investigation on Quench Rate of 7075 Aluminum Alloy Under Hot Stamping Conditions", Edited by Huazhong University of Science and Technology, Automotive Engineering Research Institute, Wuhan, China, pp 404-409, 2019, DOI 10.1142/9789813277984_0060

Appendices

Appendix A198
Appendix B200
Appendix C204
Appendix D206
Appendix E211
Appendix F213
Appendix G223
Appendix H236
Appendix I238

Appendix A

Appendix A shows the designation system after DIN EN 573-3/4. In the following table are the group names, main elements and whether the alloy is hardenable. Further, some comments about corrosion, formability and welding as well as the range of ultimate tensile strengths of each alloy group are given.

Appendix A: Overview about designation system of aluminium alloys based on DIN EN 573-3/4

group	main alloying element	hardenability	strength in N/mm ²	comment
1xxx	min. 99 % aluminium	not hardenable	70...190	<ul style="list-style-type: none"> also called pure aluminium; weldable; very corrosion resistant; used for aluminium foil, chemical tanks and pipes; high electrical conductivity.
2xxx	copper	hardenable	190...570	<ul style="list-style-type: none"> high strength used in aircraft and aerospace welding additive mostly 2xxx, sometimes also 4xxx
3xxx	manganese	not hardenable	100...350	<ul style="list-style-type: none"> low strength high corrosion resistance good formability also suitable for higher temperatures field of application from cooking pots over radiators in vehicles up to power plant construction. welding additives 1xxx, 4xxx and 5xxx
4xxx	silicon	hardenable and not hardenable alloys	170...380	<ul style="list-style-type: none"> 0.6 to 21.5 % Si only series with hardenable and non-hardenable alloys for hardenable magnesium is required in addition. Silicon reduces the melting point. ideal for welding and soldering additives
5xxx	magnesium (without silicon)	not hardenable	100...450	<ul style="list-style-type: none"> medium to high strengths weldable used for shipbuilding, pressure vessels and bridges as AA5024 (AlMgSc). Aluminium of this series with more than 3.0% Mg is not suitable for temperatures above 65°C (stress corrosion). Material with less than about 2.5% Mg can often be welded successfully with 5xxx or 4xxx filler metals.
6xxx	magnesium and silicon	hardenable	100...450	<ul style="list-style-type: none"> Si and Mg around 1 % very popular in welding constructions used mainly as extruded profiles can be heat-treated well should not be welded without welding filler (4xxx & 5xxx)
7xxx	zinc	hardenable	220...700	<ul style="list-style-type: none"> 0.8 to 12.0 % Zn used in aircraft, aerospace, mobile phone cases and watches. some alloys are not weldable with electric arc The 7005 and 7020 are well weldable with 5xxx as filler metals, because these two alloys do not contain copper.
8xxx	other elements	variable	variable	<ul style="list-style-type: none"> e.g. aluminium-lithium alloys of the first generation

Appendix B

Appendix B shows the Matlab script that calculates the material parameter for the Barlat YLD2000 material model. While it is running, the α -values are generated from the Lankfort parameter (r_0, r_{45}, r_{90} & r_b) and the yield strengths ($\sigma_0, \sigma_{45}, \sigma_{90}$ & σ_b). This programme is used in the parameter optimisation with LS-OPT and developed in cooperation with the company Altair.

Appendix B: Matlab script for calculation of the α -values for Barlat YLD2000 material model

```

global z x
global r0 r45 r90 rb sigma_0 sigma_45 sigma_90 sigma_b a

a=input('a');
r0=input('r0');
r45=input('r45');
r90=input('r90');
rb=input('rb');
sigma_0=input('sigma_0');
sigma_45=input('sigma_45');
sigma_90=input('sigma_90');
sigma_b=input('sigma_b');

zg=[1 ; 1 ; 1 ; 1 ; 1 ; 1];
z=fsolve(@yld2000_1,zg);

xg=[1 ; 1 ];
x=fsolve(@yld2000_2,xg);

alpha1=z(1);
alpha2=z(2);
alpha3=z(3);
alpha4=z(4);
alpha5=z(5);
alpha6=z(6);
alpha7=x(1);
alpha8=x(2);

try

    % Write responses and histories to MatlabOutput file
    fid = fopen('MatlabOutput','w');
    fprintf(fid,'#\n');
    fprintf(fid,'RESPONSES\n');
    % response
    fprintf(fid,'%d, %s, %f\n',0,'alpha1',alpha1);
    fprintf(fid,'%d, %s, %f\n',0,'alpha2',alpha2);
    fprintf(fid,'%d, %s, %f\n',0,'alpha3',alpha3);
    fprintf(fid,'%d, %s, %f\n',0,'alpha4',alpha4);
    fprintf(fid,'%d, %s, %f\n',0,'alpha5',alpha5);
    fprintf(fid,'%d, %s, %f\n',0,'alpha6',alpha6);
    fprintf(fid,'%d, %s, %f\n',0,'alpha7',alpha7);
    fprintf(fid,'%d, %s, %f\n',0,'alpha8',alpha8);
    fprintf(fid,'END\n');
    fprintf(fid,'#\n');

    ChkClose=fclose(fid);
    diary matstatus;
    disp('N o r m a l   t e r m i n a t i o n');
    diary off
catch
    % Write error termination status
    diary matstatus;
    disp('E r r o r   t e r m i n a t i o n');
    diary off;
end

```

```

exit

function [Fz]=yld2000_1(z)
%YLD2000_1 Summary of this function goes here
% Detailed explanation goes here

global r0 r45 r90 rb sigma_0 sigma_45 sigma_90 sigma_b a a1 a2 a3 a4
a5 a6

a1=z(1);
a2=z(2);
a3=z(3);
a4=z(4);
a5=z(5);
a6=z(6);

Fz(1)=(abs((2/3)*a1-(-1/3)*a2))^a + (abs((2/3)*a3+(-1/3)*2*a4))^a +
((abs((2/3)*2*a5+(-1/3)*a6))^a) - 2*(1/sigma_0)^a;
Fz(2)=(abs((-1/3)*a1-(2/3)*a2))^a + (abs((-1/3)*a3+(2/3)*2*a4))^a +
((abs((-1/3)*2*a5+(2/3)*a6))^a) - 2*(1/sigma_90)^a;
Fz(3)=(abs((-1/3)*a1-(-1/3)*a2))^a + (abs((-1/3)*a3+(-1/3)*2*a4))^a +
((abs((-1/3)*2*a5+(-1/3)*a6))^a) - 2*(1/sigma_b)^a;
Fz(4)=((1-r0)*a1+(2+r0)*a2)*((2/3)*a1-(-1/3)*a2)*(abs((2/3)*a1-(-
1/3)*a2))^a - 2 + ((1-r0)*a3-2*(2+r0)*a4)*((2/3)*a3+(-
1/3)*2*a4)*(abs((2/3)*a3+(-1/3)*2*a4))^a - 2 + ((1-r0)*2*a5-
(2+r0)*a6)*((2/3)*2*a5+(-1/3)*a6)*(abs((2/3)*2*a5+(-1/3)*a6))^a - 2;
Fz(5)=((2+r90)*a1+(1-r90)*a2)*((-1/3)*a1-(2/3)*a2)*(abs((-1/3)*a1-
(2/3)*a2))^a - 2 + ((2+r90)*a3-2*(1-r90)*a4)*((-
1/3)*a3+(2/3)*2*a4)*(abs((-1/3)*a3+(2/3)*2*a4))^a - 2 +
((2+r90)*2*a5-(1-r90)*a6)*((-1/3)*2*a5+(2/3)*a6)*(abs((-
1/3)*2*a5+(2/3)*a6))^a - 2;
Fz(6)=((1+2*rb)*a1+(2+rb)*a2)*((-1/3)*a1-(-1/3)*a2)*(abs((-1/3)*a1-(-
1/3)*a2))^a - 2 + ((1+2*rb)*a3-2*(2+rb)*a4)*((-1/3)*a3+(-
1/3)*2*a4)*(abs((-1/3)*a3+(-1/3)*2*a4))^a - 2 + ((1+2*rb)*2*a5-
(2+rb)*a6)*((-1/3)*2*a5+(-1/3)*a6)*(abs((-1/3)*2*a5+(-1/3)*a6))^a - 2;

end

function [Fx]=yld2000_2(x)
%YLD2000_2 Summary of this function goes here
% Detailed explanation goes here
global z
global r0 r45 r90 rb sigma_0 sigma_45 sigma_90 sigma_b a a1 a2 a3 a4
a5 a6 a7 a8

a1=z(1);
a2=z(2);
a3=z(3);
a4=z(4);
a5=z(5);
a6=z(6);
a7=x(1);
a8=x(2);

x1=(a1+a2)/3;
x2=(a1-a2)/3;
x11=(a3+2*a4+2*a5+a6)/9;
x22=(2*a5+a6-a3-2*a4)/3;

```

```
v1=a*((sqrt(x2^2+4*a7^2))/2)^(a-1);
v11=a*((3*x11-sqrt(x22^2+4*a8^2))/4)*(abs((3*x11-
sqrt(x22^2+4*a8^2))/4))^(a-2);

w11=a*((3*x11+sqrt(x22^2+4*a8^2))/4)*(abs((3*x11+sqrt(x22^2+4*a8^2))/
4))^(a-2);

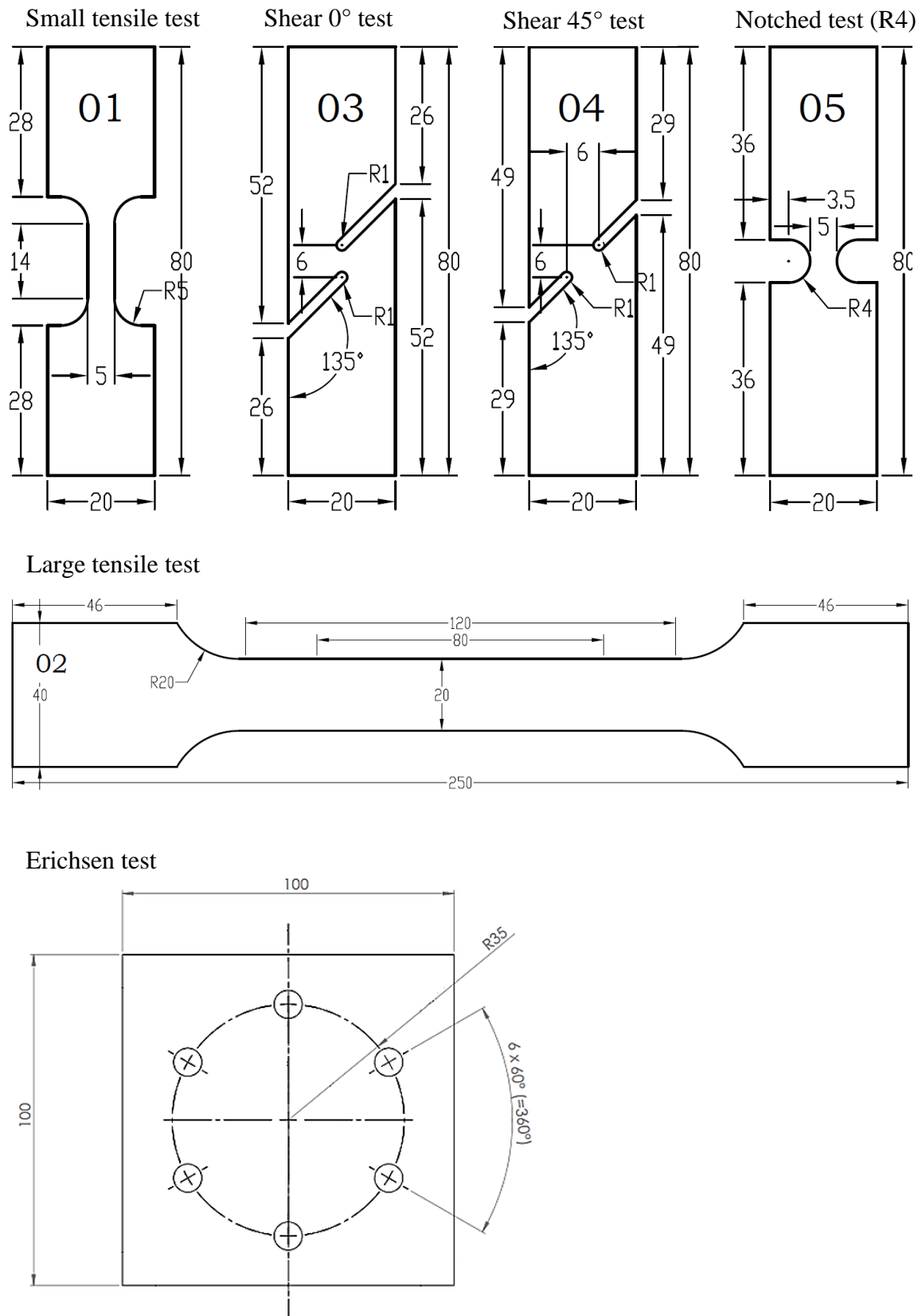
Fx(1)=(abs((sqrt(x2^2+4*a7^2))/2))^a + (abs((3*x11-
sqrt(x22^2+4*a8^2))/4))^a + (abs((3*x11+sqrt(x22^2+4*a8^2))/4))^a -
2*(1/sigma_45)^a;
Fx(2)=v1*(x2^2/(sqrt(x2^2+4*a7^2))) +
1.5*x11*(v11*w11)+0.5*(x22^2/(sqrt(x22^2+4*a8^2)))+(w11-v11)-
(2*a/(1+r45))*(1/sigma_45)^a;

end
```

Appendix C

In Appendix C the drawings of each specimen for the GISSMO failure and damage model, which are representative for different triaxiality such as tensile, shear (various shear angle), biaxiality are illustrated. For the element regularisation the large tensile specimen is used.




Appendix C: GISSMO specimen for damage and failure curve





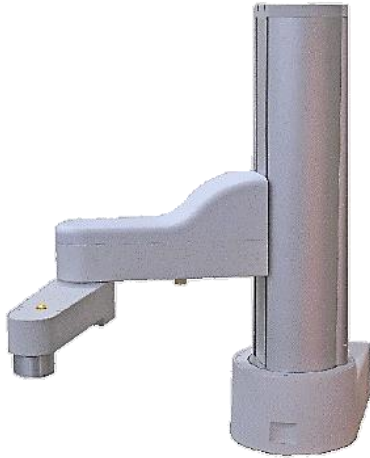
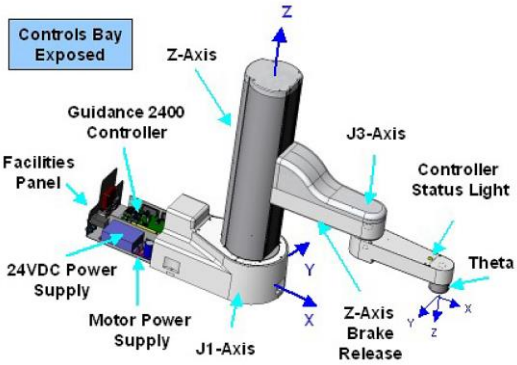

Appendix D

Appendix D gives an overview of the laboratory equipment used. More details about the individual components are listed, which are taken from data sheets, if available.

Appendix D: Overview of the equipment used and detailed specifications

<p>Schenck tensile testing machine</p> 	<ul style="list-style-type: none"> • Schenck tensile testing machine RSA • Maximum force 100 kN • Traverse stroke 1400 mm • Longitudinal compliance • $8 * 10^{-3} \text{ mm/kN}$ • Weight 500 kg • External digital controller • Doli EDC 220 • Force resolution $\pm 180,000$ steps • Climate chamber • Maximum temperature 300°C • Power 4 KW
<p>GOM Aramis Adjustable 2.3M</p> 	<ul style="list-style-type: none"> • 2x 2.3M pixel cameras resolution 1936 x 1216 pixel • Frame rate: min. 100 Hz frame rate with GOM Testing Controller: • 130 Hz at 1936 x 1216 pixels (full screen) • 240 Hz at 1936 x 604 pixels (1/2 image) • 450 Hz at 1936 x 302 pixels (1/4 image) • Calibrated and certified until 2022
<p>Muffle furnace</p> 	<ul style="list-style-type: none"> • Type Linn High Therm LM-312.27 • Controller G 800 P • Maximum temperature: 1340 °C • Heating capacity: 2.8 kW • Heating method: Resistance • Interior (W x H x D): approx. 175 x 95 x 300 mm (approx. 5 litres) • Thermocouple: PtRh-Pt, type S

<p>Heraeus VT 5050</p> 	<ul style="list-style-type: none"> • Type VT 5050 EK • No. 8554371 • Year of construction 1982 • Vacuum drying furnace • Maximum temperature 500°C • Interior (W x H x D): approx. 420 x 340 x 350 mm (approx. 50 litres) • Inner width 420 mm, Inner depth 350 mm, Inner height 340 mm • Electrical heating, Electrical power 3.96 KW, 380 Volt, 10.42 Ampere
<p>DEMA hydraulics press 20 tonnes</p> 	<ul style="list-style-type: none"> • Maximum pressure: 20 tonnes • Working range: 0 - 113 cm • Working width: 51 cm • Stamp: Ø4.8 cm & 19 cm working length • Working pressure: min. 8.5 bar - max. 12.3 bar • Basic dimensions LxDxH: approx. 59.5x700x181 cm • Total weight: Approx. 83.27 kg • Pressure indication by manometer

<p>Scara PreciseFlex 1300 Robot</p> 	<p>The robot includes an embedded Guidance 2400C fouraxis motion controller, a PrecisePower 300 Intelligent Motor Power Supply, and a 24VDC power supply located inside the base of the robot. The major elements of the PreciseFlex robot and the orientations of its World and Tool Cartesian Coordinate systems are shown in the diagram below:</p> 
<p>USB TC-08, 8-Channel 16-Bit Temperature Logger for Thermocouples</p> 	<ul style="list-style-type: none"> • 8 channel thermocouple data logger • Measures from 1 to 160 thermocouples • Measures from -270 to +1820 °C • Automatic cold junction compensation • High resolution and accuracy • Fast sampling rate - up to 10 measurements per second

Rapp u. Seidt hydraulic press



- Pressure: 120 tonnes
- Stand width: 250 mm
- Maximum press stroke: 500 mm
- Machine weight approx.:
1.75 tonnes
- Space requirement approx.:
1.85 x 1.34 x 2.70 m

Appendix E

Appendix E shows the Matlab script that calculates the von Mises flow curve out of the input parameter. The extrapolation is created after Hockett & Sherby, which contains the parameter a , b , c and n . To use the material model MAT_24 (von Mises) in LS-DYNA it is necessary to calculate the flow curve in tabular form, which has a fine resolution in the area of the yield strength and is then specified more roughly. At the end the flow curve is written to a MatlabOutput.k and a “normal termination” is carried out, which allows the optimiser parameter to continue. This file is then integrated into the simulation as a material model.

Appendix E: Matlab script for calculation of von Mises flow curve in tabular form

```

%Definition of the variable
global a b c n A B AS BS AOut BOut

% Input of the Hockett&Sherby parameter
a=input('a');
b=input('b');
c=input('c');
n=input('n');

% Generation of the strain vectors
% A is finely resolved from 0 to 0.0035
% B is roughly resolved from 0.004 to 1
A=0:0.000125:0.0035;
B=0.004:0.002:1;

% Calculation of the stress vectors according to Hockett&Sherby
AS=a-b*exp(-c*A.^n);
BS=a-b*exp(-c*B.^n);

% Merging the vectors into matrixes
AOut=[A;AS];
BOut=[B;BS];

try

    % Writing of the MatlabOutput.k file
    fid = fopen('MatlabOutput.k','w');
    % Definition of the curve for LS-DYNA
    fprintf(fid,'*DEFINE_CURVE_TITLE\n');
    fprintf(fid,'14301_geglueht\n');
    fprintf(fid,'$# lcld sidr sfa sfo offa offo dattyp lcint\n');
    fprintf(fid,' 2 0 1.0 1.0 0.0 0.0 0 0\n');
    fprintf(fid,'$#          a1          o1\n');
    % Writing the flow curve
    fprintf(fid,'          %f          %f\n',AOut);
    fprintf(fid,'          %f          %f\n',BOut);

    % Closing/saving the file
    ChkClose=fclose(fid);

    % Normal termination output for LS-OPT after successful creation
    of the file
    diary matstatus;
    disp('N o r m a l   t e r m i n a t i o n');
    diary off
catch

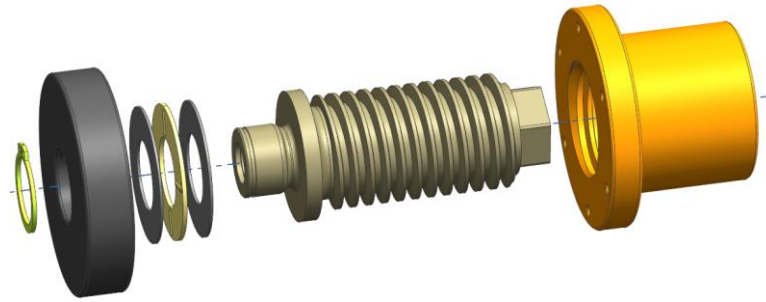
    % Error termination Output for LS-OPT on error
    diary matstatus;
    disp('E r r o r   t e r m i n a t i o n');
    diary off;
end
exit

```

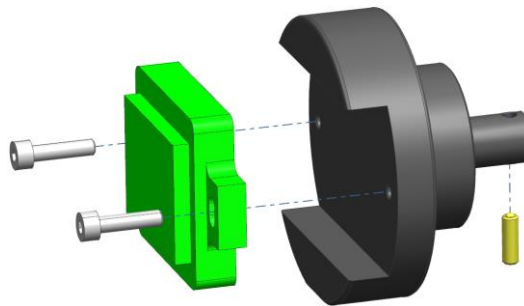
Appendix F

Assembly instructions were worked out and illustrated with figures. They explain step by step how to assemble the tool and what to pay attention to. In addition, images of the finished strip drawing test bench are attached. Different simulations are carried out to check the range measured by the strain gauge. Furthermore, a stress analysis was carried out to rule out plasticisation of the friction jaw holder. For more detailed information, the strain gauge datasheet and additional information about the lubricants used have been added.

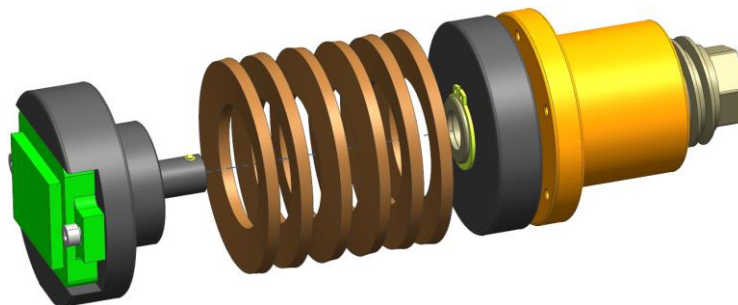
Appendix F: Overview of the individual assembly steps of the strip drawing tool



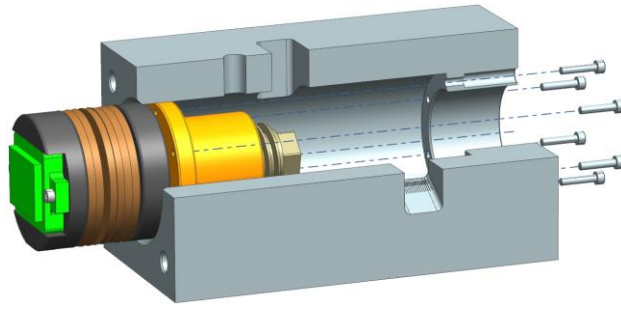
Screw the trapezoidal spindle into the threaded nut. Insert the axial needle roller bearing into the guide part and slide the shaft journal onto the trapezoidal spindle. Insert the circlip at the end of the shaft end into the groove.



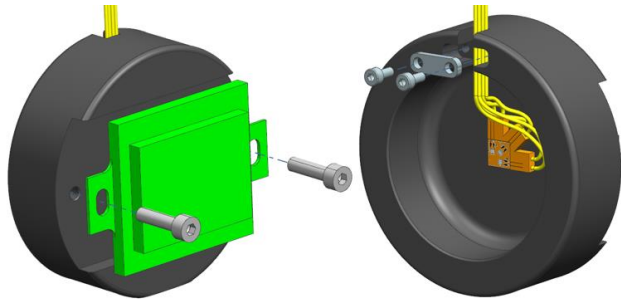
Fix the friction jaws to the friction jaw holder and screw in the thrust piece.



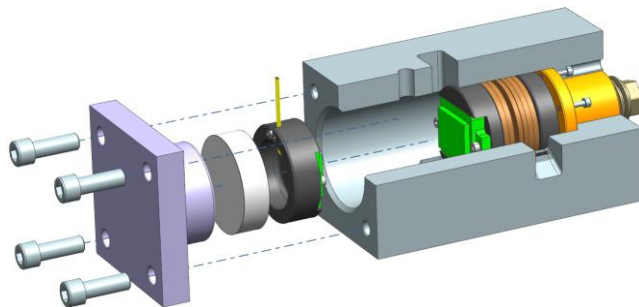
Insert the spring column between the friction jaw holder and the guide component. Push the parts together until the ball of the thrust piece locks in by itself.



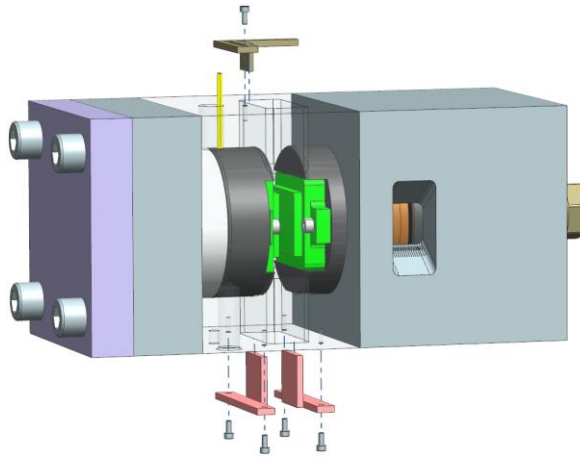
Insert the assembly from the previous step into the housing and slide it backwards. Align the threaded holes of the nut and screw to the housing.



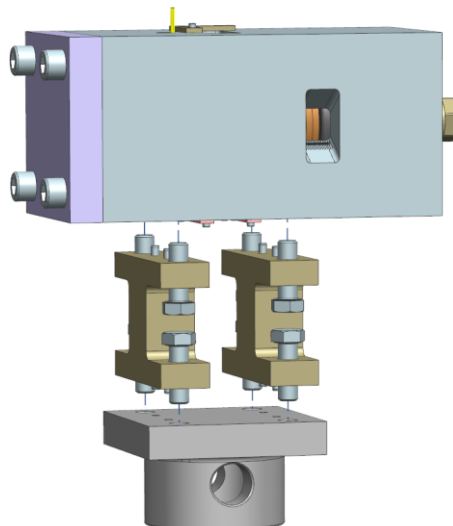
Fix the friction jaw to the holder. Secure the strain gauge cable with a cable fuse.



Insert the friction jaw holder into the housing. Lead the strain gauge cable through the through hole in the housing. Insert distance washer and screw cover tight (79Nm) to housing.



Attach sheet metal centring and anti-twist device to the housing.



Screw the strip drawing tool to the toolbars and base plate (79 Nm).

Appendix F: Images of the strip drawing tool



Appendix F: Specification of strain gauge for high temperatures; 0°/45°/90° element rosette (green box)

■ Description

Compatible adhesive & Operational temperature
 NP-50: - 20~ + 200°C
 C-1: - 20~ + 200°C CN: - 20~ + 120°C

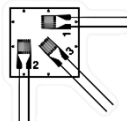
Operational temperature -20~+200°C
 Temperature compensation range +10~+100°C

HIGH TEMPERATURE USE

Gauge pattern	Type	Gauge size		Backing		Resistance in Ω
		L	W	L	W	
This gauge utilizes polyimide resin as a backing. Strain measurement in high temperature is easily realized by bonding the gauge with room temperature curing adhesive NP-50.		L : length		W : width (Unit : mm)		
	QFLG-02-11	0.2	1.4	3.5	2.5	120

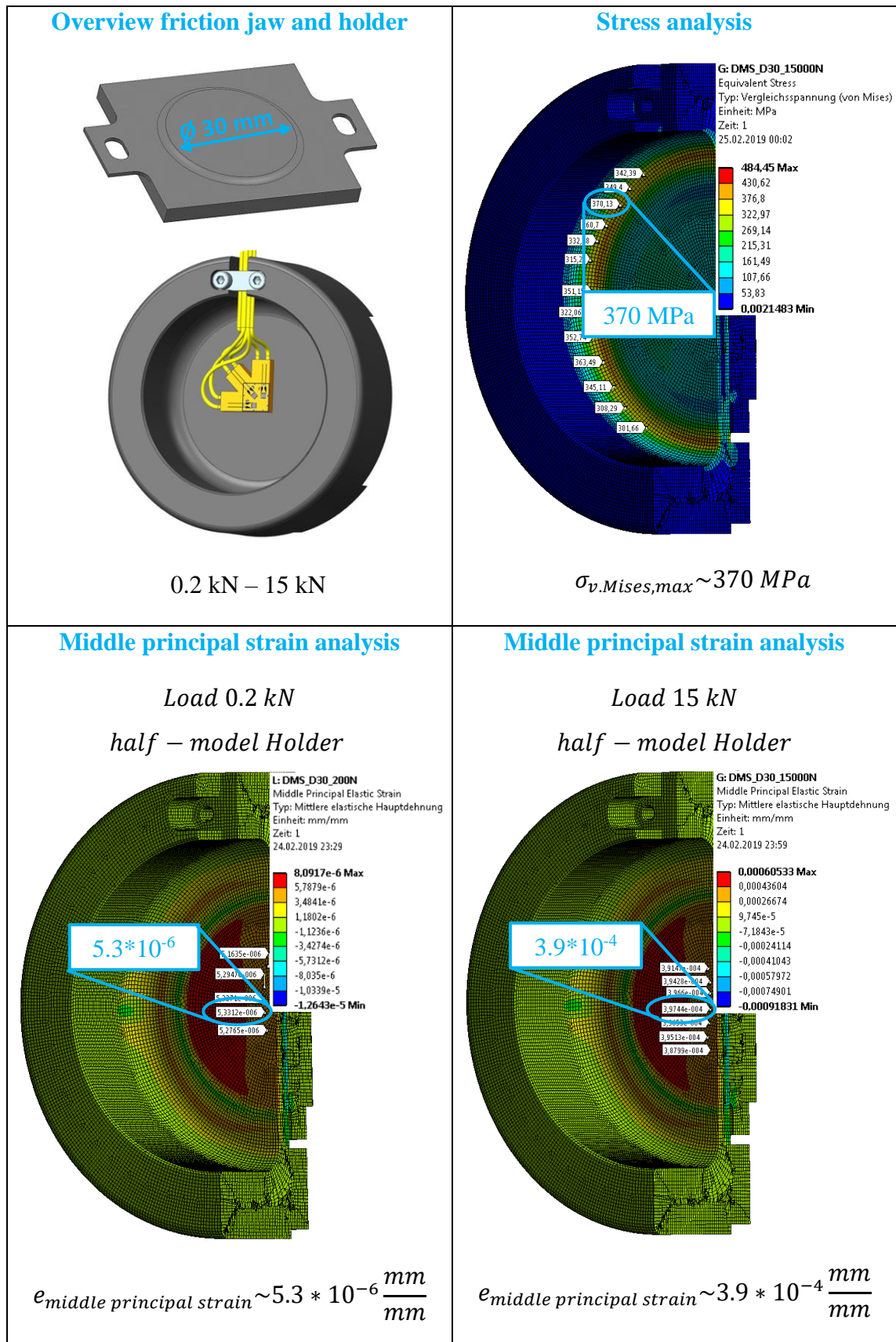
● 45° /90° 3-element Rosette

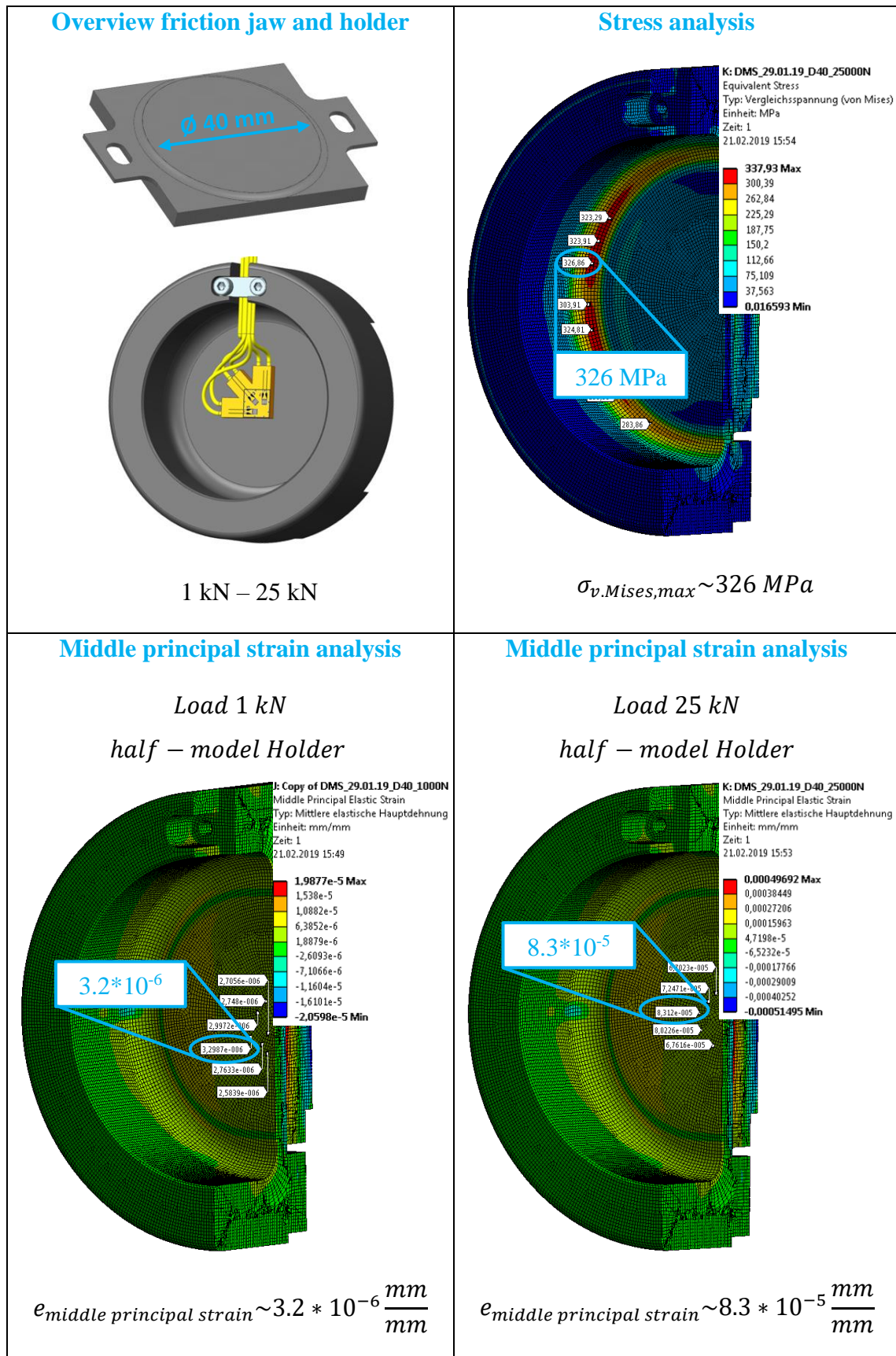
Plane type

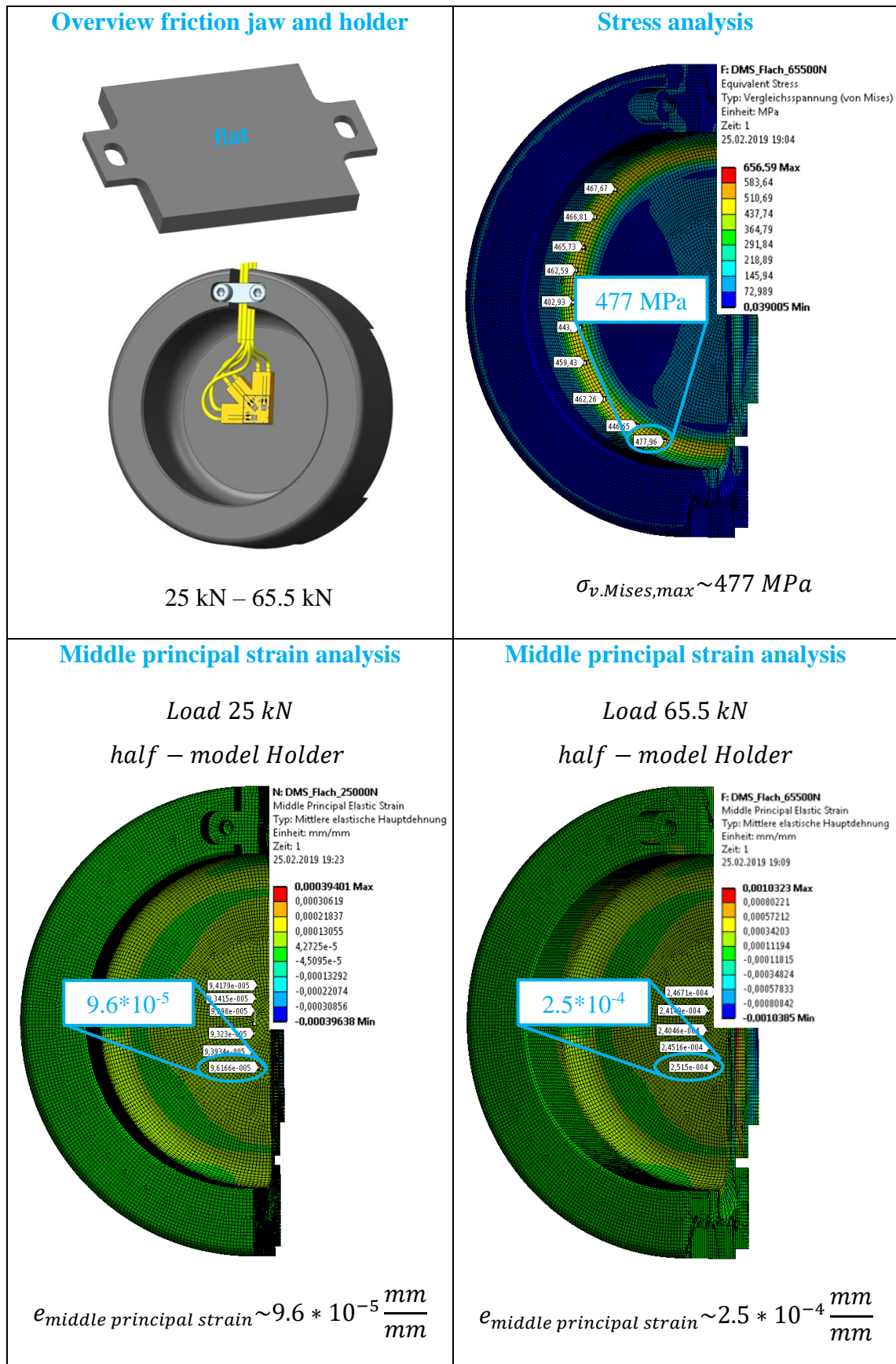


QFRA-1

45° /90° 3-element Rosette, Plane type	QFRA-1-11	1	1.3	7.2	7.2	120
	QFRA-3-11	3	1.7	11.0	11.0	120

Appendix F: Simulation results of the friction jaw and holder with Ø 30 mm heel


Appendix F: Simulation results of the friction jaw and holder with Ø 40 mm heel


Appendix F: Simulation results of the friction jaw and holder without a heel (flat)


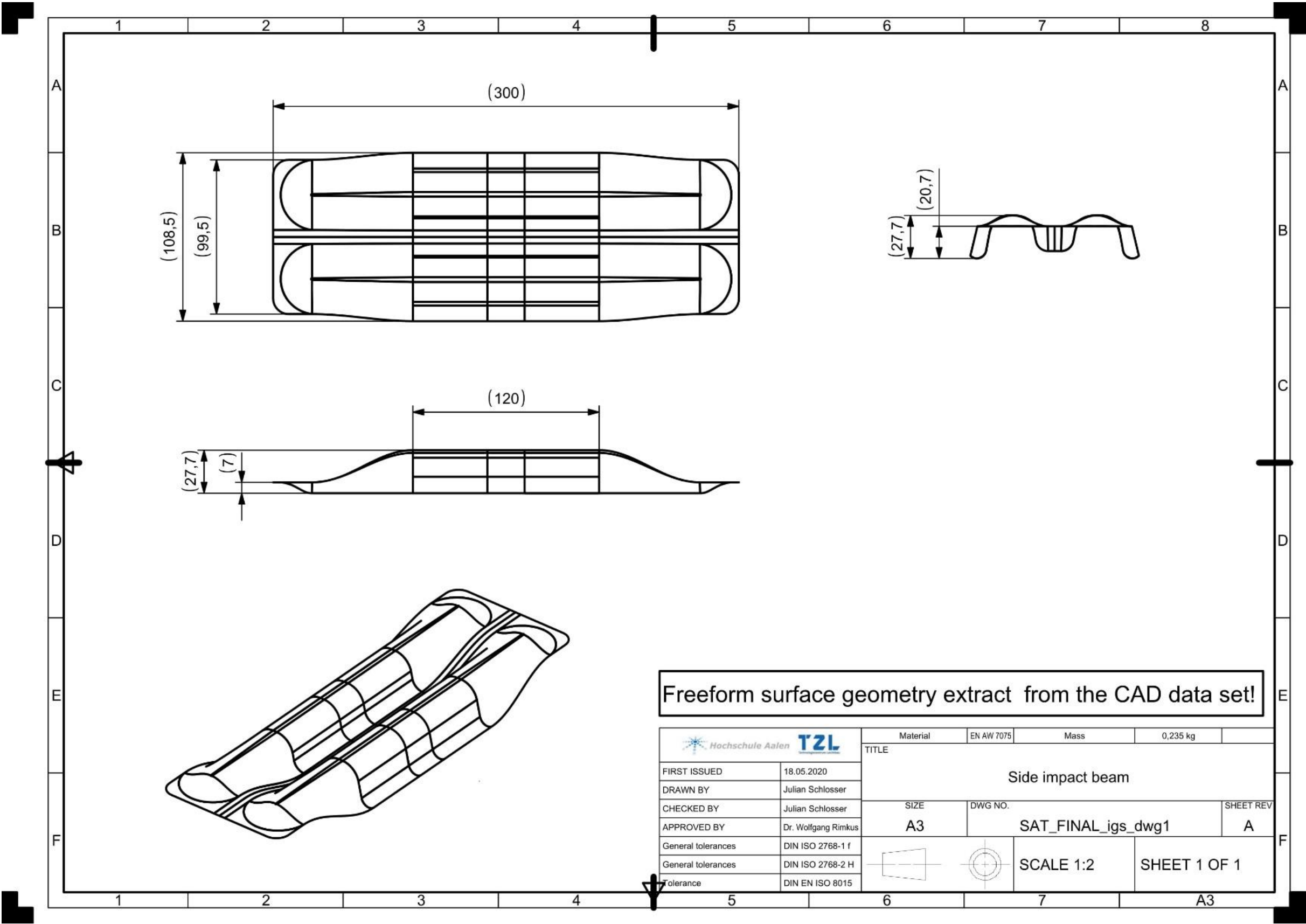
Appendix F: Lubricants specifications

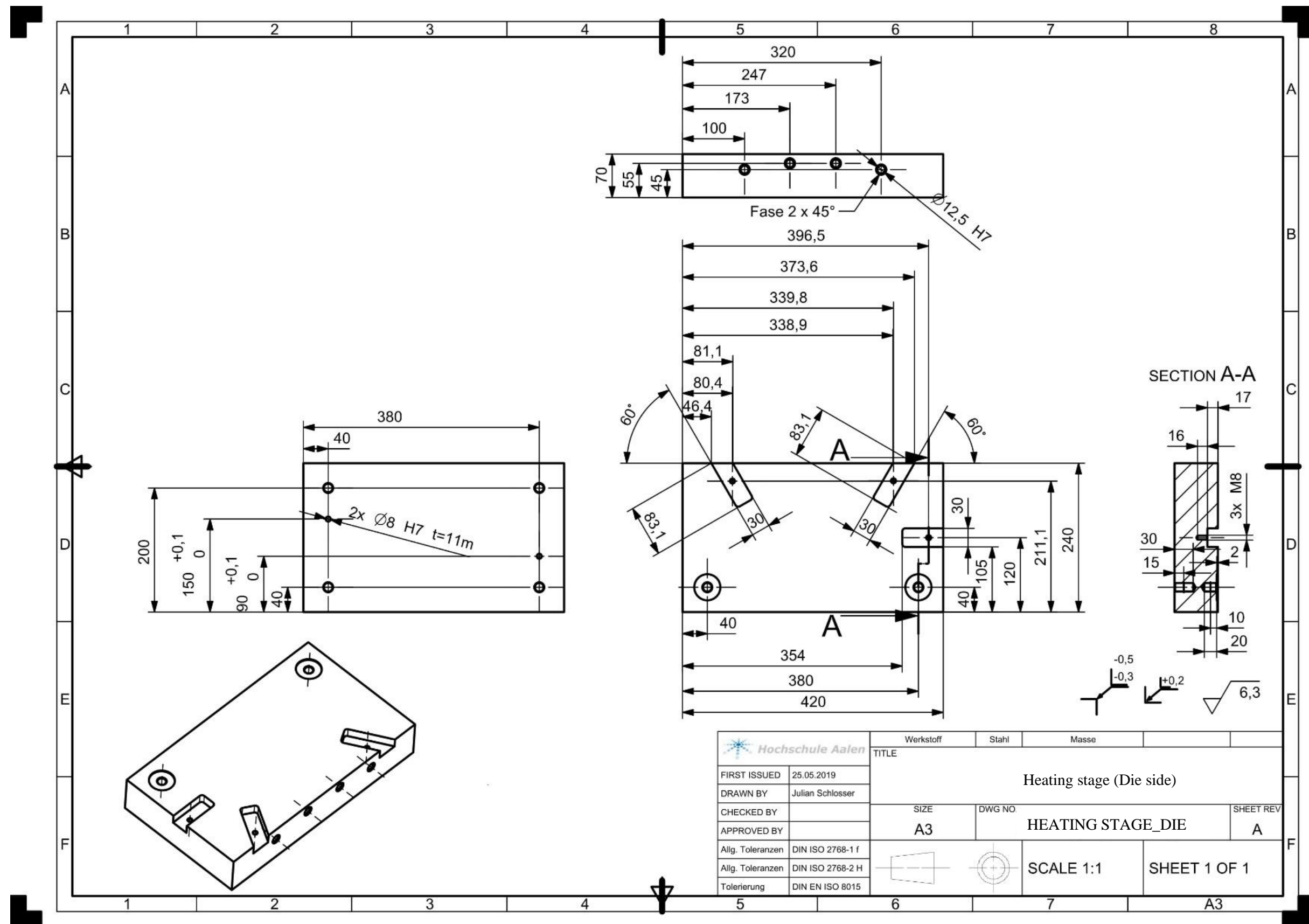
XP 10 (Bechem)	<ul style="list-style-type: none"> • Maximum temperature 950°C • Liquid lubricant <p>For more information: www.bechem.de (Hundertmark 2019)</p>	<ul style="list-style-type: none"> • Laboratory lubricant • Developed for Hotforming
Beruforge 120 D (Bechem)	<ul style="list-style-type: none"> • Colour: White • Density: 1.5-1.2 g/cm³ • Maximum temperature 320°C • Liquid lubricant • Aqueous suspension of solid lubricants • Produces very smooth surfaces • High deformation can be achieved <p>For more information: www.bechem.de (Hundertmark 2019)</p>	<ul style="list-style-type: none"> • Complex parts for cold massive forming • Deep drawing • Bending • Stamping
Berulit 935 H (Bechem)	<ul style="list-style-type: none"> • Colour: Black • Density: 1.12-1.16 g/cm³ • Maximum temperature 950°C • Liquid lubricant • Good separation capacity • Wear protective • High temperature stability <p>For more information: www.bechem.de (Hundertmark 2019)</p>	<ul style="list-style-type: none"> • Blank coating • Hotforming
Omega 35 (HumanTec)	<ul style="list-style-type: none"> • Colour: Grey / black • Density: 1.33 g/cm³ • Maximum temperature 700°C • Dry lubricant <p>For more information: www.humantec-schmierstoffe.de (Kirberich 2019)</p>	<ul style="list-style-type: none"> • Omega 35 is a universal grease for virtually every type of application

Appendix G

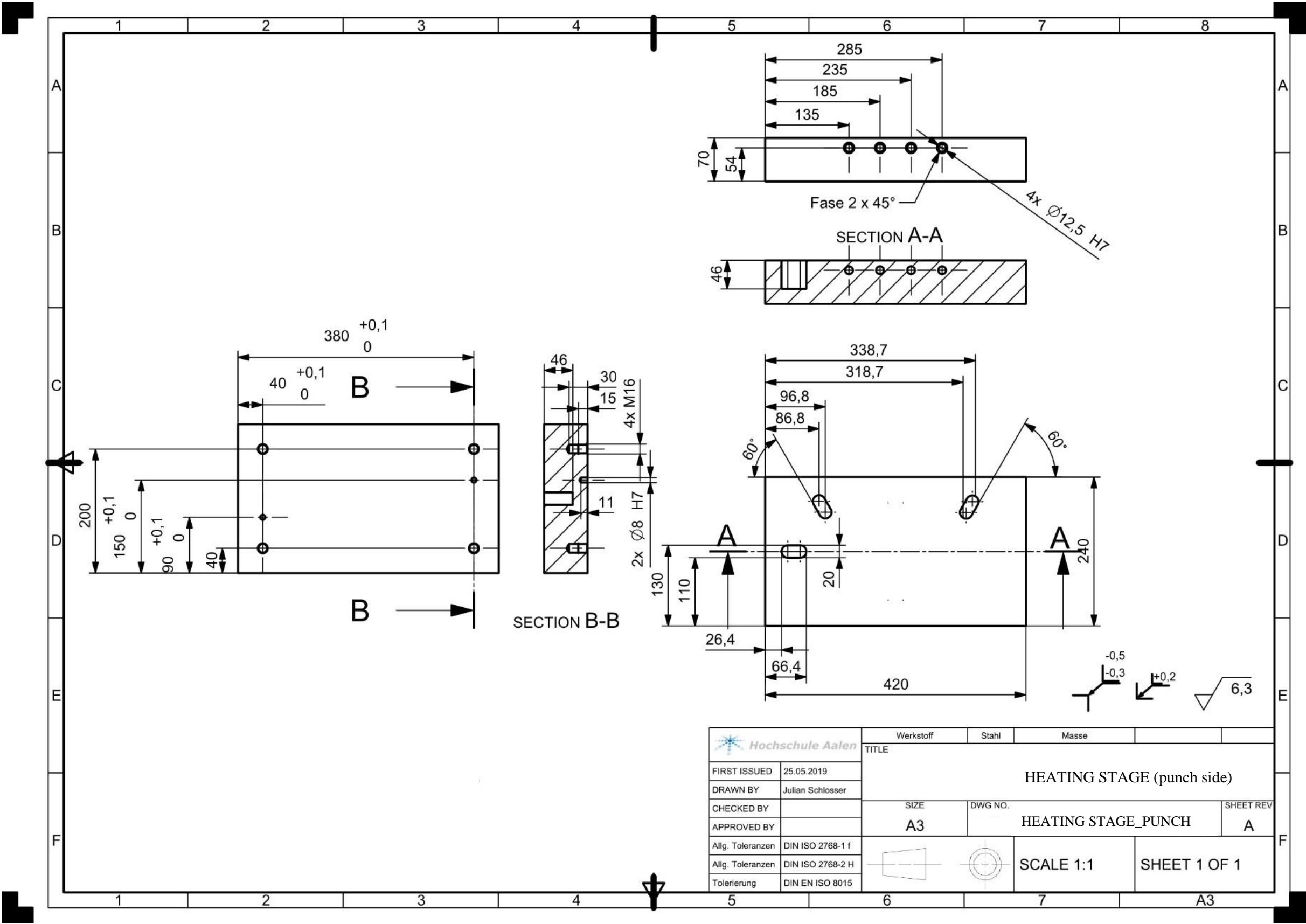
Appendix G shows various technical drawings of the forming tool and the side impact beam, which were made for the production of the individual components. Production dimensions, tolerances, surface details, etc. are shown in detail on the drawings. In addition, free-form surfaces were produced with CAD/ CAM and marked as such on the drawings.

Appendix G: Technical drawing of the side impact beam

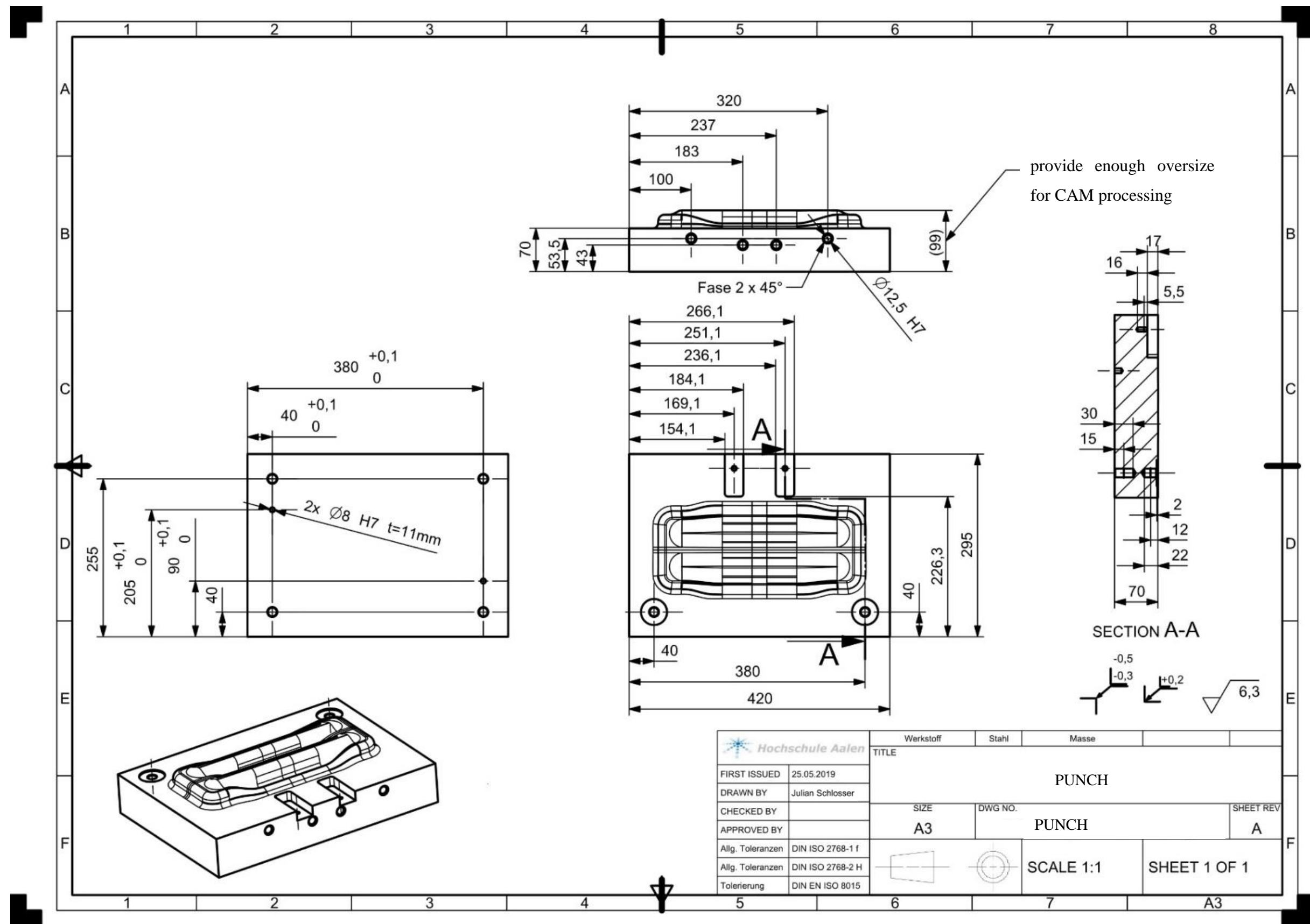




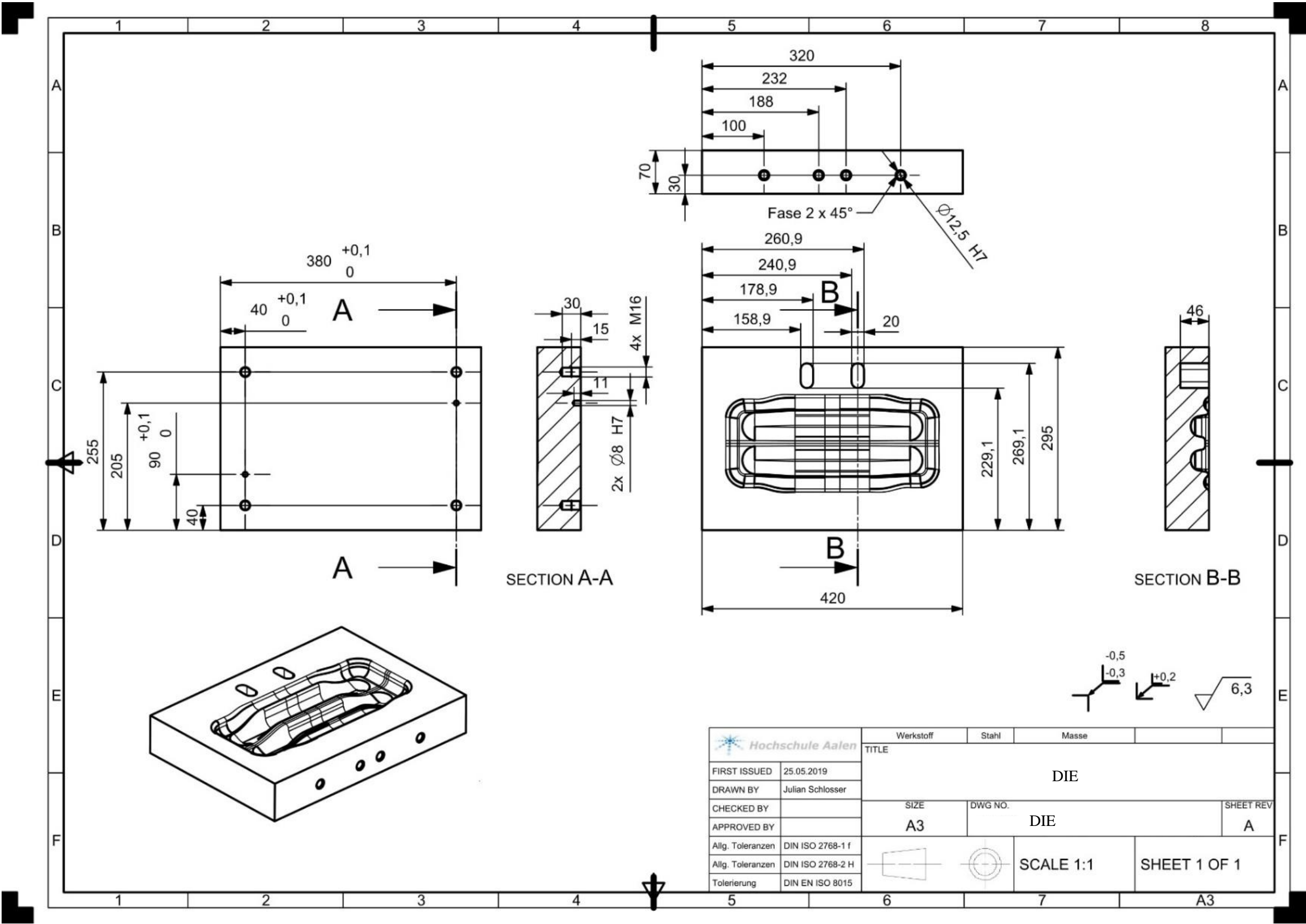
Appendix G: Technical drawing of the heating stage (punch side)

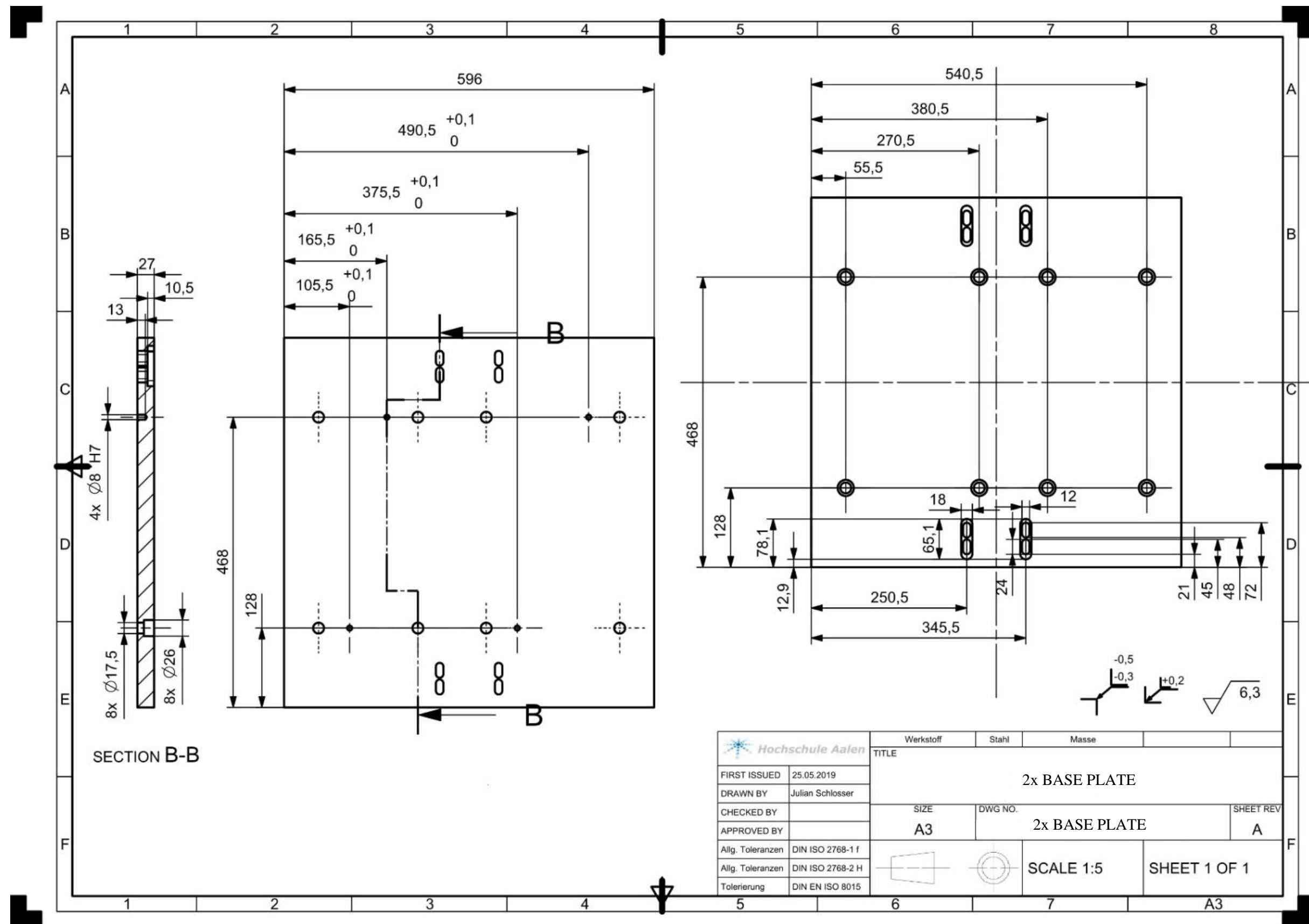


Appendix G: Technical drawing of the punch

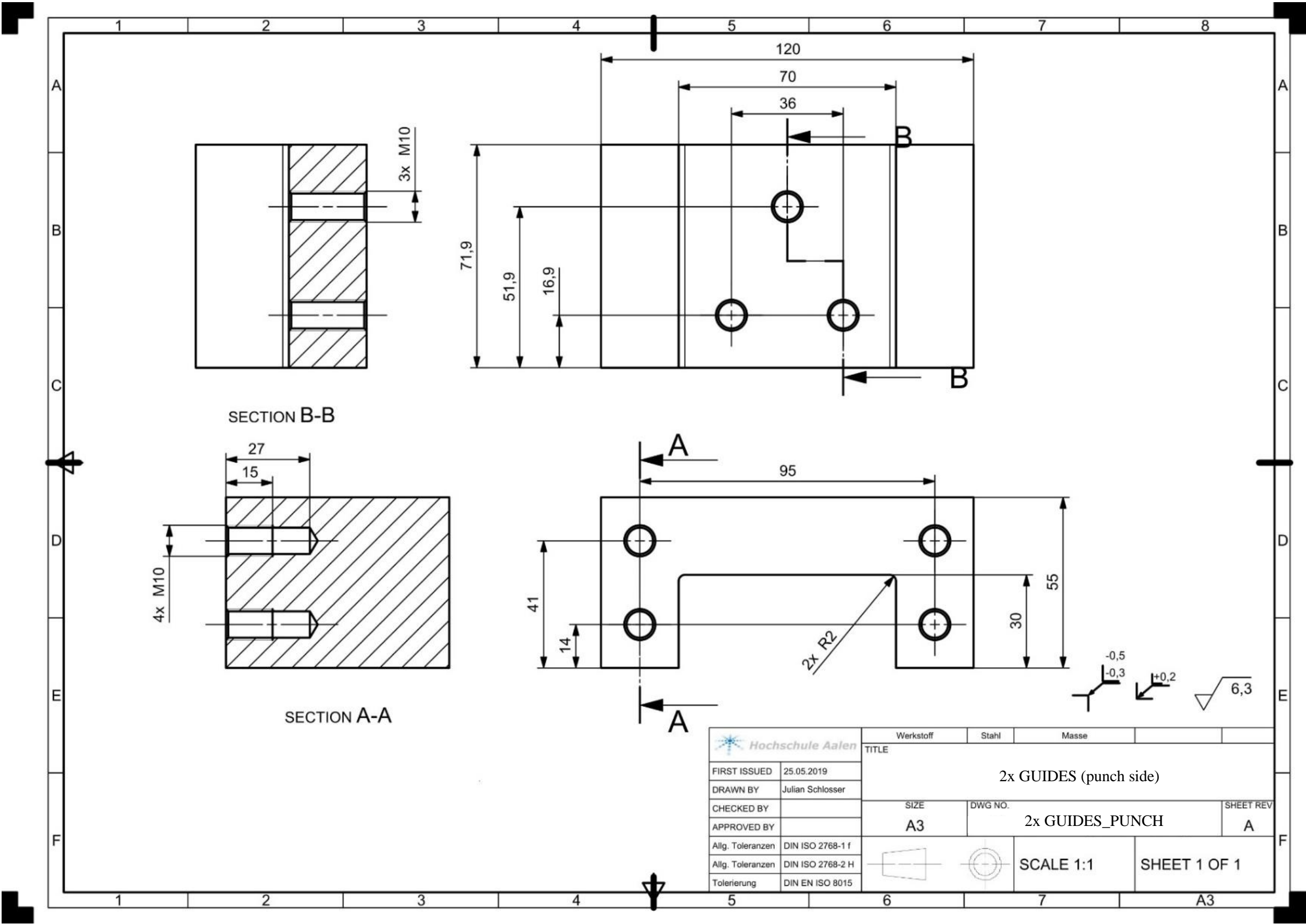


Appendix G: Technical drawing of the die

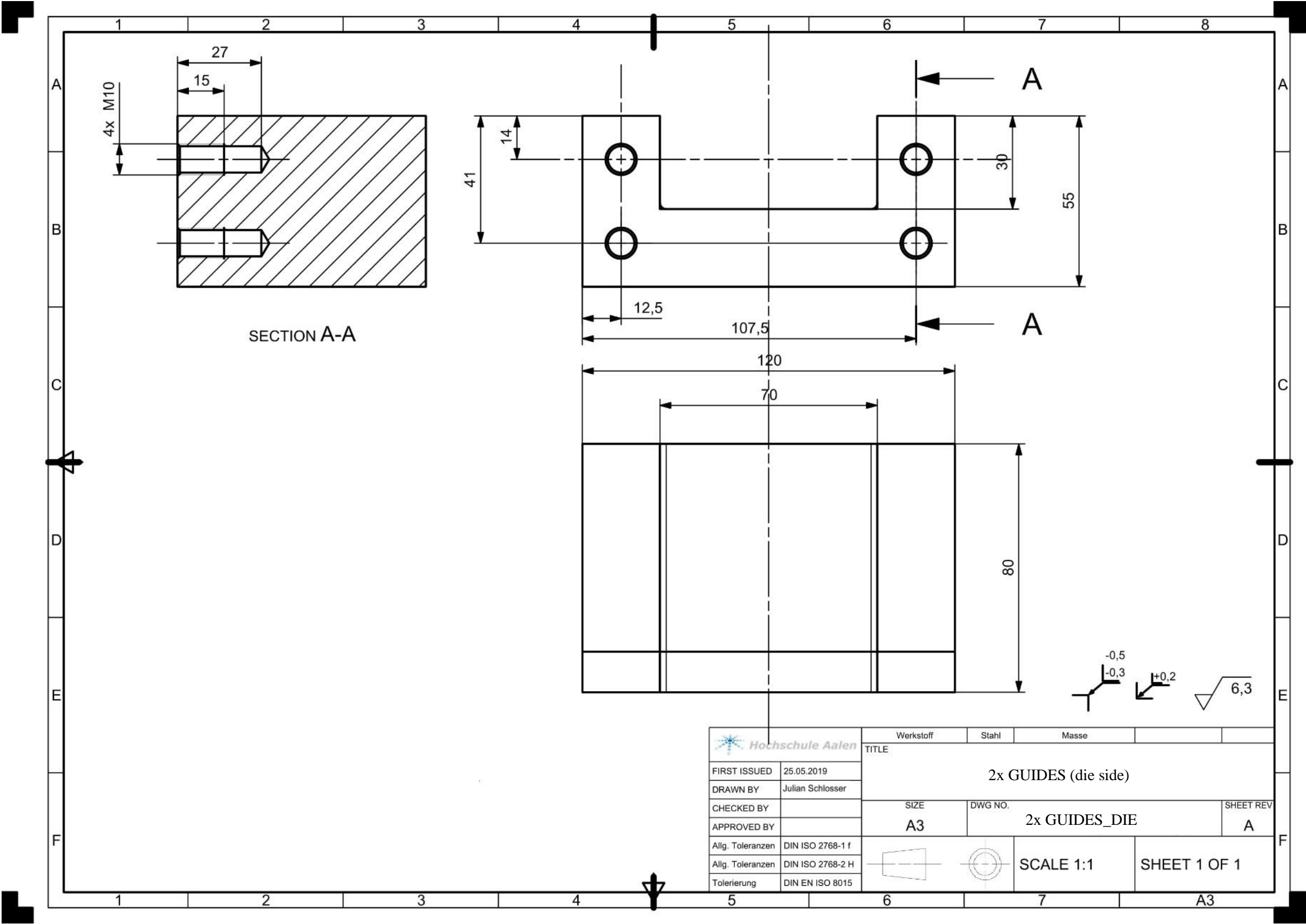




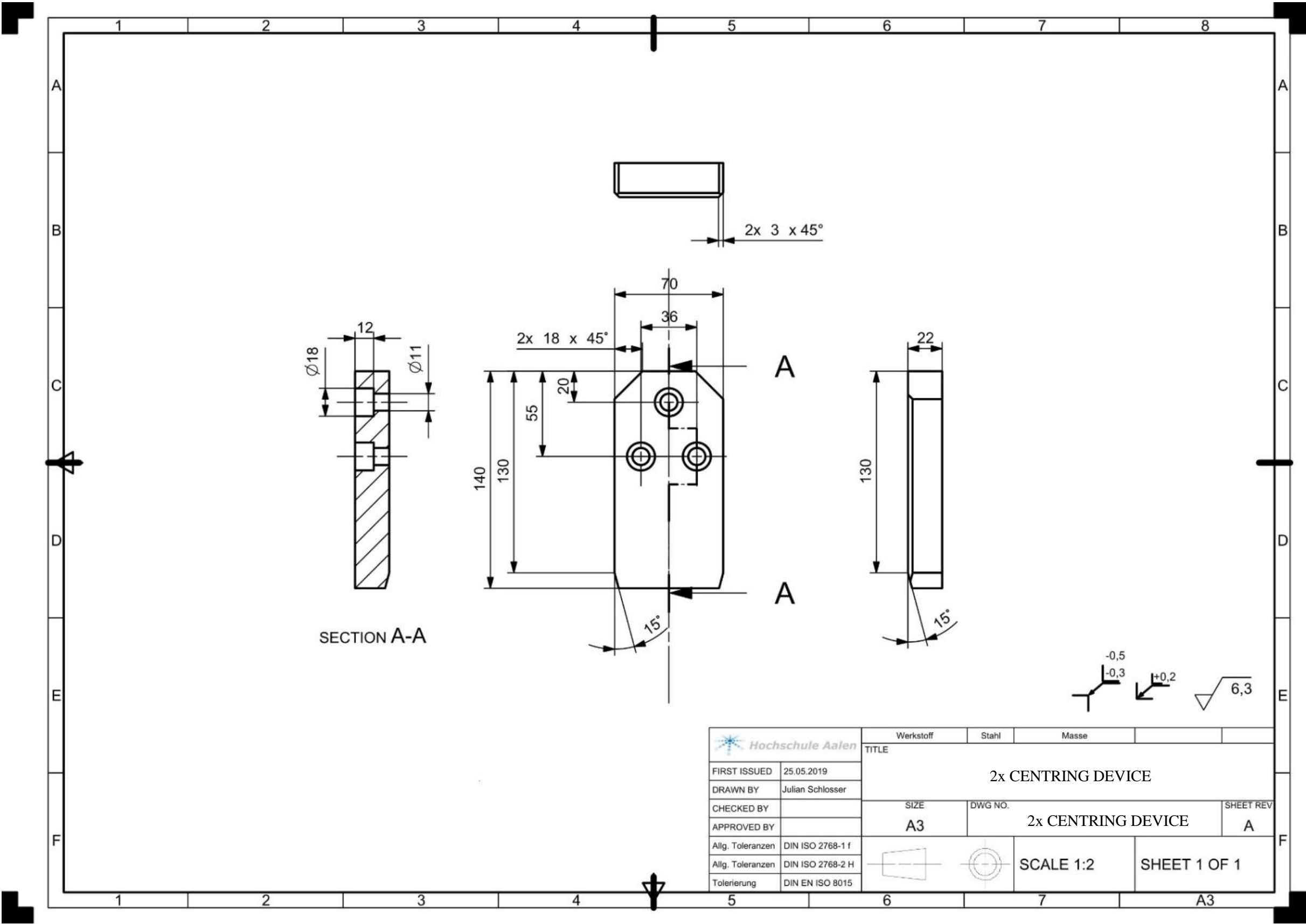
Appendix G: Technical drawing of the guides (punch side)



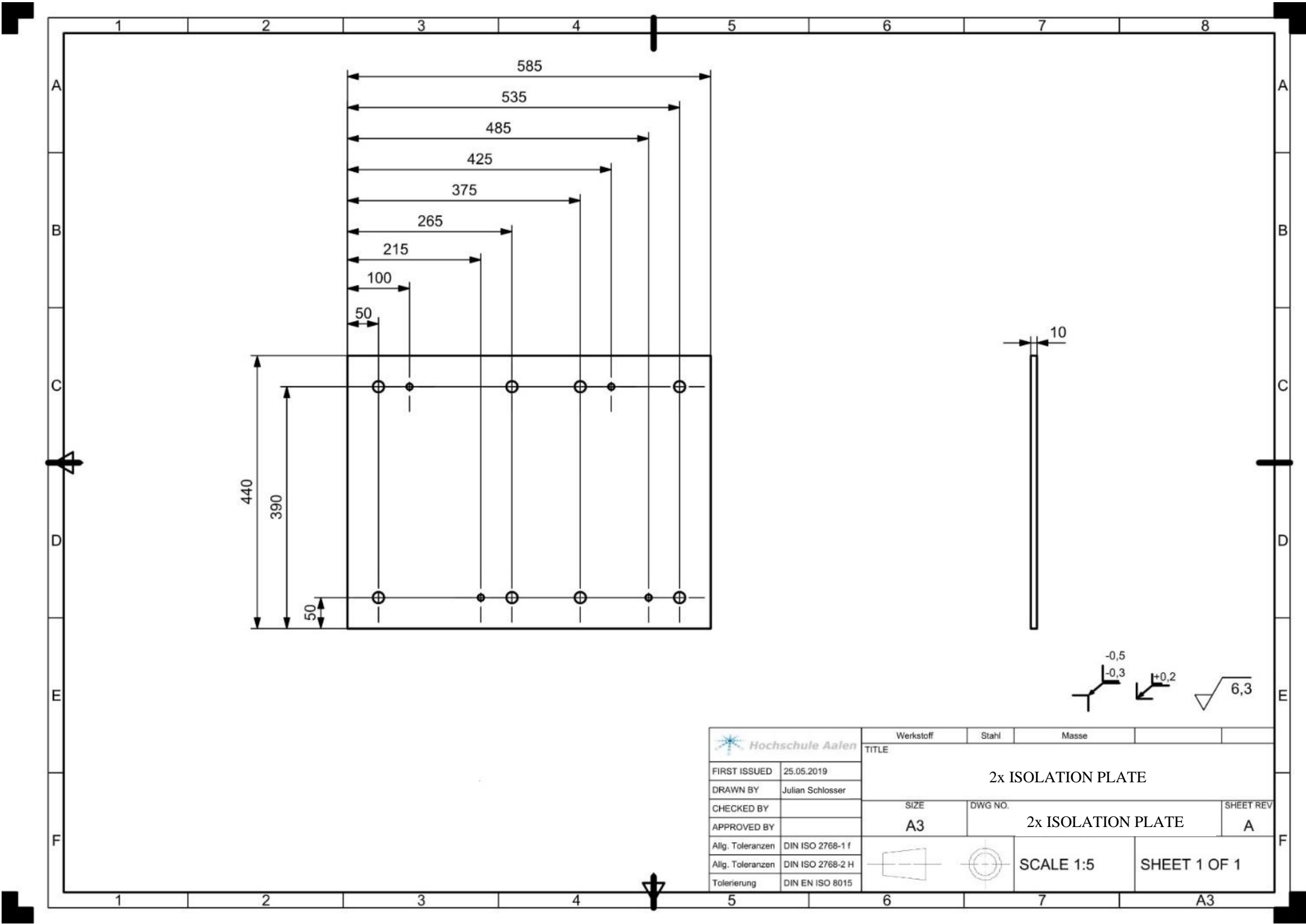
Appendix G: Technical drawing of the guides (die side)



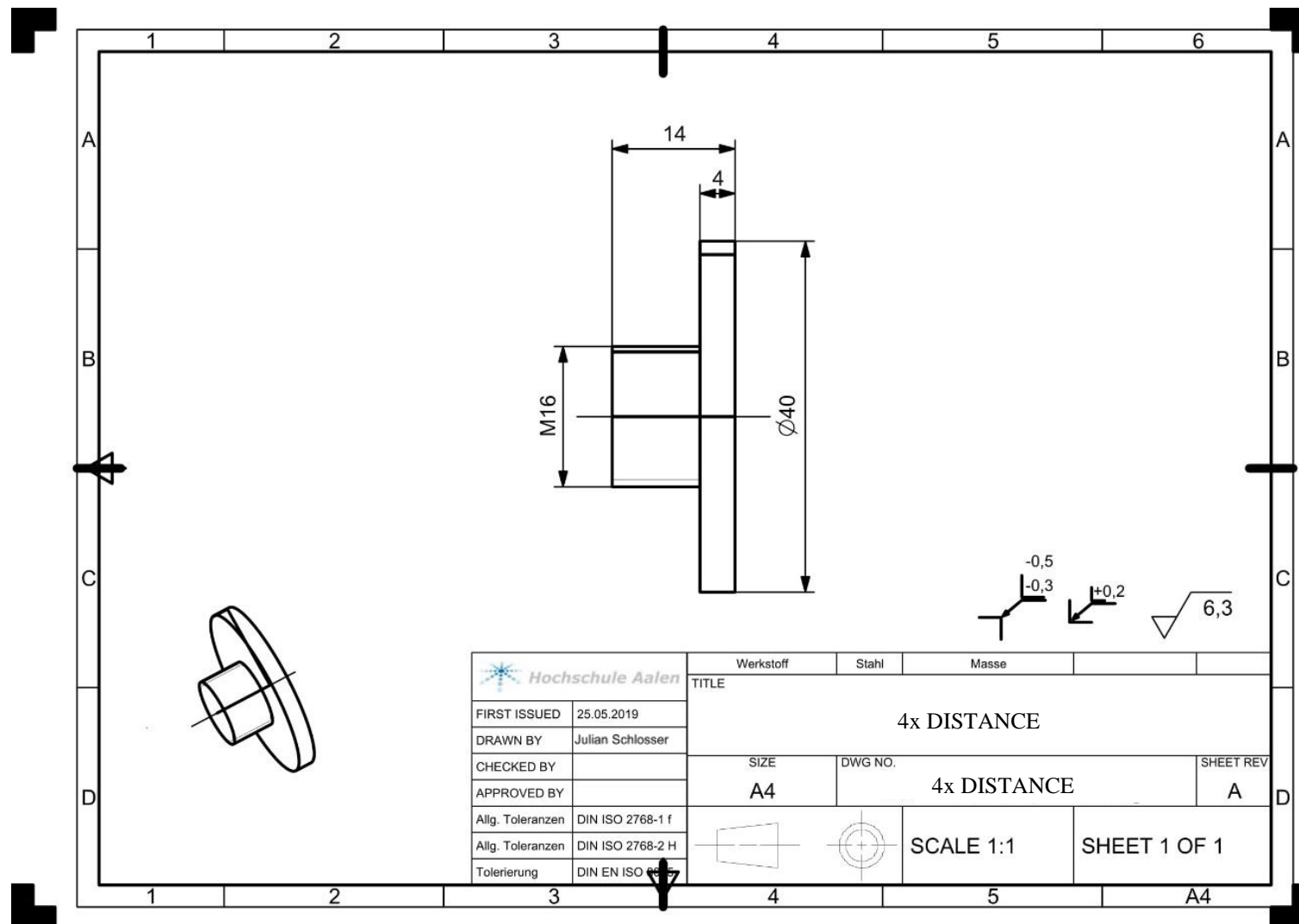
Appendix G: Technical drawing of the centring Device



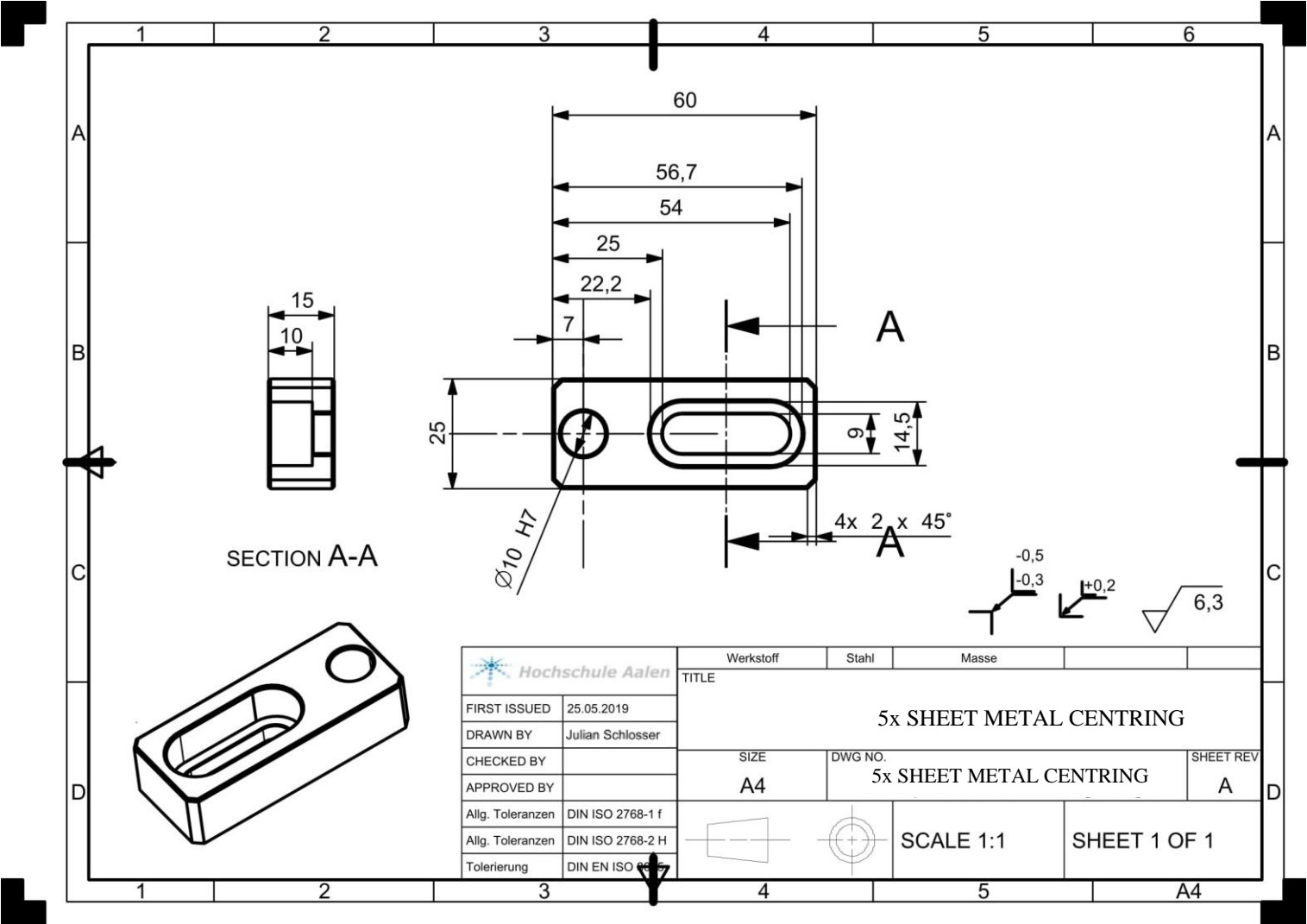
Appendix G: Technical drawing of the isolation plate



Appendix G: Technical drawing of the distance

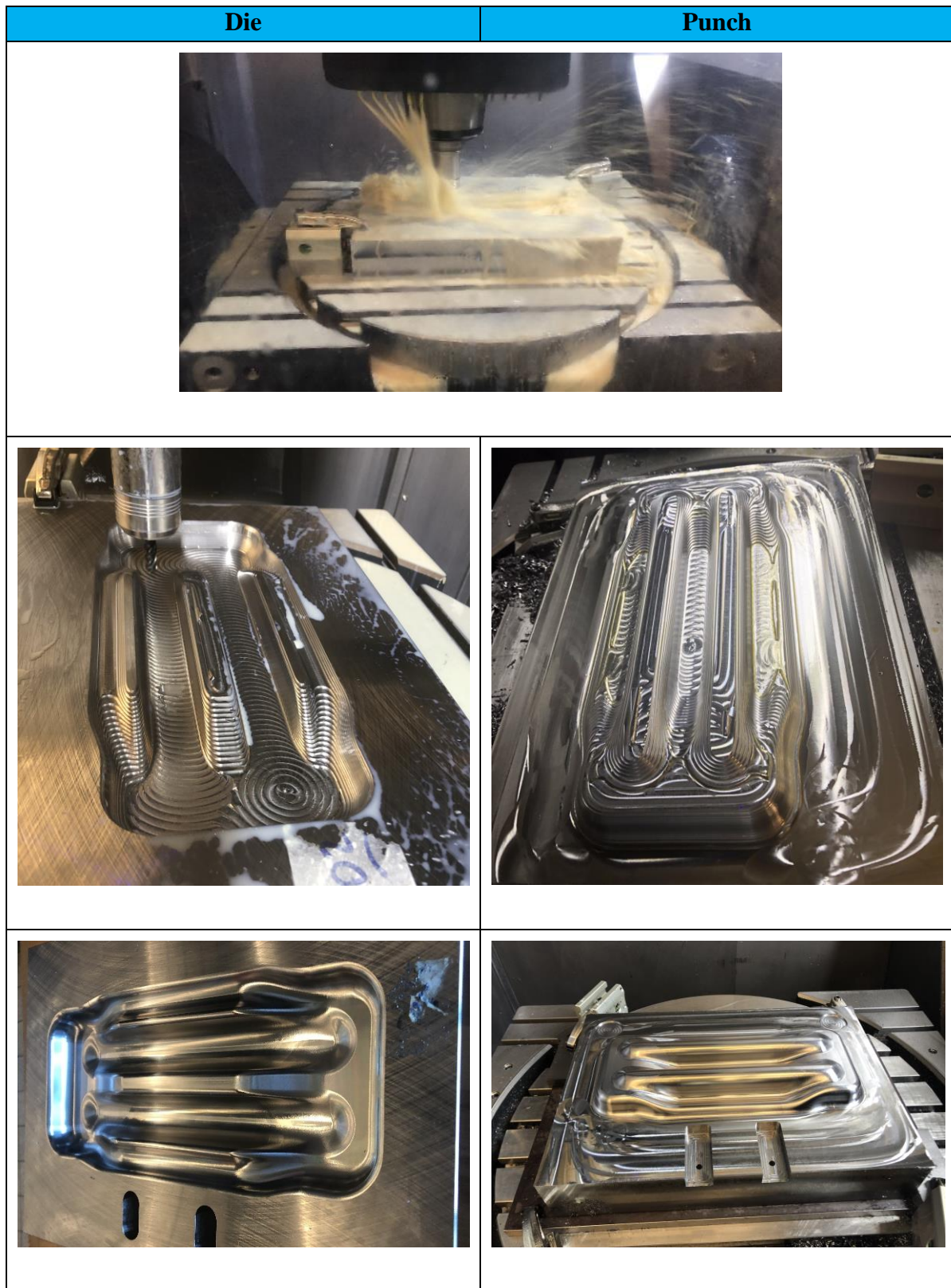


Appendix G: Technical drawing of the sheet metal centring



Appendix H

Appendix H shows pictures of the production of the forming tool. The milling was carried out on a 5-axis machine from DMG Morie (DMU 95).

Appendix H: Progress images of the production of the forming stage

Appendix I

A comparison study on the influence of various heat treatments and forming processes on the strength and elongation of the material was carried out. Furthermore, the figures show the average of strength and elongation and the associated standard deviation.

Appendix I: Detailed overview of the comparison of the different heat treatments and forming processes at elevated temperatures. Hotforming (HT) – grey, W-Temper (WT) – blue, Warm-forming (HW)– brown and the heat treatments without (W) treatment, 1-5 paint bake (1-5PB) cycle

